

School of Molecular and Life Sciences

**Direct-current triboelectricity from miniaturised sliding metal–
monolayer–semiconductor contacts**

Xin Lyu

0000-0002-6506-0392

This thesis is presented for the Degree of

Doctor of Philosophy

of

Curtin University

Mar 2024

Declaration

To the best of my knowledge and belief this thesis contains no material previously published by any other person except where due acknowledgment has been made.

This thesis contains no material which has been accepted for the award of any other degree or diploma in any university.

(Include where applicable)

Human Ethics (For projects involving human participants/tissue, etc) The research presented and reported in this thesis was conducted in accordance with the National Health and Medical Research Council National Statement on Ethical Conduct in Human Research (2007) – updated March 2014. The proposed research study received human research ethics approval from the Curtin University Human Research Ethics Committee (EC00262), Approval Number #.....Not Applicable.....

or

Animal Ethics (For projects involving animal use) The research presented and reported in this thesis was conducted in compliance with the National Health and Medical Research Council Australian code for the care and use of animals for scientific purposes 8th edition (2013). The proposed research study received animal ethics approval from the Curtin University Animal Ethics Committee, Approval Number #.....Not Applicable.....

Signature:

Date:31/03/2024.....

Acknowledgements

The journey towards completing my PhD has been a long and challenging one, and I am deeply grateful to the numerous individuals who have supported me along the way until now.

First and foremost, I extend my sincere gratitude to my supervisor, A/Prof. Simone Ciampi. His guidance, encouragement, and unwavering support have been valuable throughout my doctoral studies. His expertise and mentorship have not only shaped my research but have also contributed significantly to my personal and professional growth. I did enjoy the chats with Simone as they are always helpful and supportive. Also, he is always caring about us, both physically and mentally.

I would also like to express my appreciation to my co-supervisor, Nadim Darwish. Nadim's encouragement, assistance, and camaraderie have made this journey more manageable and enjoyable.

I am also grateful to Dr. Stuart Ferrie for his help in teaching me how to conduct the experiments and use AFM at the beginning of my Ph.D. I'd live to also say thank you for his assistance whenever I encountered challenges with the AFMs and paper writing.

Furthermore, I extend my gratitude to Curtin University, Australian Research Council for providing working space and financial support for my research. Their support played a crucial role in pursuing my academic goals and complete this doctoral journey.

Additionally, I'd also show my gratitude to all my current and former group members and colleagues, including Yan Vogel, Mattia Belotti, Harry Morris Rodriguez, Carlos Hurtado Torres, Malika Peiris, Essam Dief, Soraya Rahpeima, Tiexin Li, Jiayi Chen, and Rundong Mao. It has been a great time working alongside each of you, I have grown

both professionally and personally with our collaborations. And I do appreciate the chats and gatherings whenever I'm happy or down.

Last but not least, I would like to express my heartfelt gratitude to my parents, Fengyin Lyu & Weiqi Jiang and my beloved, Ming Zhang, for their silent but unwavering support throughout my doctoral journey. Their encouragement, understanding, and belief in me have been a constant source of strength and motivation. Despite the distance and challenges, their love and support have remained steadfast, providing me with the foundation and courage to pursue my academic goals.

Copyright Statement

I have received authorization from the copyright holders to utilize any third-party copyrighted materials included in the thesis or to incorporate any of my own previously published work (such as journal articles) for which the copyright is owned by another party (e.g., publisher, co-author). All proofs of copyright permission are in Appendix III & IV.

Table of Contents

Declaration.....	ii
Acknowledgements.....	iii
Copyright Statement	v
Table of Contents	vi
List of Abbreviations.....	ix
List of Publications	x
Abstract	xii
Chapter 1 – General Introduction	- 1 -
1.1 Semiconductor basics.....	- 2 -
1.1.1. Semiconductors electrical properties	- 2 -
1.1.2. Schottky diode and p–n junction	- 4 -
1.1.3. Photoelectric effect at semiconductors	- 7 -
1.1.4. Friction and triboelectric effect	- 9 -
1.1.5. Flexoelectric effect.....	- 12 -
1.2 Improvement of DC-TENGs by surface chemistry.....	- 15 -
1.2.1 Introduction to triboelectric nanogenerators (TENGs)	- 15 -
1.2.2 Surface modification of triboelectric materials	- 21 -
1.3 Conclusion	- 29 -
1.4 References	- 32 -
Chapter 2 – General Experimental.....	- 42 -
2.1 Materials.....	- 43 -
2.1.1 Chemicals.....	- 43 -
2.1.2 Silicon	- 43 -
2.2 Etching mechanism	- 44 -
2.3 Surface passivation and functionalization	- 45 -
2.4 Surface characterization.....	- 46 -
2.4.1 Atomic force microscopy test (AFM).....	- 46 -
2.4.2 Macroscopic current-voltage (I–V) measurement	- 49 -
2.4.3 Contact angle goniometry (CA).....	- 50 -
2.4.4 X-ray photoelectron spectroscopy (XPS).....	- 51 -
2.5 References	- 52 -
Chapter 3 – Sliding Schottky diode triboelectric nanogenerators with current output of 10^9 A/m² by molecular engineering of Si(211) surfaces	- 54 -
Abstract	- 55 -
3.1 Introduction.....	- 56 -
3.2 Experimental section.....	- 59 -
3.2.1. Materials.....	- 59 -

3.2.2.	Surface modification procedures.....	- 59 -
3.2.4.	Current–voltage measurements of static junctions.....	- 63 -
3.2.5.	Electrochemical measurements.....	- 63 -
3.2.6.	X-Ray photoelectron spectroscopy	- 64 -
3.2.7.	Contact angle goniometry	- 65 -
3.2.8.	Time-resolved photocurrent mapping	- 65 -
3.3	Results and discussion.....	- 65 -
3.3.1.	Stick-slip friction on silicon does not govern the zero-bias DC tribocurrent output	- 71 -
3.3.2.	Augmenting zero-bias DC tribocurrent with surface chemistry ..	- 77 -
3.3.3.	Sliding Schottky diodes on Si(211)	- 81 -
3.3.4.	Links between static and dynamic charge transport characteristics..	- 83 -
3.3.5.	Surface-recombination velocities and tribocurrent.....	- 85 -
3.4	Conclusion	- 88 -
3.5	References	- 90 -
Chapter 4 – Direct-current output of silicon–organic monolayer–platinum Schottky TENGs: Elusive friction-output relationship.....		
	Abstract	- 99 -
4.1	Introduction.....	- 101 -
4.2	Experimental section.....	- 103 -
4.2.1	Materials.....	- 103 -
4.2.2	Surface modification	- 103 -
4.2.3	Atomic force microscopy (AFM)	- 104 -
4.2.4	Macroscopic current-voltage (I–V) measurements with soft metal contacts.....	- 105 -
4.2.5	X-ray photoelectron spectroscopy (XPS).....	- 106 -
4.3	Results and discussion.....	- 106 -
4.3.1	Relationship between zero-bias current and friction	- 109 -
4.3.2	Carbon chain length and tribocurrent.....	- 115 -
4.3.3	Flexovoltage in static junctions.....	- 116 -
4.4	Conclusion	- 120 -
4.5	References	- 121 -
Chapter 5 – Silicon-based triboelectric nanogenerators: surface chemistry isotope effects on the device performances and durability		
	Abstract	- 129 -
5.1	Introduction.....	- 130 -
5.2	Experimental section.....	- 132 -
5.2.1.	Chemicals.....	- 132 -
5.2.2.	Surface functionalization.....	- 132 -
5.2.3.	Atomic force microscopy (AFM)	- 134 -
5.2.4.	X-ray photoelectron spectroscopy.....	- 135 -
5.2.5.	Transient photocurrent mapping (PCM)	- 135 -

5.3	Results and discussion.....	- 135 -
5.3.1.	Optimization of Si–D surface preparation.....	- 138 -
5.3.2.	Zero-bias current on monolayer-modified Si–D and Si–H samples	- 140 -
5.3.3.	Triboelectric and flexoelectric effect on Si–D and Si–H samples-	- 143 -
5.4	Conclusions.....	- 148 -
5.5	References	- 149 -
Chapter 6 – Conclusion and future outlook.....		- 157 -
6.1.	Conclusion	- 158 -
6.2.	Future Outlook	- 159 -
Appendix I.....		- 162 -
	Determination of the binding configuration for the 8-nonyl-1-ol monolayer	- 162 -
Appendix II.....		- 164 -
	Estimation of AFM platinum tip–silicon contact area	- 164 -
Appendix III.....		- 166 -
	Statement of Contribution.....	- 166 -
Appendix IV		- 171 -
	Copyright Permission	- 171 -

List of Abbreviations

AC	alternate current
AFM	atomic force microscopy
C-AFM	conductive atomic force microscopy
CA	contact angle
CuAAC	Copper-catalysed azide-alkyne coupling
CV	cyclic voltammetry
CZ	Czochralski process
DC	direct current
DCM	dichloromethane
DMT	Derjaguin–Muller–Toporov
e–h	electron–hole
F–d	force–distance
FWHM	full width half maximum
FZ	float-zone process
I–V	current–potential
PCM	photocurrent mapping
TENGs	triboelectric nanogenerators
UV	ultraviolet
XPS	x-ray photoelectron spectroscopy

List of Publications

First-author publications

1. [Lyu, X.](#), MacGregor, M., Liu, J., Darwish, N. & Ciampi, S. Direct-current output of silicon–organic monolayer–platinum Schottky TENGs: Elusive friction-output relationship. *Nano Energy* **2023**, 108627.
2. [Lyu, X.](#), Ferrie, S., Pivrikas, A., MacGregor, M. & Ciampi, S. Sliding Schottky diode triboelectric nanogenerators with current output of 10^9A/m^2 by molecular engineering of Si(211) surfaces. *Nano Energy* **2022**, 107658.
3. [Lyu, X.](#) & Ciampi, S. Improving the performances of direct-current triboelectric nanogenerators with surface chemistry. *Curr. Opin. Colloid Interface Sci* **2022**, 101627.
4. [Lyu, X.](#), MacGregor, M., Darwish, N. & Ciampi, S. Silicon-based triboelectric nanogenerators: surface chemistry isotope effects on the device performances and durability. *Friction* (In press)

Co-author publications

5. Hurtado, C.; [Lyu, X.](#); Ferrie, S.; Le Brun, A. P.; MacGregor, M.; Ciampi, S., Organic monolayers on Si(211) for triboelectricity generation: etching optimization and relationship between the electrochemistry and current output. *ACS Appl. Nano Mater* **2022**, 14263–14274
6. Zhang, S.; [Lyu, X.](#); Hurtado Torres, C.; Darwish, N.; Ciampi, S., Non-Ideal cyclic voltammetry of redox monolayers on silicon electrodes: peak splitting is caused by heterogeneous photocurrents and not by molecular disorder. *Langmuir* **2022**, 743–750.

-
7. Belotti, M.; Lyu, X.; Xu, L.; Halat, P.; Darwish, N.; Silvester, D. S.; Goh, C.; Izgorodina, E. I.; Coote, M. L.; Ciampi, S., Experimental evidence of long-lived electric fields of ionic liquid bilayers. *J. Am. Chem. Soc.* **2021**, 17431–17440.
 8. Li, T.; Dief, E. M.; Lyu, X.; Rahpeima, S.; Ciampi, S.; Darwish, N., Nanoscale silicon oxide reduces electron transfer kinetics of surface-bound ferrocene monolayers on silicon. *J. Phys. Chem. C* **2021**, 27763–27770
 9. Zhang, S.; Ferrie, S.; Peiris, C. R.; Lyu, X.; Vogel, Y. B.; Darwish, N.; Ciampi, S., Common background signals in voltammograms of crystalline silicon electrodes are reversible silica–silicon redox chemistry at highly conductive surface sites. *J. Am. Chem. Soc.* **2021**, 1267–1272.
 10. Zhang, S.; Ferrie, S.; Lyu, X.; Xia, Y.; Darwish, N.; Wang, Z.; Ciampi, S., Absence of a relationship between surface conductivity and electrochemical rates: redox-active monolayers on Si(211), Si(111), and Si(110). *J. Phys. Chem. C* **2021**, 18197–18203.

Abstract

Chapter 1 provides an overview of the principles and concepts integral to this research. Given the research focus is on metal–monolayer–semiconductor Schottky diode-based direct-current (DC) triboelectric nanogenerators (TENGs), a basic discussion on semiconductors principles, particularly with a focus on silicon, assume a central role. Consequently, this section delves into semiconductor fundamentals, including the meaning, purpose and practical value of band diagrams, the concept of Schottky and p–n junctions, and the rectification characteristics. These concepts are important for a deeper comprehension of the working mechanisms of TENGs, expounded upon in Chapters 3 and 4.

Furthermore, the first chapter introduces the photoelectric effect, which share several features with the triboelectric effect, considered the primary working mechanism of TENGs. A discussion on the photoelectric effect is particularly relevant as it aids in determining surface defects and recombination velocities, which are crucial factors influencing the direct-current generation of TENGs (Chapter 3). Towards the conclusion of this section, attention is also given to the flexoelectric effect at semiconductor surfaces. Recent studies suggest flexoelectricity is an important contributor to zero-bias current generation in TENGs alongside the triboelectric effect (Chapter 4).

Moreover, the chapter addresses basic concepts of semiconductor surface chemistry. Surface chemistry, especially monolayer chemistry, not only protects against oxidation of the substrate but also enhances electrical performance. To augment this discussion, a review article I co-authored on improving the performances and durability of DC-TENGs through surface chemistry is referenced, providing additional insights. This comprehensive approach establishes a solid foundation for the subsequent chapters, fostering a holistic understanding of the research context.

Chapter 2 gives an overview of the key chemical substances and semiconductor materials used in the study and their relevant physical and chemical properties. It

primarily discusses the crystal structure of silicon, the two manufacturing methods for silicon wafers (float-zone and Czochralski) and the differences between them.

Considering that this study involves primarily the use of silicon wafers with two different orientations, (211) and (111), the orientation of a silicon crystal will also be briefly discussed in this chapter. Additionally, it outlines the basic working principles of the main experimental equipment used in this research and their main roles in the context of this research.

Chapter 3 is based on a published paper titled “Sliding Schottky diode triboelectric nanogenerators with current output of 10^9 A/m² by molecular engineering of Si(211) surfaces”. Here I will discuss how by achieving molecular precision control on both the surface chemistry and surface trap density of an underexplored Si crystal cut – Si(211) – it was possible to reach zero-applied-bias current densities as high as 10^9 A/m², which surpasses by nearly three orders of magnitude the previous record for devices of this class (DC sliding Schottky diodes) set to 10^6 A/m² by Thundat and co-workers in 2018 (*Nat. Nanotechnol.* **2018**, 13, 2, 112).

Additionally, I found that molecular engineering of Si(211) with proton-exchangeable organic monolayers augments DC output, and record currents are obtained with surface chemistries that cause increased surface recombination velocities coupled to large surface dipoles in the form of surface alkoxide anions (Si-organic monolayer-O⁻).

Chapter 4 is based on a published paper titled “Direct-current output of silicon-organic monolayer-platinum Schottky TENGs: Elusive friction-output relationship”. Through precise control of silicon surface chemistry and conducting parallel experiments with conductive and non-conductive AFM, this chapter examines the significance of surface static voltage and flexovoltage. The data presented reveals that a static electricity-related tribovoltage may contribute to excess friction, particularly dependent on the doping level and type of silicon substrate. Interestingly, this excess friction becomes undetectable when current flows across the junction, suggesting an electrostatic origin of friction in silicon-based Schottky TENGs and implying that DC current partially neutralizes static charges. Additionally, the sign of

zero-bias tribocurrent, rather than its magnitude, appears independent of semiconductor doping type, indicating surface statics as a primary contributor to the zero-bias output. The chapter also uncovers the presence of a junction flexovoltage under typical pressures in AFM experiments. In a static Pt–monolayer–n-type Si junction, the flexovoltage aligns with the tribovoltage and can surpass external voltages up to 2V.

These findings suggest that flexovoltage likely contributes significantly to the zero-bias output of an n-Si Schottky TENG, negatively impacts the output of a p-Si TENG, and can be easily detected. Specifically, flexoelectricity manifests as an "inverted diode," where a negligible current flows even when the n-type Si–platinum diode is negatively biased, as long as the "static" diode remains under significant normal pressure.

Chapter 5 is based on a manuscript currently under review by the journal *Friction*. The manuscript is titled "Silicon-based triboelectric nanogenerators: surface chemistry isotope effect on device performance and durability". As the title indicated, the work seeks to verify or falsify a particular isotope effect on TENG's performances. Typically, silicon modification begins with an oxide-free, hydrogen-terminated surface (Si–H). Replacing hydrogen with its heavier isotope, deuterium (Si–D), does not impede established surface chemistry procedures and may improve the semiconductor's resistance to anodic decomposition. To date a systematic comparison between Si–H and Si–D surfaces as a TENG substrate is lacking. Such comparison is important as deuterium atoms chemisorbed on a silicon surface are harder to remove than hydrogen, and it has been suggested that deuterium-terminated silicon surfaces are less prone to oxidation than their hydrogen counterpart. The surface energy of Si–D (2.67 eV) is lower than that of Si–H (3.90 eV), which also suggests higher stability for the former. Recent research on nanoscale friction has also demonstrated lower friction on deuterium-terminated silicon surfaces compared to hydrogen-terminated ones.

Chapter 6 draws the conclusions for this doctoral study and suggests further directions and experiments relevant to this booming area of research at the intersection of chemistry, electrochemistry, physics, and electronics.

Chapter 1 – General Introduction

In this chapter, basic concepts on semiconductors, Schottky diodes, p–n junctions, photoelectric effect, triboelectric effect and flexoelectric effect will be discussed to facilitate a better understanding of the goals and objectives of this study. These concepts form the basis for achieving DC tribocurrent output. The second part of the chapter is based on a published review that has as its focus improvement of DC-TENGs through surface chemistry means, and its purpose is to help the reader in building a general and yet broad picture of the current research activities in the context of TENGs. The chapter also outlines the key research questions addressed in this study.

1.1 Semiconductor basics

Despite the primary target audience of this paper being individuals with a background in chemical research, and even though the experiments conducted in the research primarily pertain to surface chemistry, the exploration of semiconductor's physical characterization within this study remains crucial. Concepts related to the physical properties of semiconductors, such as the conduction band, valence band, p–n junctions, and Schottky junctions, will be briefly introduced here. These concepts lay the foundation for later discussions on triboelectricity, flexoelectricity and photocurrent decay in the subsequent chapters, both of which are integral to the broader scope of this research, as referenced in the following chapters.

1.1.1. Semiconductors electrical properties

Commonly, in conductors, such as metal, the negligible energy gap ($10^{-21}\sim 10^{-23}$ eV) between adjacent energy level (valence band and conductance band) allows charge carriers (electrons or holes) to easily gain sufficient energy and jump to a higher energy level, facilitating electrical conductivity. In contrast, insulating materials have a relatively large energy gap (typically > 9 eV) [1], making it difficult for electrons to jump to a higher energy level, resulting in poor electrical conductivity. Semiconductors fall between these two conditions. Figure 1.1 illustrates the band diagram of an ideal intrinsic semiconductor. In semiconductors, the conduction band and valence band are not overlapped like conductors, nor do they exhibit a large gap like insulators. In semiconductors and insulators, the valence band represents the uppermost range of electron energies (E_v) occupied at absolute zero temperature, whereas the conduction band represents the lowest range of available electronic states (E_c). The two bands are separated by band gap ($E_g = E_c - E_v$) [2]. The reference energy level is the energy of an electron in vacuum (E_{vac}). The electron density arrangement in the semiconductor is described by Fermi–Dirac equation [3]:

$$P_{Fermi-Dirac}(E) = 1 / \left[1 + \exp\left(\frac{E - E_f}{kT}\right) \right] \quad (1-1)$$

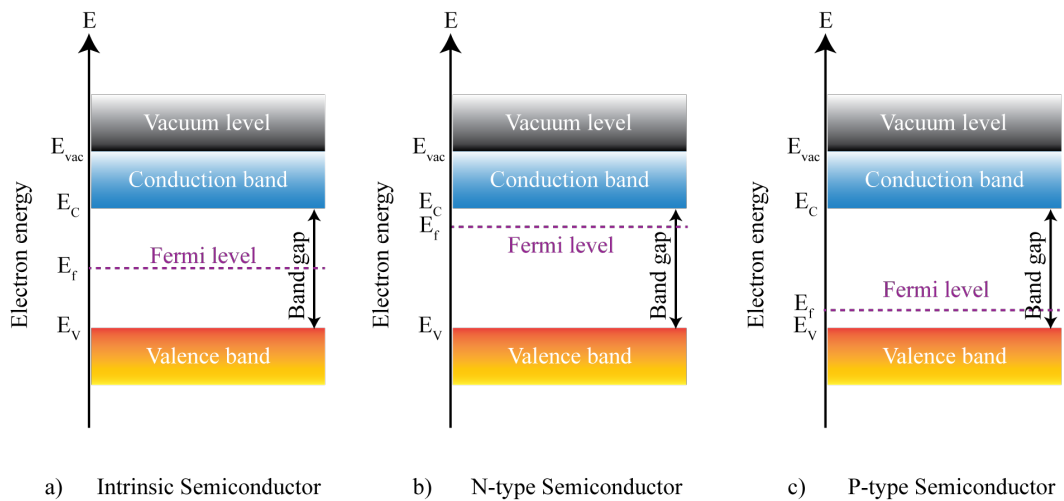


Figure 1.1. Band diagram of a) pure semiconductor at 0 K, b) n-type semiconductor, and c) p-type semiconductor. For a) intrinsic semiconductor, the outer electron shells are entirely occupied because of covalent bonds between atoms, leading to the absence of free electrons. Consequently, the valence band is fully occupied, while the conduction band remains entirely unoccupied. And the Fermi level locates at the center of band gap. For b) n-type and c) p-type semiconductor, the introduction of impurities leads to the shift of Fermi level either towards the conduction band or valence band.

Where P is the probability that a particle will have energy E , k is the Boltzmann constant, equals to 1.380649×10^{-23} J/K, and T is temperature in Kelvin.

It indicates the probability of occupancy of an electron at the energy level (E) relative to Fermi level (E_f), named in honour of physicist Enrico Fermi, which is a fundamental principle in quantum mechanics and statistical mechanics. From formula (1-1), it is easily seen that Fermi level (E_f) denotes the energy level where there is a 50% likelihood of electrons in a system being occupied.

Intrinsic semiconductors, also called undoped semiconductors, are those that remain in their pure state without any intentional doping. In intrinsic semiconductors, the concentrations of electrons and holes are approximately equal (represented by n_i), indicating that the Fermi level locates at the centre of the band gap. which exhibits the feature shown in Figure 1.1a. On the other hand, extrinsic semiconductors undergo intentional alterations in their conductivity properties through the introduction of impurity atoms. Doping, comes in two forms: n-type and p-type. n-type doping involves adding electron donor impurities, such as phosphorus or

arsenic, which introduce excess electrons, thereby increasing electron concentration and conductivity, leading to the shift of Fermi level towards the conduction band (Figure 1.1b). Conversely, p-type doping introduces electron acceptor impurities like boron or indium, increasing hole concentration, consequently enhancing conductivity, leading to the shift of Fermi level towards the valence band (Figure 1.1c). The concentration of added donor or acceptor impurities is typically represented by N_d and N_a correspondingly.

1.1.2. Schottky diode and p–n junction

Extrinsic semiconductors could form p–n junction with themselves, and Schottky diode with metal materials. Such structures can control the flow of current in electronic devices. Therefore, this is the structure commonly utilized by many direct-current triboelectric nanogenerators (DC-TENGs). The mechanisms for them to achieve this is a bit different. Because these two structures, especially the Schottky diode, will be frequently mentioned in the upcoming chapters, the fundamental principles for controlling the direction of current flow will be briefly explained here.

A p–n junction, as the name implies, is formed by connecting p-type and n-type semiconductors. Due to the large concentration of electrons in the n-type semiconductor and the large concentration of holes in the p-type semiconductor, a diffusion process of electrons and holes occurs to balance their average electrochemical potential (i.e. to align the Fermi level). Initially, recombination mainly occurs at the interface, involving electrons from the n-type semiconductor and holes from the p-type semiconductor. However, this process rapidly reaches equilibrium with a resulting positive charge (ionised dopants) on the n-type semiconductor side, caused by a reduction in electrons, and a negative charge on the p-type semiconductor side (ionised dopants), resulting from a reduction in holes [4]. This establishes a built-in electric field (V_{bi}) at the interface, oriented from the n-type semiconductor to the p-type semiconductor. The magnitude of such electric field is expressed by:

$$V_{bi} = \frac{kT}{e} \ln \left(\frac{N_a N_d}{n_i^2} \right) \quad (1-2)$$

Where N_a is the concentration of acceptor impurities, N_d is the concentration of donor impurities, and n_i is the intrinsic carrier concentration. And the space charge region at the interface is call depletion region (Figure 1.2a, upper plot). Corresponding band diagram is illustrated in Figure 1.2a (lower plot). In equilibrium state, the matching of the Fermi levels is essential to ensure no directional movement of charge and maintain a zero-current condition. As a result, the conduction band and valence band will bend at the interface, forming a barrier, hindering further diffusion of charge carriers.

When a positive bias is applied to the side of p-type side, the external electric field orients from p-type semiconductor to n-type semiconductor inside the p–n junction, which is opposite to the built-in electric field. After the bias overcomes the built-in potential, the excessive holes in p-type semiconductor continuously flows to n-type semiconductor while the excessive electrons in n-type semiconductor flows to p-type semiconductor, forming the continuous current flow. This bias regime is called forward bias. In a band diagram, this is represented by a lowered barrier, allowing charge carriers to accelerate under the applied external electric field. Contrarily, if the positive bias is applied to the n-type semiconductor, the external electric field share the same direction with the built-in electric field, which broadens the depletion region and further restricts the movement of electrons and holes. Therefore, no current flow can be detected. This is the so-called reverse bias regime.

Similarly, a Schottky diode is formed by connecting the metal and doped semiconductor [5]. Here, I take the example of an n-type semiconductor and a metal with large work function, such as platinum. The semiconductor's work function is generally smaller than that of metals. Therefore, when a metal, such as platinum, contacts a semiconductor (taking n-type as an example), electrons flow from the semiconductor into the metal. At the surface of the semiconductor, a space charge region (depletion region) composed of ions carrying positive charges is formed

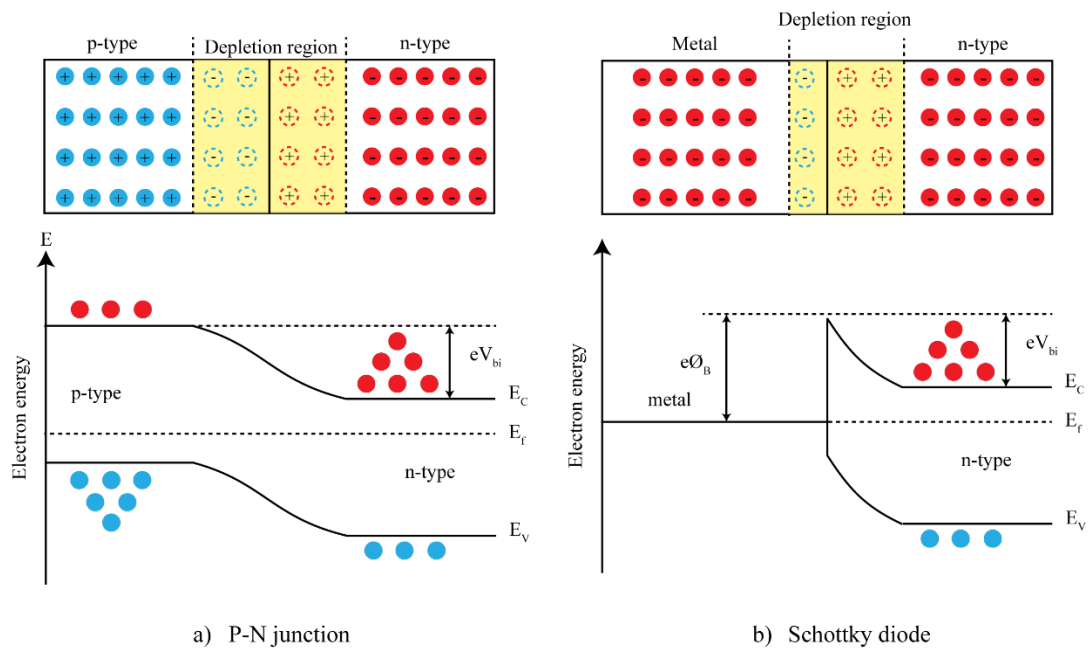


Figure 1.2. Scheme and band diagram of a) p–n junction and b) of a Schottky diode. E_v represents the energy level at the top of valance band, E_f is the Fermi level, E_c represents the energy level at the bottom of conduction band, V_{bi} represents the built-in voltage, Φ_B represents the Schottky barrier, e represents the elementary charge.

(Figure 1.2b, upper plot) [6]. Due to the presence of abundant free electrons in the metal, compared to the space charge region in semiconductor, the region in metal is negligible. As a result, there is a built-in electric field (V_{bi}), mainly existing in the semiconductor, directed from the n-type semiconductor to the metal within the region, creating a barrier (Schottky barrier, Φ_B) that prevents electrons in the semiconductor from flowing into the metal. Like a p–n junction, when the positive voltage is applied to the metal, the Schottky diode is in the condition of forward bias and vice versa.

Whether it is a p–n junction or a Schottky diode, their rectification characteristic is the foundation of many semiconductor-based DC triboelectric nanogenerators (DC-TENGs). And the surface chemistry can affect interfacial properties, such as work function, adhesion, and friction. All these factors could potentially influence the performance of DC-TENG. Therefore, many researchers enhance the performance of DC-TENGs by chemically modifying semiconductor or metal materials. This thesis primarily focuses on surface functionalization of silicon, then forming Schottky diode

with metals, and eventually achieving direct current (DC) electricity output through relative sliding movement.

1.1.3. Photoelectric effect at semiconductors

Although the photoelectric effect is not the primary working mechanism of most DC-TENGs, the commonly accepted working principle of DC-TENGs bears significant resemblance to the photoelectric effect. Many concepts in related studies are borrowed from the photoelectric concept. Additionally, since a degree of illumination is almost ubiquitous, photoelectric effects may also influence the output of tribocurrent on semiconductor devices. Therefore, this section will briefly discuss the photoelectric effect and related concepts in semiconductor devices.

For p–n and Schottky junctions, in the absence of external influences, the generation and recombination of e–h pairs reach dynamic equilibrium at the interface. Illumination of the junction will induce the generation of excess e–h pairs, break this equilibrium, hence causing the photoelectric effect. The photoelectric effect can be categorized into external and internal photoelectric effects.

The external photoelectric effect refers to the physical phenomenon in which a material emits electrons outward from its surface when illuminated by a beam of light. The emitted electrons are called "photoelectrons." Internal photoelectric effect refers to a phenomenon in which the illumination causes a change in the electrical conductivity of the materials or generating a photo-induced voltage. This usually happens in intrinsic semiconductors [7].

For internal photoelectric effect, it can be divided into photoconductive effect and photovoltaic effect. In intrinsic semiconductors, electrons in the valence band will be excited to the conduction band under illumination with energy greater than band gap, causing an increase in the conductivity of the semiconductor. This is the so-called photoconductive effect.

Photovoltaic effect is of our great interest and was firstly observed by Edmond Becquerel in 1839 [8]. It usually occurs in non-uniform semiconductors (for example,

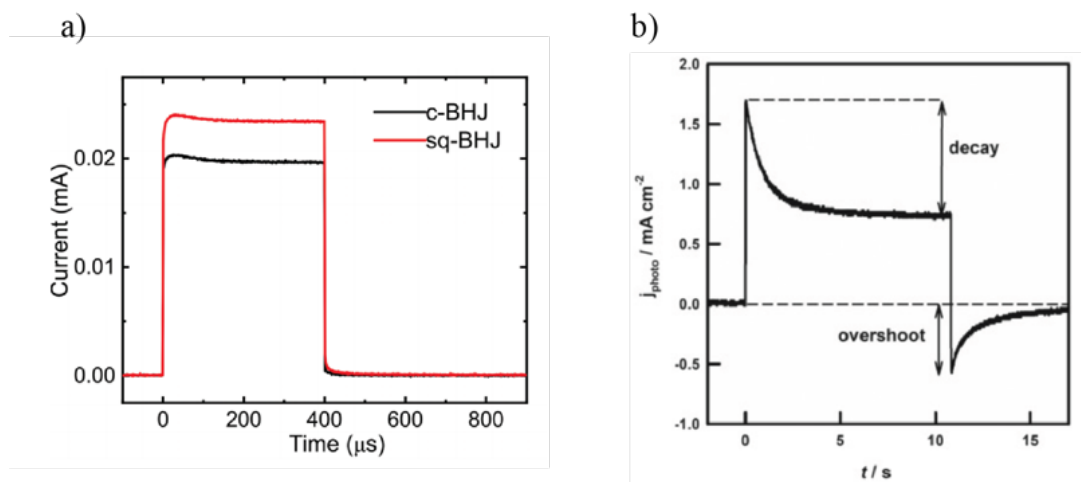


Figure 1.3. Typical photocurrent decay for (a) well-packed semiconductor device (solar cell). Adapted from the study by Zhang et al. [9] copyright (2019), with permission from WILEY-VCH Verlag GmbH. (b) semiconductor electrode (α -Fe₂O₃) in 1.0 M NaOH at 1.1 V vs. RHE (Reversible Hydrogen Electrode). Adapted from the study by Peter et al [13]. copyright (2020), with permission from Elsevier. sq-BHJ and c-BHJ in panel (a) represents bulk heterojunction (BHJ) norfullerene organic solar cells prepared through deposited donor and acceptor layers in order (sq-BHJ) and as-cast bulk heterojunction (c-BHJ) respectively. The decay and overshoot shown in panel (b) are a result of surface e–h recombination.

p–n junctions) or the junctions between semiconductors and metals (Schottky junctions). Taking the example of a p–n junction, when photons enter the junction, they excite electrons from the valence band to the conduction band, generating electron–hole pairs. The generation of charge carriers surpass the recombination of them. Under the built-in electric field (V_{bi}), electrons move towards the n-type semiconductor, while holes migrate towards the p-type semiconductor, resulting in a photocurrent flowing from the n-type to the p-type semiconductor. The photovoltaic effect in a Schottky junction follows a similar pattern. Therefore, for a semiconductor device, if a stable light source is provided, there’s supposed to be a continuously stable photocurrent output, as shown in Figure 1.3a, which illustrates a typical photocurrent decay for bulk heterojunction (BHJ) organic solar cells [9]. Figure 1.3b illustrates the transient photocurrent decay of a semiconductor electrode (α -Fe₂O₃), unlike a typical rectangular on-off response to illumination in Figure 1.3a, there’s a decay following the surge of photocurrent even the illumination is on, and an overshoot after the light is off in Figure 1.3b. This decay and overshoot are interpreted as evidence of e–h recombination at the interface due to large number

of surface states [10-12]. Therefore, in this research, the same experimental method was applied to qualitatively determine the surface states on metal-semiconductor interface, the detailed experimental principles and results can be found in Chapter 2 and 3.

In real semiconductors, surface defects are invariably present mainly due to the dangling bonds formed at the crystal surface, introducing surface states located in the band gap. These surface states act as sites for the recombination of e-h pairs (recombination centre) [14, 15], elevating surface recombination velocity and reducing the effective lifetime of charge carriers. The decrease in carrier concentration consequently diminishes the photocurrent generated by the photovoltaic effect, causing a decay right after the illumination is on and an overshoot after illumination is turned off (Figure 1.3b). Therefore, the number of surface states, hence the surface recombination velocity is a key factor influencing the transient photocurrent. To determine the surface recombination velocity on the semiconductor surface and investigate its impact on triboelectric current, photocurrent mapping was employed. The specific experimental principles will be discussed in Section 2.4.1.5 (Chapter 2), and relevant experimental data can be found in Chapter 3. In addition, chemical surface passivation aiming to control surface defects and enhance semiconductors' resistance to oxidation is mainly used in this research. The detailed methodologies will be discussed in section 2.3 (Chapter 2).

1.1.4. Friction and triboelectric effect

Friction exists everywhere in our daily life. It is caused by the interactions between two surfaces and can occur in various forms, such as dry friction, fluid friction and rolling friction. The most widely known example is that when a rubber rod is rubbed against fur, the rubber rod becomes negatively charged, while the fur becomes positively charged. It describes the charge transfer process between two materials in contact or relative movement, such as sliding. Understanding and controlling friction are crucial for improving equipment performance, reducing energy consumption, and enhancing material longevity.

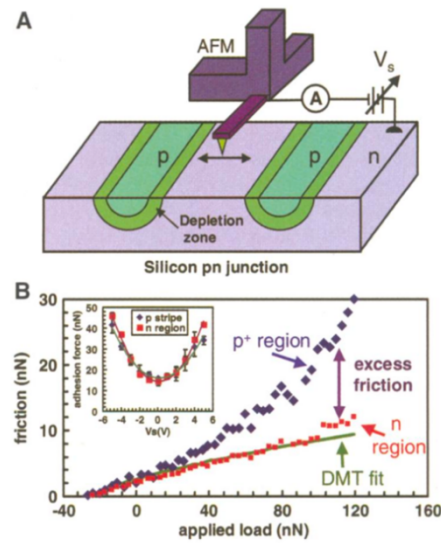


Figure 1.4. (A) A schematic of AFM measurement on p-n junction embedded on n-type silicon surface. (B) Plot of the frictional force on individual regions under a +4 V applied bias, revealing excess friction on the p-type regions. The inset demonstrates the absence of a disparity in adhesion force between the two regions under sample bias. Adapted from the study by Park et al [16]. copyright (2006), with permission from American Association for the Advancement of Science.

The simplest model describing the friction force is Amontons' Law:

$$F_{friction} = \mu \cdot F_{normal} \quad (1-3)$$

Where $F_{friction}$ is the force of friction, μ is the coefficient of friction (between 0 and 1), and F_{normal} is the normal force or the applied load. From this equation, it can be easily seen that the friction force in macroscale is proportional to the friction coefficient, which determined by the materials' characteristics, such as roughness, and the applied load. There're a few key open questions on the relationship between friction and zero-bias friction-induced current output, which will be further addressed in Chapter 3.

For semiconductors, a notable observation of electronic control of friction on silicon was presented by Park et al [16]. It's been found that there is excess friction (Figure 1.4) on p-type silicon compared to n-type silicon region under +4 V external bias. From the inset of Figure 1.4, it can be concluded that under the applied sample bias,

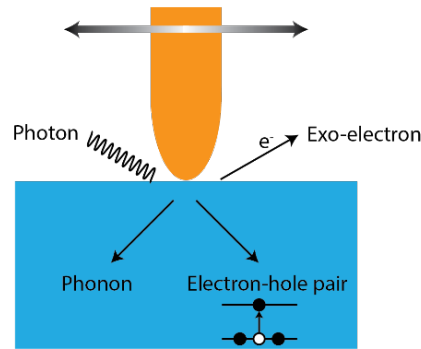


Figure 1.5. Schematic of energy dissipation of friction. Friction energy can be dissipated via photon, phonon, exo-electron, or generate e–h pair. Adapted from the study by Park et al. [17], copyright (2014), with permission from American Chemical Society.

either forward or reverse bias, there is no significant difference in adhesion force observed between the n-type and p-type silicon regions. Therefore, it is attributed to the surface states caused by the high local strain at the tip-silicon interface, leading to the enhancement of surface e–h recombination, with the energy emitted in the form of phonon. The excess friction in p-type silicon region was again observed by the same group in their follow up research [18].

Under applied voltage, frictional forces vary in silicon with different doping levels. Conversely, considering the absence of applied voltage bias, one may wonder whether the dissipative mechanisms of frictional energy have any impact on the material's electrical properties. This led to the proposal of a triboelectric effect, mimicking the principles of the photoelectric effect. Figure 1.5 shows the mechanism of energy dissipation of friction (triboelectric effect). The process of friction exciting phonons and photons is most observed, as evidenced by the luminescence and sound generated when two objects rub against each other. Analogous to photoelectric effect, the friction can also excite electrons escaping from materials' surfaces. Finally, the e–h excitation is of most interest to us, as it has been considered the primary source of the generation of tribocurrent. Due to its striking similarity to photovoltaic processes, this process is named tribovoltaic effect. Therefore, for semiconductor based TENGs, the direction of current flow is supposed to be determined by the built-in electric field, which is opposite to the current flow under forward bias, also known as leakage current.

Considering that this mechanism is like the photovoltaic effect, surface recombination caused by surface states are also one of the main factors limiting the magnitude of tribocurrent. Therefore, the process of surface passivation on the frictional materials is widely employed to minimize the impact of surface states on the lifetime of charge carriers. A review on surface passivation of triboelectric materials for DC-TENGs is presented in section 1.2.

1.1.5. Flexoelectric effect

Flexoelectric effect is a type of electromechanical coupling phenomenon occurring in solid materials, characterized by the uneven distribution of charges when the material undergoes bending or inhomogeneous deformation, leading to the generation of an electric field [19]. Unlike traditional piezoelectric effect, this phenomenon primarily focuses on the curvature or gradient of the material, while piezoelectric effect is induced by applying mechanical stress to a material, causing a homogenous deformation, leading to the non-uniform distribution of charges (Figure 1.6) [20]. In solids, the flexoelectric effect can be expressed as:

$$P_i = \mu_{ijkl} \frac{\partial \varepsilon_{jk}}{\partial x_l} \quad (1-4)$$

Where P_i is the flexoelectric polarization, μ_{ijkl} is the flexoelectric coefficient, ε_{jk} is the elastic strain, x_l is the coordinate [21].

Flexoelectric effect was firstly observed by Bursian and Zaikovskii in crystalline solids took place in 1968. They observed the bending tendency of BaTiO₃ (BTO) thin films under an external electric field [22]. After that, the field experienced a period of relative dormancy lasting several decades before seeing a resurgence recently. Throughout this subsequent phase of research, scientists gradually acknowledged the potential significance of the Flexoelectric effect and explored the diverse applications it could offer since then [23-27]. For flexoelectric effect on semiconductors, Wang et al has recently explored the flexoelectric effect of centrosymmetric semiconductor, and found that under a tip force, the barriers on

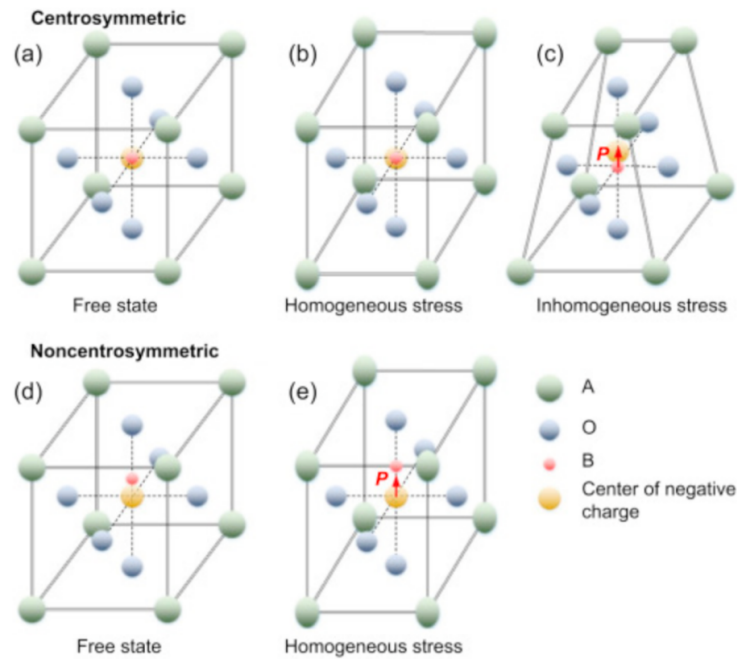


Figure 1.6. Schematic diagram of (a-c) the flexoelectric effect and (d-e) piezoelectric effect within a perovskite ionic crystal. (a) The crystal in its free state without polarization. (b) Uniform deformation leads to a zero net polarization as positive and negative charge centres overlap. (c) Non-uniform strain causes a mismatch between positive and negative charge centres, resulting in a nonzero polarization (depicted by the red arrow) due to the strain gradient. (d) In a noncentrosymmetric crystal at rest, a polarization arises from a mismatch between positive and negative charge centres. (e) Homogeneous strain alters the distance between these centres, modifying the dipole moment and inducing charge output on the crystal surfaces. Adapted from the study by Huang et al., copyright (2016), with permission from Elsevier.

metal-semiconductor surfaces were enhanced for both n-type and p-type semiconductor (Figure 1.7a (ii)) [28]. This is because that under the strain applied by an electrode, the charge carriers at the metal-semiconductor interfaces redistribute and induce an additional built-in electric field (Figure 1.7a (i)), which enhancing the Schottky barrier height. An equivalent electrical circuit, parallel resistor-capacitor (RC) circuit, is given in Figure 1.7a (iii). Such phenomenon can be further validated from Figure 1.7b,c, as the strain distribution follows the same pattern as polarization distribution. Considering that flexoelectric effects and tribovoltaic effect share the same direction, coupled with the previously mentioned energy dissipation mechanism of friction (mainly e–h pair generation), there is reasonable belief that flexoelectricity plays a facilitating role in the triboelectric effect. However, which of these effects predominantly influences the tribocurrent remains unknown. This open question will be discussed in detail in Chapter 4.

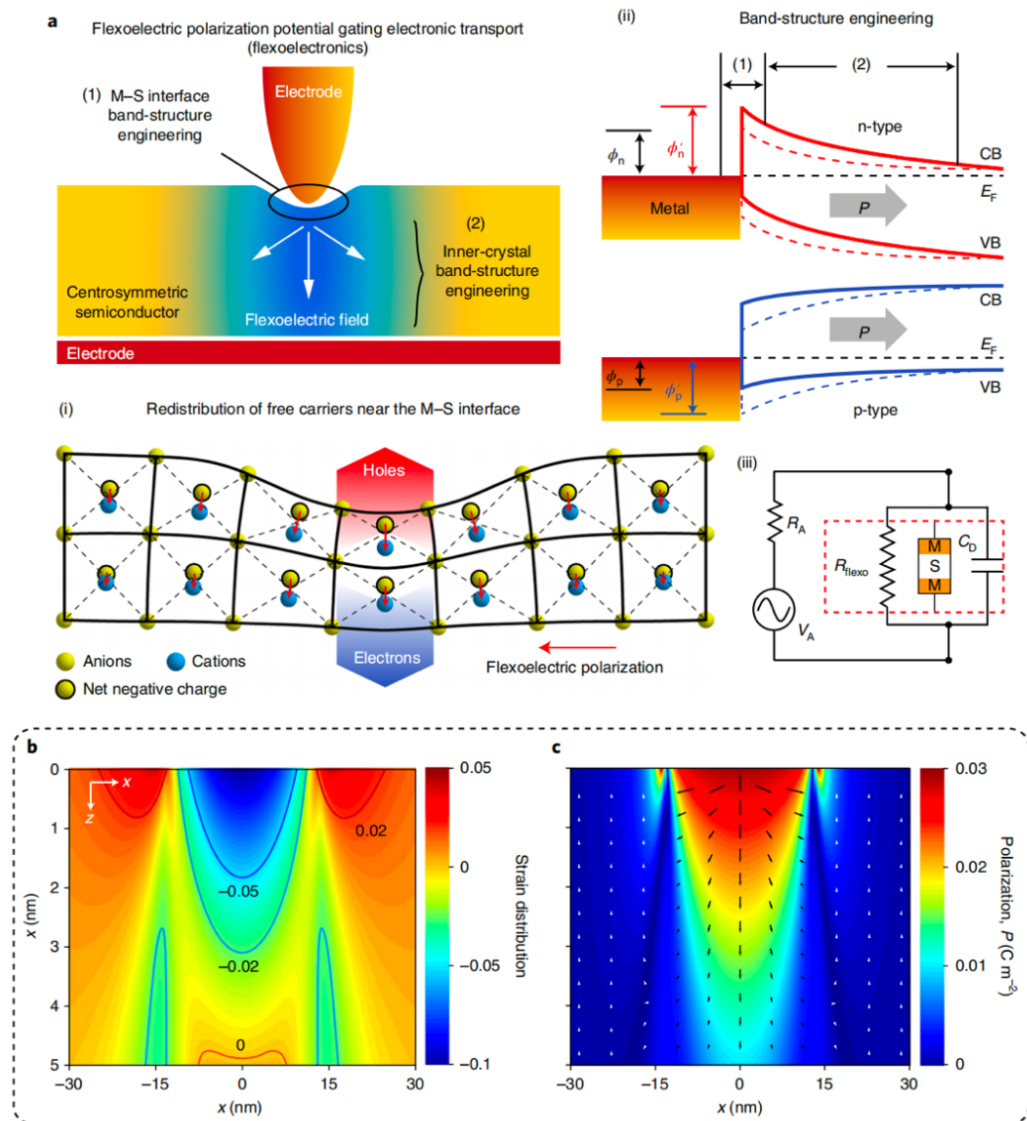


Figure 1.7. (a) The proposed mechanisms of flexoelectric effect on semiconductor by Wang et al [28]. (i) The diagram illustrates how the inhomogeneous deformation of a strained centrosymmetric crystal structure induces a flexoelectric field, which significantly influences the distribution of free charge carriers at the interface, leading to (ii) band-structure engineering, which alter the height of Schottky barrier, known as the flexoelectric effect. In the diagram, the red and blue lines represent the band structures of n-type and p-type semiconductors respectively. ϕ_n & ϕ'_n and ϕ_p & ϕ'_p denotes the Schottky barrier heights of metal and either n-type or p-type semiconductor without (dashed line) and with (solid line) applied strain. The grey arrows indicate the magnitude and direction of the flexoelectric field under nanoindentation ((iii)). The equivalent circuit for flexoelectric outlines a two-terminal device, where R_{flexo} denotes the equivalent tuneable resistor controlled by a strain gradient. Leveraging the strain-gradient-induced flexoelectric field potential as a 'gate' controlling signal. The barrier profile at interface can be modulated, enabling tuneable electronic processes under the flexoelectric effect. R_A , V_A , and C_D represent the series resistor, voltage source, and equivalent parallel capacitance respectively. (b,c) The flexoelectricity in silicon demonstrates the (b) strain distribution and (c) flexoelectric polarization distribution, respectively, under a tip load of 25 μN . Arrows in (c) indicate the direction of polarization. The force is applied downward by an AFM tip (radius, 25 nm), centered at the origin point. Copyright (2022), with permission from Nature.

1.2 Improvement of DC-TENGs by surface chemistry

Most materials on the market suffer from oxidation issues, leading to reduction of conductivity. Alternatively, when these materials are directly used in TENGs, their physical and/or electrical performance may be unsatisfactory. Therefore, surface modification of materials to enhance their resistance to oxidation and improve their performance as frictional materials appears to be necessary.

A discussion on improving DC-TENGs through surface chemistry approaches is given below. The following content is adapted from Lyu, X. & Ciampi, S. Improving the performances of direct-current triboelectric nanogenerators with surface chemistry. *Curr. Opin. Colloid Interface Sci* **2022**, 101627. Rights are retained to reuse in the thesis by the authors. An attribution statement is included as Appendix III.

1.2.1 Introduction to triboelectric nanogenerators (TENGs)

Over the past decade, triboelectric nanogenerators (TENGs) – small and portable devices designed to harvest electricity from mechanical vibrations and friction – have matured from a niche theme of electrical engineering research into multidisciplinary research encompassing engineering, physics, and chemistry. Recent advances in both the fundamental understanding and performances of TENGs have been made possible by surface chemistry, electrochemistry and theoretical chemistry research entering this active and promising field. This short review focuses on the recent developments of direct-current (DC) TENGs, where sliding friction or repetitive contact–separation cycles between the surface of polymers, metals, chemically modified semiconductors, and more recently even by the simple contact of surfaces with water solutions, can output DC suitable to power electronic devices without the need of additional rectification. We critically analyze the role of surface chemistry towards maximizing DC-TENG outputs and device longevity. The major current hypotheses about their working mechanism(s) are also discussed.

Portable technologies that in the last three decades have reshaped our social, economic, and cultural environments rely on electronics that are powered by DC current. There is therefore an ever increasing demand for small, portable,

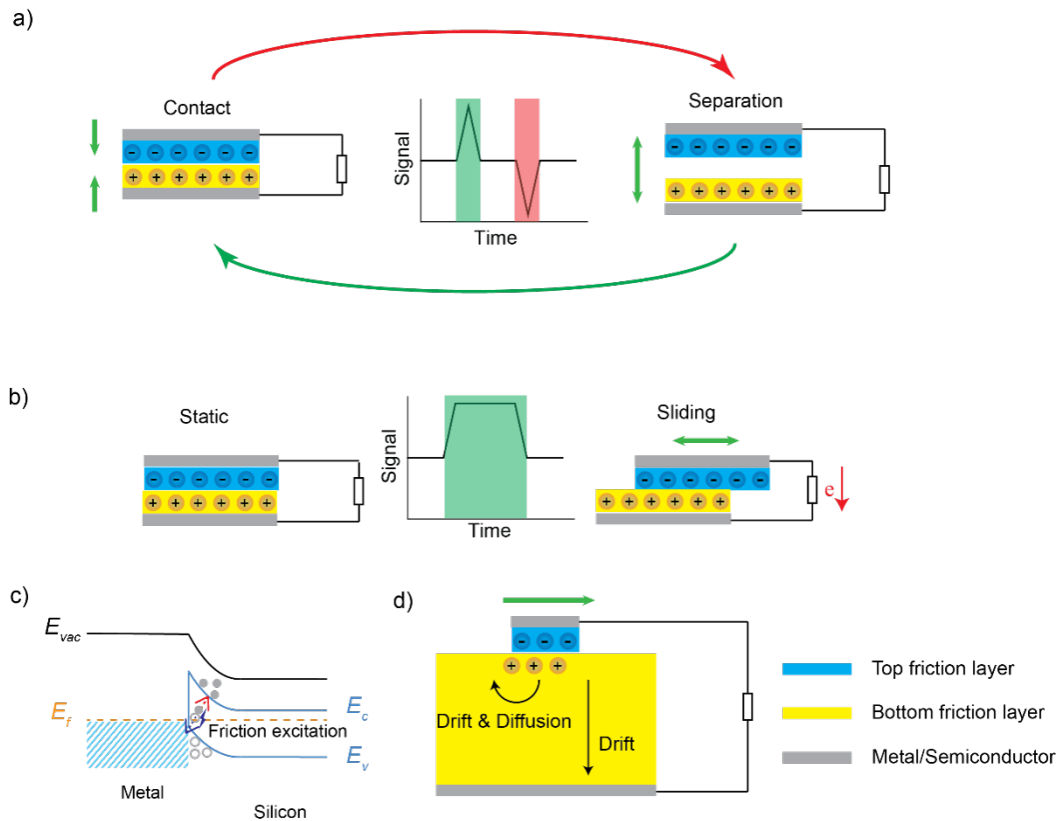


Figure 1.8. (a) Schematics of the contact–separation mode of AC TENGs. The inset shows the AC signal recorded during a cycle of contact and separation. (b–c) Schematics of the tribovoltage/flexoelectric effect [30, 31] behind the operation of semiconductor-based sliding mode DC-TENGs. (d) Depiction of the dynamic formation and equilibration of a space-charge layer leading to a competition between drift and diffusion. The sign of the charges as well as the current flow direction depends on surface characteristics, such as work function, ionization energy, electron affinity, and presence/absence of electronic defects.

regenerative and autonomous DC energy sources [29]. Most electronics still rely on non-regenerative power sources – commonly batteries – which have limitations, such as a limited lifespan [32, 33]. Furthermore, the growing popularity of wearable and implantable devices has created a need for smaller and ideally biocompatible power units [34–37]. Thus, autonomous, regenerative, microscale or even nanoscale, biocompatible energy source technologies are in growing demand.

Triboelectric nanogenerators (TENGs) are a promising source of sustainable and autonomous electricity, whose purpose is that of converting ubiquitous mechanical vibration/friction, such as thermal vibrations [38, 39], muscle movements [40], ultrasonic or ocean waves [41–43] into either AC or DC, and which open up to energy, sensing, and medical applications [44–46]. Their working modes can tentatively be grouped into four main categories: contact–separation, sliding, lateral single-

electrode, and freestanding triboelectric-layer [47-51]. The creation of a potential difference between top and bottom electrodes in relative motion, is generally electrostatic in nature. TENGs' common designs, as shown in Figure 1.8, include a top and a bottom friction layer, usually made of metals [52], semiconductors [53], organic polymers [54], 2D materials [55], or even water [56]. The contact–separation mode (Figure 1.8a) is most common among AC TENGs, where the top and bottom friction layers are usually electrically insulating organic polymers such as polyethylene terephthalate (PET) or polytetrafluoroethylene (PTFE) [48, 57]. Here surface charging is mainly due to static electrification, which builds up in part after the transfer of charged molecular fragments (*vide infra*). Electrons will move in the external circuit to balance the polymer charges, and upon separation of the two dielectrics current will flow to bring the system back to equilibrium. In essence, an AC current flows in the external circuit with the same frequency of the contact–separation events. For DC-TENGs, the sliding mode is generally more prevalent (Figure 1.8b,c) with often one of the electrodes being a semiconductor.

The actual TENGs mode(s) of action is still debated, with some authors arguing in favor of discharge of static electricity being the major driving force [29, 58, 59], others invoking an imbalance between migration and diffusion of surface charges (Figure 1.8d) [60], and some arguing for a unidirectional movement of friction- or pressure-induced electron–hole pairs – the tribovoltaic effect – being the main mechanism (Figure 1.8c) [61-65]. In addition, and probably contributing to the first and latter mechanisms, there is flexoelectricity (Figure 1.9): a band bending and ratcheting mechanism where subsequent compression/decompression of the metal–semiconductor junction forces electrons to move preferentially in one direction [30, 31]. Mechanistic studies on the ratcheting mechanism were conducted on highly doped semiconductor materials [30], but it is not clear if this will still be valid for dynamic junctions made on lowly-doped semiconductor materials where, among other factors, the space charge region is much thicker. For instance, unlike the recent finding of Marks and co-workers [30], most silicon-based TENGs yield tribocurrents with the direction of a leakage current, indicating that the interfacial field formed upon contact moves electrons either via avalanche breakdown or tunneling. Which

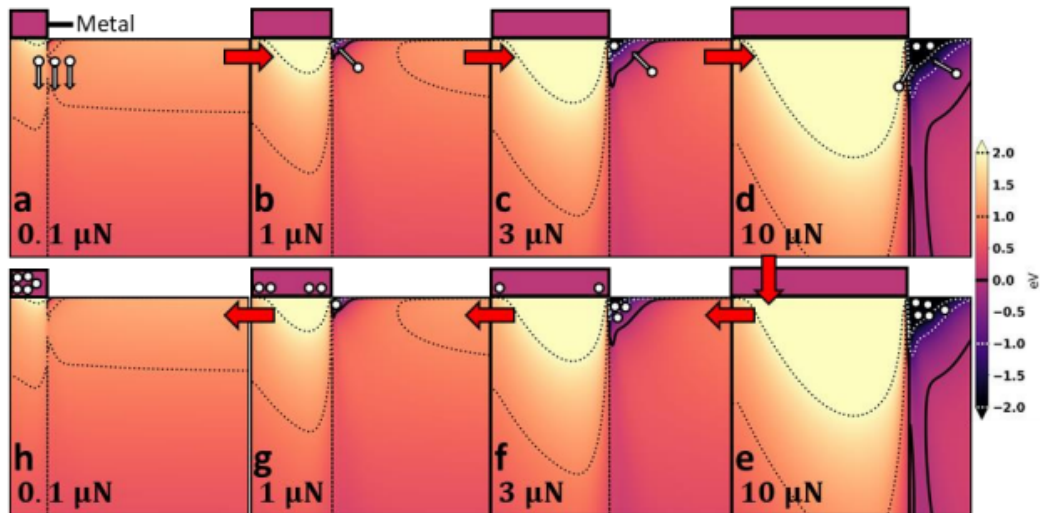


Figure 1.9. Band bending and ratcheting mechanism for metal (purple block) –semiconductor (orange block) contacts under a cyclic change in pressure. (a–d) While the force applied is ramped, electrons (illustrated by white circles) accumulate on the semiconductor side of the junction. (e–g) When the load is removed, the number of available states for electrons in the potential well drops, forcing some electrons to migrate into the metal. (h) The electrons have mostly been transferred into the metal after the external force is completely released. Adapted from the study by Olson et al. [30], copyright (2022), with permission from American Chemical Society

of the two dominates is still unclear, and answering this question will probably require designing experiments where the temperature of the sliding junction can be either controlled or at least monitored.

The debate on to what extent contact electrification is key to the operation of TENGs will not be resolved until a consensus is reached on the nature and origin of statics [60, 66, 67]. A small digression on triboelectricity is therefore needed here, first to explain why objects that cannot conduct electricity become charged in the first place. The term electron comes from the Greek word for amber – “elektra”, later Latinised in “electra” – and Thales of Miletus, who lived around the 600 B.C., left accounts of the ancient Greeks being aware of chicken’s feathers being attracted to amber after their contact with rabbit’s fur. The most striking property of electrified object is in fact that of attraction and repulsion, but it was not until the 17th century that materials other than amber, such as glass and sulphur, were also found to gain a static charge after contact and separation. The topic remained a scientific curiosity until the 18th and 19th centuries, when polymaths like Benjamin Franklin and Michael Faraday initiated its systematic study. It finally gained the attention of engineers and chemists in the 1970s, when the development of copiers and laser printers created a strong

incentive to understand the chemistry behind the triboelectrification of plastic polymers [68]. A common misconception is that electrification upon contact is limited to plastic polymers, but just as the demarcation between insulators and conductors is arbitrary, so it's a material ability to statically charge. Metals, semiconductors exchange charges upon contact [69], but because charges are here free to move, the result is that it becomes harder to accumulate them so to reach large voltages, noting that surface voltages in the excess of 30 kV/cm can be easily obtained on insulators. The nature of this charge is still debated. Do free electrons move upon contact [70, 71], are ionic species formed upon the mechanical breaking of bonds asymmetrically transferred [72], is there a role played by redox chemistry of reactive functional groups [73, 74], or is statics mainly the transfer of water-derived ions [75-79]? A lot of this is still not clear [67, 80-82]. Moreover, non-polar plastics such as PTFE and polyethylene becomes very charged, which is hard to expect based on their chemistry, and several materials form a cyclic, instead than linear, triboelectric series, suggesting that the triboelectrification process does not simply rely on a single physical characteristic [82, 83]. The shape of the object is also important [84], as well as its softness [85, 86]. What is clear beyond ambiguity is that statics is dominated by surface rather than bulk material properties. Interestingly this aspect was already appreciated in the 19th century, when it became apparent that the position of metals in the Volta series depended on whether measurements were done in air or under hydrogen sulfide, with for example copper and iron swapping position in the series in response to this.

The application of several areas of chemistry, most importantly of surface chemistry and electrochemistry, towards answering the question as to what are the charge-carrying species [84, 86, 87] is assisting today the development of TENGs as it did in the 1970s during the development of xerography [88, 89]. The scope of this short review is therefore to summarize the scope of surface chemistry towards maximizing the performances of DC-TENGs, as well as its contribution in unveiling the actual energy conversion mechanism of TENGs.

As shown in Figure 1.8a, the dielectric-displacement current generated by traditional (polymer-based) TENGs, such as in the sliding-mode design (Figure 1.8a), is AC.

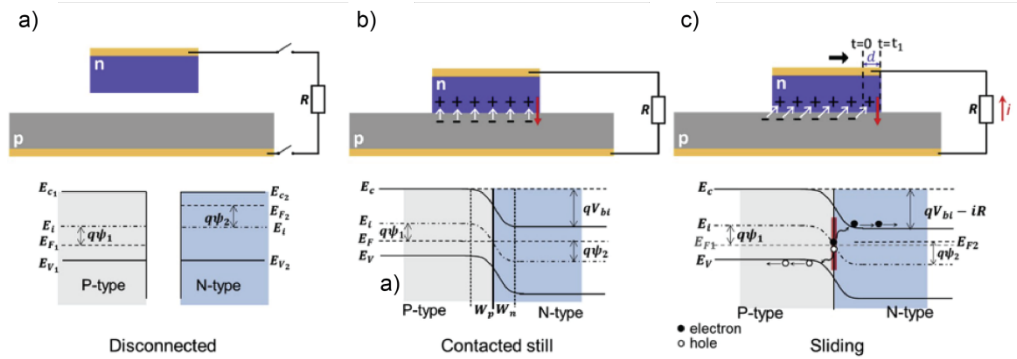


Figure 1.10. Schematics and energy band diagrams for a DC-TENG by using a n-type semiconductor as top electrode sliding on the surface of a p-type semiconductor (bottom electrode). Illustration of the condition of (a) disconnected, (b) contacted still, and (c) lateral sliding of the p–n junction. The white arrows represent the surface dipole moment, and the red arrows represent the direction of the built-in electric field. E_c is the bottom of the conduction band, E_v is the top of the valence band, E_i is the intrinsic level of the pure semiconductor without doping and E_F is the Fermi level, V_{bi} is the built-in electric field potential, $\psi_{1,2}$ are the potentials with respect to the Fermi levels in the p- and n-type semiconductors. Adapted from the study by Xu et al. [53], copyright (2019), with permission from Elsevier.

Besides the requirement of rectification to power up microelectronic devices, the impedance of polymers is a crucial constraint to the achievable current density. Both issues are removed in metal–semiconductor (Schottky diodes) TENGs [90, 91]. Semiconductors such as silicon are used in DC-TENGs owing largely to the versatility of its surface chemistry [92–94], low costs [95], and an high output current density – over 10^9 A/m² in micro/nanoscale [96] and up to 200 A/m² in macroscale [97].

Furthermore, by tethering organic monolayers it is possible to tune the interface charge transport characteristics, adhesion, and friction [80, 94, 98–101]. As briefly mentioned above, omitting the nuances of flexoelectricity, the main mechanism is here a tribovoltaic effect [61–65], which in first approximation is analogous to the photovoltaic effect, and is schematically depicted in Figure 1.10 for a sliding p–n junction [53] but will also be applicable to metal–semiconductor Schottky diodes [63]. The current generation process involves tunneling (or avalanche breakdown) across the metal–insulator–semiconductor structure [102, 103]. Electron–hole pairs excited by friction are separated by the built-in electric field at the interface, hence the current flows in the same direction of the leakage current. Indeed, the surface chemistry is quite crucial here, as it is capable of engineering surface properties such as work function, electric field, and charge transfer, then eventually tune the leakage current [104, 105].

But for such silicon-based DC-TENGs the substrate is a non-oxide semiconductor prone to oxidation, a reaction that will inevitably cause drops in surface conductivity and open-circuit voltages (V_{oc}) [103]. Although some extent of oxidation can introduce surface states that counterintuitively increase conductivity [106], this effect is only transient. The oxide layer (silica) can be removed via chemical etching, but eventually the etched surface (Si-H) [107-109] oxidizes again after exposure to the environment [110, 111]. To limit this, several surface modification strategies involving organic and inorganic chemicals, as well as metals have been proven viable [101, 112-115]. In the following, we present surface modification strategies for TENG materials and discuss their pros and cons.

1.2.2 Surface modification of triboelectric materials

1.2.2.1 Organic materials

Organic molecules that can self-assemble on metals and semiconductors are a first choice in terms of improving the performances of a TENG. In 2006 Akbulut and co-workers [52] coated Au, Ag and Ti surfaces with self-assembled monolayers (SAMs) of 1-hexadecanethiol so to prevent these metals from cold-welding, a phenomenon that inhibits the relative movement of metals and leads to material wear [116]. Interestingly the authors observed large current fluctuations when sliding different (SAM-passivated) metals against each other, while no charge transfer was observed when identical metals were sheared. For SAMs-coated Ag and Au surfaces the authors observed DC current densities up to $\sim 20 \text{ mA/m}^2$. The authors suggest a continuous entangling and disentangling, and cyclic deformation and relaxation, of SAM chains during sliding. They also speculate that amorphous SAM regions may be capable of assisting charge transport even under static conditions. These two effects, may contribute to the triboelectrification of the contact. According to the authors, the lag between current and friction after having stopped the sliding could be evidence of a slow SAM relaxation. Further studies will need to be conducted to prove a relationship between monolayer order and propensity to gain static charges. Further, as only one type of SAM was explored, an open question remains, whether

or not different SAMs, for instance, with different polarity and wettability, will show similar delays.

Similarly, in 2016 Wang and co-authors [117] used Au substrates functionalized with thiol-based SAMs as materials for AC contact–separation TENGs. They investigated five SAMs with either hydroxyl ($-\text{OH}$), methyl esters ($-\text{C}(\text{O})\text{OCH}_3$), amines ($-\text{NH}_2$), aniline ($-\text{C}_6\text{H}_5-\text{NH}_2$), or chloro ($-\text{Cl}$) functionalities as terminal group. These SAMs were formed onto an Au film deposited on Kapton by e-beam evaporation, and with a 100 nm copper layer deposited on fluorinated ethylene propylene (FEP) film (vapor deposition) as the second electrode. Under mechanical shaking (~ 2.5 Hz), $-\text{NH}_2$ surfaces showed the greater surface potential by Kelvin probe force microscopy (KPFM), and were the most effective nanogenerator, with the charge density reaching $\sim 140 \mu\text{C}/\text{m}^2$, and the open-circuit voltage (V_{oc}) and short-circuit current density (J_{sc}) reaching ~ 560 V and $\sim 18.5 \text{ mA}/\text{m}^2$, respectively. For almost all the surface chemistries investigated, TENG performances were significantly higher compared to controls with unmodified surfaces. The only exception were chloro-terminated surfaces. Furthermore, the same authors also explored amine-terminated silane-based SAMs grafted on SiO_2 surfaces. The charge density, V_{oc} , and J_{sc} increased from $\sim 34 \mu\text{C}/\text{m}^2$, ~ 150 V and $\sim 0.7 \text{ mA}/\text{m}^2$ (respectively) on the SiO_2 surface, to $\sim 51 \mu\text{C}/\text{m}^2$, ~ 240 V, and $\sim 1.75 \text{ mA}/\text{m}^2$ for the modified systems. Although the output of these TENGs is AC, these results indicate a scope for the improvement on DC-TENGs by surface chemistry, focusing especially on the material electronegativity. The authors recommended head groups with lower electronegativity for the positive side, higher electronegativity for the negative side, and longer chains.

Inspired by the research discussed above, Ciampi and co-workers [112] investigated covalent 1,8-nonadiyne monolayers (Si–C-bound) grafted on NH_4F -etched 111- and 100-oriented silicon substrates (**S1**, Figure 1.11a). The monolayer purpose is first to prevent substrate oxidation, and second to engineer charge transport on Si(111) pyramids etched on a Si(100) surface. Using platinum AFM tips as the sliding metal contact it is possible to measure simultaneously surface properties (such as friction and topography) as well as the zero-bias current. The topography (Figure 1.11b) as well as the leakage current (under an external bias) and zero-bias (TUNA) current

signal along the red dotted line (Figures 1.11b,c) were recorded simultaneously. The maximum DC current density for such structure was of $2.9 \times 10^5 \text{ A/m}^2$. Interestingly, the recorded zero-bias current reaches a peak at concave boundaries between the (100) and (111) planes, rather than at the convex pyramid [Si(100)] apex. The tribocurrent, which bears the sign of a reverse-bias current, interestingly also does not track the leakage current of static junctions (from current–voltage characteristics, Figure 1.11c). The authors suggest that the Schottky barrier may be decreasing under increasing stress, and that the concave curvature at the pyramid’s base leads to a thinner space charge. Using a semiconductor as readily available as silicon could significantly reduce the costs of DC-TENGs, as well as ensure compatibility with mainstream electronics, but such textured surface (pyramids) introduce some level of complexity in the preparation of such devices. Thus, exploring flat and unstructured silicon, and the influence of surface chemistry on performance of Schottky diode-based DC-TENGs (Figure 1.11a, **S2-X**, with X being either $-\text{NH}_2$, $-\text{OH}$ or $-\text{CH}_3$ groups), Ferrie et al. modified Si(111) crystals by Cu-catalyzed azide–alkyne cycloaddition (CuAAC) reactions [101]. Polar groups ($-\text{NH}_2$ and $-\text{OH}$) led to a greater zero-bias DC current output, which parallels the findings for AC TENGs by Wang et al. discussed above [117]. It is therefore possible to augment DC current output on flat silicon by means of surface functionalization, even though the two-step (passivation followed by functionalization) procedure involved is laborious. In an attempt to simplify the surface chemistry aspects, Lyu et al. attempted to use 1,8-nonadiyne, 1-nonyne, 1-nonanol, and 8-nonyl-1-ol to form in one step alkynyl ($-\text{C}\equiv\text{CH}$), alkyl ($-\text{CH}_3$), and hydroxyl ($-\text{OH}$) monolayers, as shown in Figure 1.11d [96]. With platinum as the sliding metal contact, 8-nonyl-1-ol coated Si(211) showed a maximum current density of $\sim 10^9 \text{ A/m}^2$. One of the most important factors causing hydroxyl-terminated Si(211) surfaces to perform well is surface polarity coupled to a relatively large surface recombination and velocity, plus the negative charge on the metal tip owing to flexoelectricity [96].

Polymers have also continued to gain popularity as the triboelectric material for DC-TENGs. Recently You et al. [118] have successfully coated poly-3,4-ethylene dioxythiophene:poly-styrene sulfonate (PEDOT:PSS) on aluminum alloy films as top

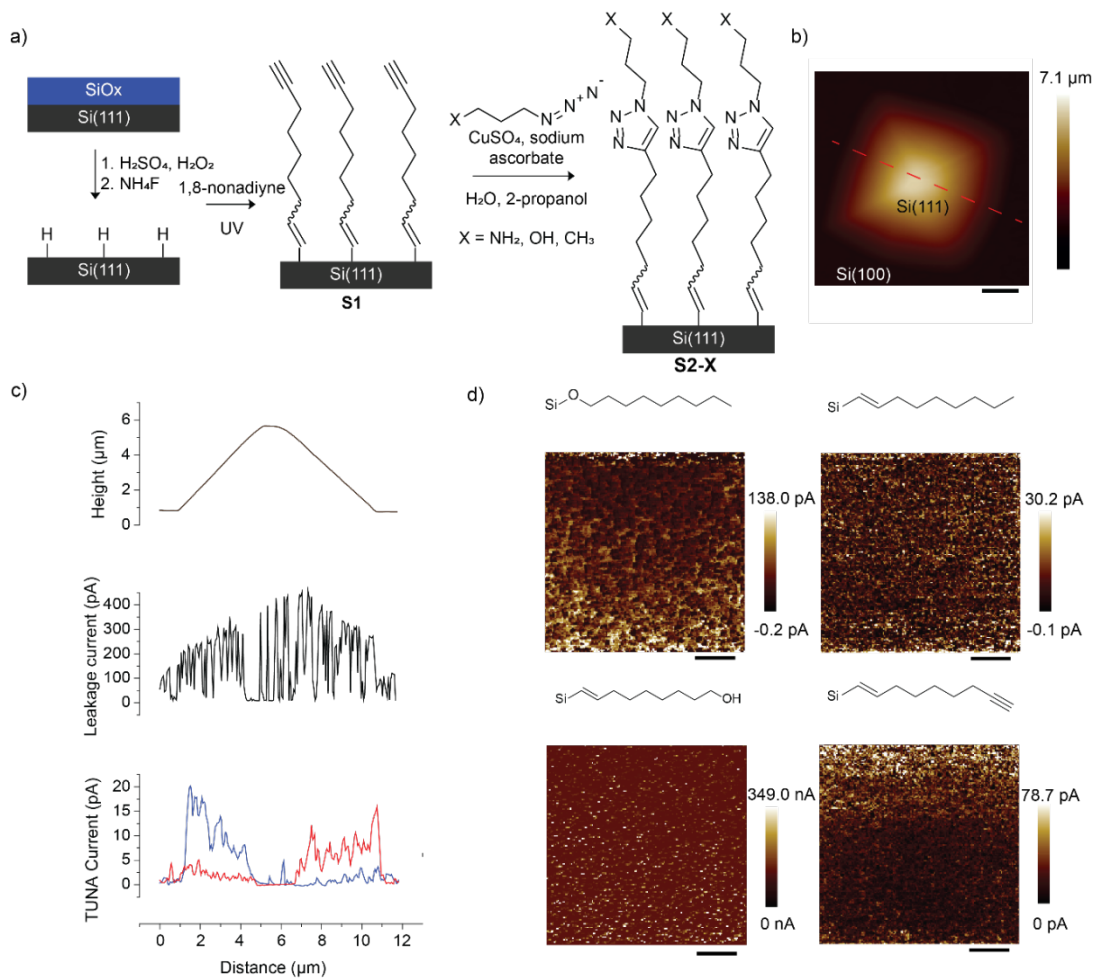


Figure 1.11. (a) Oxide-free silicon surface functionalization. Native oxide is first cleaned and etched (steps 1 and 2) to form a hydrogen-terminated surface. This surface is reacted under UV with 1,8-nonadiyne to form surface **S1**. The terminal alkyne functionality of **S1** is reacted through a CuAAC reaction to covalently attach either 3-azidopropan-1-amine (forming **S2-NH₂**), 3-azidopropan-1-ol (**S2-OH**), or 1-azidobutane (**S2-CH₃**). Adapted from the study by Ferrie et al. [101], copyright (2022), with permission from Elsevier. (b) $12 \times 12 \mu\text{m}$ AFM height image of Si(111) pyramids on lowly doped float zone (FZ) n-type Si(100). (c) Topography, leakage current (under an external bias), and zero-bias tunneling AFM (TUNA) current profiles over the dotted red line in (b). Trace data are in blue, and retrace data in red. Adapted from the study by Ferrie et al. [112], copyright (2022), with permission from Elsevier. (d) Zero-bias C-AFM $5 \times 5 \mu\text{m}$ current maps of dynamic sliding Pt-Si(211) diodes. Oxide-free Si(211) samples were coated with monolayers of 1-nonanol, 1-nonyne, 8-nonyn-1-ol, and 1,8-nonadiyne. Adapted from the study by Lyu et al. [96], copyright (2022), with permission from Elsevier.

friction layer, and used Al alloys, Si, ITO, Cu, and graphene as bottom friction layer in sliding mode TENGs, as shown in Figure 1.12a. They conclude that the work function of triboelectric materials is the main factor influencing the DC-TENGs output, as the work function difference correlates to the open-circuit voltage. As shown in Figure 1.12b, they also found out that the PEDOT:PSS/Al alloy device exhibits the greatest performance with a V_{oc} of 1 V, a I_{sc} of $309 \mu\text{A}$, and power density of 11.67 mW/m^2 .

After 1,000 successive bending events there is a reduction in the device open-circuit voltage, which highlights general concerns about the durability of TENGs. The decay of electrical performances is mainly due to frictional wear, which is the primary failure factor in TENGs [119-121].

Physical methods can also be applied to improve the output of DC-TENGs. As shown in Figure 1.12c, Chen et al. [122] added a pre-charged PTFE layer that was charged by 100 cycles of manual rubbing against nitrile rubber, also known as field enhancing layer (FEL). This layer is placed under the triboelectric layer (PTFE), then the copper tape attaching to the acrylic sheet was slid against the triboelectric layer to generate DC current under different acceleration (contact area of 2×2 cm). A current of ~ 200 nA and an open-circuit of ~ 50 V were recorded. To scale this up, the authors also designed a rotary mode TENG using the same materials to realize a constant DC current output which can power a LED array without intermitted flashing.

1.2.2.2. Inorganic materials

Various inorganic materials have been utilized to modify the surface of TENGs and improve their performances and durability. In 2007, Wang and co-workers [41] used ZnO nanowires (bottom electrode) and a surface-engineered silicon jagged electrode coated with Pt (top electrode) to develop a nanogenerator able to harvest DC electricity from ultrasonic waves. This zigzag-shaped silicon electrode can effectively enlarge its surface area, favouring contact with the nanowires. Under ultrasonic waves, the nanowires continuously act like brushes on the silicon electrode. Analogously, Xu et al. [53] used HF-etched phosphorus-doped and boron-doped silicon as sliding electrodes, with an Au coating on both electrodes as a back contact as illustrated in Figure 1.12d. They managed to continuously harvest ~ 50 nA of DC current under 1 N of load (Figure 1.12e) and found that the current direction matches the built-in electric field of the junction. The authors also performed experiments under variable sliding speed, acceleration and length of the top electrode. They observed a positive correlation between the short-circuit current and these three parameters. This design indeed provides a high current output and supports a relationship between current, velocity and acceleration. The long-term performances

of such structure is likely not to be outstanding as the silicon electrodes were only etched with HF solutions and no protective layer was incorporated in the design. The above mentioned issue of substrate re-oxidation and frictional wear remains a challenge, and to specifically address this, in 2018 Lin et al. [55] attempted to harvest DC by sliding graphene layers on silicon substrates (Figure 1.12f), given that the graphene is self-lubricant. The authors reported DC current densities up to 40 A/m^2 , and stable outputs even after 10,000 cycles. Similarly, in 2021 Huang et al. [60] used Au coated highly ordered pyrolytic graphite, prepared via electron beam lithography, electron beam evaporation, and reactive ion etching, as the top electrode, and etched n-type silicon as the bottom electrode. They fabricated a superlubric Schottky based generator (Figure 1.12g) with current and power density of $\sim 210 \text{ A/m}^2$ and $\sim 7 \text{ W/m}^2$ respectively. Such device is also capable of maintaining such high performances for over 5,000 cycles. Notably, the authors exclude a friction-induced excitation mechanism and propose a mechanism based on the continuous establishment and destruction of the depletion layer. In simple terms, the net current flow is attributed to the electronic drift induced by non-equilibrium electric field over the movement between the triboelectric materials, as shown in Figure 1.12h. Such friction-less (or minimal friction) approach defines another direction for the future improvement of outputs and durability of DC-TENGs.

The two designs outlined above rely on carbon-based materials (graphite or graphene) owing to their capacity for reducing friction [125]. Such designs undoubtedly reduce device wear, but the other contact material (silicon) was somehow neglected and in fact only treated with HF or buffered oxide etch solution to remove the native oxide. Obviously, etched silicon will re-oxidize in ambient air [107, 126] and with a growing oxide layer, current outputs will drop significantly and rapidly [103]. It is therefore surprising that this degradation was not observed as the electric field should further speed up the oxidation process [127, 128].

Protection of silicon against anodic decomposition is therefore imperative. Lu et al [123] attempted to coat HF-etched silicon substrates with AlN, HfO_2 , or Al_2O_3 via physical vapor and atomic layer deposition. As shown in Figure 1.12i, using black

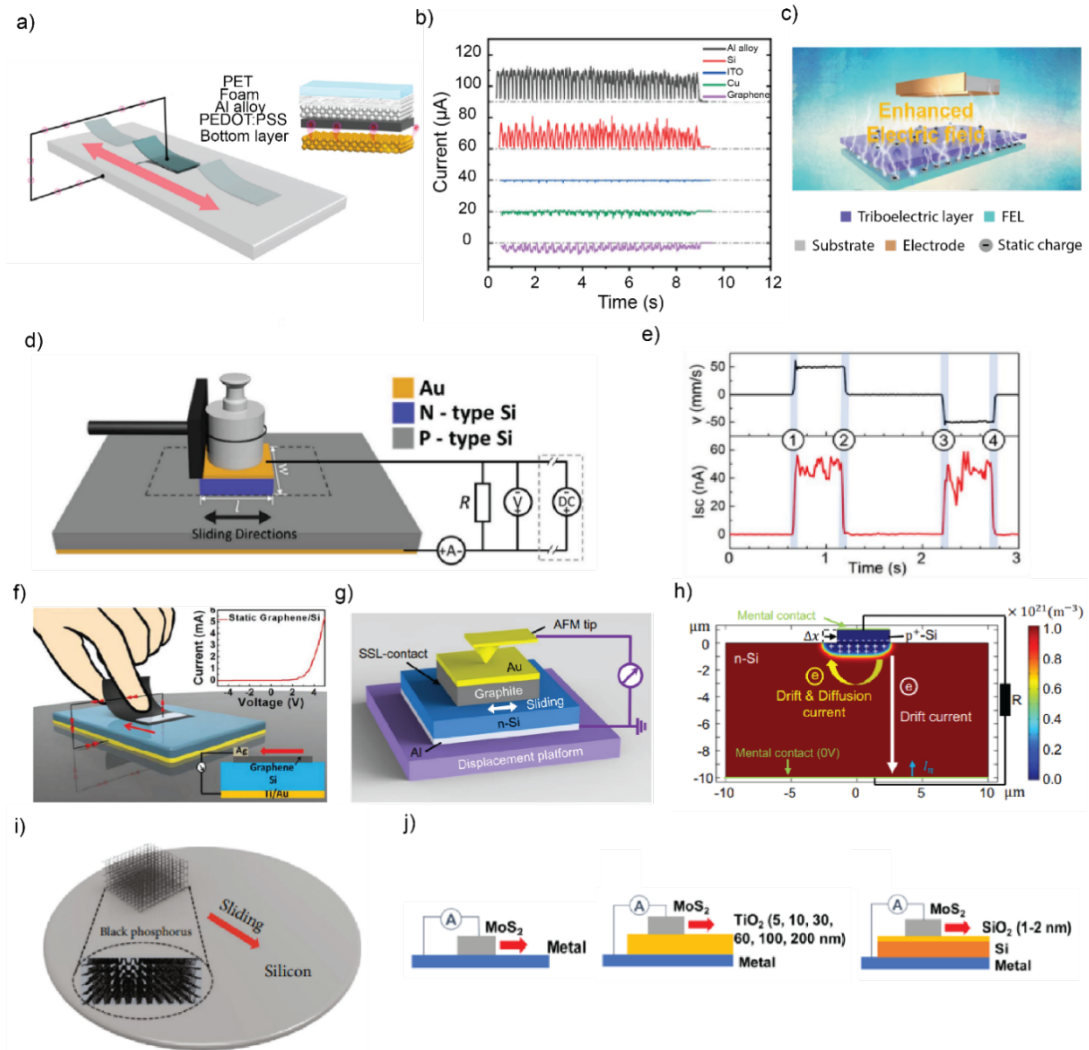


Figure 1.12. (a) Schematic of a DC-TENG where changes to the bottom friction layer (an Al alloy, Si, ITO, Cu, or graphene) are reflected in drastic changes to the short-circuit current (b). Adapted from the study by You et al. [118], copyright (2022), with permission from Elsevier. (c) Schematic of a DC-TENG where pre-charged PTFE, used as field-enhancing layer (FEL), is embedded under the triboelectric layer (PTFE). Adapted from the study by Chen et al. [122], copyright (2021), with permission from Wiley-VCH GmbH. (d) Schematic and external circuit of p–n junction based TENG. (e) Sliding velocity and corresponding short-circuit current during the reciprocating movement of the slider shown in (d). Adapted from the study by Xu et al. [53], copyright (2019), with permission from Elsevier. (f) Experimental set-up for a sliding graphene–silicon TENG. The inset is an I–V curve of the static graphene–silicon junction. Adapted from the study by Lin et al. [55], copyright (2019), with permission from Wiley-VCH GmbH. (g) Experimental set-up for sliding superlubric graphite coated Ag–silicon Schottky diode triboelectric nanogenerator. (h) Simulation mode structure and the proposed physical process of the depletion layer establishment and destruction (DLED) mechanism. The scale bar at the right side represents the electron concentration. Adapted from the study by Huang et al. [60], copyright (2022), with permission from Nature Portfolio. (i) Schematic of the black phosphorus-coated Ag–silicon Schottky diode DC-TENG. Adapted from the study by Lu et al. [123], copyright (2019), with permission from American Association for the Advancement of Science. (j) Schematic of a MoS₂–Si Schottky sliding diode DC-TENGs in three different structures (from left to right): metal/semiconductor (MS), metal/insulator/semiconductor (MIS), and semiconductor/insulator/semiconductor (SIS). Adapted from the study by Liu et al. [124], copyright (2019), with permission from American Chemical Society.

phosphorus flakes, whose intrinsic anisotropy produces outstanding electronic, transport and mechanical characteristics [129], as the other triboelectric material, they built a Schottky diode sliding DC-TENG and recorded an open-circuit voltage of 6.1 V and a short-circuit current density of 124.0 A/m² (power density of 201.0 W/m²) for black phosphorus/AlN/Si heterojunction system. In 2020, they attempted to fabricate DC-TENG using HF-etched and oxide-free n–n silicon homojunction, recording a current density of 214 A/m² and a voltage of 0.35 V [130]. They further explored the influence of different insulated dielectric layers (ZnO, HfO₂, Al₂O₃) on the performance of the silicon–dielectric layer–silicon system, and found out that the n-type Si/Al₂O₃/ n-type silicon can enhance the output voltage to 1.3 V.

Afterwards, they intentionally used water as the dielectric material and moved it at the gap between HF etched n-type and p-type silicon. In response to the movement of water droplets, a DC voltage of 0.3 V and a current of 0.64 μA was recorded [131]. The authors proposed a new dynamic semiconductor–liquid–semiconductor structure DC-TENG, which has the potential to obtain electricity from the motion of water, for instance from rain.

Analogous insulated dielectric materials between triboelectric materials are commonly used in the fabrication of DC-TENGs. Liu et al [90] firstly attached the molybdenum disulfide (MoS₂) multilayer to the silver coated Si/SiO₂ substrates by pulsed laser deposition, and successfully harvested DC electricity from such structure with current density reaching up to 10⁶ A/m². To further research on the enhancement of the MoS₂ based TENGs direct-current generation, the same authors attempted three different structures: metal–semiconductor (MS), metal–insulator–semiconductor (MIS), and semiconductor–insulator–semiconductor (SIS) (Figure 1.12j). The authors suggest that the DC output can be manipulated by interfacial engineering [124], and probed the influence of the insulator (SiO_x) thickness on the electrical performance of the sliding metal–insulator–semiconductor (Si) based DC-TENG, and concluded that the short-circuit current slightly increases at the beginning and eventually decreases significantly with the increasing oxide layer thickness. And for native oxide with a thickness less than 2 nm on silicon substrates, the theoretical

current density of such a metal-insulator-semiconductor system can reach up to 10^4 A/m² [103].

Sharov et al. [132] attached an InP layer, with its native oxide, on the HF-treated p-type Si(111), and use a silicon AFM tip with platinum or diamond coating as top contact. A peak and average current density in dark of 15 kA/m² and 7.3 kA/m² were reported. The authors also probed the photovoltaic efficiency in both the static and sliding regimes, reporting a 7% conversion efficiency. It provides a platform for coupling tribovoltaic and photovoltaic current generation.

1.3 Conclusion

Autonomous power supplies that convert mechanical energy into electricity take on a vital role when an energy storage device, most commonly battery, is not possible to be replaced or recharged, such as in life-critical medical implants or sensors in remote/dangerous places. The environment provides a broad range of mechanical energy sources, but in a nanoscale setting, the conversion of mechanical energy into DC remains a challenge. By merging innovations in both surface science and electrical engineering, DC-TENGs are becoming a viable path to miniature power supplies. Surface chemistry and surface microfabrication protocols have been extremely valuable and, for example, shown that engineering sharp lateral changes in the semiconductor barrier is dramatically more effective toward maximizing current than increasing the applied normal force or the surface friction [84]. This is a path toward removing friction – and therefore area – constraints. It is also a path toward limiting device wear: tribocurrent densities can be enhanced under minimal friction. More recently, zero-applied-bias current densities as high as 10^9 A/m² have been achieved using a proton-exchangeable organic monolayer that simultaneously introduces a sufficiently high density of surface states (assessed as changes to carrier recombination velocities) coupled to a strong surface dipole in the form of a surface alkoxide anion (Si–monolayer–O⁻) [68]. These are just key examples, and a more comprehensive summary of the status of DC-TENGs systems is in Table 1.1 To further improve the performance of DC-TENGs, including their power density and durability more surface chemistry, research is needed. Furthermore, the mechanism by which

DC-TENGs operate remains controversial. Among the key pending questions, we believe the following are particularly pressing:

1. For DC-TENGs that are essentially out-of-equilibrium diodes, the DC output grows or declines with the level of surface states? (See Chapter 3)
2. Is it all governed by the movement of charged molecular fragments or by flexoelectricity? (See Chapters 4–5)
3. Is stick–slip friction involved, or are pressure fluctuations more important than lateral friction? (See Chapters 3–5)

Table 1.1. Surface functionalization and electrical performances of DC-TENG

Materials	Surface modification	Test cond.	I_{sc}	V_{oc}	J_{max} A/m ²	Ref
Organic materials						
Ag [Au]	SAMs (1-hexadecanethiol)	Sliding			~0.02	[52]
Si(111) & Si(100) [Pt]	SAMs (1,8-nonadiyne)	Sliding			2.9×10^5	[112]
Si(111) [Pt]	SAMs & CuAAC (-NH ₂ , -OH, -CH ₃)	Sliding			4.6×10^6	[101]
Si(211) [Pt]	SAMs (-CH ₃ , -OH, -C≡CH)	Sliding			4.9×10^9	[96]
PEDOT:PSS [Al]	poly-3,4-ethylene dioxothiophene: poly-styrene sulfonate	Sliding	309 μA	1 V		[118]
PTFE [Cu]	Pre-charged PTFE	Sliding	200 nA	50 V		[122]
Inorganic materials						
ZnO nanowires [Si zigzag]		Ultrason ic Wave	0.15 nA			[41]
Si [graphene]	HF etched	Sliding			40.0	[55]
Si(100) [graphite]	Buffered oxide etch	Sliding			~210	[60]
p-type Si [n-type Si]	HF etched	Sliding	50 nA			[53]
Si [black phosphorus]	Deposition (AlN, HfO ₂ , Al ₂ O ₃)	Sliding		6.1 V	124	[123]
n-type Si [n-type Si]	HF etched	Sliding		0.35 V	214	[130]
n- & p-type Si [water]	HF etched	Sliding	0.64 μA	0.3 V		[131]
Ag [Si tip]	Pulsed laser deposition (MoS ₂)	Sliding			~10 ⁶	[90]
p-type Si(111) [diamond coated Si tip]	Molecular beam epitaxy (InP)	Sliding		15 mV	1.5×10^4	[132]

1.4 References

- [1] Gruzdev, V. E.; Komolov, V. L., The action of ultrashort laser pulses on a semiconductor: Possible processes and a possible sequence of events. *J. Opt. Technol.* 71 (2004) 509-513. <http://doi.org/10.1364/JOT.71.000509>
- [2] Yu, P. Y.; Cardona, M., *Fundamentals of Semiconductors Physics and Materials Properties*. Springer Berlin Heidelberg: Berlin, Heidelberg, 2010. <http://doi.org/10.1007/978-3-642-00710-1>
- [3] Pathria, R. K.; Beale, P. D., *Statistical mechanics*. 3rd / R.K. Pathria, Paul D. Beale. ed.; Elsevier/Academic Press: Amsterdam ;, 2011.
- [4] Mishra, U. K.; Singh, J., *Semiconductor device physics and design*. Springer Netherlands: Dordrecht, 2008. <http://doi.org/10.1007/978-1-4020-6481-4>
- [5] Laughton, M. A.; Warne, D. F., *Electrical engineer's reference book*. 6th ed.; Newnes: Oxford ;, 2003.
- [6] Baliga, B. J., *Fundamentals of Power Semiconductor Devices*. 1. Aufl. ed.; Springer-Verlag: New York, NY, 2008. <http://doi.org/10.1007/978-0-387-47314-7>
- [7] Han, T., *Photoelectric materials and devices*. World Scientific Publishing: Hackensack, New Jersey ;, 2021.
- [8] Lincot, D., The new paradigm of photovoltaics: From powering satellites to powering humanity. *Comptes rendus. Physique* 18 (2017) 381-390. <http://doi.org/10.1016/j.crhy.2017.09.003>
- [9] Zhang, J.; Futscher, M. H.; Lami, V.; Kosasih, F. U.; Cho, C.; Gu, Q.; Sadhanala, A.; Pearson, A. J.; Kan, B.; Divitini, G.; Wan, X.; Credgington, D.; Greenham, N. C.; Chen, Y.; Ducati, C.; Ehrler, B.; Vaynzof, Y.; Friend, R. H.; Bakulin, A. A., Sequentially deposited versus conventional nonfullerene organic solar cells: Interfacial trap states, vertical stratification, and exciton dissociation. *Adv. Energy Mater.* 9 (2019) 1902145-n/a. <http://doi.org/10.1002/aenm.201902145>
- [10] Cummings, C. Y.; Marken, F.; Peter, L. M.; Tahir, A. A.; Wijayantha, K. G. U., Kinetics and mechanism of light-driven oxygen evolution at thin film α -Fe₂O₃ electrodes. *Chemical communications (Cambridge, England)* 48 (2012) 2027-2029. <http://doi.org/10.1039/c2cc16382a>
- [11] Qiao, X.; Zhao, C.; Chen, B.; Luan, L.; Hu, B., In-situ investigation of interfacial effects on charge accumulation and extraction in organic solar cells based on transient photocurrent studies. *Organic electronics* 15 (2014) 1624-1630. <http://doi.org/10.1016/j.orgel.2014.04.019>
- [12] Jiang, R.; Boschloo, G., The impact of non-uniform photogeneration on mass transport in dye-sensitised solar cells. *J. Mater. Chem. A* 6 (2018) 10264–10276. <http://doi.org/10.1039/C8TA02083C>
- [13] Peter, L. M.; Walker, A. B.; Bein, T.; Hufnagel, A. G.; Kondofersky, I., Interpretation of photocurrent transients at semiconductor electrodes: Effects of band-edge unpinning. *J. Electroanal. Chem.* 872 (2020) 114234. <http://doi.org/10.1016/j.jelechem.2020.114234>
- [14] Feuchtwang, T. E., Basic theory of surface states. *Materials research bulletin* 27 (1992) 1444. [http://doi.org/10.1016/0025-5408\(92\)90011-N](http://doi.org/10.1016/0025-5408(92)90011-N)
- [15] Birdi, K. S., *Surface Chemistry Essentials*. CRC Press LLC: Boca Raton, 2017.
- [16] Park, J. Y.; Ogletree, D. F.; Thiel, P. A.; Salmeron, M., Electronic control of friction in silicon pn junctions. *Science* 313 (2006) 186–186. <http://doi.org/10.1126/science.1125017>

- [17] Park, J. Y.; Salmeron, M., Fundamental aspects of energy dissipation in friction. *Chem. Rev.* 114 (2014) 677–711. <http://doi.org/10.1021/cr200431y>
- [18] Park, J. Y.; Qi, Y.; Ogletree, D. F.; Thiel, P. A.; Salmeron, M., Influence of carrier density on the friction properties of siliconpnjunctions. *Phys. Rev. B: Condens. Matter Mater. Phys.* 76 (2007). <http://doi.org/10.1103/PhysRevB.76.064108>
- [19] Tian, D.; Jeong, D.-Y.; Fu, Z.; Chu, B., Flexoelectric effect of ferroelectric materials and its applications. *Actuators* 12 (2023) 114. <http://doi.org/10.3390/act12030114>
- [20] Cady, W. G., *Piezoelectricity : an introduction to the theory and applications of electromechanical phenomena in crystals*. McGraw-Hill: New York, 1946.
- [21] Huang, W.; Yuan, F. G.; Jiang, X., 5 - Flexoelectric effect, materials, and structures. In *Structural Health Monitoring (SHM) in Aerospace Structures*, Elsevier Ltd: 2016; pp 119–148. <http://doi.org/10.1016/B978-0-08-100148-6.00005-6>
- [22] Romyantseva, E. D.; Zaleskii, V. G., Strain of a BaTiO₃ single crystal caused by the converse flexoelectric effect. *Physics of the solid state* 58 (2016) 689-694. <http://doi.org/10.1134/S1063783416040211>
- [23] Koirala, P.; Mizzi, C. A.; Marks, L. D., Direct Observation of Large Flexoelectric Bending at the Nanoscale in Lanthanide Scandates. *Nano Lett.* 18 (2018) 3850-3856. <http://doi.org/10.1021/acs.nanolett.8b01126>
- [24] Zubko, P.; Catalan, G.; Tagantsev, A. K., Flexoelectric effect in solids. *Annu. Rev. Mater. Res.* 43 (2013) 387–421. <http://doi.org/10.1146/annurev-matsci-071312-121634>
- [25] Deng, Q.; Kammoun, M.; Erturk, A.; Sharma, P., Nanoscale flexoelectric energy harvesting. *Int. J. Solids Struct.* 51 (2014) 3218–3225. <http://doi.org/10.1016/j.ijsolstr.2014.05.018>
- [26] Li, H.; Chu, L.; Li, Y.; Dui, G.; Deng, Q., Study on PN heterojunctions associated bending coupling in flexoelectric semiconductor composites considering the effects of size-dependent and symmetry-breaking. *J. Appl. Phys.* 132 (2022) 125701. <http://doi.org/10.1063/5.0102209>
- [27] Deng, Q.; Liu, L.; Sharma, P., Flexoelectricity in soft materials and biological membranes. *Journal of the mechanics and physics of solids* 62 (2014) 209-227. <http://doi.org/10.1016/j.jmps.2013.09.021>
- [28] Wang, L.; Liu, S.; Feng, X.; Zhang, C.; Zhu, L.; Zhai, J.; Qin, Y.; Wang, Z. L., Flexoelectronics of centrosymmetric semiconductors. *Nat. Nanotechnol.* 15 (2020) 661-667. <http://doi.org/10.1038/s41565-020-0700-y>
- [29] Wu, C.; Wang, A. C.; Ding, W.; Guo, H.; Wang, Z. L., Triboelectric nanogenerator: A foundation of the energy for the new era. *Adv. Energy Mater.* 9 (2019) 1802906. <http://doi.org/10.1002/aenm.201802906>
- [30] Olson, K. P.; Mizzi, C. A.; Marks, L. D., Band bending and ratcheting explain triboelectricity in a flexoelectric contact diode. *Nano Lett.* 22 (2022) 3914–3921. <http://doi.org/10.1021/acs.nanolett.2c00107>
- [31] Mizzi, C. A.; Marks, L. D., When flexoelectricity drives triboelectricity. *Nano Lett.* 22 (2022) 3939–3945. <http://doi.org/10.1021/acs.nanolett.2c00240>
- [32] Niu, S.; Wang, Z. L., Theoretical systems of triboelectric nanogenerators. *Nano Energy* 14 (2015) 161–192. <http://doi.org/10.1016/j.nanoen.2014.11.034>
- [33] Salauddin, M.; Toyabur, R. M.; Maharjan, P.; Rasel, M. S.; Kim, J. W.; Cho, H.; Park, J. Y., Miniaturized springless hybrid nanogenerator for powering portable and

- wearable electronic devices from human-body-induced vibration. *Nano Energy* 51 (2018) 61–72. <http://doi.org/10.1016/j.nanoen.2018.06.042>
- [34] Zheng, Q.; Shi, B.; Li, Z.; Wang, Z. L., Recent progress on piezoelectric and triboelectric energy harvesters in biomedical systems. *Adv. Sci.* 4 (2017) 1700029. <http://doi.org/10.1002/advs.201700029>
- [35] Su, Y.; Wang, J.; Wang, B.; Yang, T.; Yang, B.; Xie, G.; Zhou, Y.; Zhang, S.; Tai, H.; Cai, Z.; Chen, G.; Jiang, Y.; Chen, L.-Q.; Chen, J., Alveolus-inspired active membrane sensors for self-powered wearable chemical sensing and breath analysis. *ACS Nano*. 14 (2020) 6067–6075. <http://doi.org/10.1021/acsnano.0c01804>
- [36] Lin, Z.; Yang, J.; Li, X.; Wu, Y.; Wei, W.; Liu, J.; Chen, J.; Yang, J., Large-scale and washable smart textiles based on triboelectric nanogenerator arrays for self-powered sleeping monitoring. *Adv. Funct. Mater.* 28 (2018) 1704112. <http://doi.org/10.1002/adfm.201704112>
- [37] Lai, Y. C.; Deng, J.; Zhang, S. L.; Niu, S.; Guo, H.; Wang, Z. L., Single-thread-based wearable and highly stretchable triboelectric nanogenerators and their applications in cloth-based self-powered human-interactive and biomedical sensing. *Adv. Funct. Mater.* 27 (2017) 1604462. <http://doi.org/10.1002/adfm.201604462>
- [38] San, S. T.; Yun, J.; Kim, D., Hybridized generator to simultaneously harvest tribo-thermal energy induced by vibration of fluorine rich-beads. *Nano Energy* 97 (2022). <http://doi.org/10.1016/j.nanoen.2022.107211>
- [39] Chen, J.; Wang, Z. L., Reviving vibration energy harvesting and self-powered sensing by a triboelectric nanogenerator. *Joule* 1 (2017) 480–521. <http://doi.org/10.1016/j.joule.2017.09.004>
- [40] Wang, J.; Wang, H.; Thakor, N. V.; Lee, C., Self-powered direct muscle stimulation using a triboelectric nanogenerator (TEG) integrated with a flexible multiple-channel intramuscular electrode. *ACS Nano*. 13 (2019) 3589–3599. <http://doi.org/10.1021/acsnano.9b00140>
- [41] Wang, X.; Song, J.; Liu, J.; Zhong, L. W., Direct-current nanogenerator driven by ultrasonic waves. *Science*. 316 (2007) 102–105. <http://doi.org/10.1126/science.1139366>
- [42] Tao, K.; Yi, H.; Yang, Y.; Chang, H.; Wu, J.; Tang, L.; Yang, Z.; Wang, N.; Hu, L.; Fu, Y.; Miao, J.; Yuan, W., Origami-inspired electret-based triboelectric generator for biomechanical and ocean wave energy harvesting. *Nano Energy* 67 (2020) 104197. <http://doi.org/10.1016/j.nanoen.2019.104197>
- [43] Xu, L.; Jiang, T.; Lin, P.; Shao, J. J.; He, C.; Zhong, W.; Chen, X. Y.; Wang, Z. L., Coupled triboelectric nanogenerator networks for efficient water wave energy harvesting. *ACS Nano*. 12 (2018) 1849–1858. <http://doi.org/10.1021/acsnano.7b08674>
- [44] Xi, Y.; Guo, H.; Zi, Y.; Li, X.; Wang, J.; Deng, J.; Li, S.; Hu, C.; Cao, X.; Wang, Z. L., Multifunctional TENG for blue energy scavenging and self-powered wind-speed sensor. *Adv. Energy Mater.* 7 (2017) 1602397. <http://doi.org/10.1002/aenm.201602397>
- [45] Chen, J.; Yang, J.; Li, Z.; Fan, X.; Zi, Y.; Jing, Q.; Guo, H.; Wen, Z.; Pradel, K. C.; Niu, S.; Wang, Z. L., Networks of triboelectric nanogenerators for harvesting water wave energy: A potential approach toward blue energy. *ACS Nano*. 9 (2015) 3324–3331. <http://doi.org/10.1021/acsnano.5b00534>

- [46] Zhang, S.; Bick, M.; Xiao, X.; Chen, G.; Nashalian, A.; Chen, J., Leveraging triboelectric nanogenerators for bioengineering. *Matter* 4 (2021) 845-887. <http://doi.org/10.1016/j.matt.2021.01.006>
- [47] Wang, Z. L. a., *Triboelectric nanogenerators*. 1st ed. 2016.. ed.; Cham : Springer International Publishing : Imprint: Springer: 2016.
- [48] Shin, S.-H.; Kwon, Y. H.; Kim, Y.-H.; Jung, J.-Y.; Lee, M. H.; Nah, J., Triboelectric charging sequence induced by surface functionalization as a method to fabricate high performance triboelectric generators. *ACS Nano*. 9 (2015) 4621–4627. <http://doi.org/10.1021/acsnano.5b01340>
- [49] Zi, Y.; Guo, H.; Wen, Z.; Yeh, M.-H.; Hu, C.; Wang, Z. L., Harvesting low-frequency (<5 Hz) irregular mechanical energy: a possible killer application of triboelectric nanogenerator. *ACS Nano*. 10 (2016) 4797–4805. <http://doi.org/10.1021/acsnano.6b01569>
- [50] Liu, J.; Cheikh, M. I.; Bao, R.; Peng, H.; Liu, F.; Li, Z.; Jiang, K.; Chen, J.; Thundat, T., Tribo-tunneling DC generator with carbon aerogel/silicon multi-nanocontacts. *Adv. Electron. Mater.* 5 (2019) 1900464. <http://doi.org/10.1002/aelm.201900464>
- [51] Zhou, L.; Liu, D.; Wang, J.; Wang, Z. L., Triboelectric nanogenerators: fundamental physics and potential applications. *Friction*. 8 (2020) 481–506. <http://doi.org/10.1007/s40544-020-0390-3>
- [52] Akbulut, M.; Godfrey Alig, A. R.; Israelachvili, J., Triboelectrification between smooth metal surfaces coated with self-assembled monolayers (SAMs). *J. Phys. Chem. B*. 110 (2006) 22271–22278. <http://doi.org/10.1021/jp063161j>
- [53] Xu, R.; Zhang, Q.; Wang, J. Y.; Liu, D.; Wang, J.; Wang, Z. L., Direct current triboelectric cell by sliding an n-type semiconductor on a p-type semiconductor. *Nano Energy* 66 (2019) 104185. <http://doi.org/10.1016/j.nanoen.2019.104185>
- [54] Liu, L.; Zhao, Z.; Li, Y.; Li, X.; Liu, D.; Li, S.; Gao, Y.; Zhou, L.; Wang, J.; Wang, Z. L., Achieving ultrahigh effective surface charge density of direct-current triboelectric nanogenerator in high humidity. *Small* (2022) e2201402. <http://doi.org/10.1002/sml.202201402>
- [55] Lin, S.; Lu, Y.; Feng, S.; Hao, Z.; Yan, Y., A high current density direct-current generator based on a moving van der Waals Schottky diode. *Adv. Mater.* 31 (2018) 1804398. <http://doi.org/10.1002/adma.201804398>
- [56] Lee, J. H.; Kim, S.; Kim, T. Y.; Khan, U.; Kim, S.-W., Water droplet-driven triboelectric nanogenerator with superhydrophobic surfaces. *Nano Energy* 58 (2019) 579–584. <http://doi.org/10.1016/j.nanoen.2019.01.078>
- [57] Yin, X.; Liu, D.; Zhou, L.; Li, X.; Zhang, C.; Cheng, P.; Guo, H.; Song, W.; Wang, J.; Wang, Z. L., Structure and dimension effects on the performance of layered triboelectric nanogenerators in contact-separation mode. *ACS Nano*. 13 (2019) 698–705. <http://doi.org/10.1021/acsnano.8b07935>
- [58] Liu, D.; Yin, X.; Guo, H.; Zhou, L.; Li, X.; Zhang, C.; Wang, J.; Wang, Z. L., A constant current triboelectric nanogenerator arising from electrostatic breakdown. *Sci Adv* 5 (2019) eaav6437. <http://doi.org/10.1126/sciadv.aav6437>
- [59] Liu, W.; Wang, Z.; Wang, G.; Liu, G.; Chen, J.; Pu, X.; Xi, Y.; Wang, X.; Guo, H.; Hu, C.; Wang, Z. L., Integrated charge excitation triboelectric nanogenerator. *Nat. Commun.* 10 (2019) 1426. <http://doi.org/10.1038/s41467-019-09464-8>
- [60] Huang, X.; Xiang, X.; Nie, J.; Peng, D.; Yang, F.; Wu, Z.; Jiang, H.; Xu, Z.; Zheng, Q., Microscale Schottky superlubric generator with high direct-current density and

ultralong life. *Nat. Commun.* 12 (2021) 2268. <http://doi.org/10.1038/s41467-021-22371-1>

[61] Zheng, M.; Lin, S.; Tang, Z.; Feng, Y.; Wang, Z. L., Photovoltaic effect and tribovoltaic effect at liquid-semiconductor interface. *Nano Energy* 83 (2021) 105810. <http://doi.org/10.1016/j.nanoen.2021.105810>

[62] Zheng, M.; Lin, S.; Xu, L.; Zhu, L.; Wang, Z. L., Scanning probing of the tribovoltaic effect at the sliding interface of two semiconductors. *Adv. Mater.* 32 (2020) e2000928. <http://doi.org/10.1002/adma.202000928>

[63] Zhang, Z.; He, T.; Zhao, J.; Liu, G.; Wang, Z. L.; Zhang, C., Tribo-thermoelectric and tribovoltaic coupling effect at metal-semiconductor interface. *Mater. Today Phys.* 16 (2021). <http://doi.org/10.1016/j.mtphys.2020.100295>

[64] Lin, S.; Chen, X.; Wang, Z. L., The tribovoltaic effect and electron transfer at a liquid-semiconductor interface. *Nano Energy* 76 (2020) 105070. <http://doi.org/10.1016/j.nanoen.2020.105070>

[65] Zhang, Z.; Jiang, D.; Zhao, J.; Liu, G.; Bu, T.; Zhang, C.; Wang, Z. L., Tribovoltaic effect on metal-semiconductor interface for direct-current low-impedance triboelectric nanogenerators. *Adv. Energy Mater.* 10 (2020) 1903713. <http://doi.org/10.1002/aenm.201903713>

[66] Zhang, J.; Coote, M. L.; Ciampi, S., Electrostatics and electrochemistry: mechanism and scope of charge-transfer reactions on the surface of tribocharged insulators. *J. Am. Chem. Soc.* 143 (2021) 3019–3032. <http://doi.org/10.1021/jacs.0c11006>

[67] Kim, W.-G.; Kim, D.-W.; Tcho, I.-W.; Kim, J.-K.; Kim, M.-S.; Choi, Y.-K., Triboelectric nanogenerator: Structure, mechanism, and applications. *ACS Nano*. 15 (2021) 258–287. <http://doi.org/10.1021/acsnano.0c09803>

[68] Duke, C. B.; Noolandi, J.; Thieret, T., The surface science of xerography. *Surf. Sci.* 500 (2002) 1005–1023. [http://doi.org/10.1016/S0039-6028\(01\)01527-8](http://doi.org/10.1016/S0039-6028(01)01527-8)

[69] Wang, Z. L.; Wang, A. C., On the origin of contact-electrification. *Mater. Today*. 30 (2019) 34–51. <http://doi.org/10.1016/j.mattod.2019.05.016>

[70] Liu, C.-y.; Bard, A. J., Electrostatic electrochemistry: Nylon and polyethylene systems. *Chem. Phys. Lett.* 485 (2010) 231–234. <http://doi.org/10.1016/j.cplett.2009.12.009>

[71] Bard, A. J.; Liu, C., Electrostatic electrochemistry at insulators. *Nat Mater* 7 (2008) 505–509. <http://doi.org/10.1038/nmat2160>

[72] Burgo, T. A. L.; Ducati, T. R. D.; Francisco, K. R.; Clinckspoor, K. J.; Galembeck, F.; Galembeck, S. E., Triboelectricity: Macroscopic charge patterns formed by self-arraying ions on polymer surfaces. *Langmuir* 28 (2012) 7407–7416. <http://doi.org/10.1021/la301228j>

[73] Zhang, L.; Laborda, E.; Darwish, N.; Noble, B. B.; Tyrell, J. H.; Pluczyk, S.; Le Brun, A. P.; Wallace, G. G.; Gonzalez, J.; Coote, M. L.; Ciampi, S., Electrochemical and electrostatic cleavage of alkoxyamines. *J. Am. Chem. Soc.* 140 (2018) 766–774. <http://doi.org/10.1021/jacs.7b11628>

[74] Zhang, J.; Rogers, F. J. M.; Darwish, N.; Gonçalves, V. R.; Vogel, Y. B.; Wang, F.; Gooding, J. J.; Peiris, M. C. R.; Jia, G.; Veder, J.-P.; Coote, M. L.; Ciampi, S., Electrochemistry on tribocharged polymers is governed by the stability of surface charges rather than charging magnitude. *J. Am. Chem. Soc.* 141 (2019) 5863–5870. <http://doi.org/10.1021/jacs.9b00297>

- [75] Chaplin, M., Theory vs Experiment: What is the surface charge of water? *Water* 1 (2009) 1–28.
- [76] Burgo, T. A. L.; Galembeck, F.; Pollack, G. H., Where is water in the triboelectric series? *J. Electrostat.* 80 (2016) 30–33. <http://doi.org/10.1016/j.elstat.2016.01.002>
- [77] Beattie, J. K.; Djerdjev, A. M., The pristine oil/water interface: Surfactant-free hydroxide-charged emulsions. *Angew. Chem.* 43 (2004) 3568–3571. <http://doi.org/10.1002/anie.200453916>
- [78] Vogel, Y. B.; Evans, C. W.; Belotti, M.; Xu, L.; Russell, I. C.; Yu, L.-J.; Fung, A. K. K.; Hill, N. S.; Darwish, N.; Gonçalves, V. R.; Coote, M. L.; Swaminathan Iyer, K.; Ciampi, S., The corona of a surface bubble promotes electrochemical reactions. *Nat. Commun.* 11 (2020) 6323–6323. <http://doi.org/10.1038/s41467-020-20186-0>
- [79] Ciampi, S.; Iyer, K. S., Bubbles pinned on electrodes: Friends or foes of aqueous electrochemistry? *Curr. Opin. Electrochem.* 34 (2022). <http://doi.org/10.1016/j.coelec.2022.100992>
- [80] Lin, S.; Xu, L.; Chi Wang, A.; Wang, Z. L., Quantifying electron-transfer in liquid-solid contact electrification and the formation of electric double-layer. *Nat. Commun.* 11 (2020) 399. <http://doi.org/10.1038/s41467-019-14278-9>
- [81] Chen, Z.; Khajeh, A.; Martini, A.; Kim, S. H., Chemical and physical origins of friction on surfaces with atomic steps. *Sci Adv* 5 (2019) eaaw0513. <http://doi.org/10.1126/sciadv.aaw0513>
- [82] McCarty, L. S.; Whitesides, G. M., Electrostatic charging due to separation of ions at interfaces: contact electrification of ionic electrets. *Angew. Chem.* 47 (2008) 2188–2207. <http://doi.org/10.1002/anie.200701812>
- [83] Gooding, D. M.; Kaufman, G. K., *Tribocharging and the triboelectric series*. Chichester, UK: John Wiley & Sons, Ltd: Chichester, UK, (2011); pp 1–14. <http://doi.org/10.1002/9781119951438.eibc2239.pub2>
- [84] Zhang, J.; Ciampi, S., Shape and charge: Faraday’s ice pail experiment revisited. *ACS Cent. Sci* 6 (2020) 611–612. <http://doi.org/10.1021/acscentsci.0c00298>
- [85] Zhang, J.; Darwish, N.; Coote, M. L.; Ciampi, S., Static electrification of plastics under friction: The position of engineering-grade polyethylene terephthalate in the triboelectric series. *Adv. Eng. Mater.* (2019).
- [86] Zhang, J.; Ferrie, S.; Zhang, S.; Vogel, Y. B.; Peiris, C. R.; Darwish, N.; Ciampi, S., Single-electrode electrochemistry: chemically engineering surface adhesion and hardness to maximize redox work extracted from tribocharged silicon. *ACS Appl. Nano Mater.* 2 (2019) 7230–7236. <http://doi.org/10.1021/acsanm.9b01726>
- [87] Zhang, J.; Su, C.; Rogers, F. J. M.; Darwish, N.; Coote, M. L.; Ciampi, S., Irreproducibility in the triboelectric charging of insulators: Evidence of a non-monotonic charge: Versus contact time relationship. *Phys. Chem. Chem. Phys.* 22 (2020) 11671–11677. <http://doi.org/10.1039/d0cp01317j>
- [88] Jacobs, H. O.; Campbell, S. A.; Steward, M. G., Approaching nanoxerography: The use of electrostatic forces to position nanoparticles with 100 nm scale resolution. *Adv. Mater* 14 (2002) 1553–1557. [http://doi.org/10.1002/1521-4095\(20021104\)14:21<1553::AID-ADMA1553>3.0.CO;2-9](http://doi.org/10.1002/1521-4095(20021104)14:21<1553::AID-ADMA1553>3.0.CO;2-9)
- [89] Palleau, E.; Sangeetha, N. M.; Viau, G.; Marty, J.-D.; Rossier, L., Coulomb force directed single and binary assembly of nanoparticles from aqueous dispersions by AFM nanoxerography. *ACS Nano.* 5 (2011) 4228–4235. <http://doi.org/10.1021/nn2011893>

- [90] Liu, J.; Goswami, A.; Jiang, K. R.; Khan, F.; Kim, S.; McGee, R.; Li, Z.; Hu, Z. Y.; Lee, J.; Thundat, T., Direct-current triboelectricity generation by a sliding Schottky nanocontact on MoS₂ multilayers. *Nat. Nanotechnol.* 13 (2018) 112–116. <http://doi.org/10.1038/s41565-017-0019-5>
- [91] Shao, H.; Fang, J.; Wang, H.; Dai, L.; Lin, T., Polymer-metal Schottky contact with direct-current outputs. *Adv. Mater* 28 (2016) 1461–1466. <http://doi.org/10.1002/adma.201504778>
- [92] Linford, M. R.; Chidsey, C. E. D., Alkyl monolayers covalently bonded to silicon surfaces. *J. Am. Chem. Soc.* 115 (1993) 12631–12632. <http://doi.org/10.1021/ja00079a071>
- [93] Hunger, R.; Jaegermann, W.; Merson, A.; Shapira, Y.; Pettenkofer, C.; Rappich, J., Electronic Structure of Methoxy-, Bromo-, and Nitrobenzene Grafted onto Si(111). *J. Phys. Chem. B* 110 (2006) 15432–15441. <http://doi.org/10.1021/jp055702v>
- [94] Barrelet, C. J.; Robinson, D. B.; Cheng, J.; Hunt, T. P.; Quate, C. F.; Chidsey, C. E. D., Surface characterization and electrochemical properties of alkyl, fluorinated alkyl, and alkoxy monolayers on silicon. *Langmuir* 17 (2001) 3460–3465. <http://doi.org/10.1021/la010333p>
- [95] Kim, I.; Roh, H.; Yu, J.; Jeon, H.; Kim, D., A triboelectric nanogenerator using silica-based powder for appropriate technology. *Sens. Actuators, A* 280 (2018) 85–91. <http://doi.org/10.1016/j.sna.2018.07.013>
- [96] Lyu, X.; Ferrie, S.; Pivrikas, A.; MacGregor, M.; Ciampi, S., Sliding Schottky diode triboelectric nanogenerators with current output of 10⁹A/m² by molecular engineering of Si(211) surfaces. *Nano Energy* (2022) 107658. <http://doi.org/10.1016/j.nanoen.2022.107658>
- [97] Yang, R.; Xu, R.; Dou, W.; Benner, M.; Zhang, Q.; Liu, J., Semiconductor-based dynamic heterojunctions as an emerging strategy for high direct-current mechanical energy harvesting. *Nano Energy* 83 (2021) 105849. <http://doi.org/10.1016/j.nanoen.2021.105849>
- [98] Chaudhury, M. K., Adhesion and friction of self-assembled organic monolayers. *Curr. Opin. Colloid Interface Sci.* 2 (1997) 65–69. [http://doi.org/10.1016/S1359-0294\(97\)80009-X](http://doi.org/10.1016/S1359-0294(97)80009-X)
- [99] Kim, H. I.; Koini, T.; Lee, T. R.; Perry, S. S., Systematic studies of the frictional properties of fluorinated monolayers with atomic force microscopy: Comparison of CF₃- and CH₃-terminated films. *Langmuir* 13 (1997) 7192–7196. <http://doi.org/10.1021/la970539j>
- [100] Ehlert, G. J.; Galan, U.; Sodano, H. A., Role of surface chemistry in adhesion between ZnO nanowires and carbon fibers in hybrid composites. *ACS Appl. Mater. Interfaces.* 5 (2013) 635–645. <http://doi.org/10.1021/am302060v>
- [101] Ferrie, S.; Le Brun, A. P.; Krishnan, G.; Andersson, G. G.; Darwish, N.; Ciampi, S., Sliding silicon-based Schottky diodes: maximizing triboelectricity with surface chemistry. *Nano Energy* 93 (2022) 106861. <http://doi.org/10.1016/j.nanoen.2021.106861>
- [102] Liu, J.; Zhang, Y.; Chen, J.; Bao, R.; Jiang, K.; Khan, F.; Goswami, A.; Li, Z.; Liu, F.; Feng, K.; Luo, J.; Thundat, T., Separation and quantum tunneling of photo-generated carriers using a tribo-induced field. *Matter* 1 (2019) 650–660. <http://doi.org/10.1016/j.matt.2019.05.017>

- [103] Liu, J.; Miao, M.; Jiang, K.; Khan, F.; Goswami, A.; McGee, R.; Li, Z.; Nguyen, L.; Hu, Z.; Lee, J.; Cadien, K.; Thundat, T., Sustained electron tunneling at unbiased metal-insulator-semiconductor triboelectric contacts. *Nano Energy* 48 (2018) 320–326. <http://doi.org/10.1016/j.nanoen.2018.03.068>
- [104] Vogel, Y. B.; Zhang, L.; Darwish, N.; Gonçalves, V. R.; Le Brun, A.; Gooding, J. J.; Molina, A.; Wallace, G. G.; Coote, M. L.; Gonzalez, J.; Ciampi, S., Reproducible flaws unveil electrostatic aspects of semiconductor electrochemistry. *Nat. Commun.* 8 (2017) 2066. <http://doi.org/10.1038/s41467-017-02091-1>
- [105] Aragonès, A. C.; Darwish, N.; Ciampi, S.; Sanz, F.; Gooding, J. J.; Diéz-Pérez, I., Single-molecule electrical contacts on silicon electrodes under ambient conditions. *Nat. Commun.* 8 (2017) 15056. <http://doi.org/10.1038/ncomms15056>
- [106] Peiris, C. R.; Ferrie, S.; Ciampi, S.; Rickard, W. D. A.; Darwish, N., Memristor arrays formed by reversible formation and breakdown of nanoscale silica layers on Si–H surfaces. *ACS Appl. Nano Mater.* 5 (2022) 6609–6617. <http://doi.org/10.1021/acsnm.2c00663>
- [107] Li, T.; Dief, E. M.; Lyu, X.; Rahpeima, S.; Ciampi, S.; Darwish, N., Nanoscale silicon oxide reduces electron transfer kinetics of surface-bound ferrocene monolayers on dilicon. *J. Phys. Chem. C* 125 (2021) 27763–27770. <http://doi.org/10.1021/acs.jpcc.1c07788>
- [108] Zhang, S.; Ferrie, S.; Lyu, X.; Xia, Y.; Darwish, N.; Wang, Z.; Ciampi, S., Absence of a relationship between surface conductivity and electrochemical rates: redox-active monolayers on Si(211), Si(111), and Si(110). *J. Phys. Chem. C* 125 (2021) 18197–18203. <http://doi.org/10.1021/acs.jpcc.1c05023>
- [109] Dief, E. M.; Brun, A. P. L.; Ciampi, S.; Darwish, N., Spontaneous grafting of OH-terminated molecules on Si–H surfaces via Si–O–C covalent bonding. *Surfaces* 4 (2021) 81–88. <http://doi.org/10.3390/surfaces4010010>
- [110] Veerbeek, J.; Huskens, J., Applications of monolayer-functionalized H-terminated silicon surfaces: A review. *Small Methods* 1 (2017) 1700072. <http://doi.org/10.1002/smt.201700072>
- [111] Linford, M. R.; Fenter, P.; Eisenberger, P. M.; Chidsey, C. E. D., Alkyl monolayers on silicon prepared from 1-alkenes and hydrogen-terminated silicon. *J. Am. Chem. Soc.* 117 (1995) 3145–3155. <http://doi.org/10.1021/ja00116a019>
- [112] Ferrie, S.; Darwish, N.; Gooding, J. J.; Ciampi, S., Harnessing silicon facet-dependent conductivity to enhance the direct-current produced by a sliding Schottky diode triboelectric nanogenerator. *Nano Energy* 78 (2020) 105210. <http://doi.org/10.1016/j.nanoen.2020.105210>
- [113] Zhao, Y.; Descamps, J.; Ababou-Girard, S.; Bergamini, J. F.; Santinacci, L.; Léger, Y.; Sojic, N.; Loget, G., Metal-insulator-semiconductor anodes for ultrastable and site-selective upconversion photoinduced electrochemiluminescence. *Angew. Chem.* 134 (2022) n/a. <http://doi.org/10.1002/ange.202201865>
- [114] Loget, G.; Fabre, B.; Fryars, S. p.; Mériadec, C.; Ababou-Girard, S., Dispersed Ni nanoparticles stabilize silicon photoanodes for efficient and inexpensive sunlight-assisted water oxidation. *ACS Energy Lett.* 2 (2017) 569–573. <http://doi.org/10.1021/acsenenergylett.7b00034>
- [115] Zhao, Y.; Yu, J.; Xu, G.; Sojic, N.; Loget, G., Photoinduced electrochemiluminescence at silicon electrodes in water. *J. Am. Chem. Soc.* 141 (2019) 13013–13016. <http://doi.org/10.1021/jacs.9b06743>

- [116] Wagle, D. V.; Baker, G. A., Cold welding: a phenomenon for spontaneous self-healing and shape genesis at the nanoscale. *Mater. Horiz.* 2 (2015) 157-167. <http://doi.org/10.1039/c4mh00105b>
- [117] Wang, S.; Zi, Y.; Zhou, Y. S.; Li, S.; Fan, F.; Lin, L.; Wang, Z. L., Molecular surface functionalization to enhance the power output of triboelectric nanogenerators. *J. Mater. Chem. A* 4 (2016) 3728–3734. <http://doi.org/10.1039/c5ta10239a>
- [118] You, Z.; Wang, S.; Li, Z.; Zou, Y.; Lu, T.; Wang, F.; Hu, B.; Wang, X.; Li, L.; Fang, W.; Liu, Y., High current output direct-current triboelectric nanogenerator based on organic semiconductor heterojunction. *Nano Energy* 91 (2022) 106667. <http://doi.org/10.1016/j.nanoen.2021.106667>
- [119] Xu, C.; Liu, Y.; Liu, Y.; Zheng, Y.; Feng, Y.; Wang, B.; Kong, X.; Zhang, X.; Wang, D., New inorganic coating-based triboelectric nanogenerators with anti-wear and self-healing properties for efficient wave energy harvesting. *Appl. Mater. Today* 20 (2020) 100645. <http://doi.org/10.1016/j.apmt.2020.100645>
- [120] Zeng, Q.; Wu, Y.; Tang, Q.; Liu, W.; Wu, J.; Zhang, Y.; Yin, G.; Yang, H.; Yuan, S.; Tan, D.; Hu, C.; Wang, X., A high-efficient breeze energy harvester utilizing a full-packaged triboelectric nanogenerator based on flow-induced vibration. *Nano Energy* 70 (2020) 104524. <http://doi.org/10.1016/j.nanoen.2020.104524>
- [121] Chen, P.; An, J.; Shu, S.; Cheng, R.; Nie, J.; Jiang, T.; Wang, Z. L., Super-durable, low-wear, and high-performance fur-brush triboelectric nanogenerator for wind and water energy harvesting for smart agriculture. *Adv. Energy Mater.* 11 (2021) 2003066. <http://doi.org/10.1002/aenm.202003066>
- [122] Chen, S.; Liu, D.; Zhou, L.; Li, S.; Zhao, Z.; Cui, S.; Gao, Y.; Li, Y.; Wang, Z. L.; Wang, J., Improved output performance of direct-current triboelectric nanogenerator through field enhancing breakdown effect. *Adv. Mater. Technol.* 6 (2021) 2100195. <http://doi.org/10.1002/admt.202100195>
- [123] Lu, Y.; Feng, S.; Shen, R.; Xu, Y.; Hao, Z.; Yan, Y.; Zheng, H.; Yu, X.; Gao, Q.; Zhang, P.; Lin, S., Tunable dynamic black phosphorus/insulator/Si heterojunction direct-current generator based on the hot electron transport. *Research* 2019 (2019) 5832382. <http://doi.org/10.34133/2019/5832382>
- [124] Liu, J.; Liu, F.; Bao, R.; Jiang, K.; Khan, F.; Li, Z.; Peng, H.; Chen, J.; Alodhayb, A.; Thundat, T., Scaled-up direct-current generation in MoS₂ multilayer-based moving heterojunctions. *ACS Appl. Mater. Interfaces* 11 (2019) 35404–35409. <http://doi.org/10.1021/acsami.9b09851>
- [125] Berman, D.; Erdemir, A.; Sumant, A. V., Graphene: a new emerging lubricant. *Mater. Today* 17 (2014) 31–42. <http://doi.org/10.1016/j.mattod.2013.12.003>
- [126] Ciampi, S.; Eggers, P. K.; Le Saux, G.; James, M.; Harper, J. B.; Gooding, J. J., Silicon (100) Electrodes Resistant to Oxidation in Aqueous Solutions: An Unexpected Benefit of Surface Acetylene Moieties. *Langmuir* 25 (2009) 2530-2539. <http://doi.org/10.1021/la803710d>
- [127] Peiris, C. R.; Ferrie, S.; Ciampi, S.; Rickard, W. D. A.; Darwish, N., Memristor arrays formed by reversible formation and breakdown of nanoscale silica layers on Si–H surfaces. *ACS Appl. Nano Mater.* 5 (2022) 6609–6617. <http://doi.org/10.1021/acsanm.2c00663>
- [128] Abadal, G.; Pérez-Murano, F.; Barniol, N.; Aymerich, X., Field induced oxidation of silicon by SPM: study of the mechanism at negative sample voltage by STM, ESTM

and AFM. *Appl. Phys. A: Mater. Sci. Process.* 66 (1998) S791–S795.
<http://doi.org/10.1007/s003390051244>

[129] Pang, J.; Bachmatiuk, A.; Yin, Y.; Trzebicka, B.; Zhao, L.; Fu, L.; Mendes, R. G.; Gemming, T.; Liu, Z.; Rummeli, M. H., Applications of phosphorene and black phosphorus in energy conversion and storage devices. *Adv. Energy Mater.* 8 (2018) 1702093. <http://doi.org/10.1002/aenm.201702093>

[130] Lu, Y.; Gao, Q.; Yu, X.; Zheng, H.; Shen, R.; Hao, Z.; Yan, Y.; Zhang, P.; Wen, Y.; Yang, G.; Lin, S., Interfacial built-in electric field-driven direct current generator based on dynamic silicon homojunction. *Research* 2020 (2020) 5714754. <http://doi.org/10.34133/2020/5714754>

[131] Lu, Y.; Yan, Y.; Yu, X.; Zhou, X.; Feng, S.; Xu, C.; Zheng, H.; Yang, Z.; Li, L.; Liu, K.; Lin, S., Polarized water driven dynamic PN junction-based direct-current generator. *Research* 2021 (2021) 7505638. <http://doi.org/10.34133/2021/7505638>

[132] Sharov, V. A.; Alekseev, P. A.; Borodin, B. R.; Dunaevskiy, M. S.; Reznik, R. R.; Cirlin, G. E., InP/Si heterostructure for high-current hybrid triboelectric/photovoltaic generation. *ACS Appl. Energy Mater.* 2 (2019) 4395–4401. <http://doi.org/10.1021/acsaem.9b00576>

Chapter 2 – General Experimental

Throughout the thesis, experimental details on surface functionalization procedures, AFM measurements and electrochemical techniques are presented in corresponding chapter. This chapter aims at presenting the general experimental aspects common to all results chapters.

2.1 Materials

2.1.1 Chemicals

All chemicals used in this research, unless specified otherwise, were of analytical grade and used as received. Detailed information of chemical used for each procedure of experiment can be found in experimental section under each chapter.

2.1.2 Silicon

Silicon is the most common semiconductor especially in electronic devices. It's been widely used in electronics due to its low cost and easy access. Figure 2.1 shows the crystal structure of silicon. Its crystal structure is a face-centered diamond cubic [1]. In such diamond lattice structure, each atom forms four identical covalent bonds with its neighbours.

For single crystal silicon commonly used in research and industry, there are two manufacturing methods: Czochralski (CZ) or float-zone (FZ) process. In CZ process, a seed crystal is slowly inserted into a molten silicon melt in a crucible. As the seed is pulled upward, it gradually solidifies to form a single silicon crystal. The crucible containing the molten silicon is usually rotated continuously to maintain a uniform crystal structure [2]. FZ process is a crucible-free method for crystal growth. During the process, a seed crystal on a polycrystalline silicon rod is introduced to a molten

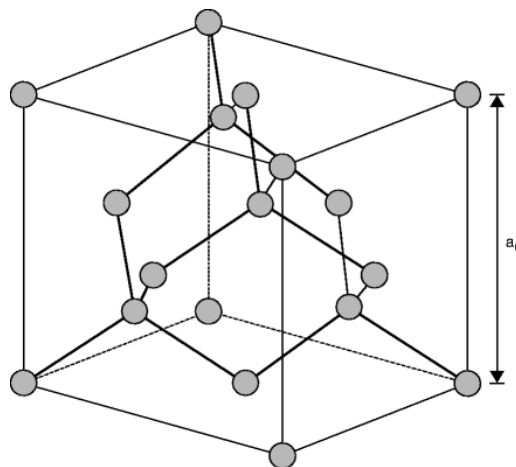


Figure 2.1. Crystallographic structure of the diamond cubic (Silicon). a_0 is the lattice constant of a relaxed lattice. Copyright (2011), with permission from Springer-Verlag/Wien [2].

zone. The molten zone is then moved along the rod, and the single crystal is gradually formed as impurities being pushed to the trailing end of the rod. Due to the absence of crucible, the contamination by crucible materials is eliminated and the crystal defects resulting from the interaction between growing crystal and container is prevented. Therefore, FZ process is more suitable for making highly reactive materials although the cost is higher than CZ process [3]. In this research, all silicon wafers used were of CZ process unless specified otherwise. The readily made large silicon crystal will usually then be cut into wafers for further uses. In addition, some other elements will be introduced to make either n-type or p-type silicon.

A single silicon crystal can expose different facets based on different cutting angles. Si(111) and Si(100) are two most common silicon facets. The number indicates the Miller indices, which are a set of three integers that determine the orientation of the planes or directions relative to the crystal lattice. Especially Si(100) is widely used in technological applications. The cross section perpendicular to Si(111) and Si(100) facets are Si(211) and Si(111) facets [4]. In this dissertation, Si(111) were primarily used as a research platform. After wet chemical etching, Si(211) facet were exposed and can be seen under AFM due to its different topographical and electrical characteristics. The details can be found in Chapter 3.

2.2 Etching mechanism

Commercially available silicon wafers are coated with a layer of oxide that needs to be removed before further reaction. Wet chemical etching process, which use etchants to remove the native oxide layer, organic impurities and expose the hydrogen-terminated surface, was utilized in this research. At first, Piranha solution,

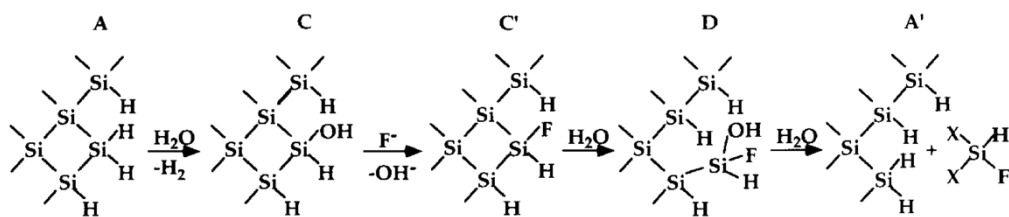


Figure 2.2. 2D model showing the n-type Si dissolve in NH_4F solution. Copyright (1995), with permission from Elsevier [6].

mixture of sulfuric acid and hydrogen peroxide, effectively removes organic compounds from substrates. Then, aqueous ammonium fluoride solution (NH_4F), rather than hydrofluoric acid (HF), were used as an etchant, considering its low level hazardous. Also, an atomically flat and clean surface can be obtained under room temperature with ammonium fluoride solution [5, 6]. The chemical reaction of the etching process is illustrated in Figure 2.2. It starts with the hydrolysis process of the hydrogen-terminated silicon (step A-C), then the Si-OH bond was replaced with Si-F bond (step C-C') followed by the chemical disruption of back bonds (step C-D).

Eventually, silicon atom enters into the solution as $\text{HSiF}(\text{OH})_2$ [6]. As time goes by, more and more Si atoms dissolve into the solution, thinning the silicon wafer and possibly making it rougher. Hence, the etching rate and duration is a key factor influencing the etching. Different etching solution and etching time were attempted to adapt to different silicon facets. More details can be found in Chapter 3 and Chapter 5.

2.3 Surface passivation and functionalization

Hydrogen-terminated surface after etching is not stable and can be easily oxidized at ambient condition within a day. Therefore, a carbon-based monolayer was then attached for surface passivation and functionalization, as different functional group

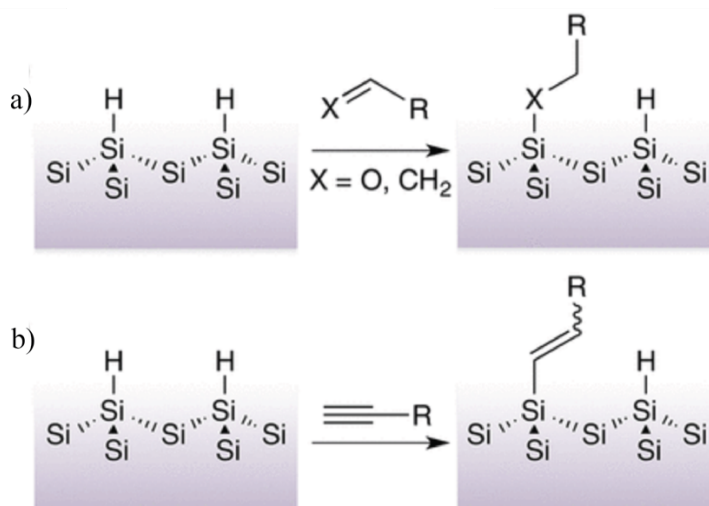


Figure 2.3. Hydrosilylation reaction of (a) an aldehyde, an alkene, and (b) an alkyne, on Si(111)-H. Copyright (2014), with permission from American Chemical Society [8].

at the end of carbon chain and their influence on zero-bias current is of the research interest. Linford and Chidsey firstly bonded alkyl monolayer onto silicon surfaces in 1993 [7]. The powerful reaction achieving it is hydrosilylation reaction, which can convert Si-H into Si-C bond. Usually C=C (alkene) or C≡C (alkyne) is required for hydrosilylation reaction [8, 9].

However, various conditions can trigger such reactions, including ultraviolet light, thermal catalysis, or resorting to a radical initiator [10-12]. Figure 2.3 illustrates the hydrosilylation process of an aldehyde, alkene or alkyne on hydrogen-terminated silicon. The monolayer attached via hydrosilylation reaction can effectively protect the silicon substrates from oxidation and exhibits different electrical features contacting with platinum tip under AFM with different terminal functional groups. The detailed results are presented in Chapter 3, Chapter 4 and Chapter 5.

2.4 Surface characterization

The well-prepared silicon substrates were then mainly analysed by atomic force microscopy (AFM) to obtain their topography, zero-bias current map, lateral friction, and current-potential (I-V) profiles. The detailed settings of each instrument and corresponding measurements are given under experimental section in each chapter. Here, the basic theory and principles of each test will be briefly introduced.

2.4.1 Atomic force microscopy test (AFM)

Atomic force microscopy (AFM) is one of the high-resolution techniques used to visualize the surface structure of materials at the atomic and molecular levels. It is a type of scanning probe microscopy that provides detailed three-dimensional images of the sample's surface and probes samples' thermal, electrical, and optical characteristics. AFM uses a sharp probe, usually with a sharp tip at the end, to scan across the sample's surface. The interaction force between tip end and sample surface is captured and amplified through the reflected laser light at the back of probe. A high-resolution image is eventually obtained by analysis the laser light signal captured by photodiode at the other end. Figure 2.4 exhibits the structure of an AFM

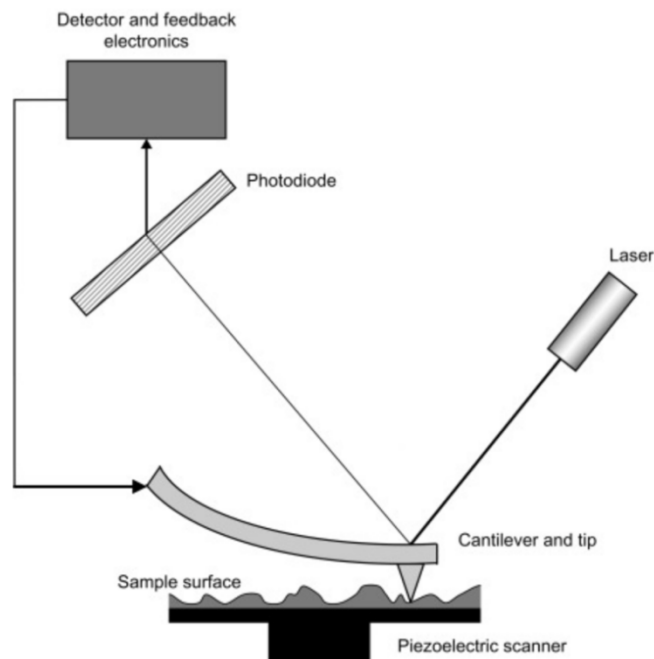


Figure 2.4. Simplified structure of atomic force microscopy. Copyright (2019), with permission from Elsevier [13].

[13]. Due to the fine end of the tip used in AFM, it can achieve nanoscale resolution. In addition, unlike other types of microscopies, AFM is non-destructive to sample as it does not require direct contact with sample surface in non-contact mode, so the samples can be analysed in their natural state. Typically, an AFM is equipped with various working modes including conductive AFM (C-AFM), Kelvin probe force microscopy (KPFM), electrochemical AFM (EC-AFM) et al. It allows to obtain a height image of a sample and probe other properties of interest at the same time.

2.4.1.1 Conductive-AFM scan (C-AFM)

In this research, conductive AFM (C-AFM) mode was primarily used. It is one of the contact modes, which establish a direct contact between tip and sample, allowing us to capture high-resolution image of sample surface, recording friction force and zero-bias current signal simultaneously while scanning across the surface. As mentioned above, the topography is measured by detecting the deflection of the cantilever using an optical system (laser & photodiode), while the current is captured and recorded

using an external current-to-voltage amplifier [14]. The current recorded by AFM obey the following relationship:

$$I = J \cdot A_{eff} \quad (2-1)$$

Where I is current, J is current density, and A_{eff} represents the effective contact area which electrons can flow through. From this, the current data obtained by AFM needs to be divided by the effective contact area to obtain meaningful current density. This facilitates comparisons between different samples. Considering that the tip-sample contact is in nanoscale, an estimation model called Derjaguin–Muller–Toporov model is used in this research. Further details can be found in Chapters 3–5.

2.4.1.2 Force–distance spectroscopy (F–d)

Force–distance spectroscopy is a reliable and straightforward technique to study nanomaterials' physical properties such as adhesion force and Young's modulus. It measures the force between tip and sample as a function of distance between them [15]. Figure 2.5 shows a typical profile of force distance curve. The tip gradually approaches the sample until get in contact and reaches the force limit (red line), then

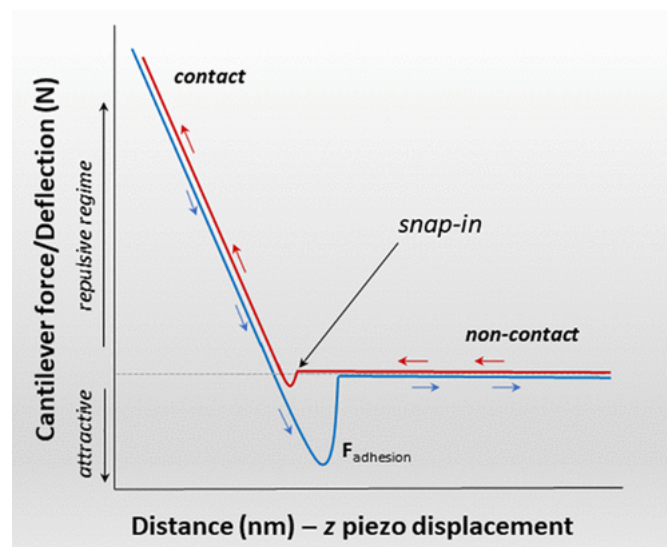


Figure 2.5. Representative profile of force distance curve measured by AFM. Copyright (2021), with permission from American Chemical Society [15].

it retracts from the surface until overcomes the adhesion force and lose contact with the sample surface (blue line). The lowest point of the retract line (blue line) represents the adhesion force between tip and sample. This value is crucial for effective contact area estimation.

2.4.1.3 Current-potential spectroscopy (I–V)

Current-potential spectroscopy (I–V) is a visualization of the relationship between current and applied voltage of electronic devices. It is usually used to characterize the electrical behavior of semiconductor-based device, such as p-n junction, Schottky diode, and solar cells. It records the current signal by sweeping the voltage in a certain range, both positive and negative. In this research, I–V measurement was used to exhibits forward bias and reverse bias region of Schottky diode formed between tip and samples, which further helps to determine the direction of tribocurrent and its possible correlation to static I–V profile. Further details will be discussed in Chapter 3.

2.4.1.4 Time-resolved photocurrent mapping (PCM)

As discussed in Section 1.1.3, transient photocurrent decay is a powerful tool to qualitatively determine the surface states and charge carriers' lifetime on semiconductor's surface. The AFM we used is equipped with an external laser light for photocurrent mapping. The precise controlling capability of AFM enables conducting photocurrent decay measurements at specific locations. Therefore, I can conduct PCM tests accurately at the points of interest and compare them with other locations or samples to investigate the influence of surface defects and recombination velocity on tribocurrent. The results and further discussion can be found in Chapter 3 and Chapter 5.

2.4.2 Macroscopic current-voltage (I–V) measurement

Considering the high contact pressure at AFM tip and sample interface, a macroscopic current–voltage (I–V) measurement using mercury drop was conducted. Figure 2.6 illustrates the schematic of such macroscopic I–V. Such mercury drop-silicon sample

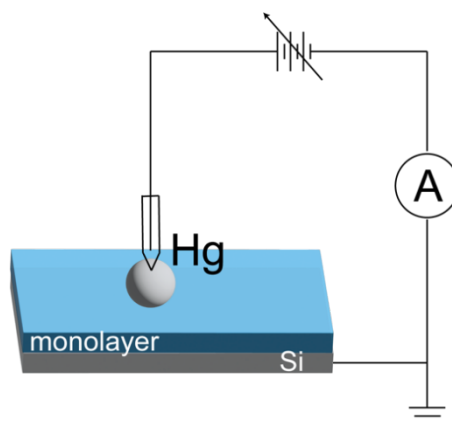


Figure 2.6. Schematic of macroscopic current-voltage (I-V) measurement device using mercury drop as contact material.

soft contact significantly reduces the pressure at interface when using AFM, and therefore tune the electrical response to external voltage. Detailed results can be found in section 4.3.3 (Chapter 4).

2.4.3 Contact angle goniometry (CA)

Contact angle goniometry is a technique used to measure the contact angle formed between a liquid droplet and a solid surface. This angle provides insights into the wetting properties of the surface, helping to characterize its hydrophobic or hydrophilic nature [16]. The schematic of contact angle goniometry is illustrated in

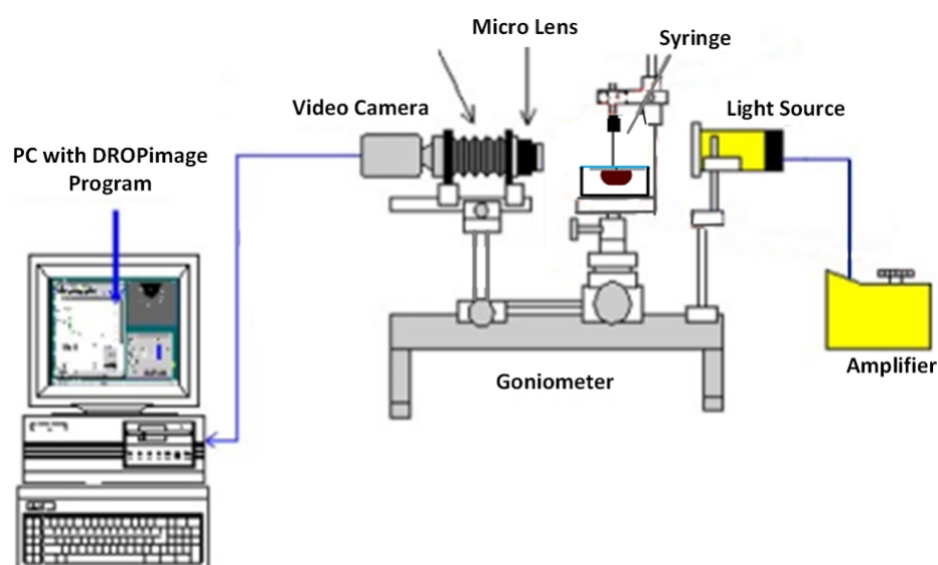


Figure 2.7. Schematic of contact angle goniometer. Copyright (2022), with permission from PLoS One [16].

Figure 2.7. It captures an image of the liquid droplet (usually water) on the sample's surface, and then processed with computer program to get the value of contact angle for further determination of the wettability of sample's surfaces. In this research, the contact angle goniometry is mainly used to help us to determine the terminal functional group of the organic monolayer attached.

2.4.4 X-ray photoelectron spectroscopy (XPS)

X-ray Photoelectron Spectroscopy (XPS) is an analytical technique with surface sensitivity employed for the chemical analysis of materials. It is highly effective in discerning the elemental composition and chemical state of a sample's surface. Its working mechanism is based on photoelectric effect. When the X-rays strike the sample, it can eject inner-shell (core-level) electrons from the atoms in the material. The ejected photoelectrons carry information about the chemical environment of the atoms from which they originated. By measuring the kinetic energy of the photoelectrons, the binding energy and, consequently, the chemical state of the corresponding elements in the sample can be determined [17]. In this research, XPS was used to confirm if the monolayer is successfully attached and to check if the treated surface is oxidized or not.

2.5 References

- [1] Sverdlov, V., *Strain-Induced Effects in Advanced MOSFETs*. Springer Vienna: Vienna, 2011. <http://doi.org/10.1007/978-3-7091-0382-1>
- [2] Usami, N., 4 - Types of silicon–germanium (SiGe) bulk crystal growth methods and their applications. Elsevier Ltd: 2011; pp 72–82. <http://doi.org/10.1533/9780857091420.2.72>
- [3] Mishra, U. K.; Singh, J., *Semiconductor device physics and design*. Springer Netherlands: Dordrecht, 2008. <http://doi.org/10.1007/978-1-4020-6481-4>
- [4] Qin, Z.; Gao, Y.; Jia, J.; Ding, X.; Huang, L.; Li, H., The Effect of the Anisotropy of Single Crystal Silicon on the Frequency Split of Vibrating Ring Gyroscopes. *Micromachines* (Basel) 10 (2019) 126. <http://doi.org/10.3390/mi10020126>
- [5] Higashi, G. S.; Becker, R. S.; Chabal, Y. J.; Becker, A. J., Comparison of Si(111) surfaces prepared using aqueous-solutions of NH₄F versus HF. *Appl. Phys. Lett.* 58 (1991) 1656–1658. <http://doi.org/10.1063/1.105155>
- [6] Allongue, P.; Kieling, V.; Gerischer, H., Etching mechanism and atomic structure of H-Si(111) surfaces prepared in NH₄F. *Electrochim. Acta.* 40 (1995) 1353–1360. [http://doi.org/10.1016/0013-4686\(95\)00071-L](http://doi.org/10.1016/0013-4686(95)00071-L)
- [7] Linford, M. R.; Chidsey, C. E. D., Alkyl monolayers covalently bonded to silicon surfaces. *J. Am. Chem. Soc.* 115 (1993) 12631–12632. <http://doi.org/10.1021/ja00079a071>
- [8] Barrelet, C. J.; Robinson, D. B.; Cheng, J.; Hunt, T. P.; Quate, C. F.; Chidsey, C. E. D., Surface characterization and electrochemical properties of alkyl, fluorinated alkyl, and alkoxy monolayers on silicon. *Langmuir* 17 (2001) 3460–3465. <http://doi.org/10.1021/la010333p>
- [9] Ciampi, S.; Böcking, T.; Kilian, K. A.; James, M.; Harper, J. B.; Gooding, J. J., Functionalization of acetylene-terminated monolayers on Si(100) surfaces: A click chemistry approach. *Langmuir* 23 (2007) 9320–9329. <http://doi.org/10.1021/la701035g>
- [10] Terry, J.; Linford, M. R.; Wigren, C.; Cao, R.; Pianetta, P.; Chidsey, C. E. D., Determination of the bonding of alkyl monolayers to the Si(111) surface using chemical-shift, scanned-energy photoelectron diffraction. *Appl. Phys. Lett.* 71 (1997) 1056–1058. <http://doi.org/10.1063/1.119726>
- [11] Buriak, J. M., Illuminating Silicon Surface Hydrosilylation: An Unexpected Plurality of Mechanisms. *Chemistry of materials* 26 (2014) 763–772. <http://doi.org/10.1021/cm402120f>
- [12] Thissen, P.; Seitz, O.; Chabal, Y. J., Wet chemical surface functionalization of oxide-free silicon. *Progress in surface science* 87 (2012) 272–290. <http://doi.org/10.1016/j.progsurf.2012.10.003>
- [13] Ardebili, H.; Zhang, J.; Pecht, M. G.; Licari, J. J., *Defect and Failure Analysis Techniques for Encapsulated Microelectronics*. 2nd Edition ed.; Elsevier: United States, 2019; pp 1–2. <http://doi.org/10.1016/B978-0-12-811978-5.00008-0>
- [14] Lanza, M., *Conductive atomic force microscopy : applications in nanomaterials*. Wiley-VCH: Weinheim, Germany, 2017.
- [15] Olubowale, O. H.; Biswas, S.; Azom, G.; Prather, B. L.; Owoso, S. D.; Rinee, K. C.; Marroquin, K.; Gates, K. A.; Chambers, M. B.; Xu, A.; Garno, J. C., “May the Force Be with You!” Force–Volume Mapping with Atomic Force Microscopy. *ACS omega* 6 (2021) 25860–25875. <http://doi.org/10.1021/acsomega.1c03829>

- [16] Adil, M.; Zaid, H. M.; Raza, F.; Agam, M. A., Experimental evaluation of oil recovery mechanism using a variety of surface-modified silica nanoparticles; role of in-situ surface-modification in oil-wet system. PloS one 2020 (2020) e0236837. <http://doi.org/10.1371/journal.pone.0236837>
- [17] Van der Heide, P., *X-ray photoelectron spectroscopy an introduction to principles and practices*. Wiley: Hoboken, N.J, 2012.

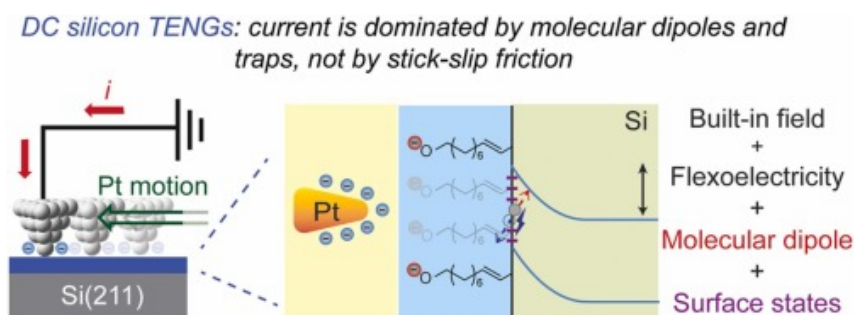
Chapter 3 – Sliding Schottky diode triboelectric nanogenerators with current output of 10^9 A/m² by molecular engineering of Si(211) surfaces

Adapted from Lyu, X.; Ferrie, S.; Pivrikas, A.; MacGregor, M.; Ciampi, S., Sliding Schottky diode triboelectric nanogenerators with current output of 10^9 A/m² by molecular engineering of Si(211) surfaces. *Nano Energy* **2020**, 78, 105210. Some content from supporting information has been moved into the main text for clarity of this study. Rights are retained to reuse in the thesis by the authors. An attribution statement is included as Appendix III.

Abstract

Triboelectric nanogenerators (TENGs) are an autonomous and sustainable power-generation technology, seeking to harvest small vibrations into electricity. Here, by achieving molecular control of oxide-free Si crystals and using conductive atomic force microscopy, we address key open questions and use this knowledge to demonstrate zero-applied-bias current densities as high as 10^9 A/m². Key to achieve this output, is to use a proton-exchangeable organic monolayer that simultaneously introduces a sufficiently high density of surface states (assessed as changes to carrier recombination velocities) coupled to a strong surface dipole in the form of a surface alkoxide anion (Si–monolayer–O⁻). We also demonstrate that the DC output of a Schottky diode TENG does not track the energy released as friction. This removes the complexity of controlling an unavoidable stick–slip motion, bypassing the requirement of aligning sliding motion and substrate topographical features. We reveal that there is no apparent correlation between the current of a static (biased) junction and the tribocurrent of the same junction when under motion and unbiased.

Graphical abstract



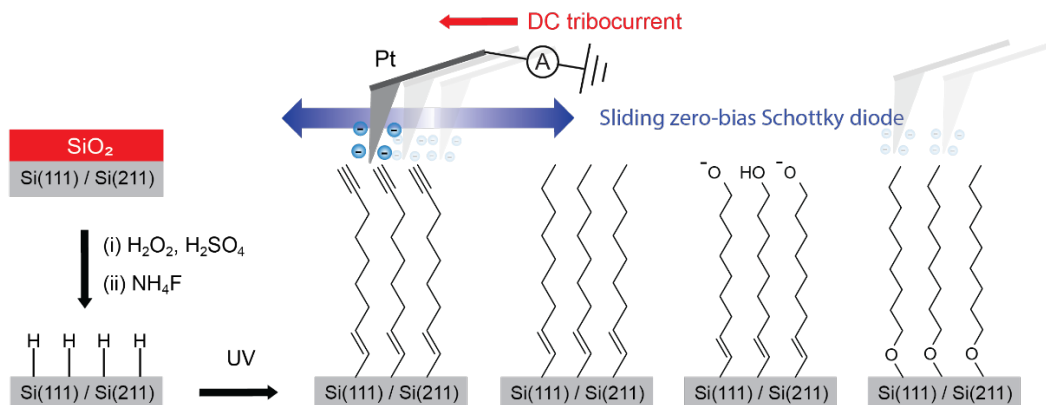
3.1 Introduction

Physics and chemistry textbooks often exemplify the first law of thermodynamics by referring to large machineries designed to convert mechanical into electrical energy. From wind turbines to tidal generators, everyday examples of sustainable-energy technologies that turns kinetic into electrical energy are, almost entirely, drawn from the macroscopic world. Most of such technologies remain based on electromagnetic generators, whose coils and moving magnets introduce significant limitations towards miniaturization of the power supply [1, 2]. Yet, miniature power supplies are a vital component of all small and portable electronic devices [3], with batteries being generally the most feasible option. However, for devices operating in poorly accessible or remote locations, battery replacement, or recharging, is often not viable [4, 5]. Microscopic autonomous power technologies dependent on solar radiation [6], thermal energy [7] or piezoelectricity [8] are one option towards recharging or supplementing batteries, but they are not free from drawbacks. Most notably, photovoltaic cells will fail when not illuminated, while piezoelectric generators can have cost, biocompatibility and size issues [9].

Ambient mechanical vibrations at the microscopic scale are ubiquitous and can be efficiently harvested into electricity [10], making triboelectric nanogenerators (TENGs) one of the most actively explored forms of autonomous, miniaturizable and sustainable power generation technology [11-15]. Conventional TENGs relies upon coupling contact electrification and electromagnetic induction: conductive plates that are in relative motion, but electrically isolated, output an alternating current (AC) [16, 17]. If used to power electronics, the AC output will first need to be rectified by additional circuitry, which will inevitably detract from the TENG's miniaturization claim. A recent technological breakthrough in the TENG technology was the observation of direct current (DC) flowing across a sharp metal wire as it slides across grains of molybdenum disulphide (MoS_2) [18, 19]. MoS_2 is a 2D semiconductor targeted for high-end electronic applications, which leads to the question of viability of the metal–semiconductor DC-TENG design in a significantly more widespread and low cost semiconductor: silicon [19-28].

Si-based triboelectricity has the potential of opening up an entirely new and fundamental area in energy and semiconductor research – one with strong conceptual links to the ongoing quest to use surface chemistry to control the rectifying “diode-like” properties of semiconductors [29-32]. The DC current density reported to date for a metal–semiconductor TENGs is of $\sim 10^6$ – 10^8 A/m² [18, 33, 34], which is highly encouraging since the full spectrum of chemical and electronic factors at play still remains unclear. The fundamental understanding of this new miniature, biocompatible, and continuous source of DC electricity is poor. The purpose of this paper is to fill gaps in the fundamental understanding of Schottky diodes TENGs, with the goal of improving their design, hence their current density output. Progress towards a systematic maximization of DC-TENG performances will require addressing open questions, and among the most pressing there are (i) how big of a role, if any, friction stick–slip events play in the conversion of kinetic into electrical energy? (ii) Will surface conductivity, as that of readily available, but seldom utilized, low-index silicon crystals [35, 36], affect device output? (iii) What governs the magnitude of the tribocurrent? Is it the outmost surface chemistry (metal–semiconductor interface), which also define the junction’s friction? Or is it the chemistry at the buried organic–inorganic interface, which also dominates charge transport [37]? (iv) Is there a link between charge transport in static junctions and charge generation under dynamic conditions? (v) Is there scope in optimizing surface recombination velocities as means to maximize the extraction of a tribocurrent?

The laboratory model system we used to answer the above questions is the inorganic semiconductor–organic molecule assembly depicted in Scheme 3.1. Formation of covalently bound molecular assemblies on oxide-free silicon crystals was achieved by wet chemistry methods, with the forward-looking idea that such methods can be implemented in any basic laboratory without specialized equipment [38, 39]. The importance and scope of surface chemistry functionalization is known to researchers working on polymer- and metal-based TENGs [40-42]. The common starting point of all surfaces studied in this work is the hydrogen-terminated surface (Si–H) obtained by etching native oxide-coated crystals in aqueous ammonium fluoride solutions [43]. Si–H surfaces are then reacted under UV-assisted chemisorption reaction through the



Scheme 3.1. Chemical passivation and functionalization of an oxide-free silicon surface. Native oxide-coated Si(111) and Si(211) crystals are first cleaned (i), and then etched (ii) to generate an hydrogen-terminated surface (Si–H). The Si–H surface is then reacted under UV radiation with liquid samples of either 1-nonanol, 1-nonyne, 8-nonyl-1-ol, and 1,8-nonadiyne, yielding the four monolayer-functionalized surfaces depicted respectively left to right. The zero-bias DC current output, friction, adhesion, charge recombination of dynamic silicon–monolayer–platinum Schottky diodes are studied by atomic force microscopy-based techniques.

radical chain reaction to form, respectively, Si–C-bound or Si–O-bound carbonaceous monolayers [44, 45]. The purpose of the organic monolayer is two-fold: preventing anodic decomposition of silicon [32, 36, 46], which is a non-oxide semiconductor and hence prone to such reaction, as well as enabling the rapid engineering of the sliding diode’s interfacial properties. Properties such as charge transfer, friction and adhesion [30, 47-49] can be predictably engineered by a surface-tethered organic monolayer bearing specific chemical functionalities [50, 51]. Friction has been previously observed to affect the current output of dynamic metal–semiconductor contacts [23], but the use in TENGs of inorganic substrate–organic molecule hybrids is still underexplored, with only a handful of examples available for metal–monolayer–metal [52] and metal–monolayer–semiconductor [19, 53] sliding junctions. Also prompting our investigation, and pertinent to the second and third questions outlined above, is the recent discovery of a strong facet-dependent conductivity for silicon crystals [35]. Low-index crystal facets, such as Si(110) and Si(211), despite being readily available have been entirely overlooked as potential substrate for TENGs, mainly because silicon electronics and electrochemical research has been historically focused on the widespread, but significantly less conductive, $\langle 100 \rangle$ and $\langle 111 \rangle$ facets [54-57].

3.2 Experimental section

3.2.1. Materials

Unless otherwise specified, all reagents were of analytical grade and used as received. Aqueous hydrogen peroxide (30% w/w, Sigma-Aldrich), sulfuric acid (95–97%, Sigma-Aldrich), and aqueous ammonium fluoride (40% w/w, Sigma-Aldrich) were of semiconductor grade. Redistilled solvents and Milli-Q™ water (>18 MΩ cm) were used to clean silicon substrates and to prepare electrolytic solutions. Perchloric acid (70%, Sigma-Aldrich, ACS reagent grade) was used to prepare electrolytic solutions for electrochemical measurements. Silicon wafers were purchased from Siltronix, S.A.S (Archamps, France), and were prime grade, (111)- and (211)-oriented ($\pm 0.5^\circ$ and $\pm 0.05^\circ$ miscut angle, respectively), 475–525 μm thick, single-side polished, n-type (phosphorous-doped), and 7–13 $\Omega\text{ cm}$ (lowly doped) in resistivity. Molecules used for silicon derivatization procedures were 1,8-nonadiyne (98%, Sigma-Aldrich), 1-nonyne (99%, Sigma-Aldrich), 8-nonyl-1-ol (97%, Biosynth Carbosynth), and 1-nonanol (98%, Biosynth Carbosynth).

3.2.2. Surface modification procedures

Silicon wafers were first cut into 10 × 10 mm squares, rinsed with dichloromethane, blow-dried under a stream of nitrogen, immersed for 30 min in hot piranha solution [100 °C, a 3:1 mixture (v/v) of concentrated sulfuric acid and hydrogen peroxide (30%)], and then rinsed extensively with water. The clean samples were then etched for 13 min in argon-saturated (Ar, 99.997%, Coregas) aqueous 40% solution of ammonium fluoride. The etching was carried out under ambient light. A small quantity (~10 mg) of ammonium sulfite is added to the etching solution as oxygen scavenger. The etching of Si(211) is performed as above, but in a 3:1 (v/v) mixture of aqueous 40% ammonium fluoride and methanol. The addition of methanol limits the nucleation of hydrogen bubbles on Si(211), preventing undesirable surface roughening (Figure 3.1). After the etching, the hydrogen-terminated (Si–H) samples were rinsed with water, dichloromethane, and then blow-dried under a stream of nitrogen. Si–H surfaces were then immediately covered with a small sample (~0.1 mL) of either 1,8-nonadiyne, 1-nonyne, 8-nonyl-1-ol, or 1-nonanol. Prior to this step,

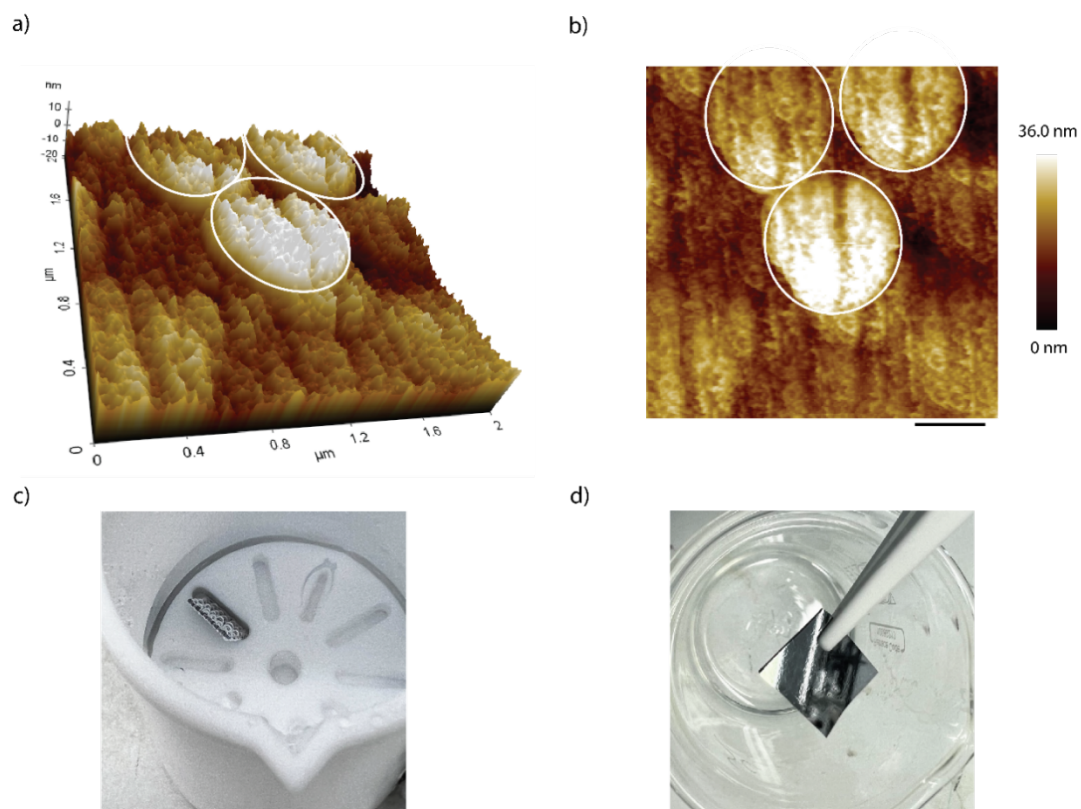


Figure 3.1. (a–b) Representative 3D and 2D AFM height images of a Si(211) wafer etched in aqueous (40%) NH_4F , without any added methanol. The Si–H surface is reacted with 8-nonyl-1-ol prior to AFM analysis. The root mean square roughness of the surface is 7.1 ± 5.6 nm. The height of the circular regions (highlighted by white circles) reaches over 15 nm above the rest of the sample. These protrusions are reflecting a heterogeneous rate of surface etching, specifically surface regions masked by surface-pinned hydrogen bubbles. (c) The formation of surface-adherent gas bubbles is noticeable by naked-eye during the etching if no methanol is added to reduce the liquid surface tension. As a result, as shown in panel (d), the sample gain a very corrugated texture (13 min of etching). The scale bar in panel (b) is 1 μm .

argon gas was bubbled for at least 15 min through the liquid adsorbate stock. The monolayer-forming reaction followed previous procedures with minor modifications [56, 58]. In brief, the aerial surface of the liquid sample was covered with a 1 mm thick quartz plate (part 01031-AB, SPI Supplies) and placed for 2 h under an UV light (Vilber, VL-215.M, 312 nm, nominal power output of 30 W) to initialize the chemisorption reaction through the radical chain reaction [38, 59]. The sample–UV light distance was of approximately 200 mm, and the reaction chamber was kept under continuous nitrogen flow (N_2 , 99.9%, Coregas). To stop the monolayer-forming reaction, silicon samples were first removed from the reaction chamber and then extensively washed with dichloromethane. As a dichloromethane rinse has been

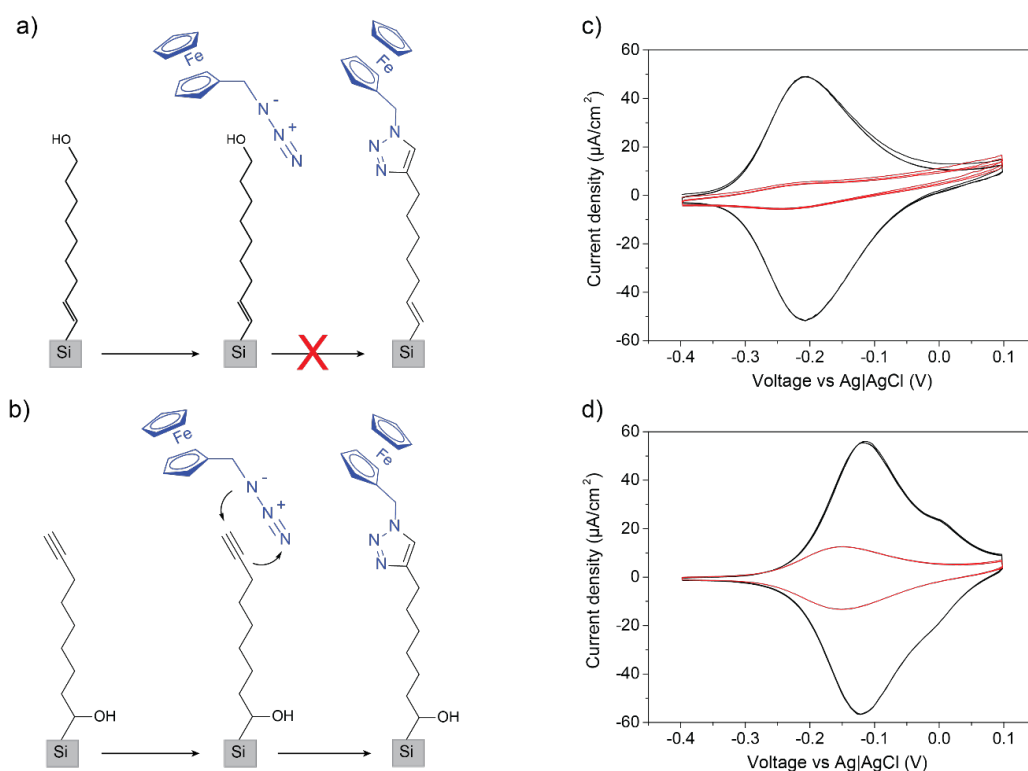


Figure 3.2. Surface-derivatization controls to elucidate the binding mode of the the bifunctional (alcohol, acetylene) 8-nonyl-1-ol monolayer-forming molecule. The covalent attachment of the redox-active probe azidomethylferrocene (blue ink) can only occur on a monolayer exposing a terminal acetylene (b) but is prevented on an hydroxy-terminated sample (a). Detection of the redox-probe attachment (or lack of it) was carried out by cyclic voltammetry (CV). Cyclic voltammograms (CVs) acquired for Si(111) and Si(211) electrodes [(c) and (d), respectively] coated with either 1-nonadiyne (black lines, controls with a symmetrical α,ω -dialkyne) or 8-nonyl-1-ol (red lines) monolayers. It indicates that the terminal group of 8-nonyl-1-ol monolayer either on Si(111) or Si(211) is hydroxyl group ($-\text{OH}$) instead of triple bond. The scan rate is 0.25 V/s, and the electrolyte is 1.0 M HClO_4 .

previously demonstrated to be effective in removing traces of water from similarly modified silicon surfaces [53, 60, 61], the monolayer-modified samples were rested at $+4^\circ\text{C}$ in a sealed vial under dichloromethane, until analyzed or further reacted with azidomethylferrocene through a copper (I)-catalyzed azide-alkyne cycloaddition (CuAAC) reaction. The CuAAC reaction, which served to obtain a ferrocene-functionalized silicon surface, followed in part previous procedures (Figure 3.2) [30, 62, 63]. In brief, to a reaction vial containing either 1,8-nonadiyne or 8-nonyl-1-ol modified silicon samples, 4 mL of a 0.5 mM solution of azidomethylferrocene in 2-propanol, 1 mL of 50 mM aqueous sodium ascorbate solution, and 1 mL of 400 mM copper(II) sulfate pentahydrate aqueous solution were added in one portion and in

this order. The reaction vial was sealed, and the CuAAC reaction carried out at room temperature, shielded from ambient light, and with gentle agitation. After 30 min of reaction time the liquid was decanted and the ferrocene-modified electrode removed from the vial. The electrode was then rinsed sequentially with 2-propanol, water, aqueous hydrochloric acid (0.5 M), water, 2-propanol, dichloromethane and then blow-dried under a stream of nitrogen before the electrochemical analysis.

3.2.3. Atomic force microscopy

Maps of surface topography, zero-bias current, and lateral force for the monolayer-modified silicon samples were acquired simultaneously using an atomic force microscope (AFM) from Park (NX10, Park Systems Corporation, Suwon, Korea). The AFM is fitted with a variable enhanced conductive (VECA) probe holder for conductive-AFM (C-AFM) experiments. The AFM tips are solid platinum tips (part 25Pt300B, Rocky Mountain Nanotechnology, Holladay) with a nominal resonance frequency of 14 kHz and a nominal spring constant of 18 N/m. The sample routing is such that positive currents are indicative of an electronic flow from the AFM tip to the silicon substrate. Samples were secured on the AFM sample stage by carbon tape, after having ensured ohmic contact between sample and stage by scratching the back of the silicon and applying on it a small amount of gallium–indium eutectic. The image resolution was set to 256 points/line, the imaging size to $5 \times 5 \mu\text{m}$ ($5 \mu\text{m} \times 500 \text{ nm}$ for the friction mapping, see below), and the scan rate to 1.0 Hz, unless specified otherwise. Data were analyzed with XEI processing software (Park Systems). The reported values of maximum current were taken as the 99th percentile (sampled points with zero-bias current output higher than 99% of the total sampled points). Platinum–sample friction was measured by imaging a $5 \mu\text{m} \times 500 \text{ nm}$ sample's region and subtracting the retrace friction image from the trace friction image, and then dividing the results by a factor of 2 to yield a friction loop image. This eliminates the likelihood of edge artifacts. In the force–distance (F–D) curve measurements used to estimate the sample's adhesion force, the maximum deflection was set to 2000 nN, the ramp size to 300 nm, and the ramp speed to 300 nm/sec. The adhesion force was determined from the pull-off force required for the cantilever to retract from the surface. Pull-off force data (F–D curves) were processed with the XEI software in

order to estimate the force at the lowest point of the retract trace. For each sample, F–D curves were recorded at nine separate locations and the mean pull-off force, hence adhesion force, were used for contact area estimation. A titanium roughness sample (part RS-12M, Bruker Corporation, Santa Barbara) was used to measure the probe radius. Topography data of the test sample were analyzed in Gwyddion 2.59 (Czech Metrology Institute) using the blind estimation function. The silicon–platinum contact area of each monolayer-based sliding diode system was then estimated by relying on the DMT model of adhesion [65] (Appendix II). The results are displayed in Table S1.

3.2.4. Current–voltage measurements of static junctions

Current–voltage (I–V) measurements of silicon–monolayer–metal static junctions were recorded inside a grounded and lightproof Faraday cage, using a source–measure unit (model B2902A, Keysight) and a spherical stationary mercury top contact controlled by a hanging drop electrode apparatus (HMDE WK2, Institute of Physical Chemistry, Polish Academy of Sciences). The junction voltage was ramped cyclically between –0.5 and 0.2 V in steps of 20 mV. The duration of each step was of 400 ms, and the current signal was sampled after a 300 ms delay from the potential step-up event. The bias routing is from the metal to the semiconductor, and two voltage ramps were recorded for each sampling location on individually prepared and analyzed samples. A minimum of three sampling locations on each sample, and three samples of each surface chemistry, were analyzed. The 99% confidence limit of the mean value was calculated as $t_{n-1}s/n^{1/2}$, where t_{n-1} is 3.34, s is the standard deviation, and n the number of measurements [66]. Current values were corrected by the contact area of the metal–semiconductor junction. The contact area was determined from bright-field optical images acquired with a CCD camera (DCC1240C, Thorlabs) fitted with a 6.5× zoom (MVL6X123Z and MVL133A, Thorlabs). Images were analyzed using Fiji image processing package [67]. Ohmic contact between the back of the silicon sample and a copper plate was obtained by scribing the silicon with emery paper before applying a small amount of gallium–indium eutectic.

3.2.5. Electrochemical measurements

Cyclic voltammograms were recorded in aqueous perchloric acid (1.0 M), under air, and using a CHI650D electrochemical workstation (CH Instruments, Austin). A single-compartment, three-electrode polytetrafluoroethylene cell was used for the electrochemical analysis, with the monolayer-modified surfaces serving as the working electrode, a platinum mesh as counter electrode, and an Ag/AgCl (in 3.0 M aqueous NaCl solution) electrode as potential reference. The Ag/AgCl reference measured +0.16 V against a standard hydrogen electrode (in 3.0 M aqueous KCl). A circular rectilinear cross-section Kalrez[®] gasket set the geometric area of the working electrode to 0.28 cm². Ohmic contact to the sample was achieved as for the current–potential measurements. The electrochemical measurements were performed inside a grounded and lightproof Faraday cage, at 24 °C, in quiescent electrolyte solutions, and under either dark or light conditions. When specified, illumination of the silicon electrode was achieved by means of a deep red LED light (part M660L4, Thorlabs, 660 nm, nominal power output 1050 mW) fitted with a collimator adapter (SM1P25-A, Thorlabs). The silicon electrode was illuminated through the electrolyte compartment. The light intensity measured at the silicon surface was adjusted to ~40,000 lx by controlling the current output of the LED driver (LEDD1B, Thorlabs). Illuminance was measured with a light meter from Amprobe (part IC-LM-200).

3.2.6. X-Ray photoelectron spectroscopy

X-ray photoelectron spectroscopy (XPS) analysis of the monolayer-modified silicon surfaces was performed on a Kratos Axis Ultra DLD fitted with a monochromatic Al K α (hu1486.6 eV) radiation source operating at 225 W, and a hemispherical analyzer (165 mm radius) running in fixed analyzer transmission mode. The photoelectron take-off angle was normal to the sample, and the chamber operated at 2×10^{-8} Torr. The analysis area was $300 \times 700 \mu\text{m}$, and an internal flood gun was used to minimize sample charging. Survey spectra (accumulation of three scans) were acquired between 0 and 1100 eV, with a dwell time of 55 ms, a pass energy of 160 eV, and a step size of 0.5 eV. High-resolution scans (accumulation of 10 scans) used a pass energy of 20 eV, and a step size of either 0.05 eV (Si 2p, 90–110 eV), or 0.1 eV (C 1s, 277–300 eV). XPS data were processed in CasaXPS (version 2.3.18) and any residual

charging was corrected by applying a rigid shift to bring the main C 1s emission (C–C) to 285.0 eV.

3.2.7. Contact angle goniometry

Static water contact angle measurements were performed with a custom-built goniometer consisting of a CCD camera (DCC1240C, Thorlabs) fitted with a 6.5× zoom (MVL6X123Z and MVL133A, Thorlabs), a screw-plunger syringe (part 100-10-20, Ramé-Hart Instrument co.) and a manual three-axis translation stages for sample mounting (PT3, Thorlabs). Measurements were performed using the sessile drop method (10 μ L drop volume), and for each surface chemistry three different sample locations, on each of three independently prepared and analyzed samples, were analyzed. Reported data for each surface chemistry are the arithmetic average of the nine measurements. Images were analyzed with the circle fitting function of Fiji image processing package [67, 68].

3.2.8. Time-resolved photocurrent mapping

Spatially resolved measurements of photocurrent decay kinetics (photocurrent mapping, PCM) were performed with a NX10 AFM (Park Systems Corporation) fitted with a PCM module controlling a pulsed red laser (635 nm, 5 mW nominal power output). The laser on/off time was controlled by the Systems SmartScan™ software, and dark C-AFM conditions were ensured by temporarily switching off the AFM tip feedback. The photocurrent acquisition time was set to 20 ms, and a 4 ms laser pulse started after a 3-ms delay from the acquisition start point. No external bias was applied during the measurements. Junctions analyzed in the time-resolved PCM experiments were formed by contacting monolayer-coated silicon wafers and AFM platinum tips (25Pt300B) with no relative movement between them. For each sample, PCM measurements were taken at 100 different locations.

3.3 Results and discussion

All the four silicon surface chemistries explored here (Scheme 3.1) – intended to provide a broad range of friction, wettability, leakage current and charge recombination velocity (*vide infra*) – are of very high quality, regardless of the crystal

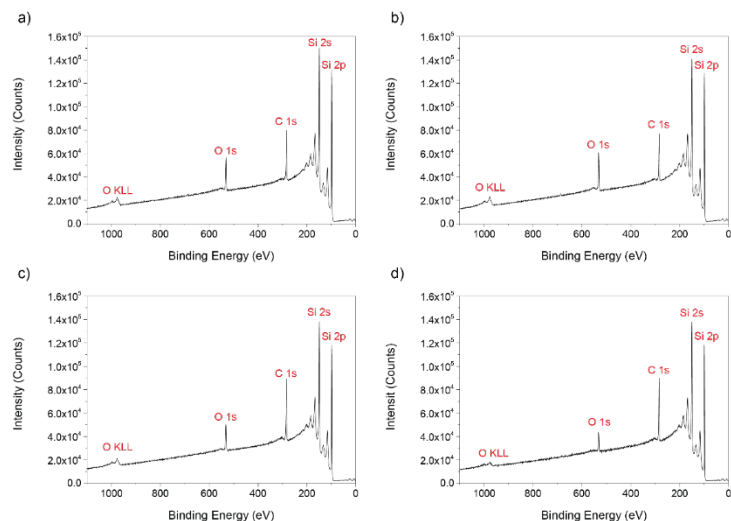


Figure 3.3. XPS survey scans of hydrogen-terminated (Si–H) Si(111) substrates reacted with (a) 1,8-nonadiyne (C/Si ratio = 0.214), (b) 1-nonyne (C/Si ratio = 0.163), (c) 8-nonyn-1-ol (C/Si ratio = 0.336), and (d) 1-nonanol (C/Si ratio = 0.284).

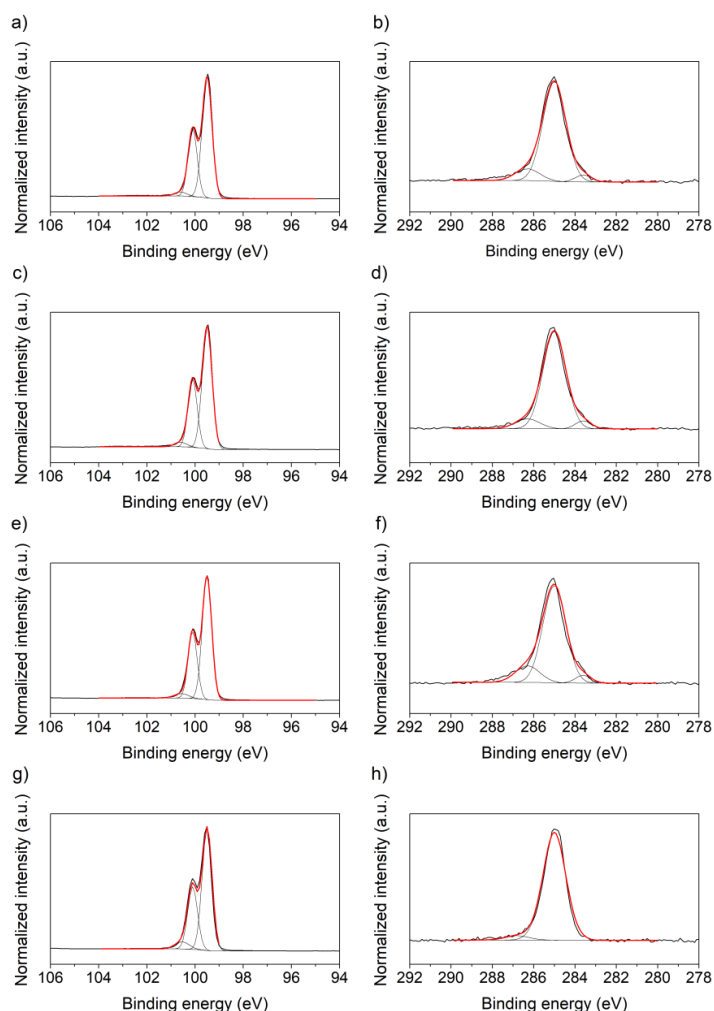


Figure 3.4. XPS narrow scans of the Si 2p (94–106 eV) and C 1s (278–292 eV) regions for hydrogen terminated Si(111) substrates reacted with (a–b) 1,8-nonadiyne, (c–d) 1-nonyne, (e–f) 8-nonyn-1-ol, and (g–h) 1-nonanol.

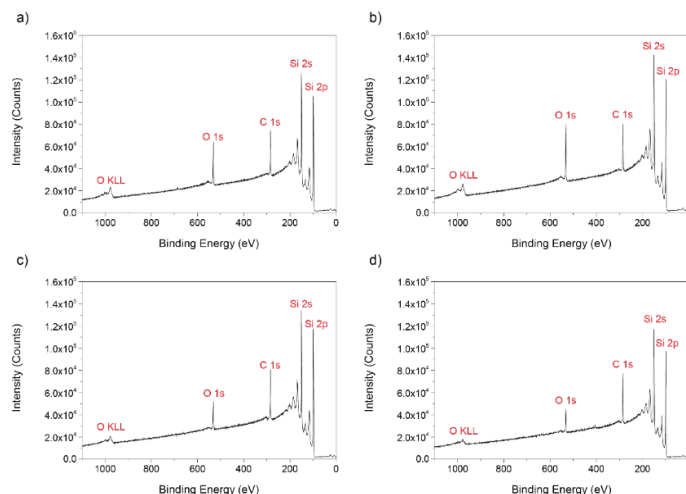


Figure 3.5. XPS survey scans of hydrogen-terminated Si(211) substrates reacted with (a) 1,8-nonadiyne (C/Si ratio = 0.315), (b) 1-nonyne (C/Si ratio = 0.290), (c) 8-nonyl-1-ol (C/Si ratio = 0.272), and d) 1-nonanol (C/Si ratio = 0.358).

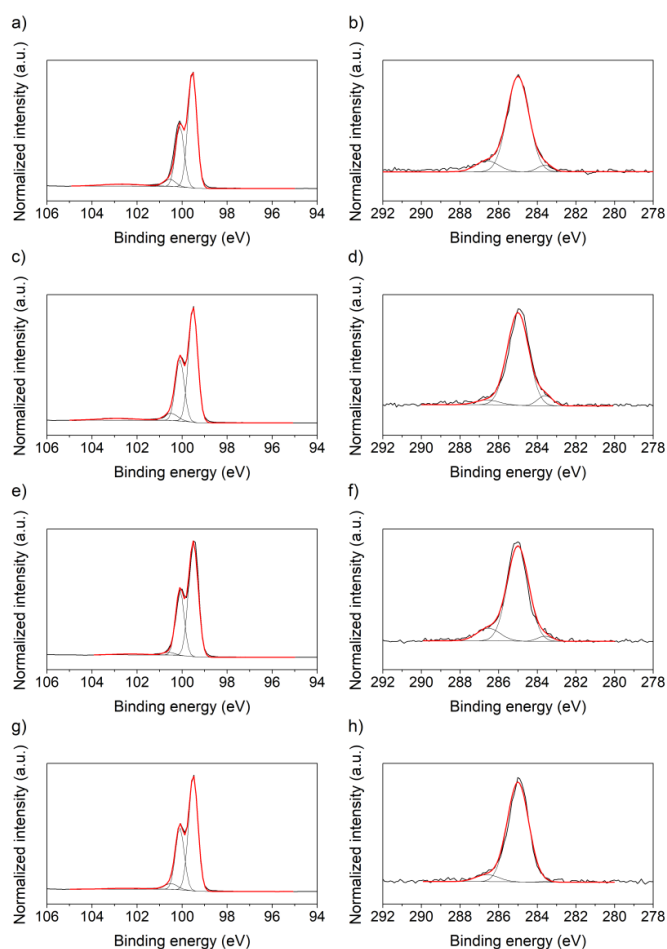


Figure 3.6. XPS narrow scans of the Si 2p (94–106 eV) and C 1s (278–292 eV) regions for hydrogen terminated Si(211) substrates reacted with (a–b) 1,8-nonadiyne, (c–d) 1-nonyne, (e–f) 8-nonyl-1-ol, and (g–h) 1-nonanol.

orientation [Si(111) or Si(211)]. X-ray photoelectron spectroscopy (XPS) data shown in Figures 3.3–3.6 demonstrate the lack of substrate oxidation, and the only elements present are those expected from the molecular structure of the adsorbate. All wide scans (Figure 3.3 and 3.5) showed on the atomic emissions in agreement with the chemical nature of the monolayer forming molecule and substrate. Oxygen contaminations are ubiquitous in XPS, and most likely arising from the presence of oxygenated co-adsorbates, such as tightly bound water [64]. Analysis of the detailed spectra (Figure 3.4 and 3.6) involved background subtraction (Shirley routine) and photoelectron emission fitting to Gaussian–Lorentzian (GL) functions. Narrow scans of the Si 2p region were fitted to functions having 95% Gaussian and 5% Lorentzian character. Black thick lines are experimental XPS data, black thin traces are individual refined envelopes, and solid red traces are the sum of individual contributions. Refined contributions for the Si 2p_{3/2} and Si 2p_{1/2} spin–orbit-split emissions were centered at 99.5 eV (0.6 eV, FWHM) and 100.1 eV (0.6 eV, FWHM1) [69], respectively. The Si 2p shoulder visible at 100.8 eV (0.9 eV, FWHM) is often observed in similar monolayers and tentatively ascribed to photoelectrons emitted from Si atoms bound to hydrogen (Si–H) [36, 69]. Peaks in the range 100.8–103.7 eV are attributed to the Si¹⁺–Si⁴⁺. For each surface, three mixed Gaussian–Lorentzian (80% Gaussian, 20% Lorentzian) functions were used to fit the experimental C 1s band. These three refined components were centered at 283.6, 285.0 and 286.3 eV corresponding respectively to C–Si (silicon-bound carbons) [70], C–C (carbon-bound carbons) [71], and carbon in either a C–OH or C≡C bonding configuration for the high energy component) [72]. and asymmetric 8-nonyl-1-ol molecule (either Si=C–C or Si–O–C/Si–C(OH) surface bridges) [45, 73] we used an highly selective copper (I)-catalyzed alkyne–azide cycloaddition (CuAAC) reaction [58] between the monolayer and an azide-tagged redox-active ferrocene molecule to infer that almost all surface-confined molecules in the 8-nonyl-1-ol monolayer have hydroxyl groups as their terminal group (Figure 3.2). The actual binding configuration is therefore that depicted in Scheme 3.1. These control experiments, together with complementary static water contact angle measurements (Figure 3.7), are conducted to determine the actual bonding configuration. From the analysis of three independently prepared and analyzed samples, static water contact angle values were (a) 74° ± 3°,

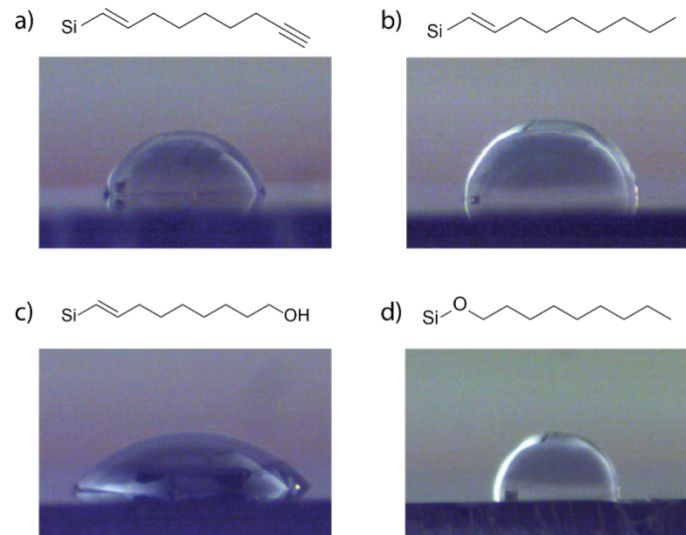


Figure 3.7. Representative bright-field images used to assess the wettability of monolayer-coated Si(211) samples.

Considering the possibility of alternative binding configurations for the bi-functional 1,8-nonyne-modified surfaces; (b) $91^\circ \pm 3^\circ$, 1-nonyne surfaces; (c) $54^\circ \pm 1^\circ$, 8-nonyn-1-ol surfaces; and (d) $87^\circ \pm 4^\circ$, 1-nonanol surfaces. The lower contact angle at 8-nonyn-1-ol surfaces also proves that the 8-nonyn-1-ol monolayer have hydroxyl groups as their terminal group. This surface chemistry knowledge is key when discussing the specific role of the interfacial bond towards maximizing DC outputs of the sliding Pt–monolayer–silicon junctions. As it will be shown in the following sections, all of the sliding junctions explored in this study yielded a zero-bias DC output. Its magnitude varied enormously depending on the surface chemistry, and the most likely underlying physical process for the tribocurrent generation is given in Figure 3.8. The basic mechanism is the formation of electron–hole pairs triggered by a mechanical stimulus, which are then separated by the built-in electric field of the Schottky diode [18, 28, 74, 75]. In addition, it is possible that negative charges generated on the platinum tip by flexoelectricity are enhancing the built-in semiconductor electric field [76-79], all in conjunction with a similar effect mediated by negative molecular charges (*vide infra*).

Another general note is that significant photoeffects are ruled out. This point is demonstrated by a series of C-AFM control experiments, performed on Si(211) samples modified with 8-nonyn-1-ol, where the feedback laser focal point was progressively shifted away from the end of the AFM cantilever under which the tip is

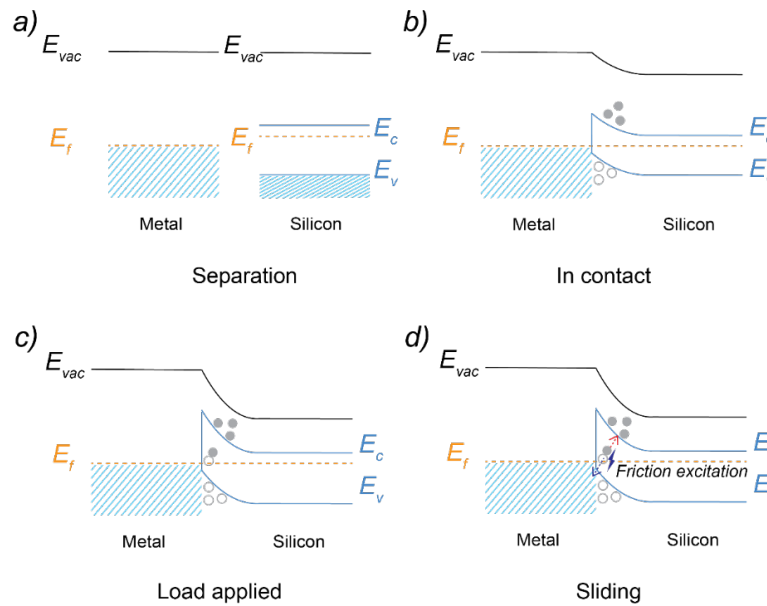


Figure 3.8. Band diagram for junction made by the platinum AFM tip and lowly doped n-type silicon. Junction (a) before contact, (b) after the contact, (c) after applying load on surfaces, the electric field is increased due to the flexoelectricity of the metal (Pt tip) on silicon substrates. And (d) during sliding. During the sliding process, the friction/pressure induced electron–hole pairs are separated by the in-built electric field, which gives a DC current having the direction of leakage current. E_{vac} , E_f , E_c , E_v represent the vacuum energy level, the Fermi level, the bottom of the conduction band, and the top of the valence band, respectively.

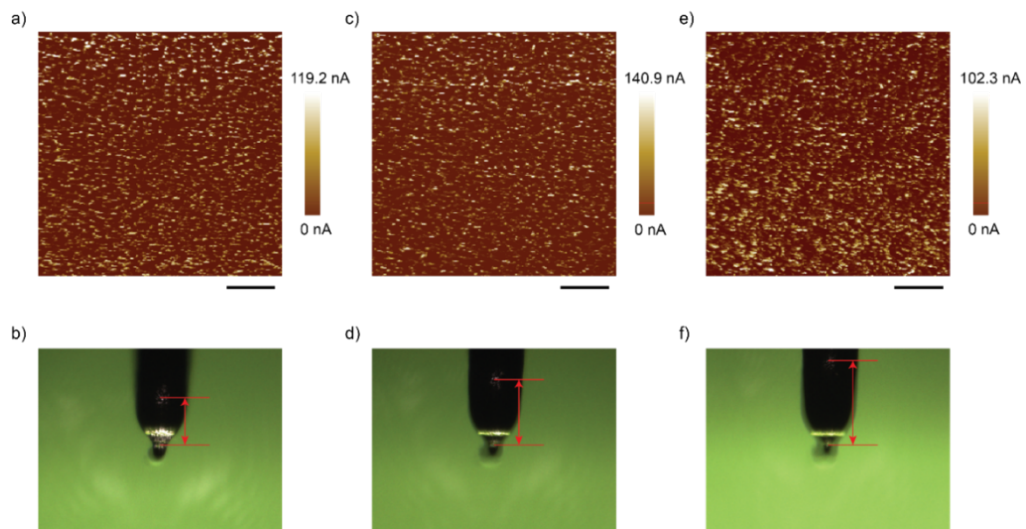


Figure 3.9. C-AFM zero-bias current maps acquired on lowly doped n-type Si(211) samples coated with a monolayer of 8-nonyl-1-ol. Panels (a, c, e) show current maps obtained when the feedback laser focal point is progressively shifted away from the tip–sample contact point. The laser position on the cantilever is shown in panels (b, d, f). The maximum (mean) current acquired in C-AFM experiments using the three different laser locations are (a,b) 119.2 nA (12.2 nA), (c,d) 140.9 nA (12.1 nA), and (e,f) 102.3 nA (14.5 nA). After contact area estimation, the maximum current density obtained for the three different laser positions were 1.7×10^9 , 2.0×10^9 , and 1.5×10^9 A/m². The background illumination visible in panels (b, d, f) is used to ensure a clear view of the cantilever and was completely turned off during the measurements. The scale bars in (a, c, e) indicates 1 μ m.

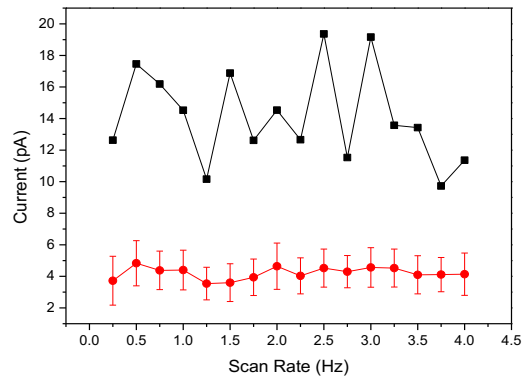


Figure 3.10. Zero-bias tribocurrent output versus AFM scan rate. C-AFM data measured on a 1-nonyne coated Si(111) sample. The red symbols indicate the mean current (error bars are the standard deviation for the recorded DC current across the whole AFM image). The black symbols represent the maximum DC current value.

located. As shown in Figure 3.9, the maximum (mean) current acquired in C-AFM experiments using the three different laser locations are (Figure 3.9a,b) 119.2 nA (12.2 nA), (Figure 3.9c,d) 140.9 nA (12.1 nA), and (Figure 3.9e,f) 102.3 nA (14.5 nA). After contact area estimation, the maximum current density obtained for the three different laser positions were 1.7×10^9 , 2.0×10^9 , and 1.5×10^9 A/m². The background illumination visible in panels (Figure 3.9b, d, f) is used to ensure a clear view of the cantilever and was completely turned off during the measurements. Since the zero-bias current did not scale with the distance between the laser and the tip-sample contact, we rule out a measurable contribution of a photocurrent to the triboelectric output.

Furthermore, the C-AFM data measured on a 1-nonyne coated Si(111) sample shown in Figure 3.10 indicates that increasing or decreasing the sliding velocity had no measurable effect on the DC output, no matter on the mean current (red symbols) or the maximum current (black symbols) recorded. Therefore, unless specified otherwise, all AFM experiments of this work were conducted at 1.0 Hz.

3.3.1. Stick-slip friction on silicon does not govern the zero-bias DC tribocurrent output

Friction is putatively linked to the DC output in a sliding Schottky diode TENG, the stick-slip nature of friction is undisputed [80], and stick-slips are remarkably high-

energy events [81, 82]. Further, a survey of the recent literature on silicon-based TENGs [20, 23, 83] shows that spike-like current outputs (i.e. very frequent current glitches) are a very common feature. All these points led to the first of the five unanswered questions outlined in the introduction: whether a zero-bias tribocurrent, and its ubiquitous glitches, are associated with either sticks, slips, or neither of them. Towards this end, the stepped nature of an ammonium fluoride-etched Si(111) crystal becomes particularly valuable. Topographic data shown in Figure 3.11a are a reminder that an atomically flat silicon electrode is an idealization, and even well-prepared surfaces are a continuous of flat terraces separated by small vertical steps [30, 36, 84]. Si(111) facets are clearly visible, there is negligible oxide, which would appear as rounded AFM topographical features [85], and the samples root-mean-square (RMS) roughness is only 0.22 ± 0.17 nm. For the electrical characterization of DC-TENGs based on these monolayer-modified surfaces we relied on conductive AFM

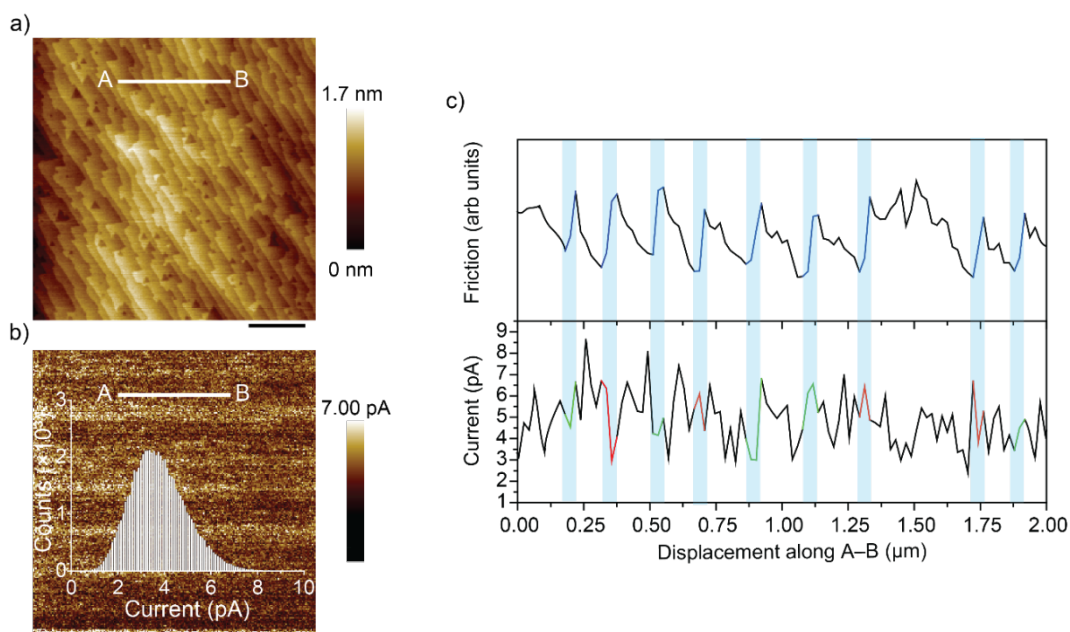


Figure 3.11. (a) Representative AFM height image, and (b) corresponding C-AFM zero-bias current map of a Si(111) surface coated with a monolayer of 1-nonyne (methyl-terminated monolayer). (c) Cross-sectional analysis, along the A–B line, of the friction and current maps of (a,b). Regions highlighted in blue in the friction trace are stick events. The green and red segments of the current profile indicate sample’s regions in correspondence of stick events with either increasing or decreasing (respectively) zero-bias current. The scan direction was set from left to right (from A to B), forcing the tip to move up crystal terraces. The positive sign of the zero-bias current indicates a leakage current (electrons moving from the Pt tip towards the n-type Si). Scale bars in panels (a–b) are 1 μ m.

(C-AFM), so to minimize output fluctuations due to inconsistent contact area and force. Another advantage of C-AFM is that electrical, topographical and friction data can be acquired simultaneously. Figure 3.11b shows one of such C-AFM current maps, obtained under zero-bias and without any external rectifying circuitry. The zero-bias DC output ranged from 0.5 to 12.5 pA, with $\sim 1\%$ of the total sampled points (ca. 65,000) reaching currents larger than 7.0 pA, and the average maximum current density, from six independent samples, reaching up to $4.8 \times 10^4 \text{ A/m}^2$.

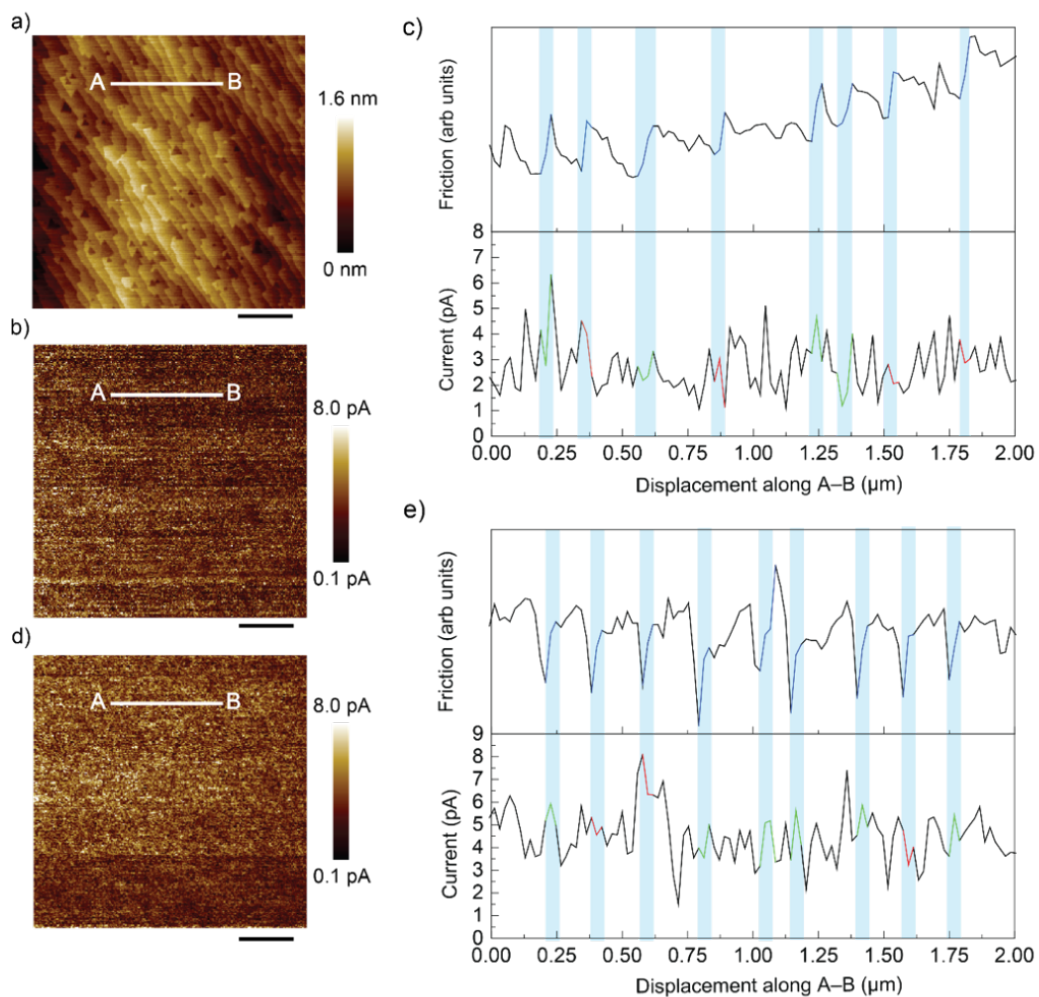


Figure 3.12. (a) Representative $5 \times 5 \mu\text{m}$ AFM height image, and the corresponding C-AFM zero-bias current map of a Si(111) surface coated with a monolayer of 1-nonyne (methyl-terminated monolayer) under sliding speeds of (b) $2.5 \mu\text{m/s}$, and (d) $40 \mu\text{m/s}$. (c, e) Cross-sectional analysis along the A–B lines indicated in the friction and current maps of (b, d) respectively. Regions highlighted in blue represent stick events. The green and red lines in current profile stand for the overall increase and decrease of the current respectively in corresponding stick event. The scan direction was set from right to left (from point B to point A), indicating that the tip moved up the steps separating crystal terraces. The scale bars in panels (a, b, d) are $1 \mu\text{m}$.

Data in Figure 3.11c (upper plot) shows a continuous friction profiling for a smooth but terraced Si(111) surface, sampled along the A–B line marked in Figure 3.11a. The Si(111) crystal is coated with a monolayer of 1-nonyne (CH_3 -terminated surface). This friction mapping demonstrates that, as for the macroscopic world [82], stick–slip events are still present in this microscopic setting. The friction profile in Figure 3.11c reveals a continuous conversion between elastic energy and kinetic energy, and the periodic fluctuation of friction [86] is a near-perfect match of the platinum sliding contact (the AFM tip) repetitively moving up steps separating adjacent terraces.

Surprisingly, the current trace plotted in the lower part of Figure 3.11c reveals that there is no direct relationship between the zero-bias current output, sampled by the tip, and changes to the lateral tip–sample force: peaks in current output do not systematically occur in correspondence of stick (blue shaded regions), nor of slip events. A correlation between current and stick–slip motion cannot be found, as stick events (blue regions, upper panel of Figure 3.11c) do not strictly correspond to an increase (green lines) or decrease (red lines) of the current signal (lower panel). The

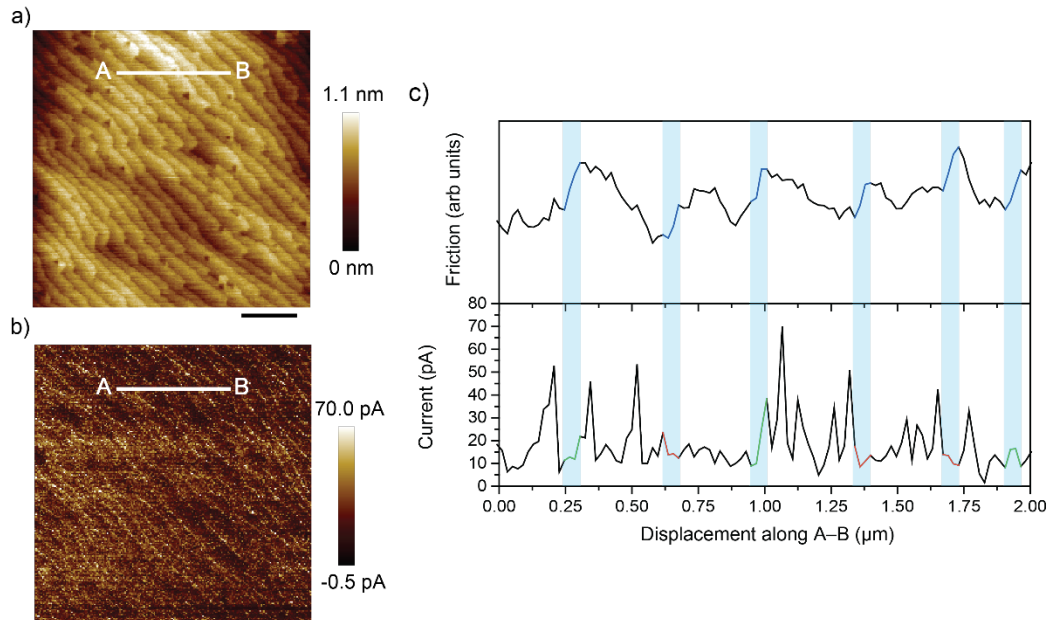


Figure 3.13. (a) Representative $5 \times 5 \mu\text{m}$ AFM height image, and (b) the corresponding C-AFM zero-bias current map of a Si(111) surface coated with a monolayer of 1,8-nonadiyne (alkynyl-terminated monolayer). (c) Cross-sectional analysis along the A–B lines indicated in the friction and current maps of (a–b). Regions highlighted in blue represent stick events. The green and red lines in current profile stand for the overall increase and decrease of the current respectively in corresponding stick event. The scan direction were set from right to left (from point B to point A), indicating that the tip moved up the steps separating crystal terraces. The scale bars in panels (a–b) are $1 \mu\text{m}$.

conclusions are similar regardless of the surface chemistry. Analogous experiments carried out on the 1-nonyne coated Si(111) substrate under different sliding speeds, and on Si(111) coated with monolayers bearing more polar terminations ($-\text{OH}$, 8-nonyl-1-ol; $-\text{C}\equiv\text{CH}$, 1,8-nonadiyne) are shown in Figures 3.12–3.14. That is, as found for the CH_3 -terminated samples of Figure 3.11, there are no links between stick–slip friction and the zero-bias current of a sliding diode TENG.

This finding – tribocurrent not being a response to energy released upon stick–slip dynamics – is of utmost practical importance since this type of movement is a major cause of frictional wear. It ideally needs to be removed or minimized to improve the longevity of a TENG. In support of this conclusion are also the recent findings of Egberts and co-workers, who have demonstrated an inverse correlation between current (under an external bias) and lateral force during atomic stick–slip events of contacts between highly oriented pyrolytic graphite and diamond [87].

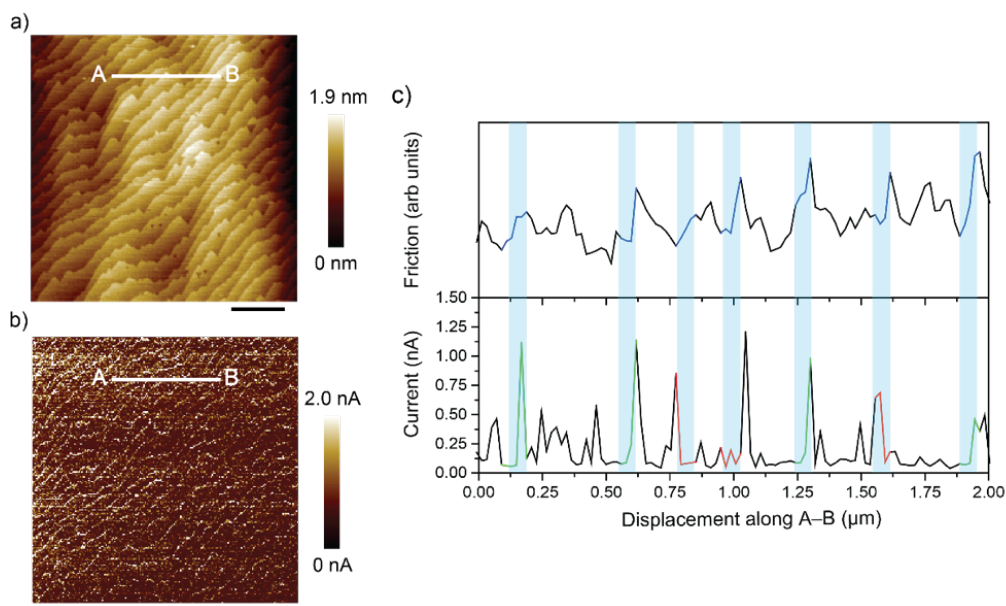


Figure 3.14. (a) Representative $5 \times 5 \mu\text{m}$ AFM height image, and (b) the corresponding C-AFM zero-bias current map of a Si(111) surface coated with a monolayer of 8-nonyl-1-ol (hydroxyl-terminated monolayer). (c) Cross-sectional analysis along the A–B line of the friction and current maps of (a–b). Regions highlighted in blue represent stick events. The green and red lines in current profile stand for the overall increase and decrease of the current respectively in corresponding stick event. The scan direction were set from left to right (from point A to point B), indicating that the tip moved up the crystal terraces. The scale bars in panel (a–b) are $1 \mu\text{m}$.

However, to further validate the above conclusions we performed controls where the sliding direction was varied from across the sample's terraces (Figure 3.15a), to along the terraces (Figure 3.15c). The latter scanning direction (along the terraces, Figure 3.15c) is intended to minimize the likelihood of sticks–slips as the moving contact is not forced to overcome crystal steps (on average 0.29 nm in height) separating terraces. As shown in Figures. 3.15b and 3.15d, the maximum current density was largely independent on scanning direction, with the maximum DC density (and mean outputs) being $5.5 \pm 1.0 \times 10^4 \text{ A/m}^2$ ($1.7 \pm 0.1 \text{ pA}$) across the terraces (Figures. 3.15a,b), and $8.2 \pm 1.3 \times 10^4 \text{ A/m}^2$ ($2.0 \pm 0.1 \text{ pA}$) along the terraces (Figures. 3.15c,d). All the values specified above are the average of forward and backward scan direction data. The slightly higher DC output obtained by moving the metal contact along the semiconductor terraces is attributed to the increased likelihood of scanning the platinum tip close to the $\langle 211 \rangle$ facets present at the edge of the $\langle 111 \rangle$ terraces, a point that will be discussed in greater details later.

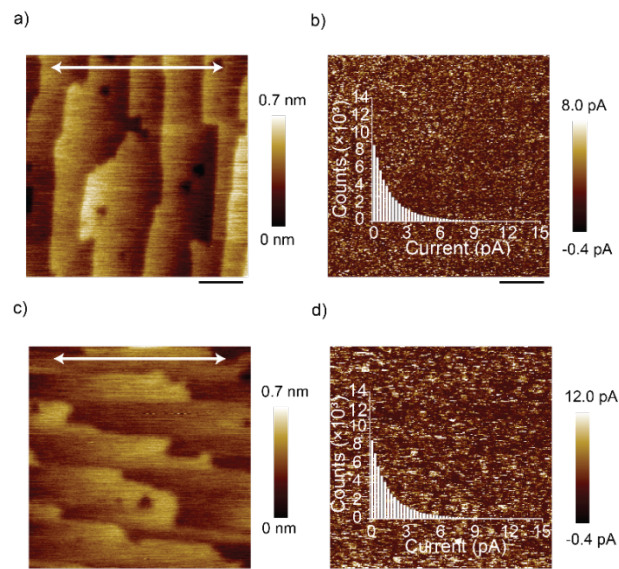


Figure 3.15. Alignment of the diode sliding direction with edges of the silicon crystal steps. (a, c) AFM topography images, and (b, d) zero-bias C-AFM current maps (and histograms) of sliding Schottky diodes made on oxide-free Si(111) crystals coated with monolayers of 1-nonyne. The scanning direction of the platinum AFM tip is indicated by the white arrows [(a, b), across terraces; (c, d), along terraces]. The insets in panels (b, d) are histograms showing the zero-bias current distribution across the sample. Data shown in figure are for the tip moving left to right (forward scan). Scale bars in panels (a, c) are 200 nm.

In summary, combined data of Figures 3.11 and 3.15 allow to rule out a link between DC tribocurrent generation and stick–slip friction, suggesting that the design of highly efficient TENGs should not focus on a search of systems that can maximize stick–slip dissipation. Importantly, it can also be concluded that no particular attention should be given, during the device design, to attempt aligning sliding motion with the microscopic topographical features of the semiconductor’s surface.

3.3.2. Augmenting zero-bias DC tribocurrent with surface chemistry

The previous section has demonstrated how the putative friction-induced current of DC Schottky diode TENG does not track energy released as friction. This finding led us to postulate that engineering the chemistry of the interface may be an effective strategy to maximize DC outputs: instead of targeting surface chemistry to tune friction, rather focusing on surface chemistry as means to optimize charge transport across the metal–semiconductor junction.

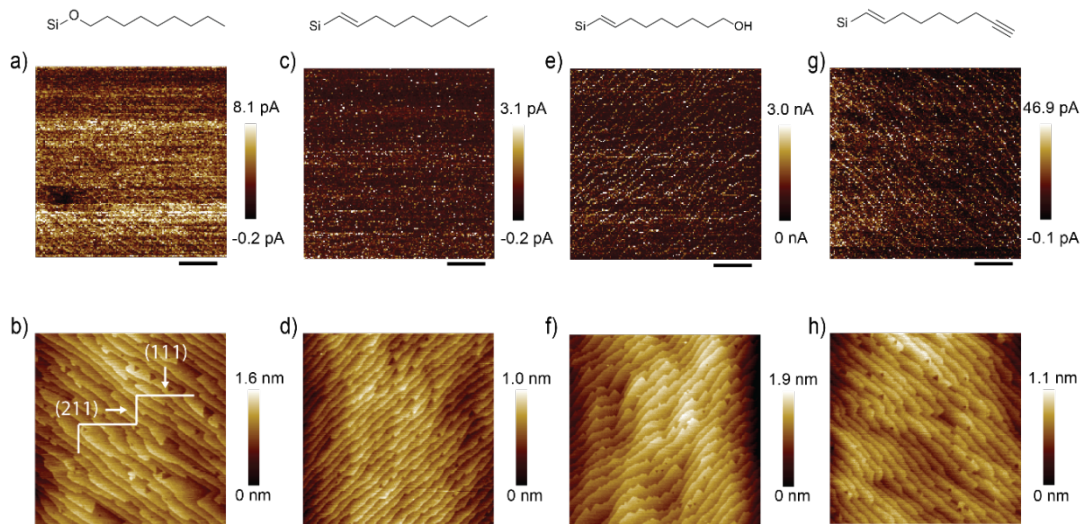


Figure 3.16. Zero-bias C-AFM $5 \times 5 \mu\text{m}$ current maps (a, c, e, g), and the corresponding height images (b, d, f, h), of dynamic sliding Pt–monolayer–Si(111) diodes coated with monolayers of 1-nonanol (a–b), 1-nonyne (c–d), 8-nonyl-1-ol (e–f), and 1,8-nonadiyne (g–h). For all four surfaces, steps separating terraces are roughly oriented at 30° from the major flat of the parent wafer (the manufacturer reference of the (110)-orientation). It indicates that the steps of terrace are mostly (211)-oriented surfaces. The maximum (mean) current output for (a) 1-nonanol, (c) 1-nonyne, (e) 8-nonyl-1-ol, and (g) 1,8-nonadiyne are 8.1 pA (4.0 pA), 3.1 pA (0.6 pA), 3.0 nA (0.5 nA), and 46.9 pA (12.2 pA), respectively. The positive sign of the zero-bias current indicates a leakage current (electrons moving from the Pt tip towards the n-type Si). Scale bars in panels a–h are $1 \mu\text{m}$.

Figure 3.16 shows the typical topography data of monolayer-coated Si(111) surfaces and the corresponding C-AFM zero-bias current maps. The maximum current density output of sliding junctions reached 8.2×10^4 A/m², 3.4×10^4 A/m², 3.4×10^7 A/m², and 4.9×10^5 A/m², for the 1-nonanol, 1-nonyne, 8-nonyn-1-ol, and 1,8-nonadiyne coated surfaces, respectively. Among all surface chemistries explored here, the alkynol monolayer (8-nonyn-1-ol) showed the highest current density. As shown in Figure 3.7, the 8-nonyn-1-ol monolayer shows relatively higher hydrophilicity in terms of water contact angle measurements. Hence, it can be speculated that a surface water layer may be one of the reasons contributing to the high current density, as the formation of water can possibly increase the actual tip-sample contact area [61]. Three technical notes are important here. Firstly, all the surfaces of this study were rinsed with dichloromethane prior to analysis, which as previously demonstrated by X-ray reflectometry data, is effective in removing any adsorbed sub-nanometer water layer [53, 60, 61]. Secondly, this water layer takes several hours (>15 h) to reform and reach its equilibrium thickness of few Å, while all AFM measurements were generally concluded within 3 h of the initial DCM rinse. Thirdly, there is no strict and general link between the macroscopic wettability of a surface (contact angle) and the kinetics of water build-up on this surface: relatively hydrophobic surfaces, like those assembled from 1,8-nonadiyne, accumulate few Å of water faster than surfaces of greater water contact angle [53, 60, 61]. It is therefore possible, but hard to prove unambiguously, to what degree, if any, increased wettability can cause an increase in contact area. What is perhaps more likely is that a nanoscopic water layer associated to the hydroxyl groups may augment the formation of triboelectric charges [88, 89]. Furthermore, since all the zero-bias tribocurrent of this study bear the sign of a leakage process (a net electron flow from the Pt tip to the n-type Si), it is probable that the local electrostatic environment, such as a negative static charge on the Pt contact [79] will favor the molecular deprotonation to an alcoxide anion [90-92]. Such molecular dipole (Si-monolayer-O⁻) will augment the space charge layer (SCL) band bending. In favor of this argument there is the observation that the oxygen bridge in the 1-nonanol surface, which lacks an exchangeable proton, does not yield large current outputs like the proton-exchangeable 8-nonyn-1-ol surface. The monolayer molecular dipole will therefore

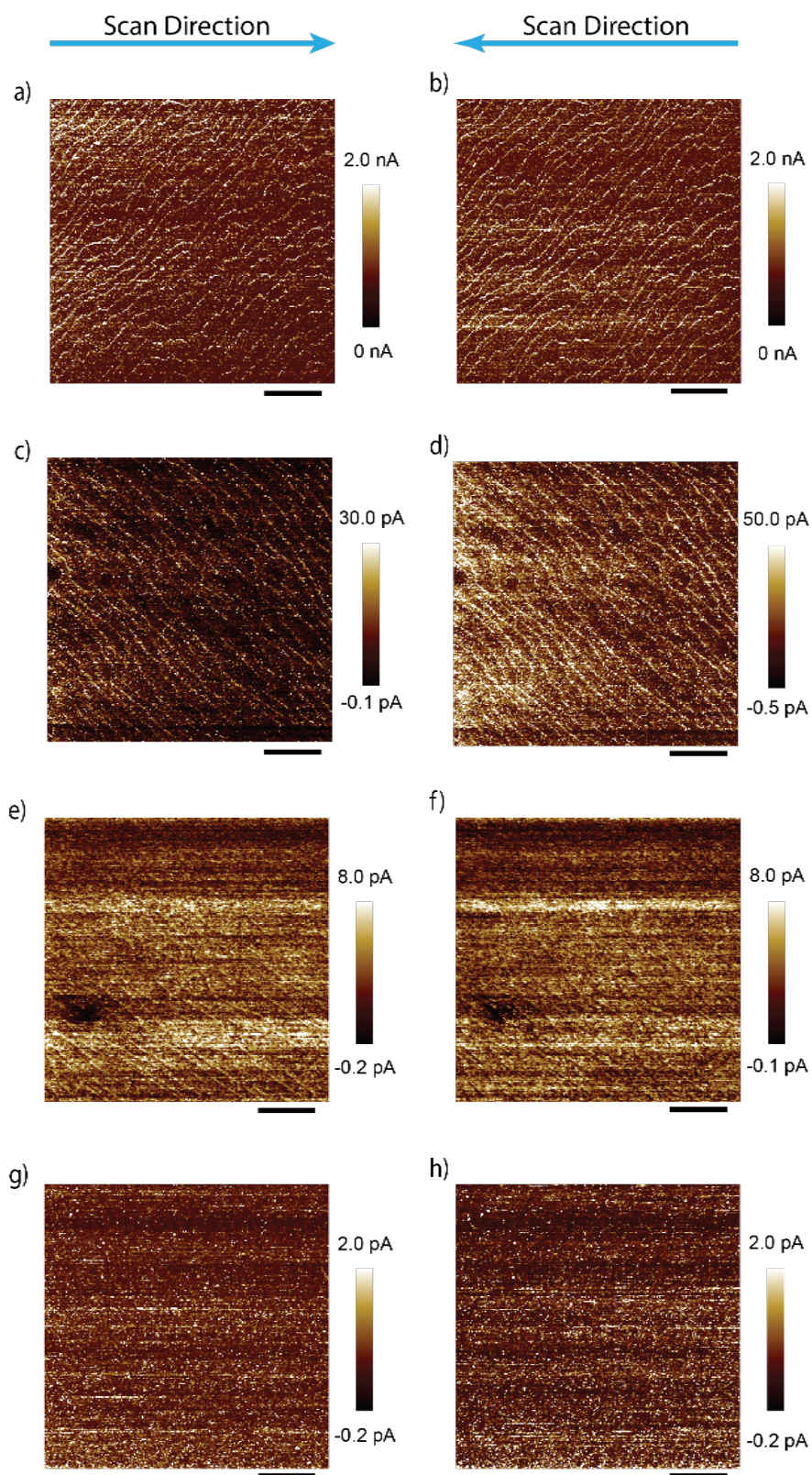


Figure 3.17. C-AFM maps of Si(111) samples coated with monolayers of (a–b) 8-nonyl-1-ol, (c–d) 1,8-nonadiyne, (e–f) 1-nonanol, and (g–h) 1-nonyne. In the left-column panels (a,c,e,g), the platinum AFM tip is scanned in the forward direction – from the left to the right of the image. In the right-column panels (b,d,f,h), the tip is scanned backwards, from right to left.

electrostatically assist the flow of currents away from the interface, towards the silicon bulk. The current maps of the two best performing chemistries (Figures 3.16e, g) indicate how the current is peaking near terrace edges, and to such an extent that current maps resemble topography maps. This remarkable match holds for C-AFM scans recorded in both forward and backward directions (Figure 3.17), hence further confirming that current peaking near edges is not a cause of a stick–slip (vide supra), nor an artifact due increased tip contact area. As briefly mentioned in the previous section, the most likely cause for the output current peaking near crystal edges is an increase of surface conductivity near/on facets [35] separating Si(111) terraces [36, 93].

Commercially available silicon wafers are usually marked with a lapped edge indicating a specific reference orientation. By carefully noting the angle between the lapped edge ($\langle 110 \rangle$ in our wafers) and the AFM scan direction, a straightforward analysis of a stereographic projection (Figure 3.18) indicates that crystal steps are exposing mainly $\langle 211 \rangle$ facets. Si(211) facets are perpendicular to the Si(111) and form 30 or 90 degree angles to the supplier’s reference (lapped edge) marking the Si(110) facet. Hence, cleaving the Si(111) wafer along a direction that forms a 30 degree angle to the lapped edge will expose the Si(211) surface. Similar consideration holds at the microscopic scale for the alignment of terrace edges with respect to the lapped edge.

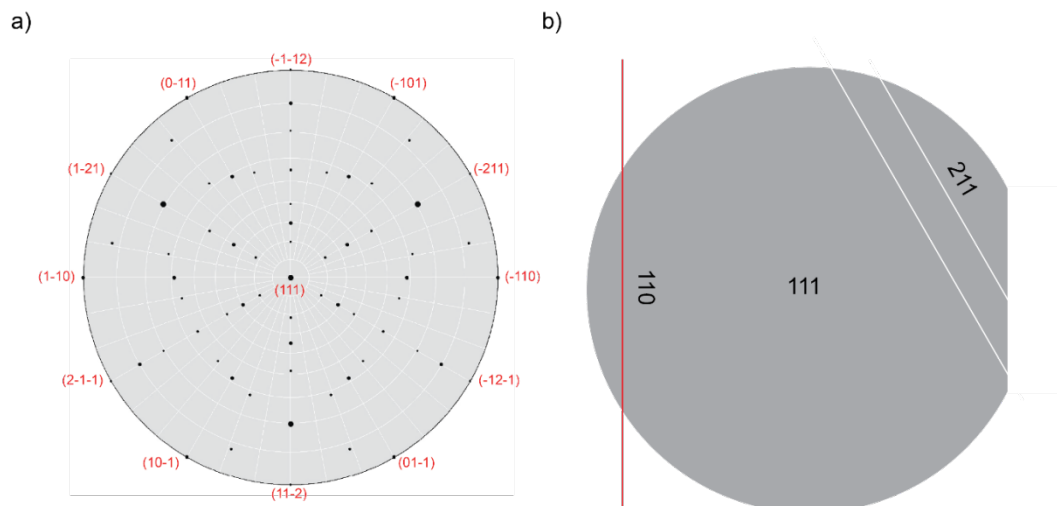


Figure 3.18. (a) A stereographic projection depicting the crystallographic relationship between the $\langle 111 \rangle$, $\langle 110 \rangle$ and $\langle 211 \rangle$ silicon facets. (b) Schematic illustration of the directions along which cutting a commercial Si(111) wafer expose the Si(110) and Si(211) facets.

This finding is an extremely important finding as the Si(211) surface is highly conductive [35]. To clarify on the origin of this pattern of high outputs near $\langle 211 \rangle$ defects on a nominal Si(111) wafer we then turned to analogous zero-bias C-AFM current mapping done on Si(211) substrates

3.3.3. Sliding Schottky diodes on Si(211)

As the overwhelming majority of silicon surface chemistry research deals with Si(100) and Si(111) we first assessed by XPS the quality of monolayers prepared on hydrogenated Si(211). Wide scan and high resolution XPS data shown in Figures 3.4–3.5 show negligible substrate oxidation on Si(211), and all spectral features are those expected from the chemical identity of the molecular adsorbate. XPS data for monolayers prepared on Si(211) are both qualitatively and quantitatively analogous to those of Si(111) Surface coverages are also indistinguishable within the experimental error. After CuAAC reactions to attach ferrocene units, voltammetric data shown in Figure 3.6 reveals that 111- and 211-oriented substrates have similar coverages of 1,8-nonadiyne molecules. Figure 3.19 presents AFM height images and C-AFM tribocurrent maps obtained on monolayer-modified Si(211) electrodes. The terraced structure characteristic of Si(111) is absent on Si(211) but the overall current

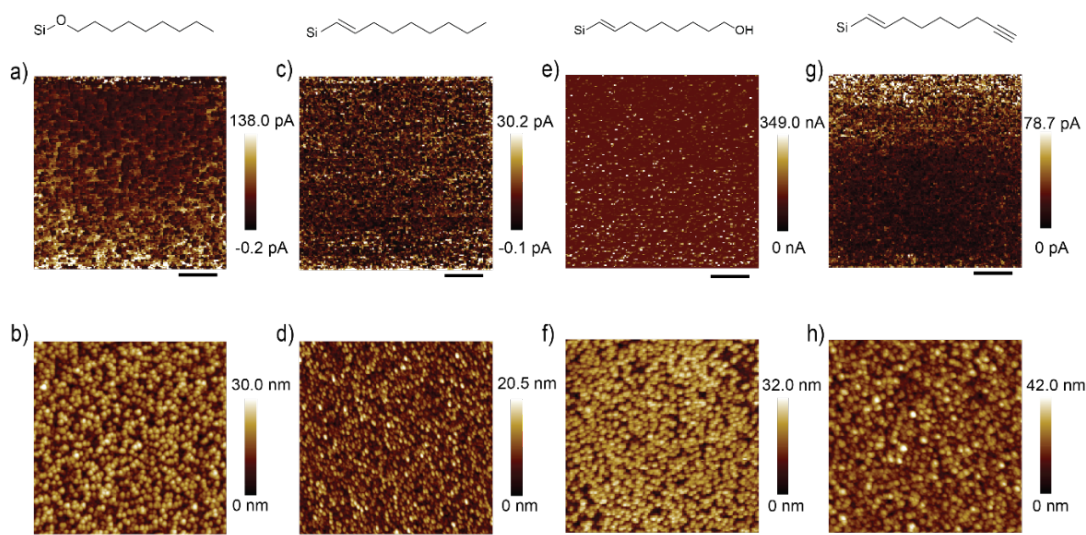


Figure 3.19. Zero-bias C-AFM $5 \times 5 \mu\text{m}$ current maps, and corresponding height images, of dynamic sliding Pt-Si(211) diodes. Oxide-free Si(211) samples were coated with monolayers of (a–b) 1-nonanol, (c–d) 1-nonyne, (e–f) 8-nonyn-1-ol, and (g–h) 1,8-nonadiyne. The maximum (mean) zero-bias current signal for junctions made on (a) 1-nonanol, (c) 1-nonyne, (e) 8-nonyn-1-ol, and (g) 1,8-nonadiyne Si(211) samples are 138.0 pA (37.7 pA), 30.2 pA (9.2 pA), 349.0 nA (17.9 nA), and 78.7 pA (22.4 pA), respectively. The positive sign of the zero-bias current indicates a leakage current (electrons moving from the Pt tip towards the n-type Si). Scale bars in panels (a–h) are 1 μm .

output greatly surpasses that of the 111-oriented substrates (Figure 3.16a, 3.16c, 3.16e, 3.16g). The zero-bias current density of the 1-nonanol, 1-nonyne, 8-nonyl-1-ol, and 1,8-nonadiyne coated Si(211) surfaces reaches up to 1.9×10^6 A/m², 4.1×10^5 A/m², 4.9×10^9 A/m², and 1.0×10^6 A/m², respectively. Samples covalently coated with 8-nonyl-1-ol showed the highest zero-bias DC output current density, $\sim 10^9$

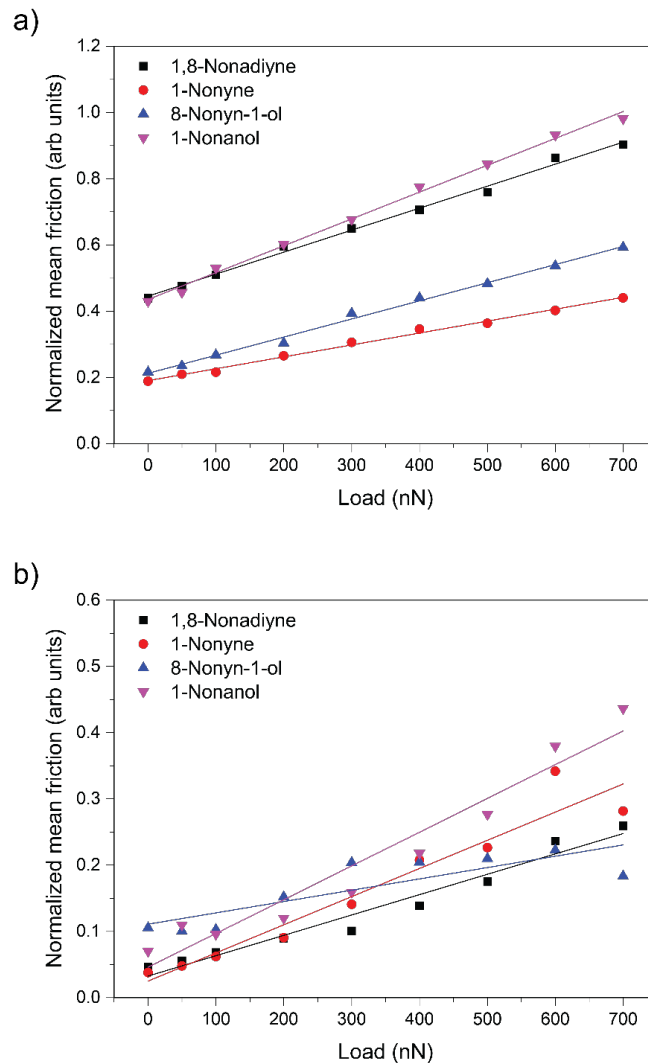


Figure 3.20. Change in friction with load in air for modified (a) Si(111) and (b) Si(211) substrates. The scan velocity was fixed at 10 $\mu\text{m/s}$. The friction is the average value of the friction loop (lateral force retrace image minus trace image then divided by a factor of two) normalized by the maximum value (friction at 700 nN for 1-nonanol monolayer coated silicon) for each surface chemistry and applied load. The solid lines in panels (a) and (b) are linear fittings. According to the modified Amontons' Law, the friction coefficient can therefore be represented by the slopes of the linear fitting lines [94]. By comparing the linear fitting slopes of different chemistry on Si(211) and Si(111), the friction on Si(111) surface are generally higher than it on Si(211) surface. On the other hand, on both Si(211) and Si(111) substrates, the surface chemistry giving highest DC current signal (8-nonyl-1-ol) doesn't display a relatively higher friction coefficient compared to other surface chemistries.

A/m², which is ~4000 times higher than currently best performing Schottky diode on silicon [95], and comparable to sliding zero-bias Schottky diodes made with less readily available MoS₂ multilayers [18]. Therefore, answering the question that closed the previous section, it is most probable that given both the high DC current signal achieved on Si(211), and the experimental alignment of Si(111) steps relative to the lapped <110> edge, localized current spikes on a conventional Si(111) wafer (Figure 3.16) are the result of the sliding contact approaching <211> facets.

As a further note, neither on Si(111) nor on Si(211) did the current density scale with the surface friction coefficient (Figure 3.20). As expected, friction increased with the applied load, and according to the modified Amonton's Law, the friction coefficient can be expressed as the slope of the friction versus load data [94]. For TENGs made on both Si(111) and Si(211) friction and friction coefficients of the best performing chemistries (hydroxyl-terminated substrates made from 8-nonyl-1-ol) are not standing out from the rest. Conversely, the 1-nonanol monolayer, with the highest friction coefficient among all samples, did not show a particularly high zero-bias current signal.

3.3.4. Links between static and dynamic charge transport characteristics

As discussed above, the zero-bias DC output of a sliding Schottky diode is generally reported to take the form of a leakage instead of forward bias current. Given that the leakage current magnitude in a silicon-based static junction can be engineered by surface chemistry methods [37, 96, 97], it is possible that the terminal group, the anchoring group and the quality of the monolayer could be optimized to influence the static charge transport, and in turn the dynamic output.

Figure 3.21 illustrates the leakage current density measured under reverse bias (–0.4 V, metal bias) for 111- and 211-oriented silicon. The diode leakage is measured during the potential sweep of a macroscopic and static metal–monolayer–semiconductor junction. Representative full current–potential sweeps are shown in Figure 3.22. The choice of the sample bias used in Figure 3.21 is such as to closely match the external

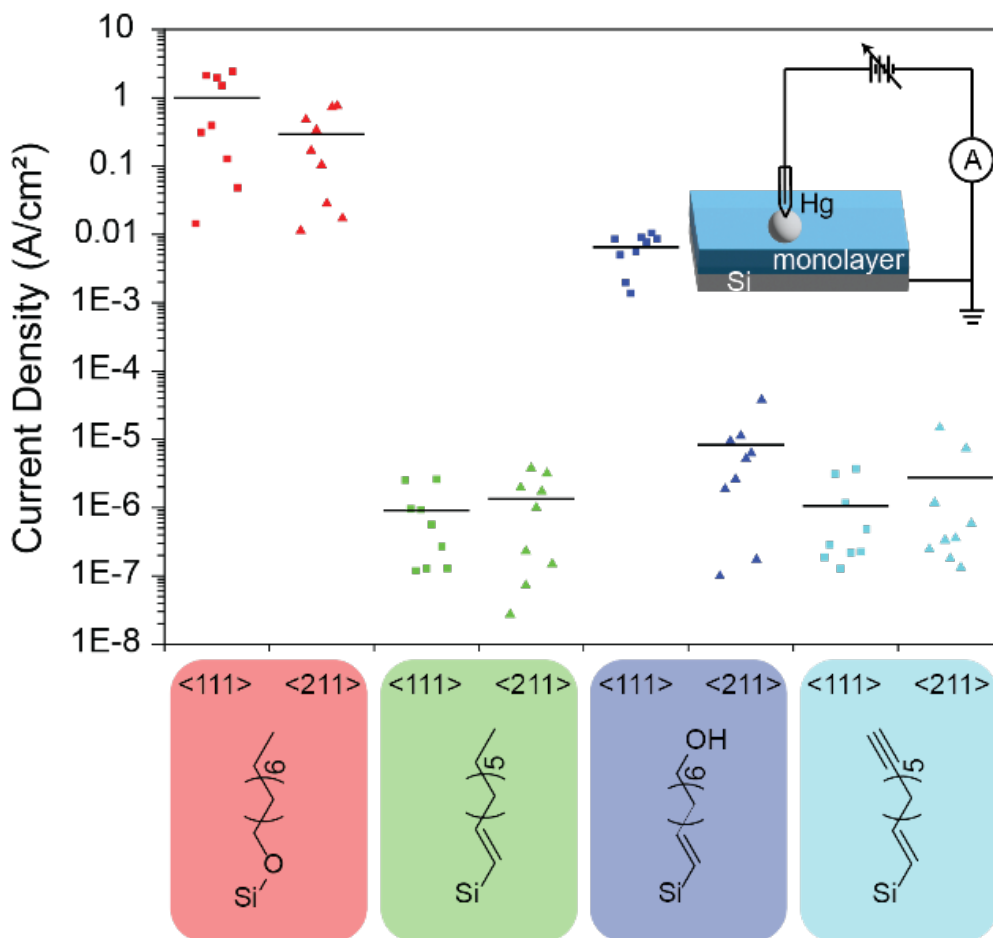


Figure 3.21. Leakage current of static macroscopic silicon–monolayer–metal junctions. Leakage currents sampled at -0.4 V (metal bias) on (111)- and (211)-oriented silicon samples coated with organic monolayers (x-axis labels). Representative I–V traces over the full bias range (-0.5 to $+0.2$ V) are in Figure 3.22. The solid horizontal lines represent the average value of nine measurements acquired in three locations of three independently prepared and analyzed samples of each surface chemistry and crystal orientation.

bias magnitude which would null the tribocurrent in the C-AFM experiments (Figure 3.23). The leakage current of Si(111) substrate with 8-nonyl-1-ol monolayer is over 100 times that of 1,8-nonadiyne or 1-nonyne systems, while for Si(211) the leakage current on 8-nonyl-1-ol coated substrate is similar to that for 1,8-nonadiyne samples. In essence, there appears to be no link between leakage current of the static diode and the experimental zero-bias current performances of an out-of-equilibrium system (Figures 3.16 and 3.19). Answering one of the key questions set out in the introduction, leaky static diodes do not lead to larger DC outputs.

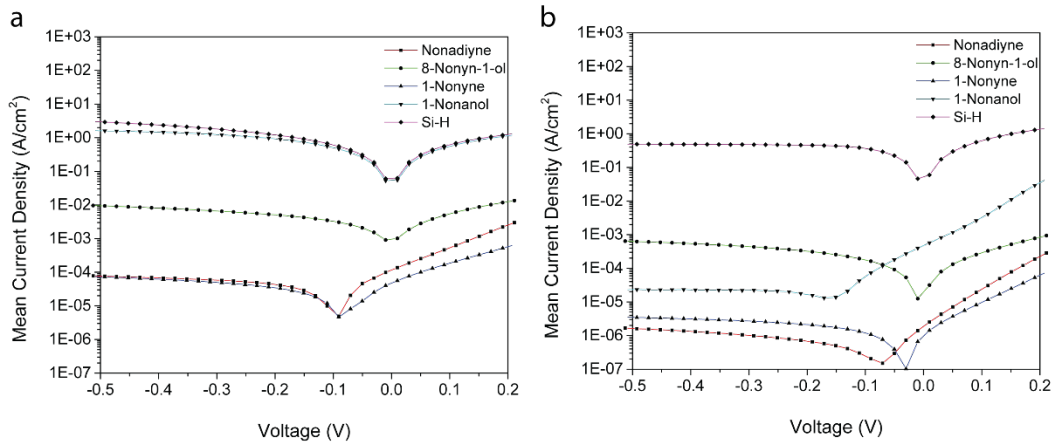


Figure 3.22. Average of 18 current–voltage (I–V) curves recorded on three independently prepared samples for each surface chemistry. The data are obtained on static metal–monolayer–silicon junctions made on (a) 111- and (b) 211-oriented silicon substrates coated with the specified organic molecular monolayer (indicated in figure). To check the repeatability, we conducted multiple repeated I–V measurements (5 times or more) on the same sample location. Repeatability of the reverse-bias current is within 0.1%, and the sample-to-sample reproducibility within 0.8%. The bias routing is from the metal (mercury) contact to the silicon substrate.

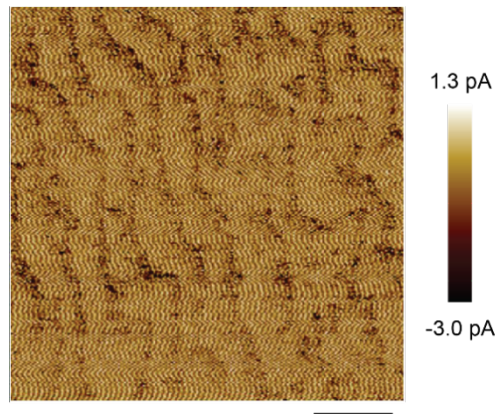


Figure 3.23. C-AFM current map for a 1,8-nonadiyne-coated Si(111) surface biased at forward bias of 400 mV, such to null the tribocurrent. The scale bar is 400 nm.

3.3.5. Surface-recombination velocities and tribocurrent

Considering the similarities between the tribovoltaic effect and photovoltaic effect [16], and seeking to explain the superiority of Si(211) over Si(111) as TENG substrate, we then moved to explore whether there was a relationship between surface recombination velocities and zero-bias current output. We used spatially and time-resolved photoconductivity measurements to probe in 2D the recombination

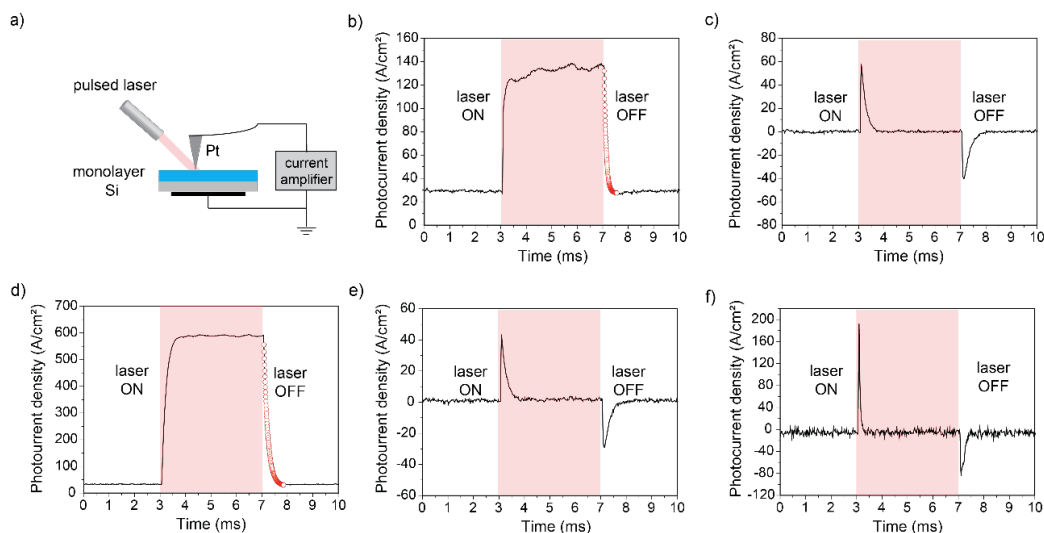


Figure 3.24. Transient microscopic photocurrent map measurements (PCM) on static silicon-monolayer-platinum junctions. (a) Schematic of the PCM measurement used to extract the time constant of photocurrent. (b–f) Representative photocurrent decay curves measured on a Si(211) surface bearing either a 1,8-nonadiyne monolayer (b–c), a 1-nonyne monolayer (d–e), or a 8-nonyl-1-ol monolayer (f). The red circles in panels (b, d) indicate exponential curve fittings of the experimental photocurrent decay, revealing time constants of 126.9 μs and 198.4 μs , respectively. Panels (c, e, f) are representative PCM data of sample locations showing a charge and discharge process typical of a resistor–capacitor circuit.

velocities of charge carriers as function of surface chemistry and crystal orientation. Figure 3.24a illustrates the schematic of the photocurrent map measurement (PCM), and Figures 3.24b, c are representative photocurrent decay traces obtained with Pt junctions made on 1,8-nonadiyne-coated Si(211) surfaces. Some sample's locations, as those shown in Figure 3.24b, were characterized by a good photoconductivity and a stable current signal while the laser pulse is on. This is quite common on Si(211)–H surfaces (Figure 3.25a), which can be taken as reference of a surface with relatively few electrical traps (although unfortunately rather chemically unstable). On Si(211)–H around half of the 100 tested spots showed similar photo-response trends, with photocurrent densities reaching up to 6000 A/cm², ~40 times higher than 1,8-nonadiyne coated substrates. Although the other half test locations do not show a stable current signal with the laser on, none of them displayed the similar feature shown in Figure 3.24c. But within a given sample of 1,8-nonadiyne coated Si(211), it was rather common to find locations with curves as those of Figure 3.24c. At these locations the illuminated junction behaves like the charging and discharging of a capacitor, indicating that a resistor and capacitor series (RC) equivalent circuit forms at the interface. More quantitatively, of 100 sampled locations, 15 were found to be

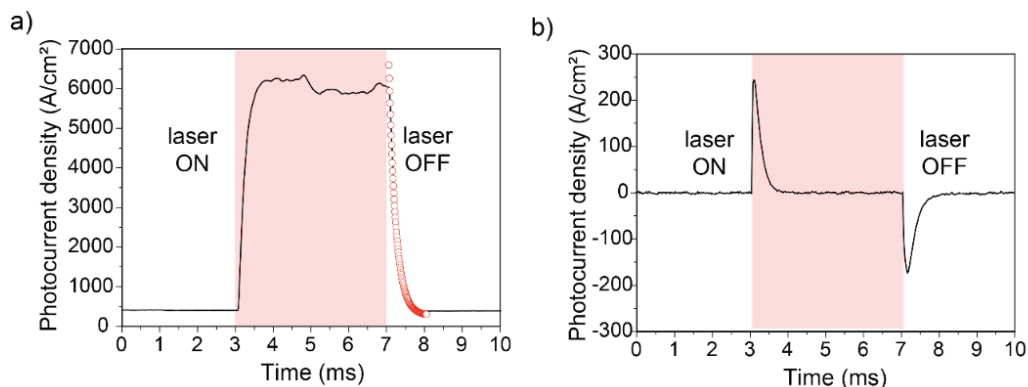


Figure 3.25. Representative photocurrent decay curves measured on (a) hydrogen-terminated Si(211) and (b) 1,8-nonadiyne coated Si(111) substrates. The red circles in panels (a) illustrate the exponential curve fittings of the experimental photocurrent decay. Curve fitting indicates a time constant of $170.5 \mu\text{s}$.

photoconductive as in Figure 3.24b, while 85 were capacitive as in Figure 3.24c. For the photoconductive locations, the average time constants was $172.5 \pm 20.1 \mu\text{s}$, with the 99% confidence limit of the mean value calculated as $t_{n-1}s/n^{1/2}$, where t_{n-1} is 3.01 for 15 samples, s is the standard deviation, and n the number of measurements [66]. Using the same method, for the other tested spots, the time constants is obtained to be $162.9 \pm 9.2 \mu\text{s}$. For 1,8-nonadiyne-coated Si(111) samples shown in Figure 3.25b, which showed a tribocurrent approximately half in magnitude than that obtained on Si(211) crystals, all PCM data exhibited RC responses similar to those in Figure 3.24c.

We then conducted analogous experiments on 1-nonyne (Figures 3.24d–e) and 8-nonyl-1-ol (Figure 3.24f) coated Si(211) surfaces, which are, respectively, the surface chemistries with the lowest and highest DC current output. On 1-nonyne, out of 100 spatially resolved measurements, 16% showed a typical photoconductive response, with a time constant of $201.9 \pm 22.5 \mu\text{s}$. The great majority (84%) had a time constant of $164.8 \pm 9.0 \mu\text{s}$ at (first decay). We recall that the surface recombination velocity of charge carriers is inversely proportional to their lifetime [98]. Relatively longer lifetime of electron–hole pairs on 1-nonyne monolayer, whichever the type of photo-response is, indicates a lower surface recombination velocity compared to the 1,8-nonadiyne monolayer. In other words, the overall number of the surfaces defects (surface states), is greater on 1,8-nonadiyne than on 1-nonyne samples, surprisingly appears to be a key factor in enhancing the tribocurrent extraction during the sliding

process. However it is not the sole. For 8-nonyl-1-ol coated Si(211) sample, the best performing TENGs system, none of the 100 tested locations display a typical photocurrent decay curve like in Figures 3.24b, d. Instead, all the transient photocurrent traces behave like a RC circuit (Figure 3.24f). But unlike data of Figures 3.24c, e, the initial photocurrent spike when the laser is switched on is up to three times as large as that of 1,8-nonadiyne surfaces, and it then drops quickly. The initial strong current spike could be attributed to the photo-generated electrons being transferred to the holes trapped at surface states [99]. With more surface states being introduced to the silicon surface by the surface chemistry modification, a stronger current spike appears on 8-nonyl-1-ol coated Si(211) samples. Besides, for all the photo-response curve on 8-nonyl-1-ol surface, the time constant is obtained to be $159.6 \pm 9.7 \mu\text{s}$. Compared to other surface chemistries, 8-nonyl-1-ol possesses the lowest time constant, hence the highest surface recombination velocity, which indicates the introduction of an higher number of surface states via surface modification, despite the near-perfect chemical passivation (Figures 3.3–3.6) and static I–Vs indicating larger leakages and higher number of surface states for the Si(111)-based samples [74, 100, 101]. It is probable that the chemical nature of these energy levels is that of silica (SiO_x), as the passage of current, regardless of its polarity [102], can induce silicon oxidation. Silicon has no conductive bulk oxide phases, and it is at first therefore counterintuitive to link increased in tribocurrent with silica-related defects. However, despite being counterintuitive, a similar relationship between increased levels of surface states and augmented zero-bias current was also reported recently for PN and NN heterojunctions [74], and also demonstrated indirectly as a drop in anodization voltage observed as soon as silica adlayers form over a silicon electrode during its constant-current deliberate oxidation [103, 104].

3.4 Conclusion

This study has unveiled the surface chemistry of a readily available but overlooked crystal cut of silicon – Si(211) – as a promising DC-TENG platform. We have provided explicit evidence of the zero-bias current not being a response to the microscale dynamics of stick–slip friction. Further, the zero-bias DC output of a Si sliding diode

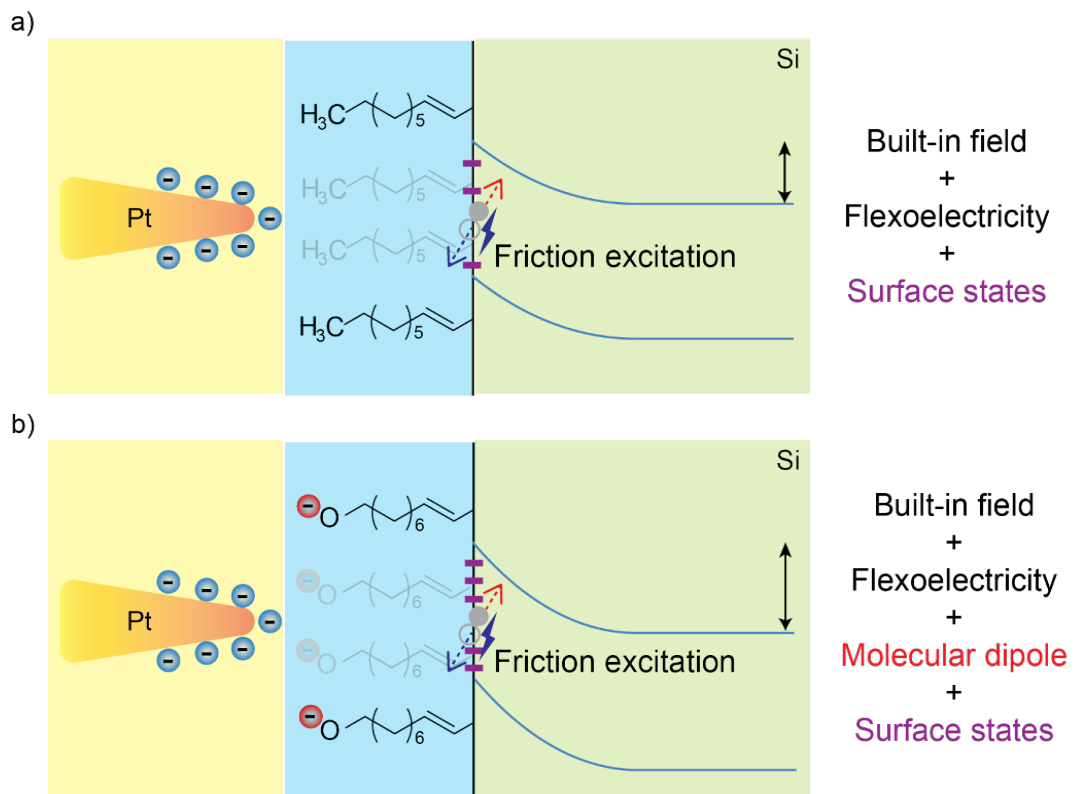


Figure 3.26. Comprehensive triboelectricity generation mechanism for (a) alkyne and (b) hydroxyl terminated silicon-metal Schottky diode TENGs. The built-in electric field enhanced by negatively charged Pt tip owing to flexoelectricity and surface states are presented in all surface chemistries. But for hydroxyl group terminated surface, the oxide ions by deprotonation further enhanced the electric field for 8-nonyl-1-ol coated surfaces. Thus, an ultra-high DC. current density was reported.

TENG has the direction of a leakage current, but analysis of the leakage of static junctions is not a priori a good indicator of device performances: static charge transport and dynamic DC outputs are seemingly unrelated. Silicon surfaces with abundant electrical defects, provided that they are being kept oxide-free and conductive by means of chemical passivation, are more likely to yield larger DC outputs when incorporated in a Schottky diodes TENG. Electrical traps coupled to the presence of surface-tethered proton-exchangeable, hence negatively charged functional groups, coupled to a metal contact possibly negatively charged by flexoelectricity (Figure 3.26) significantly improve DC outputs, to the extent that zero-bias current densities of 10^9 A/m² were recorded on hydroxyl-terminated monolayer coated Si(211) substrates. These findings give a path to improve the design of semiconductor-based DC-TENGs in a way to minimize frictional wear.

3.5 References

- [1] Zi, Y.; Guo, H.; Wen, Z.; Yeh, M.-H.; Hu, C.; Wang, Z. L., Harvesting low-frequency (<5 Hz) irregular mechanical energy: a possible killer application of triboelectric nanogenerator. *ACS Nano*. 10 (2016) 4797–4805. <http://doi.org/10.1021/acsnano.6b01569>
- [2] Wang, X.; Niu, S.; Yin, Y.; Yi, F.; You, Z.; Wang, Z. L., Triboelectric nanogenerator based on fully enclosed rolling spherical structure for harvesting low-frequency water wave energy. *Adv. Energy Mater.* 5 (2015) 1501467. <http://doi.org/10.1002/aenm.201501467>
- [3] Morita, T., Miniature piezoelectric motors. *Sens. Actuators, A*. 103 (2003) 291–300. [http://doi.org/10.1016/S0924-4247\(02\)00405-3](http://doi.org/10.1016/S0924-4247(02)00405-3)
- [4] Wang, X.; Song, J.; Liu, J.; Zhong, L. W., Direct-current nanogenerator driven by ultrasonic waves. *Science*. 316 (2007) 102–105. <http://doi.org/10.1126/science.1139366>
- [5] Salauddin, M.; Toyabur, R. M.; Maharjan, P.; Rasel, M. S.; Kim, J. W.; Cho, H.; Park, J. Y., Miniaturized springless hybrid nanogenerator for powering portable and wearable electronic devices from human-body-induced vibration. *Nano Energy* 51 (2018) 61–72. <http://doi.org/10.1016/j.nanoen.2018.06.042>
- [6] Hashemi, S. A.; Ramakrishna, S.; Aberle, A. G., Recent progress in flexible–wearable solar cells for self-powered electronic devices. *Energy Environ. Sci.* 13 (2020) 685–743. <http://doi.org/10.1039/c9ee03046h>
- [7] Xue, H.; Yang, Q.; Wang, D.; Luo, W.; Wang, W.; Lin, M.; Liang, D.; Luo, Q., A wearable pyroelectric nanogenerator and self-powered breathing sensor. *Nano Energy* 38 (2017) 147–154. <http://doi.org/10.1016/j.nanoen.2017.05.056>
- [8] Sezer, N.; Koç, M., A comprehensive review on the state-of-the-art of piezoelectric energy harvesting. *Nano Energy* 80 (2021) 105567. <http://doi.org/10.1016/j.nanoen.2020.105567>
- [9] Zheng, Q.; Shi, B.; Li, Z.; Wang, Z. L., Recent progress on piezoelectric and triboelectric energy harvesters in biomedical systems. *Adv. Sci.* 4 (2017) 1700029. <http://doi.org/10.1002/advs.201700029>
- [10] Wang, Z. L.; Chen, J.; Lin, L., Progress in triboelectric nanogenerators as a new energy technology and self-powered sensors. *Energy Environ. Sci.* 8 (2015) 2250–2282. <http://doi.org/10.1039/c5ee01532d>
- [11] Cuiying, Y.; Di, L.; Xiao, P.; Yang, J.; Renwei, C.; Chuan, N.; Feifan, S.; Yihan, Z.; Kai, D.; Zhong Lin, W., A hydrophobic self-repairing power textile for effective water droplet energy harvesting. *ACS Nano*. 15 (2021) 18172–18181. <http://doi.org/10.1021/acsnano.1c06985>
- [12] Rui, P.; Zhang, W.; Zhong, Y.; Wei, X.; Guo, Y.; Shi, S.; Liao, Y.; Cheng, J.; Wang, P., High-performance cylindrical pendulum shaped triboelectric nanogenerators driven by water wave energy for full-automatic and self-powered wireless hydrological monitoring system. *Nano Energy* 74 (2020) 104937. <http://doi.org/10.1016/j.nanoen.2020.104937>
- [13] Yang, Y.; Zhang, H.; Lin, Z.-H.; Zhou, Y. S.; Jing, Q.; Su, Y.; Yang, J.; Chen, J.; Hu, C.; Wang, Z. L., Human skin based triboelectric nanogenerators for harvesting biomechanical energy and as self-powered active tactile sensor system. *ACS Nano*. 7 (2013) 9213–9222. <http://doi.org/10.1021/nn403838y>

- [14] Bai, P.; Zhu, G.; Liu, Y.; Chen, J.; Jing, Q.; Yang, W.; Ma, J.; Zhang, G.; Wang, Z. L., Cylindrical rotating triboelectric nanogenerator. *ACS Nano*. 7 (2013) 6361–6366. <http://doi.org/10.1021/nn402491y>
- [15] Song, W.-Z.; Qiu, H.-J.; Zhang, J.; Yu, M.; Ramakrishna, S.; Wang, Z. L.; Long, Y.-Z., Sliding mode direct current triboelectric nanogenerators. *Nano Energy* 90 (2021) 106531. <http://doi.org/10.1016/j.nanoen.2021.106531>
- [16] Wang, Z. L.; Wang, A. C., On the origin of contact-electrification. *Mater. Today*. 30 (2019) 34–51. <http://doi.org/10.1016/j.mattod.2019.05.016>
- [17] Zhou, L.; Liu, D.; Wang, J.; Wang, Z. L., Triboelectric nanogenerators: fundamental physics and potential applications. *Friction*. 8 (2020) 481–506. <http://doi.org/10.1007/s40544-020-0390-3>
- [18] Liu, J.; Goswami, A.; Jiang, K. R.; Khan, F.; Kim, S.; McGee, R.; Li, Z.; Hu, Z. Y.; Lee, J.; Thundat, T., Direct-current triboelectricity generation by a sliding Schottky nanocontact on MoS₂ multilayers. *Nat. Nanotechnol.* 13 (2018) 112–116. <http://doi.org/10.1038/s41565-017-0019-5>
- [19] Ferrie, S.; Darwish, N.; Gooding, J. J.; Ciampi, S., Harnessing silicon facet-dependent conductivity to enhance the direct-current produced by a sliding Schottky diode triboelectric nanogenerator. *Nano Energy* 78 (2020) 105210. <http://doi.org/10.1016/j.nanoen.2020.105210>
- [20] Lin, S.; Chen, X.; Wang, Z. L., The tribovoltaic effect and electron transfer at a liquid-semiconductor interface. *Nano Energy* 76 (2020) 105070. <http://doi.org/10.1016/j.nanoen.2020.105070>
- [21] Lin, S.; Lu, Y.; Feng, S.; Hao, Z.; Yan, Y., A high current density direct-current generator based on a moving van der Waals Schottky diode. *Adv. Mater.* 31 (2018) 1804398. <http://doi.org/10.1002/adma.201804398>
- [22] Liu, J.; Cheikh, M. I.; Bao, R.; Peng, H.; Liu, F.; Li, Z.; Jiang, K.; Chen, J.; Thundat, T., Tribo-tunneling DC generator with carbon aerogel/silicon multi-nanocontacts. *Adv. Electron. Mater.* 5 (2019) 1900464. <http://doi.org/10.1002/aelm.201900464>
- [23] Liu, J.; Miao, M.; Jiang, K.; Khan, F.; Goswami, A.; McGee, R.; Li, Z.; Nguyen, L.; Hu, Z.; Lee, J.; Cadien, K.; Thundat, T., Sustained electron tunneling at unbiased metal-insulator-semiconductor triboelectric contacts. *Nano Energy* 48 (2018) 320–326. <http://doi.org/10.1016/j.nanoen.2018.03.068>
- [24] Lu, Y.; Feng, S.; Shen, R.; Xu, Y.; Hao, Z.; Yan, Y.; Zheng, H.; Yu, X.; Gao, Q.; Zhang, P.; Lin, S., Tunable dynamic black phosphorus/insulator/Si heterojunction direct-current generator based on the hot electron transport. *Research* 2019 (2019) 5832382. <http://doi.org/10.34133/2019/5832382>
- [25] Lu, Y.; Gao, Q.; Yu, X.; Zheng, H.; Shen, R.; Hao, Z.; Yan, Y.; Zhang, P.; Wen, Y.; Yang, G.; Lin, S., Interfacial built-in electric field-driven direct current generator based on dynamic silicon homojunction. *Research* 2020 (2020) 5714754. <http://doi.org/10.34133/2020/5714754>
- [26] Lu, Y.; Hao, Z.; Feng, S.; Shen, R.; Yan, Y.; Lin, S., Direct-current generator based on dynamic PN junctions with the designed voltage output. *iScience*. 22 (2019) 58–69. <http://doi.org/10.1016/j.isci.2019.11.004>
- [27] Lu, Y.; Yan, Y.; Yu, X.; Zhou, X.; Feng, S.; Xu, C.; Zheng, H.; Yang, Z.; Li, L.; Liu, K.; Lin, S., Polarized water driven dynamic PN junction-based direct-current generator. *Research* 2021 (2021) 7505638. <http://doi.org/10.34133/2021/7505638>

- [28] Xu, R.; Zhang, Q.; Wang, J. Y.; Liu, D.; Wang, J.; Wang, Z. L., Direct current triboelectric cell by sliding an n-type semiconductor on a p-type semiconductor. *Nano Energy* 66 (2019) 104185. <http://doi.org/10.1016/j.nanoen.2019.104185>
- [29] Aragonès, A. C.; Darwish, N.; Ciampi, S.; Sanz, F.; Gooding, J. J.; Diéz-Pérez, I., Single-molecule electrical contacts on silicon electrodes under ambient conditions. *Nat. Commun.* 8 (2017) 15056–15056. <http://doi.org/10.1038/ncomms15056>
- [30] Vogel, Y. B.; Zhang, L.; Darwish, N.; Gonçalves, V. R.; Le Brun, A.; Gooding, J. J.; Molina, A.; Wallace, G. G.; Coote, M. L.; Gonzalez, J.; Ciampi, S., Reproducible flaws unveil electrostatic aspects of semiconductor electrochemistry. *Nat. Commun.* 8 (2017) 2066. <http://doi.org/10.1038/s41467-017-02091-1>
- [31] Vogel, Y. B.; Zhang, J.; Darwish, N.; Ciampi, S., Switching of current rectification ratios within a single nanocrystal by facet-resolved electrical wiring. *ACS Nano.* 12 (2018) 8071–8080. <http://doi.org/10.1021/acsnano.8b02934>
- [32] Fabre, B., Functionalization of oxide-free silicon surfaces with redox-active assemblies. *Chem. Rev.* 116 (2016) 4808–4849. <http://doi.org/10.1021/acs.chemrev.5b00595>
- [33] Deng, S.; Xu, R.; Seh, W.; Sun, J.; Cai, W.; Zou, J.; Zhang, Q., Current degradation mechanism of tip contact metal-silicon Schottky nanogenerator. *Nano Energy* 94 (2021) 106888. <http://doi.org/10.1016/j.nanoen.2021.106888>
- [34] Song, Y.; Wang, N.; Fadlallah, M. M.; Tao, S.; Yang, Y.; Wang, Z. L., Defect states contributed nanoscale contact electrification at ZnO nanowires packed film surfaces. *Nano Energy* 79 (2021) 105406. <http://doi.org/10.1016/j.nanoen.2020.105406>
- [35] Tan, C. S.; Hsieh, P. L.; Chen, L. J.; Huang, M. H., Silicon wafers with facet-dependent electrical conductivity properties. *Angew. Chem.* 56 (2017) 15339–15343. <http://doi.org/10.1002/anie.201709020>
- [36] Zhang, S.; Ferrie, S.; Peiris, C. R.; Lyu, X.; Vogel, Y. B.; Darwish, N.; Ciampi, S., Common background signals in voltammograms of crystalline silicon electrodes are reversible silica–silicon redox chemistry at highly conductive surface sites. *J. Am. Chem. Soc.* 143 (2021) 1267–1272. <http://doi.org/10.1021/jacs.0c10713>
- [37] Salomon, A.; Böcking, T.; Gooding, J. J.; Cahen, D., How important is the interfacial chemical bond for electron transport through alkyl chain monolayers? *Nano Lett.* 6 (2006) 2873–2876. <http://doi.org/10.1021/nl062089y>
- [38] Linford, M. R.; Fenter, P.; Eisenberger, P. M.; Chidsey, C. E. D., Alkyl monolayers on silicon prepared from 1-alkenes and hydrogen-terminated silicon. *J. Am. Chem. Soc.* 117 (1995) 3145–3155. <http://doi.org/10.1021/ja00116a019>
- [39] Sieval, A. B.; Demirel, A. L.; Nissink, J. W. M.; Linford, M. R.; van der Maas, J. H.; de Jeu, W. H.; Zuilhof, H.; Sudhölter, E. J. R., Highly stable Si–C linked functionalized monolayers on the silicon (100) surface. *Langmuir* 14 (1998) 1759–1768. <http://doi.org/10.1021/la971139z>
- [40] Xu, J.; Zou, Y.; Nashalian, A.; Chen, J., Leverage surface chemistry for high-performance triboelectric nanogenerators. *Front. Chem.* 8 (2020) 577327. <http://doi.org/10.3389/fchem.2020.577327>
- [41] Wang, S.; Zi, Y.; Zhou, Y. S.; Li, S.; Fan, F.; Lin, L.; Wang, Z. L., Molecular surface functionalization to enhance the power output of triboelectric nanogenerators. *J. Mater. Chem. A.* 4 (2016) 3728–3734. <http://doi.org/10.1039/c5ta10239a>
- [42] Ahmed, A.; Hassan, I.; Pourrahimi, A. M.; Helal, A. S.; El-Kady, M. F.; Khassaf, H.; Kaner, R. B., Toward high-performance triboelectric nanogenerators by

- engineering interfaces at the nanoscale: looking into the future research roadmap. *Adv. Mater. Technol.* 5 (2020) 2000520. <http://doi.org/10.1002/admt.202000520>
- [43] Higashi, G. S.; Becker, R. S.; Chabal, Y. J.; Becker, A. J., Comparison of Si(111) surfaces prepared using aqueous-solutions of NH_4F versus HF. *Appl. Phys. Lett.* 58 (1991) 1656–1658. <http://doi.org/10.1063/1.105155>
- [44] Veerbeek, J.; Huskens, J., Applications of monolayer-functionalized H-terminated silicon surfaces: A review. *Small Methods* 1 (2017) 1700072. <http://doi.org/10.1002/smt.201700072>
- [45] Dief, E. M.; Brun, A. P. L.; Ciampi, S.; Darwish, N., Spontaneous grafting of OH-terminated molecules on Si–H surfaces via Si–O–C covalent bonding. *Surfaces* 4 (2021) 81–88. <http://doi.org/10.3390/surfaces4010010>
- [46] Ciampi, S.; Eggers, P. K.; Le Saux, G.; James, M.; Harper, J. B.; Gooding, J. J., Silicon (100) electrodes resistant to oxidation in aqueous solutions: An unexpected benefit of surface acetylene moieties. *Langmuir* 25 (2009) 2530–2539. <http://doi.org/10.1021/la803710d>
- [47] Zhang, J.; Ferrie, S.; Zhang, S.; Vogel, Y. B.; Peiris, C. R.; Darwish, N.; Ciampi, S., Single-electrode electrochemistry: chemically engineering surface adhesion and hardness to maximize redox work extracted from tribocharged silicon. *ACS Appl. Nano Mater.* 2 (2019) 7230–7236. <http://doi.org/10.1021/acsnm.9b01726>
- [48] Vogel, Y. B.; Darwish, N.; Ciampi, S., Spatiotemporal control of electrochemiluminescence guided by a visible light stimulus. *Cell Rep. Phys. Sci.* 1 (2020) 100107. <http://doi.org/10.1016/j.xcrp.2020.100107>
- [49] Chaudhury, M. K., Adhesion and friction of self-assembled organic monolayers. *Curr. Opin. Colloid Interface Sci.* 2 (1997) 65–69. [http://doi.org/10.1016/S1359-0294\(97\)80009-X](http://doi.org/10.1016/S1359-0294(97)80009-X)
- [50] Ciampi, S.; Harper, J. B.; Gooding, J. J., Wet chemical routes to the assembly of organic monolayers on silicon surfaces via the formation of Si-C bonds: surface preparation, passivation and functionalization. *Chem. Soc. Rev.* 39 (2010) 2158–2183. <http://doi.org/10.1039/b923890p>
- [51] Gooding, J. J.; Ciampi, S., The molecular level modification of surfaces: From self-assembled monolayers to complex molecular assemblies. *Chem. Soc. Rev.* 40 (2011) 2704–2718. <http://doi.org/10.1039/c0cs00139b>
- [52] Akbulut, M.; Godfrey Alig, A. R.; Israelachvili, J., Triboelectrification between smooth metal surfaces coated with self-assembled monolayers (SAMs). *J. Phys. Chem. B.* 110 (2006) 22271–22278. <http://doi.org/10.1021/jp063161j>
- [53] Ferrie, S.; Le Brun, A. P.; Krishnan, G.; Andersson, G. G.; Darwish, N.; Ciampi, S., Sliding silicon-based Schottky diodes: maximizing triboelectricity with surface chemistry. *Nano Energy* 93 (2022) 106861. <http://doi.org/10.1016/j.nanoen.2021.106861>
- [54] Rohde, R. D.; Agnew, H. D.; Yeo, W.-S.; Bailey, R. C.; Heath, J. R., A non-oxidative approach toward chemically and electrochemically functionalizing Si(111). *J. Am. Chem. Soc.* 128 (2006) 9518–9525. <http://doi.org/10.1021/ja062012b>
- [55] O’Leary, L. E.; Rose, M. J.; Ding, T. X.; Johansson, E.; Brunschwig, B. S.; Lewis, N. S., Heck coupling of olefins to mixed methyl/thienyl monolayers on Si(111) surfaces. *J. Am. Chem. Soc.* 135 (2013) 10081–10090. <http://doi.org/10.1021/ja402495e>

- [56] Zhang, L.; Vogel, Y. B.; Noble, B. B.; Gonçalves, V. R.; Darwish, N.; Brun, A. L.; Gooding, J. J.; Wallace, G. G.; Coote, M. L.; Ciampi, S., TEMPO monolayers on Si(100) electrodes: electrostatic effects by the electrolyte and semiconductor space-charge on the electroactivity of a persistent radical. *J. Am. Chem. Soc.* 138 (2016) 9611–9619. <http://doi.org/10.1021/jacs.6b04788>
- [57] Yang, Y.; Ciampi, S.; Gooding, J. J., Coupled thermodynamic and kinetic changes in the electrochemistry of ferrocenyl monolayers induced by light. *Langmuir* 33 (2017) 2497–2503. <http://doi.org/10.1021/acs.langmuir.6b04106>
- [58] Ciampi, S.; Böcking, T.; Kilian, K. A.; James, M.; Harper, J. B.; Gooding, J. J., Functionalization of acetylene-terminated monolayers on Si(100) surfaces: A click chemistry approach. *Langmuir* 23 (2007) 9320–9329. <http://doi.org/10.1021/la701035g>
- [59] Linford, M. R.; Chidsey, C. E. D., Alkyl monolayers covalently bonded to silicon surfaces. *J. Am. Chem. Soc.* 115 (1993) 12631–12632. <http://doi.org/10.1021/ja00079a071>
- [60] James, M.; Darwish, T. A.; Ciampi, S.; Sylvester, S. O.; Zhang, Z.; Ng, A.; Gooding, J. J.; Hanley, T. L., Nanoscale condensation of water on self-assembled monolayers. *Soft Matter*. 7 (2011) 5309–5318. <http://doi.org/10.1039/c1sm05096f>
- [61] James, M.; Ciampi, S.; Darwish, T. A.; Hanley, T. L.; Sylvester, S. O.; Gooding, J. J., Nanoscale Water Condensation on Click-Functionalized Self-Assembled Monolayers. *Langmuir* 27 (2011) 10753–10762. <http://doi.org/10.1021/la202359c>
- [62] Yang, Y.; Ciampi, S.; Choudhury, M. H.; Gooding, J. J., Light activated electrochemistry: light intensity and pH dependence on electrochemical performance of anthraquinone derivatized silicon. *J. Phys. Chem. C*. 120 (2016) 2874–2882. <http://doi.org/10.1021/acs.jpcc.5b12097>
- [63] Zhang, L.; Espíndola, R.; Noble, B.; Gonçalves, V.; Wallace, G.; Darwish, N.; Coote, M.; Ciampi, S., Switchable interfaces: redox monolayers on Si(100) by electrochemical trapping of alcohol nucleophiles. *Surfaces* 1 (2018) 3–11. <http://doi.org/10.3390/surfaces1010002>
- [64] Baio, J. E.; Weidner, T.; Brison, J.; Graham, D. J.; Gamble, L. J.; Castner, D. G., Amine terminated SAMs: Investigating why oxygen is present in these films. *J. Electron Spectrosc. Relat. Phenom.* 172 (2009) 2–8. <http://doi.org/10.1016/j.elspec.2009.02.008>
- [65] Park, J. Y.; Salmeron, M., Fundamental aspects of energy dissipation in friction. *Chem. Rev.* 114 (2014) 677–711. <http://doi.org/10.1021/cr200431y>
- [66] Miller, J. N., *Statistics and chemometrics for analytical chemistry* / James N. Miller and Jane C. Miller. 5th . ed.; Harlow, England : Pearson/Prentice Hall: Harlow, England, 2005.
- [67] Schindelin, J.; Arganda-Carreras, I.; Frise, E.; Kaynig, V.; Longair, M.; Pietzsch, T.; Preibisch, S.; Rueden, C.; Saalfeld, S.; Schmid, B.; Tinevez, J.-Y.; White, D. J.; Hartenstein, V.; Eliceiri, K.; Tomancak, P.; Cardona, A., Fiji: An open-source platform for biological-image analysis. *Nat. Methods*. 9 (2012) 676–682. <http://doi.org/10.1038/nmeth.2019>
- [68] Schneider, C. A.; Rasband, W. S.; Eliceiri, K. W., NIH Image to ImageJ: 25 years of image analysis. *Nat. Methods*. 9 (2012) 671–675. <http://doi.org/10.1038/nmeth.2089>

- [69] Cerofolini, G. F.; Galati, C.; Renna, L., Accounting for anomalous oxidation states of silicon at the Si/SiO₂ interface. *Surf. Interface Anal.* 33 (2002) 583–590. <http://doi.org/10.1002/sia.1424>
- [70] Yaffe, O.; Scheres, L.; Segev, L.; Biller, A.; Ron, I.; Salomon, E.; Giesbers, M.; Kahn, A.; Kronik, L.; Zuilhof, H.; Vilan, A.; Cahen, D., Hg/Molecular monolayer–Si junctions: electrical interplay between monolayer properties and semiconductor doping density. *J. Phys. Chem. C.* 114 (2010) 10270–10279. <http://doi.org/10.1021/jp101656t>
- [71] Wallart, X.; Henry de Villeneuve, C.; Allongue, P., Truly quantitative XPS characterization of organic monolayers on silicon: study of alkyl and alkoxy monolayers on H–Si(111). *J. Am. Chem. Soc.* 127 (2005) 7871–7878. <http://doi.org/10.1021/ja0430797>
- [72] Scheres, L.; Arafat, A.; Zuilhof, H., Self-assembly of high-quality covalently bound organic monolayers onto silicon. *Langmuir* 23 (2007) 8343–8346. <http://doi.org/10.1021/la701359k>
- [73] Yaffe, O.; Ely, T.; Har-Lavan, R.; Egger, D. A.; Johnston, S.; Cohen, H.; Kronik, L.; Vilan, A.; Cahen, D., Effect of molecule–surface reaction mechanism on the electronic characteristics and photovoltaic performance of molecularly modified Si. *J. Phys. Chem. C.* 117 (2013) 22351–22361. <http://doi.org/10.1021/jp4027755>
- [74] Zheng, M.; Lin, S.; Xu, L.; Zhu, L.; Wang, Z. L., Scanning probing of the tribovoltaic effect at the sliding interface of two semiconductors. *Adv. Mater.* 32 (2020) e2000928. <http://doi.org/10.1002/adma.202000928>
- [75] Zhang, Z.; Jiang, D.; Zhao, J.; Liu, G.; Bu, T.; Zhang, C.; Wang, Z. L., Tribovoltaic effect on metal–semiconductor interface for direct-current low-impedance triboelectric nanogenerators. *Adv. Energy Mater.* 10 (2020) 1903713. <http://doi.org/10.1002/aenm.201903713>
- [76] Mizzi, C. A.; Lin, A. Y. W.; Marks, L. D., Does flexoelectricity drive triboelectricity? *Phys. Rev. Lett.* 123 (2019) 1. <http://doi.org/10.1103/PhysRevLett.123.116103>
- [77] Yurkov, A. S.; Yudin, P. V., Flexoelectricity in metals. *J. Appl. Phys.* 129 (2021) 195108. <http://doi.org/10.1063/5.0048890>
- [78] Sun, L.; Zhu, L.; Zhang, C.; Chen, W.; Wang, Z., Mechanical manipulation of silicon-based Schottky diodes via flexoelectricity. *Nano Energy* 83 (2021) 105855. <http://doi.org/10.1016/j.nanoen.2021.105855>
- [79] Gooding, D. M.; Kaufman, G. K., *Tribocharging and the Triboelectric Series*. Chichester, UK: John Wiley & Sons, Ltd: Chichester, UK, (2011); pp 1–14. <http://doi.org/10.1002/9781119951438.eibc2239.pub2>
- [80] Berman, A. D.; Ducker, W. A.; Israelachvili, J. N., Origin and characterization of different stick–slip friction mechanisms. *Langmuir* 12 (1996) 4559–4563. <http://doi.org/10.1021/la950896z>
- [81] Budakian, R.; Putterman, S. J., Correlation between charge transfer and stick–slip friction at a metal–insulator interface. *Phys. Rev. Lett.* 85 (2000) 1000–1003. <http://doi.org/10.1103/PhysRevLett.85.1000>
- [82] Camara, C. G.; Escobar, J. V.; Hird, J. R.; Putterman, S. J., Correlation between nanosecond X-ray flashes and stick–slip friction in peeling tape. *Nature* 455 (2008) 1089–1092. <http://doi.org/10.1038/nature07378>
- [83] Liu, J.; Liu, F.; Bao, R.; Jiang, K.; Khan, F.; Li, Z.; Peng, H.; Chen, J.; Alodhayb, A.; Thundat, T., Scaled-up direct-current generation in MoS₂ multilayer-based

- moving heterojunctions. *ACS Appl. Mater. Interfaces*. 11 (2019) 35404–35409. <http://doi.org/10.1021/acsami.9b09851>
- [84] Allongue, P.; Henry de Villeneuve, C.; Morin, S.; Boukherroub, R.; Wayner, D. D. M., The preparation of flat H–Si(111) surfaces in 40% NH₄F revisited. *Electrochim. Acta*. 45 (2000) 4591–4598. [http://doi.org/10.1016/S0013-4686\(00\)00610-1](http://doi.org/10.1016/S0013-4686(00)00610-1)
- [85] Li, T.; Dief, E. M.; Lyu, X.; Rahpeima, S.; Ciampi, S.; Darwish, N., Nanoscale silicon oxide reduces electron transfer kinetics of surface-bound ferrocene monolayers on dilicon. *J. Phys. Chem. C*. 125 (2021) 27763–27770. <http://doi.org/10.1021/acs.jpcc.1c07788>
- [86] Helseth, L. E., Excitation of energy harvesters using stick–slip motion. *Smart Mater. Struct.* 23 (2014) 085024. <http://doi.org/10.1088/0964-1726/23/8/085024>
- [87] Chan, N.; Vazirisereshk, M. R.; Martini, A.; Egberts, P., Insights into dynamic sliding contacts from conductive atomic force microscopy. *Nanoscale Adv.* 2 (2020) 4117–4124. <http://doi.org/10.1039/D0NA00414F>
- [88] Lin, S.; Xu, L.; Chi Wang, A.; Wang, Z. L., Quantifying electron-transfer in liquid-solid contact electrification and the formation of electric double-layer. *Nat. Commun.* 11 (2020) 399. <http://doi.org/10.1038/s41467-019-14278-9>
- [89] Vu, D. L.; Le, C. D.; Vo, C. P.; Ahn, K. K., Surface polarity tuning through epitaxial growth on polyvinylidene fluoride membranes for enhanced performance of liquid-solid triboelectric nanogenerator. *Composites, Part B* 223 (2021) 109135. <http://doi.org/10.1016/j.compositesb.2021.109135>
- [90] Burgess, I.; Seivewright, B.; Lennox, R. B., Electric field driven protonation/deprotonation of self-assembled monolayers of acid-terminated thiols. *Langmuir* 22 (2006) 4420–4428. <http://doi.org/10.1021/la052767g>
- [91] Kolodner, P.; Lukashev, E. P.; Ching, Y.-C.; Rousseau, D. L., Electric-field-induced Schiff-base deprotonation in D85N mutant bacteriorhodopsin. *Proc. Natl. Acad. Sci. U. S. A.* 93 (1996) 11618–11621. <http://doi.org/10.1073/pnas.93.21.11618>
- [92] Delley, M. F.; Nichols, E. M.; Mayer, J. M., Interfacial acid–base equilibria and electric fields concurrently probed by in situ surface-enhanced infrared spectroscopy. *J. Am. Chem. Soc.* 143 (2021) 10778–10792. <http://doi.org/10.1021/jacs.1c05419>
- [93] Zhang, S.; Ferrie, S.; Lyu, X.; Xia, Y.; Darwish, N.; Wang, Z.; Ciampi, S., Absence of a relationship between surface conductivity and electrochemical rates: redox-active monolayers on Si(211), Si(111), and Si(110). *J. Phys. Chem. C* 125 (2021) 18197–18203. <http://doi.org/10.1021/acs.jpcc.1c05023>
- [94] Brewer, N. J.; Beake, B. D.; Leggett, G. J., Friction force microscopy of self-assembled monolayers: influence of adsorbate alkyl chain length, terminal group chemistry, and scan velocity. *Langmuir* 17 (2001) 1970–1974. <http://doi.org/10.1021/la001568o>
- [95] Lin, S.; Shen, R.; Yao, T.; Lu, Y.; Feng, S.; Hao, Z.; Zheng, H.; Yan, Y.; Li, E., Surface states enhanced dynamic Schottky diode generator with extremely high power density over 1000 W m⁻². *Adv. Sci.* 6 (2019) 1901925. <http://doi.org/10.1002/advs.201901925>
- [96] Salomon, A.; Boecking, T.; Chan, C. K.; Amy, F.; Girshevitz, O.; Cahen, D.; Kahn, A., How do electronic carriers cross Si-bound alkyl monolayers? *Phys Rev Lett.* 95 (2005) 266807.1–266807.4. <http://doi.org/10.1103/PhysRevLett.95.266807>
- [97] Seitz, O.; Böcking, T.; Salomon, A.; Gooding, J. J.; Cahen, D., Importance of monolayer quality for interpreting current transport through organic molecules:

- alkyls on oxide-free Si. *Langmuir* 22 (2006) 6915–6922. <http://doi.org/10.1021/la060718d>
- [98] Royea, W. J.; Juang, A.; Lewis, N. S., Preparation of air-stable, low recombination velocity Si(111) surfaces through alkyl termination. *Appl. Phys. Lett.* 77 (2000) 1988–1990. <http://doi.org/10.1063/1.1312203>
- [99] Tan, B.; Zhang, Y.; Long, M., Large-scale preparation of nanoporous TiO₂ film on titanium substrate with improved photoelectrochemical performance. *Nanoscale Res. Lett.* 9 (2014) 1–6. <http://doi.org/10.1186/1556-276X-9-190>
- [100] Kimoto, T.; Miyamoto, N.; Matsunami, H., Performance limiting surface defects in SiC epitaxial p-n junction diodes. *IEEE Trans. Electron Devices.* 46 (1999) 471–477. <http://doi.org/10.1109/16.748864>
- [101] Lu, X.; Jiang, H.; Liu, C.; Zou, X.; Lau, K. M., Off-state leakage current reduction in AlGa_N/Ga_N high electron mobility transistors by combining surface treatment and post-gate annealing. *Semicond. Sci. Technol.* 31 (2016) 55019. <http://doi.org/10.1088/0268-1242/31/5/055019>
- [102] Peiris, C. R.; Ferrie, S.; Ciampi, S.; Rickard, W. D. A.; Darwish, N., Memristor arrays formed by reversible formation and breakdown of nanoscale silica layers on Si–H surfaces. *ACS Appl. Nano Mater.* 5 (2022) 6609–6617. <http://doi.org/10.1021/acsanm.2c00663>
- [103] V.X., U., Role of electron / hole processes in the initial stage of silicon anodization. *Mater. Sci. Forum.* 185/188 (1995) 115–118.
- [104] Young, L., An ellipsometric study of steady-state high field ionic conduction in anodic oxide films on tantalum, niobium, and silicon. *J. Electrochem. Soc.* 113 (1966) 277–284. <http://doi.org/10.1149/1.2423932>

Chapter 4 – Direct-current output of silicon–organic monolayer–platinum Schottky TENGs: Elusive friction-output relationship

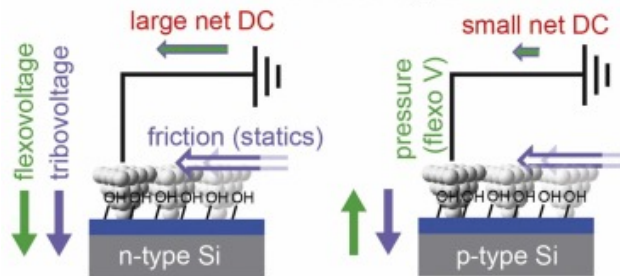
Adapted from Lyu, X.; MacGregor, M.; Liu, J.; Darwish, N.; Ciampi, S., Direct-current output of silicon–organic monolayer–platinum Schottky TENGs: Elusive friction-output relationship. *Nano Energy* **2023**, 224, 108627. Some content from the published Supporting Information file has been moved into the main text for clarity of this study. Rights are retained to reuse in the thesis by the authors. An attribution statement is included in Appendix III.

Abstract

Triboelectric nanogenerators (TENGs) are an emerging energy harvesting technology able to convert ubiquitous mechanical energy into electricity. Friction, static charging and flexoelectricity are all involved in the mechanism underpinning TENG operation, but their relative contribution has remained elusive. Here we used dynamic and static conductive atomic force microscopy (C-AFM) measurements on monolayer-modified silicon crystals to detect evidence of a relationship between friction and zero-bias current, and between pressure and the direction of the putative flexovoltage. We demonstrate that a static electricity-related tribovoltage is probably responsible for a friction excess, and that surprisingly this friction excess is found to be dependent on the doping level and type of the silicon substrate. Such friction excess is however no longer measurable once current is allowed to flow across the junction. This observation points to an electrostatic origin of friction in silicon-based Schottky TENGs, and suggests that the zero external bias DC current is at least in part an electronic flow to neutralize static charges. Further, the sign of the zero-bias current, but not its magnitude, is independent of the semiconductor doping type, which is again suggestive of surface statics being a main contributor to the zero-bias output rather than exclusively a space-charge effect. We also reveal the presence of a junction flexovoltage under pressures common in AFM experiments (GPa), even for negligible lateral friction. In a static Pt–monolayer–n-type Si junction the flexovoltage carries the same sign as the tribovoltage, and can reach such magnitude to overwrite external voltages as high as 2 V. The immediate implication is that the flexovoltage is likely to have i) a strong contribution to the zero-bias output of a n-Si Schottky TENG, ii) a negative effect on the output of a p-Si TENG, and iii) its detection can be straightforward, as we discovered that flexoelectricity manifests as an “inverted diode”: a n-type Si–platinum diode with negligible current even when the n-type material is negatively biased as long as the “static” diode remains under a large normal pressure.

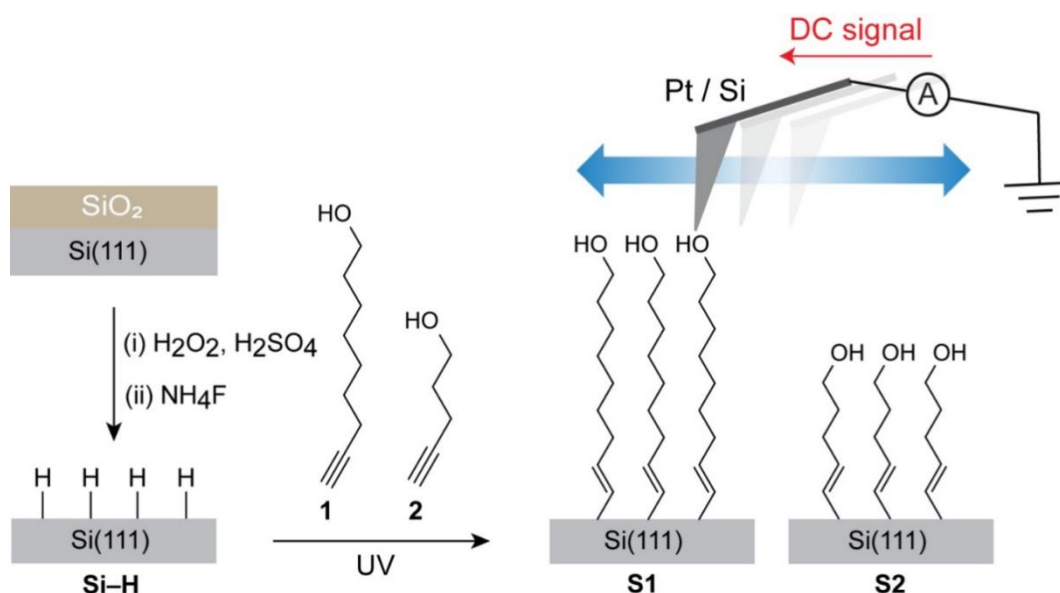
Graphical abstract

DC silicon SchottkyTENGs: net DC output is a balance of flexo and tribovoltages



4.1 Introduction

The continuous shift from analogue to digital technologies – the so-called digital revolution that started around 1980 – has transformed society [1, 2]. Electronic components at the core of digital devices such as ubiquitous mobile phones, lifesaving pacemakers, niche wearable electronics or microscopic sensors, share a common feature: their operation requires a reliable source of direct current (DC). In most cases, chemical energy stored in a battery remains the source of this DC power. However, all batteries need replacement or periodic recharging, posing a challenge for the continuous operation of devices that are installed in locations of difficult access, such as remote environmental sensors or life-critical medical implants [3-8]. Triboelectric nanogenerators (TENGs) are a class of power sources that convert small-scale vibrations, pressure and mechanical friction into electricity [9-12]. Most TENGs described in the literature are alternated-current TENGs [11, 13-15], but over the last five years there has been an ever increasing research effort towards the development of DC-TENGs, TENGs outputting DC current and voltage [6, 16-28]. Sliding Schottky diodes, that is, out of equilibrium metal–semiconductor junctions under some form of mechanical stress, are a promising form of DC-TENG [17, 19, 24, 26, 29-31],



Scheme 4.1. Surface passivation and functionalization of oxide-free Si(111) substrates. Silicon surfaces were (i) cleaned with Piranha solution and (ii) etched in ammonium fluoride aqueous solutions. The hydrogen-terminated samples (Si-H) were then reacted with either 8-nonyn-1-ol (1), or 4-pentyn-1-ol (2) under UV light to yield the monolayer-modified Si(111) surfaces S1 and S2, respectively.

outputting DC densities as high as $\sim 10^9$ A/m² for nanoscale contacts, and up to ~ 210 A/m² for microscale contacts [24, 27]. A complete and correct understanding of the mechanism by which friction, adhesion and pressure/strain lead to a DC output in a sliding diode is still lacking, but what is clear is that surface engineering by monolayer chemistry is one of the routes towards a better understanding of TENGs' working principles, as well as towards maximizing their output [30, 32-34]. For example, the relationship between friction and current output remains unclear [25, 35-37]. The zero-bias current output of a Schottky TENG defines its performance as an autonomous power source, and a tribovoltaic effect in response to friction is commonly accepted as the principal mechanism [38-40] leading to such current [36, 41]. However, what is also known is that the voltage applied to a rectifying contact, especially in the forward bias, will cause excess friction between metal and semiconductor [37, 42]. Surprisingly the origin of this forward-bias-triggered increase in resistance to a lateral movement has not yet been fully explained. The caveat in the TENG context is, of course, that frictional wear will negatively affect the device lifetime [43, 44], and should therefore, when possible, be minimized. Friction has been previously reported to influence the triboelectric process [35, 45, 46], and the influence of electronic drag on friction has also been researched [37, 42, 44, 47], but analogous research on zero-bias rectifying junction is lacking.

Herein we systematically explore the relationship between current output and friction in sliding metal contact–monolayer–semiconductor systems by means of comparing friction and zero-bias current data obtained by atomic force microscopy (AFM) experiments performed with either non-conductive or conductive AFM tips. Changes to the AFM tip but not to the surface chemistry (organic monolayer) of the semiconductor are intended to block, or to allow for, the flow of tribocurrent. This experimental system allows to address open questions such as (i) whether the zero-bias current is purely caused by friction, or whether some of the excess friction is a response to the passage of current and/or generation of a tribovoltage, (ii) whether or not the length of organic monolayer molecular chain (length of the tunnelling barrier) influences the current output [34], and (iii) clarify the role and direction of a putative flexovoltage.

The monolayer system we selected to answer the above questions is shown in Scheme 4.1. A hydrogen-terminated oxide-free silicon surface was covalently derivatized with an organic film by wet chemistry methods [48-54]. Analogous methods of surface passivation and functionalization have been proven effective in improving the performances of TENGs [33, 34, 55-57], but are underexplored and carry the advantage of a very simple means of tuning at will substrate properties (doping level and type), nature of the top contact (conductive versus insulating), and thickness of the tunnelling barrier (monolayer length), all while leaving the outmost surface chemistry of the semiconductor side of the diode unchanged.

4.2 Experimental section

4.2.1 Materials

Sulfuric acid (VLSI Puranal™, 95–97 %, Honeywell), hydrogen peroxide solution (MOS Puranal™, 30 wt% in water, Honeywell), aqueous ammonium fluoride solution (40 wt%, Sigma–Aldrich), redistilled solvents and Milli-Q™ water (>18 MΩ cm) were used for silicon cleaning and etching procedures. Prime grade, single-side polished, (111)-oriented ($\pm 0.05^\circ$) silicon wafers (Siltronix, S.A.S, Archamps, France) were 475–525 μm thick, and either lowly (7–13 Ω cm), intermediately (0.010–0.100 Ω cm) or highly doped (0.007–0.013 Ω cm), and with the exception of the wafers of intermediate doping, they were either p-type (boron-doped) or n-type (phosphorous-doped). 8-Nonyl-1-ol (97 %, Biosynth Carbosynth) and 4-pentyn-1-ol (97 %, Sigma–Aldrich) used for monolayer assembly were used as received. Gallium–indium eutectic (99.99 %, Sigma–Aldrich) was used to ensure ohmic contact between the back of the silicon sample and the steel AFM sample holder.

4.2.2 Surface modification

Prior to their chemical derivatization, silicon wafers were cut into 1 × 1 cm squares and rinsed sequentially with dichloromethane (DCM), isopropanol, and water. Samples were then blown dry under a stream of nitrogen and immersed for 30 min in hot Piranha solution (a 3:1 mixture (v/v) of sulfuric acid (95–97 %) and hydrogen peroxide (30 %) heated to 100 °C). The clean wafers were then rinsed with water and

H-terminated (Si–H) by immersion for 13 min in argon-saturated (99.997 %, Coregas) 40 % ammonium fluoride etching solution. The wafer polished side faced upwards during the etching. The etching process was carried out under ambient light while maintaining a gentle flow of argon over the etching bath, and periodically shaking the samples so to minimize the formation of etching pits. Few grains of ammonium sulfite (~10 mg) were added to the etching solution (~20 mL of NH_4F) as oxygen scavenger. The freshly prepared Si–H samples were then rinsed with water, DCM, blown dry under a stream of nitrogen gas, and placed inside a Petri dish. The Si–H sample's polished side was then covered with 1–2 drops of either degassed 8-nonyl-1-ol or degassed 4-pentyn-1-ol. The monolayer-forming liquid was gently contacted with a 1-mm thick, 75 mm \times 75 mm, quartz plate (GE 124, SPI Supplies) so to minimize liquid evaporation. The Petri dish was placed inside nitrogen-gas filled (>99.999 %, Coregas) acrylate reaction chamber. The reaction chamber was fitted with an UV light (Vilber, VL-215. M, 312 nm, nominal power output of 30 W) placed at a distance of approximately 200 mm from the samples. Samples were illuminated for 2 h while keeping the chamber under a positive pressure of nitrogen gas. The monolayer-functionalized samples (**S1** and **S2**, Scheme 4.1) were then rinsed with DCM, placed inside a glass reaction tube, covered with DCM, and rested at + 4 °C until analyzed.

4.2.3 Atomic force microscopy (AFM)

AFM topography, friction, and current maps were acquired simultaneously using the conductive AFM (C-AFM) mode of a Park NX10 (Park Systems Corporation, Suwon, Korea) fitted with a variable enhanced conductive (VECA) probe hand and FEMTO current amplifier (DLPCA-200). All AFM data were analyzed with the XEI software (Park Systems Corporation) unless specified otherwise. AFM tips were either non-conductive n-type silicon tips (TESPA-V2, Bruker, USA) with a nominal resonance frequency of 320 kHz and a spring constant of 42 N/m, or conductive solid platinum tips (25Pt300B, Rocky Mountain Nanotechnology, USA) with a nominal resonance frequency of 14 kHz and a spring constant of 18 N/m. Unless specified otherwise the scan size was set to 5 \times 5 μm and the scan rate to 1.0 Hz. The current routing is such that a positive sign indicates an electronic flow from the AFM tip to the silicon sample. The reported maximum current is the 99th percentile, that is, the current at sampling

points with zero-bias current output higher than 99% of the total ~65000 sampled points). To minimize edge artifacts, tip-sample friction data were acquired by scanning a $5\ \mu\text{m} \times 500\ \text{nm}$ region and subtracting the retrace (scan from right to left) friction profile from the trace (scan from left to right) friction profile, and then dividing the results by 2 to obtain a friction loop image [25]. Force-distance (F-D) measurements were used to estimate adhesion force and contact area, and by setting the maximum deflection to 2000 nN, the ramp speed to 300 nm/sec, and the ramp size to 300 nm. F-D curves were processed with OriginPro 9.0 (OriginLab Corp.) to estimate the pull-off force (the force at the lowest point of the retract trace) [58]. For each sample (3 samples of each type), F-D curves were recorded at 25 separate locations over a $5\ \mu\text{m} \times 5\ \mu\text{m}$ region, and the mean and standard deviation of the pull-off force, hence adhesion force, were obtained and used for contact area estimation. A titanium roughness test sample (part RS-12M, Bruker, USA) was used to estimate the tip radius by analyzing the experimental topography data in Gwyddion 2.59 (Czech Metrology Institute) through the blind estimation software function. The silicon-platinum contact area of each sample was estimated against the Derjaguin, Muller and Toporov (DMT) model of adhesion [36, 59, 60] covered in Appendix II. For all current-potential (I-V) measurements, a 360 nN set point was selected. The external bias was ramped between -2.0 and $2.0\ \text{V}$ at a sweep rate of $8\ \text{V/s}$. I-Vs were sampled at 25 evenly distributed sample locations across a $5 \times 5\ \mu\text{m}$ sample area. Platinum tips (25Pt300B) were used for the I-V measurements. Before each measurement the open-circuit current was manually adjusted to zero.

4.2.4 Macroscopic current-voltage (I-V) measurements with soft metal contacts

Current-voltage (I-V) measurements of silicon-monolayer-mercury junctions were conducted inside a lightproof and grounded Faraday cage, with a source-measure unit (model B2902A, Keysight) and a spherical mercury top contact controlled by a hanging electrode apparatus (HMDE WK2, Institute of Physical Chemistry, Polish Academy of Sciences). The voltage was ramped cyclically between -2.0 and $2.0\ \text{V}$ in steps of $20\ \text{mV}$. The duration of each step was of $400\ \text{ms}$, and the current signal was sampled after a $300\ \text{ms}$ delay from the potential step-up event. The bias routing is from the semiconductor to the metal, so to match the AFM settings, and two voltage

ramps were recorded for each sampling location on individually prepared and analyzed samples. A minimum of three sampling locations on each sample were analyzed. Current values were corrected by the contact area of the metal–semiconductor junction. The contact area was estimated from bright-field optical images acquired with a CCD camera (DCC1240C, Thorlabs) fitted with a 6.5× zoom (MVL6X123Z and MVL133A, Thorlabs). Silicon samples were scribed with emery paper before and after applying a small amount of gallium–indium eutectic to ensure the ohmic contact between the back of the silicon sample and a copper plate. All images were analyzed using Fiji image processing software [61], and data were analyzed and plotted using OriginPro 9.0 (OriginLab Corp.).

4.2.5 X-ray photoelectron spectroscopy (XPS)

XPS analysis of the silicon surfaces was performed on a Kratos Axis Ultra DLD (Kratos Analytical Ltd, UK) fitted with a monochromatic Al K α (1486.6 eV) radiation source operating at 225 W, and a hemispherical analyzer (165 mm radius) running in fixed analyzer transmission mode. The photoelectron take-off angle was normal to the sample, and the chamber operated at 2×10^{-8} Torr. The analysis area was $300 \times 700 \mu\text{m}$, and an internal flood gun was used to minimize sample charging. Survey spectra (accumulation of three scans) were acquired between 0 and 1100 eV, with a dwell time of 55 ms, a pass energy of 160 eV, and a step size of 0.5 eV. High-resolution scans (accumulation of 10 scans) used a pass energy of 20 eV, and a step size of either 0.05 eV (Si 2p, 95–110 eV), or 0.1 eV (C 1s, 274–298 eV) [51, 62–66]. XPS data were processed in CasaXPS (version 2.3.18) and any residual charging was corrected by applying a rigid shift to bring the main C 1s emission (C–C) to 285.0 eV.

4.3 Results and discussion

Silicon samples used here were stripped of the native oxide layer and then modified with a silicon–carbon-bound hydroxyl-terminated monolayer, as this chemistry introduces an effective surface protection against substrate oxidation (Figures 4.1–4.2) and simultaneously yields high triboelectric DC current outputs when used as the semiconductor component of a sliding Schottky diode TENG [27]. The modification of hydrogen-terminated (Si–H) Si(111) with 8-nonyl-1-ol (**S1**, Scheme 4.1) has been

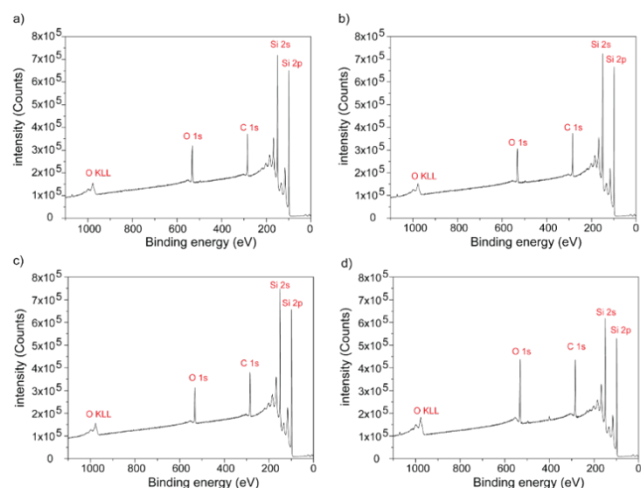


Figure 4.1. XPS survey scans of hydrogen-terminated (Si-H) samples prepared on (a) lowly doped n-type, (b) lowly doped p-type, (c) highly doped n-type, and (d) highly doped p-type Si(111) substrates that were reacted with 8-nonyl-1-ol (S1).

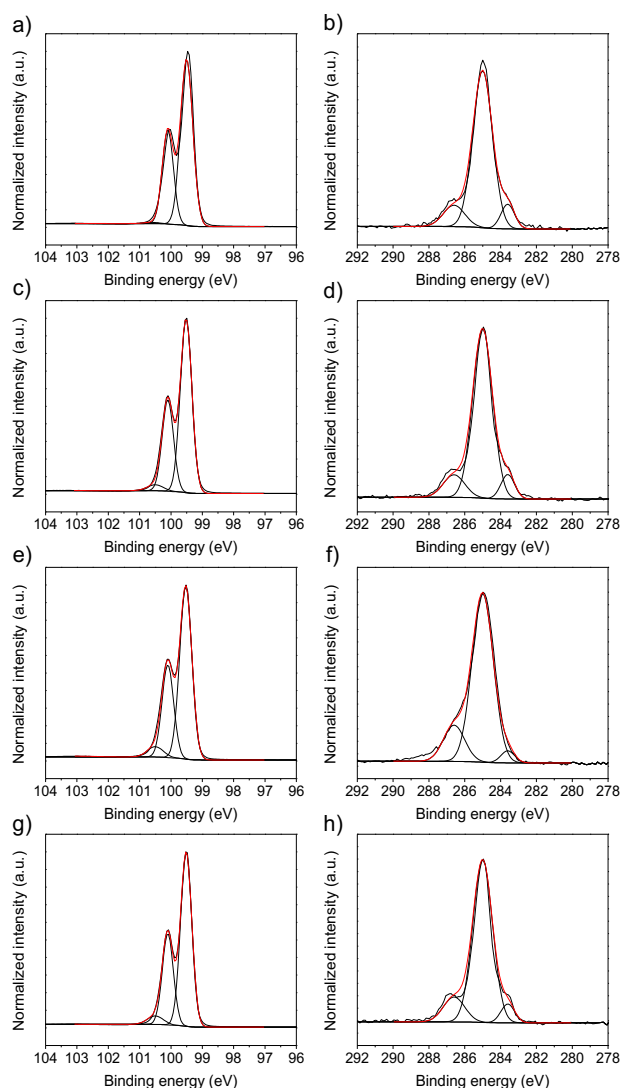


Figure 4.2. XPS narrow scans of the Si 2p (96–104 eV) and C 1s (278–292 eV) regions for hydrogen terminated samples prepared on (a–b) lowly doped n-type, (c–d) lowly doped p-type, (e–f) highly doped n-type, and (g–h) highly doped p-type Si(111) substrates and reacted with 8-nonyl-1-ol (S1).

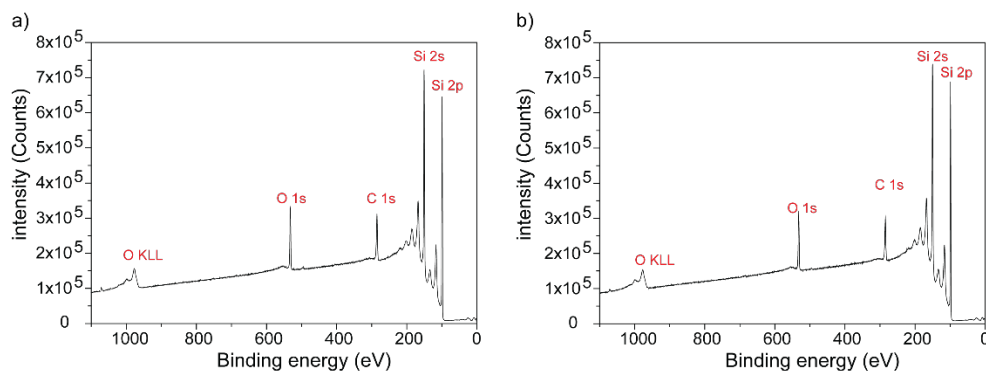


Figure 4.3. XPS survey scans of hydrogen-terminated (Si-H) samples prepared on (a) lowly doped n-type and (b) lowly doped p-type Si(111) that were reacted with 4-pentyn-1-ol (S2).

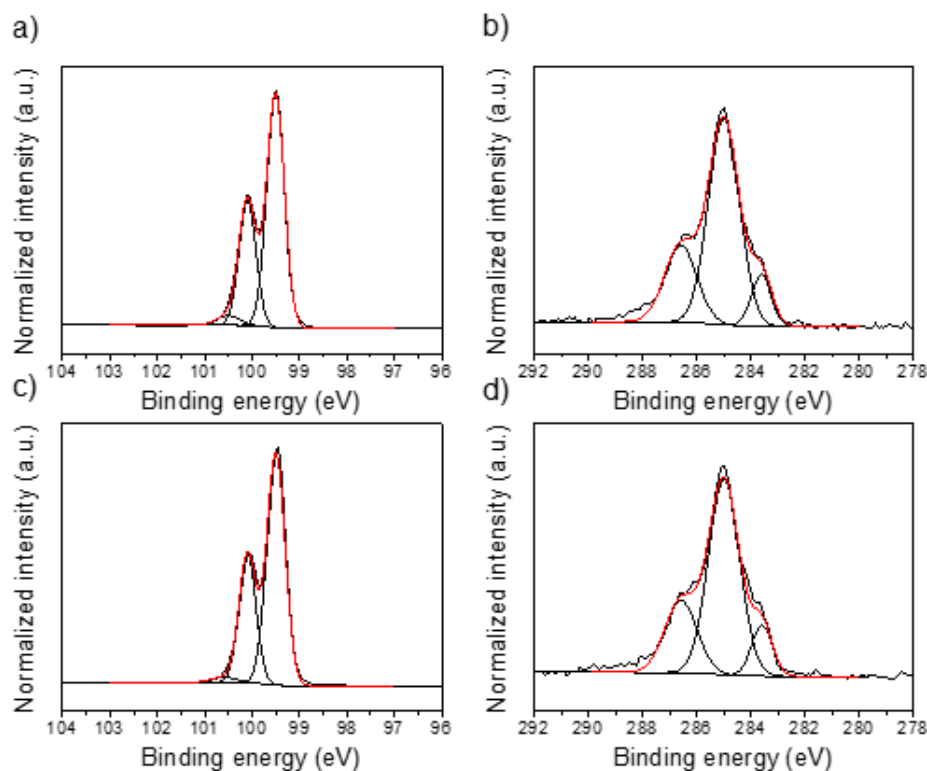


Figure 4.4. XPS narrow scans of the Si 2p (96–104 eV) and C 1s (278–292 eV) regions for hydrogen terminated samples prepared on (a–b) lowly doped n-type, (c–d) lowly doped p-type Si(111) reacted with 4-pentyn-1-ol (S2).

reported before [27], and an analogous chemical approach with a shorter alkyl chain (4-pentyn-1-ol, **2**, Scheme 4.1) was also successful in yielding an oxide-free surface (S2, Figures 4.3-4.4).

All survey scans (Figure 4.1 and 4.3) showed elemental emissions in agreement with the chemical nature of the monolayer-forming molecule and substrate. Oxygen

contaminations are ubiquitous in XPS, and most likely arising from the presence of oxygenated co-adsorbates, such as tightly bound water [63].

For analysis of the detailed spectrum (Figure 4.2 and 4.4), background subtraction (Shirley routine) and photoelectron emission fitting to Gaussian–Lorentzian (GL) functions were involved in analysis of the spectrum. Narrow scans of the Si 2p region were fitted to functions having 95% Gaussian and 5% Lorentzian character. Black thick lines are experimental XPS data, black thin traces are individual refined envelopes, and solid red traces are the sum of individual contributions. Refined contributions for the Si 2p^{3/2} and Si 2p^{1/2} spin–orbit-split emissions were centered at 99.5 eV (0.6 eV, FWHM) and 100.1 eV (0.6 eV, FWHM1) [62], respectively. The Si 2p shoulder visible at 100.6 eV (0.9 eV, FWHM) is often observed in similar monolayers and tentatively ascribed to photoelectrons emitted from Si atoms bound to hydrogen (Si–H) [51, 62]. Peaks in the range 100.8–103.7 eV are attributed to the Si¹⁺–Si⁴⁺. For each surface, three mixed Gaussian–Lorentzian (80% Gaussian, 20% Lorentzian) functions were used to fit the experimental C 1s band. These three refined components were centered at 283.6, 285.0 and 286.3 eV corresponding respectively to C–Si (silicon-bound carbons) [64], C–C (carbon-bound carbons) [66], and carbon in either a C–OH or C≡C bonding configuration for the high energy component [65].

4.3.1 Relationship between zero-bias current and friction

It is commonly accepted that in a Schottky TENG friction induces a current flow by generating electron–hole pairs [36]. Equally accepted is that current output is proportional to friction [41, 67-71]. An effective way to improve the current output therefore could be to increase friction by establishing closer contact through increasing the applied load [72]. Unfortunately such gain will come undoubtedly at the cost of reducing the lifespan of the triboelectric material [43, 73]. Hence, a detailed exploration on the relationship between current and friction is necessary, especially to understand the cause–effect relationship questioned in the introduction section. In an AFM experiment, friction and current signals can be recorded simultaneously. Given the possibility of an electronic contribution to friction [37, 42] we carried out a simple but very informative experiment with an insulating top

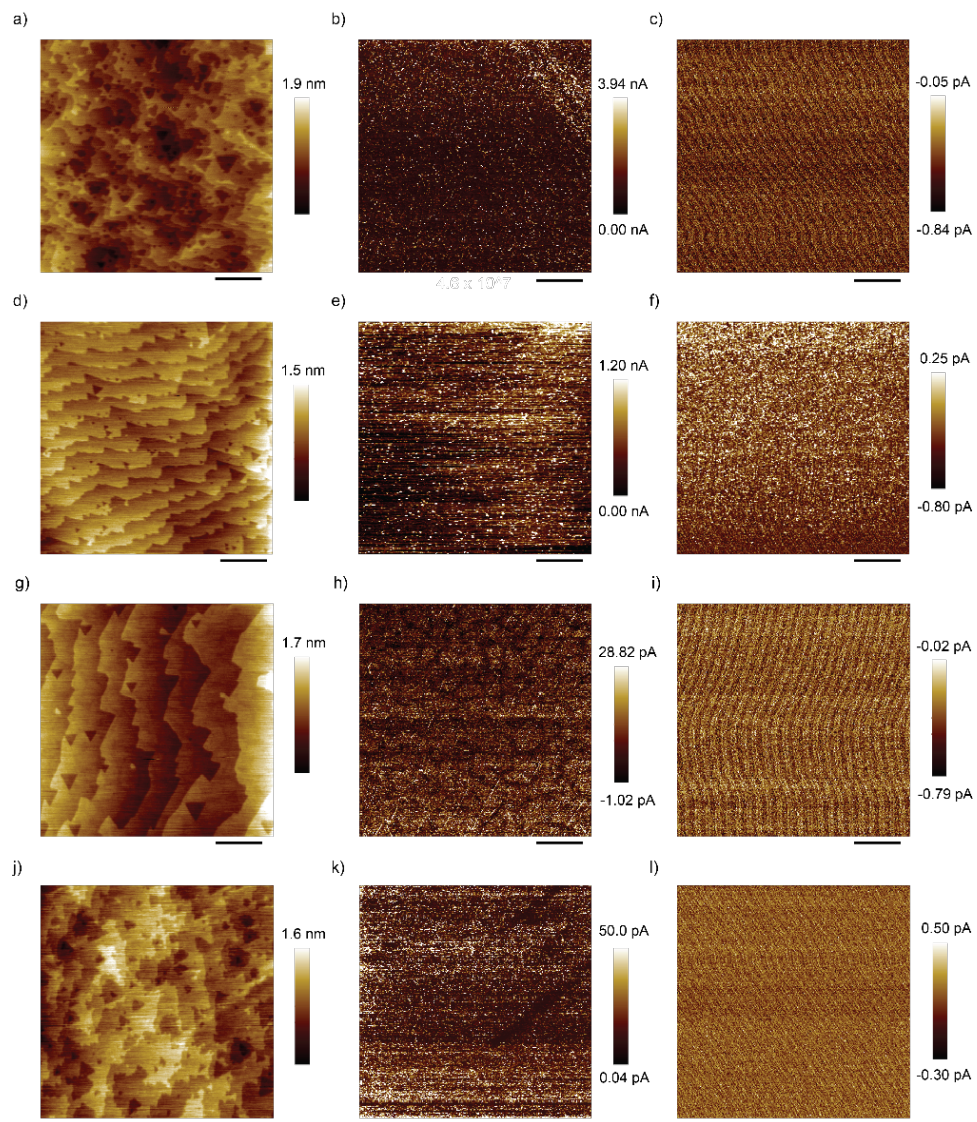


Figure 4.5. AFM height $5 \times 5 \mu\text{m}$ images of 8-nonyl-1-ol coated (**S1**) samples prepared on either lowly doped n-type (a), highly doped n-type (d), lowly doped p-type (g), or highly doped p-type (j) Si(111) substrates, and the corresponding zero-bias current C-AFM maps recorded with either conductive platinum tips (b,e,h,k) or non-conductive silicon tips (c,f,i,l). The scale bars in all panels represent $1\mu\text{m}$. The applied force was set to 360 nN.

contact (Si AFM tip) such to block the flow of DC current. The choice of a non-conductive top contact removes the possibility of an electronic drag force but obviously leaves the possibility of an electrostatics build-up and consequent attractive forces.

Figure 4.5 shows topography and current AFM maps for 8-nonyl-1-ol coated Si(111) substrates (**S1**) of different doping type and level, acquired with either conductive platinum or non-conductive silicon tips. Using sliding platinum AFM tips, the highest

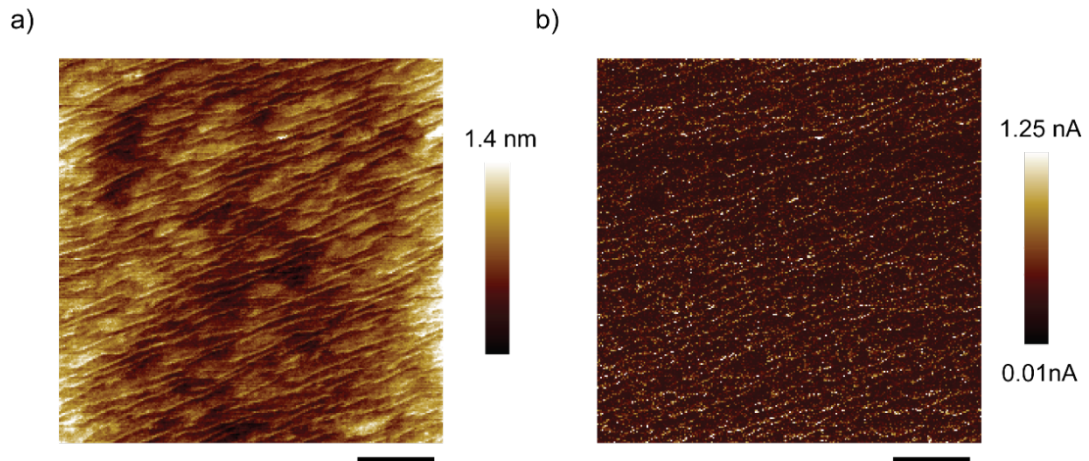


Figure 4.6. (a) AFM height $5 \times 5 \mu\text{m}$ image and (b) zero-bias current map recorded on 8-nonyl-1-ol-coated (S1) samples prepared on n-type Si(111) of intermediate doping ($0.010\text{--}0.100 \Omega \text{ cm}$). The scale bars in all panels represent $1 \mu\text{m}$. The applied force was set to 360 nN .

zero-bias DC signal was recorded on lowly doped n-type S1 Si(111) substrates (Figure 4.5b). This doping level and type had the highest output among all the different doping levels tested (Figure 4.5b, e, h, k), with the maximum current density reaching up to $4.40 \pm 0.85 \times 10^7 \text{ A/m}^2$. The current density recorded on highly-doped n-type Si(111) substrates comes as second high, with a value of $1.60 \pm 0.40 \times 10^7 \text{ A/m}^2$, followed by highly-doped p-type Si(111) with $6.45 \pm 0.31 \times 10^5 \text{ A/m}^2$, and then by lowly-doped p-type Si(111) substrates, $3.25 \pm 0.79 \times 10^5 \text{ A/m}^2$. As evident from the data in Fig. 1, the experimental zero-bias currents are of positive sign on all samples, indicating a flow of electrons from tip to sample. This is the direction of a leakage current in a n-type Si–Pt junction, but of a forward current on a p-type based junction. To further probe the relationship between doping level and zero-bias current, we also performed measurements on samples of intermediate doping (Figure 4.6). The maximum current density reached up to $1.73 \pm 0.43 \times 10^7 \text{ A/m}^2$, which is intermediate between the lowly doped and highly doped silicon substrates. We also note that higher current outputs tend to be localized at the edge of the Si(111) terraces, which are likely to expose more conductive Si(211) planes [27]. As shown in Figure 4.5c, f, i, l, current mapping of samples analyzed with non-conductive tips exhibited, as expected, only electrical noise.

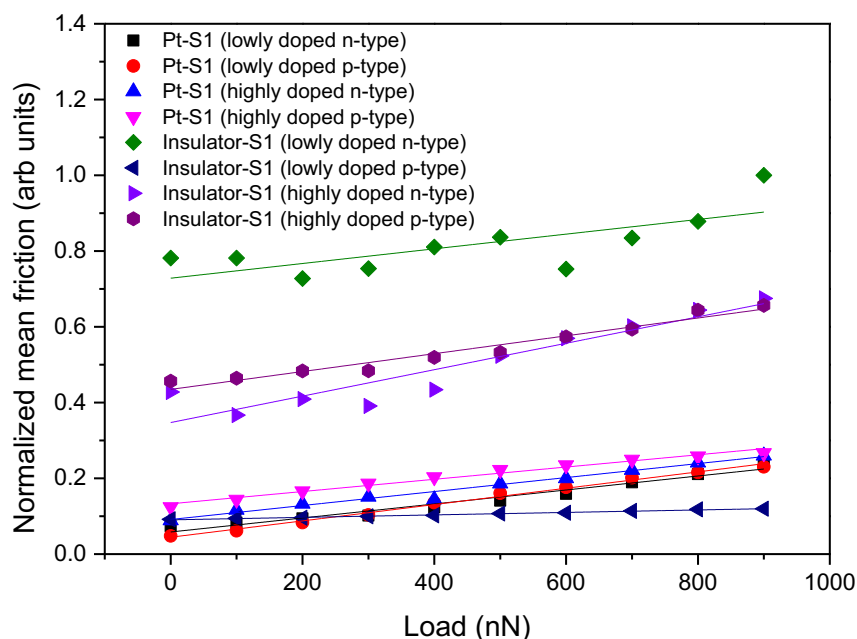


Figure 4.7. Plots of the normalized mean friction (all friction data was normalized by the maximum data recorded under different loads) measured by AFM as the function of applied normal load. Samples were 8-nonyl-1-ol coated (S1), covalently grafted on either highly doped or lowly doped, p-type or n-type, Si(111) substrates.

To qualitatively determine the samples' friction coefficients, the normalized mean experimental friction was plotted against the applied load (Figure 4.7). When using conductive tips, the friction coefficients (represented by the slope of the regression lines in Figure 4.7) of junctions made on all four substrates (S1 samples on lowly doped n-type, highly doped n-type, lowly doped p-type, and highly doped p-type) are quite similar, and the actual friction values were all of relatively low level compared to those recorded with non-conductive AFM tips. Remarkably, for the same surface chemistry, when the flow of DC current was deliberately blocked by using non-conductive tips, the friction data across the four doping types and levels varied significantly. The changes in friction observed across the four samples using non-conductive tips tracked closely the magnitude of the zero-bias current recorded with conductive tips shown in Figure 4.5b, e, h, k. The higher the sample's zero-bias current (conductive tips), the more friction was observed under open-circuit conditions (insulating tips). The current data are the first reported evidence of a difference in friction, under no external bias [37], linked to changes to the doping

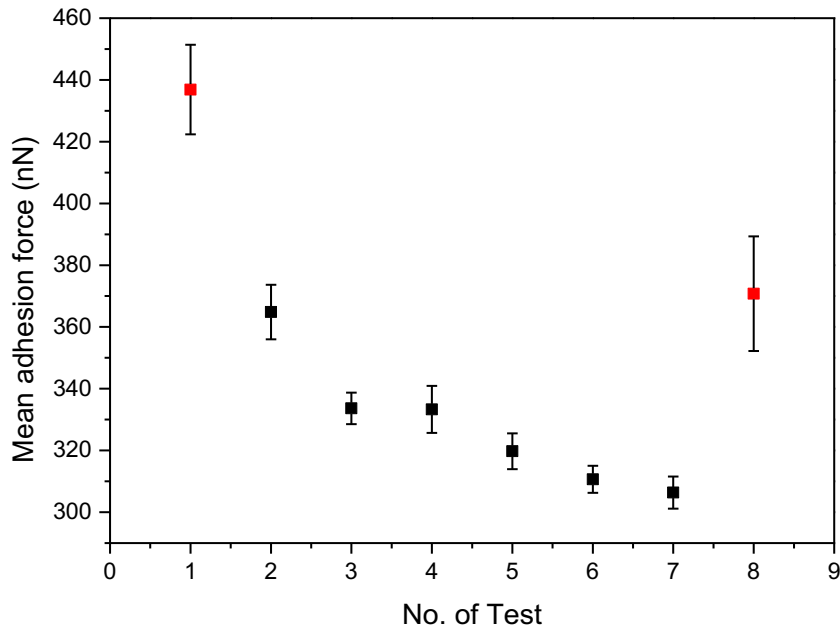


Figure 4.8. Adhesion force acquired in force–distance test using non-conductive tip (TESPA-V2) on lowly doped 1×1 cm n-type Si(111) coated with 8-nonyl-1-ol (S1). The set point was 360 nN. The UV light was supplied by a UVC LED 250–260 nm (~10 mW placed approximately 5 cm from the sample). The 1st test was acquired right after a first full image scan. All tests following the first run (from run 2 through run 7) were preceded by 20 s of UV light irradiation. One whole region scan was conducted prior to the 8th test. The 1st and 8th tests results are marked in red as they were acquired right after a full region scan (no UV illumination).

type and level of silicon, and although this difference can be tentatively ascribed to differences in surface statics, a direct evidence is unfortunately lacking. To the best of our knowledge there are no experimental evidence pointing to different propensity for silicon to gain surface static charges based on differences in bulk doping type and level – doped silicon position in the triboelectric series is unclear [74]. For some semiconductors there is an established link between the material work function and its position in the triboelectric series, but similar data are not available for silicon, and any attempt to measure the static charging of a macroscopic silicon sample with a Faraday pail lead to charge readings below the detection limit of our setup ($\sim 0.1 \text{ nC/cm}^2$). Based on the parallel between Figure 4.5 and Figure 4.7 (high friction at open circuit and TENG current) we propose that tribocurrents recorded with Pt tips are at least in part a flow of current such to neutralize static charging of the junction, and conversely that increase in friction, when the current cannot flow

because of the insulating character of the tip, is a lateral tilt of the tip caused by statics.

To further prove this last point we recorded force–distance (F–D) curves on lowly-doped n-type Si(111) surfaces coated with 8-nonyl-1-ol by (**S1**) under UV light (250–260 nm), so to use the UV-mediated ionization of air to gradually eliminate surface static charges [75, 76]. Figure 4.8 shows the adhesion force between the lowly doped **S1** sample and a non-conductive tip. All the reported adhesion forces are the mean value of 100 measurements at spots evenly distributed across the imaging region shown in Fig. 4.5a. UV light was initially kept off, and a first set of F–D measurements (1st test) performed, which returned a surface adhesion force of 436.88 ± 14.52 nN. The UV light was then switched on for 20 s, causing surface adhesion to drop significantly (364.83 ± 8.84 nN, 2nd test). The adhesion force kept decreasing with increasing UV exposure times (2nd to 6th test). After six 20-s cycles of UV illumination the surface adhesion force reached a plateau of 306.36 ± 5.21 nN. Finally, to further verify that the sliding diode motion causes statics we conducted F–D measurements again after another whole region scan (8th test). The adhesion force returned back to 370.77 ± 18.58 nN, which is ~ 6 nN higher than the 2nd test results (1st UV cycle). These results indicate that surface statics is established upon tip sliding over the sample, but these charges are nearly completely (but not entirely) neutralized by ionized species formed upon UV illumination. Electrostatic charging, which at least in its sign appears to be independent of the silicon doping level and type, is therefore a clear contributor to the DC tribocurrent measured with Pt tips, although, as stated above, when measured with Pt tips, any sizable difference in friction between samples disappears.

Another interesting finding from the above section is that regardless of the silicon substrate doping type, the zero-bias current (Figure 4.5b, e, h, k) have the same direction: from semiconductor to metal. One reason could be Fermi level pinning caused by the introduction of the large number of surface states on the 8-nonyl-1-ol coated Si surfaces [27, 77]. Contributing to these surface states could be deprotonation of the monolayer terminal functional group (R–OH) to alkoxide anion (R–O⁻) [78-80]. Another reason for the sign of the tribocurrent not varying with the

doping type of the substrate could be a flexoelectric band bending and ratcheting mechanism [81] is present and leads to flexovoltage independent of the doping type.

4.3.2 Carbon chain length and tribocurrent

Following from the conclusion of the previous section, we then tried to answer the question on the role of surface alkoxide anions, which in part resembles a question first raised by Wang and co-workers in 2016 [34], that is whether or not the length a molecular carbon chain influences the zero-bias current in a sliding metal–monolayer–semiconductor TENG system. Since we propose that the alkoxide anion ($R-O^-$) has an effect on the silicon band bending, given that the electrostatic force is inversely proportional to the square of the distance [82], such effect should be maximised if the length of the dielectric barrier (the carbonaceous monolayer) between semiconductor and the anion is shortened. To address this we conducted

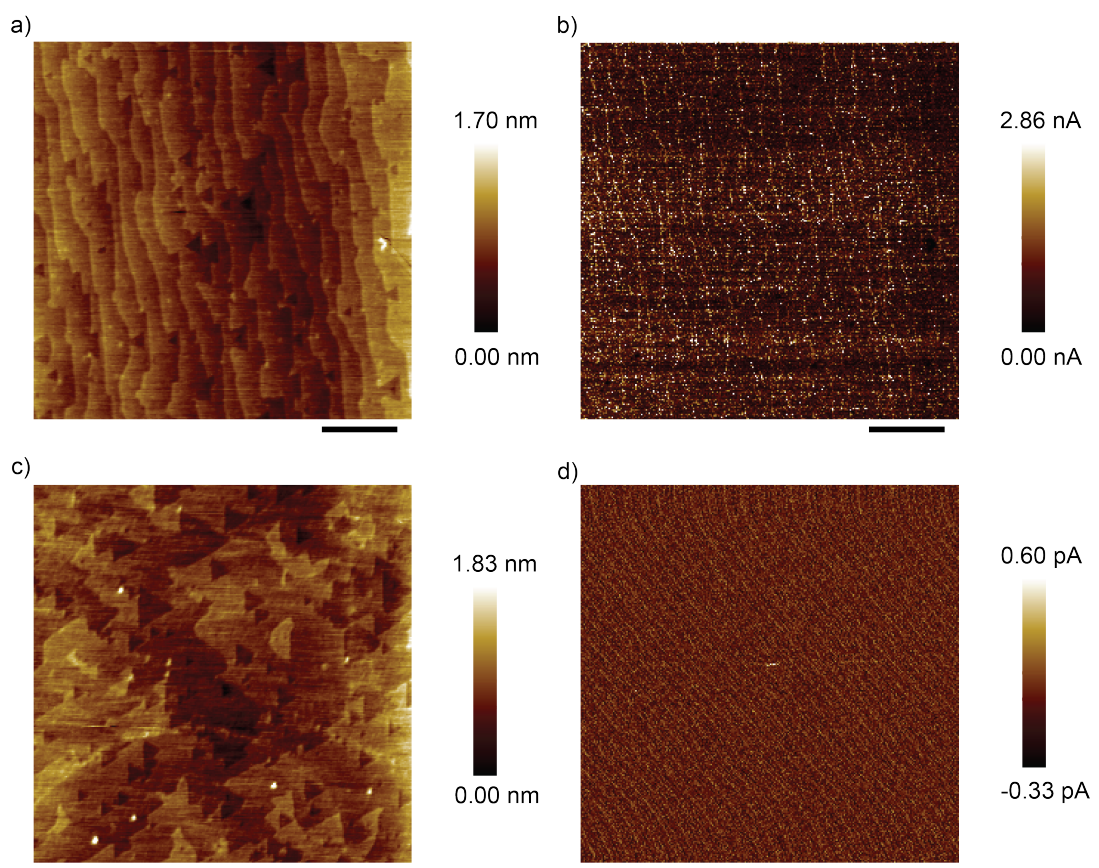


Figure 4.9. AFM topography images and zero-bias current maps recorded on on 4-pentyn-1-ol functionalized (a-b) lowly doped n-type or (c-d) lowly doped p-type Si(111) surfaces (S2 samples). All images are obtained using platinum tip (25Pt300B). The scale bars in panels (a,c) represents 1 μm.

experiments analogous to those reported in the previous section (**S1**) but with a shorter monolayer, 4-pentyn-1-ol monolayer (**S2**, Scheme 4.1). Figure 4.9 shows AFM height images and zero-bias current maps obtained on **S2** samples prepared on lowly doped n- and p-type Si(111). Negatively charged siloxyl groups from silica (oxidized Si(111)) could be a source of electrical traps and dipoles competing with the monolayer charges, but no significant signs of semiconductor oxidation, usually detectable as rounded topographical features [52, 83, 84], were found in the AFM height images (Figure 4.9a,c). XPS data in Figure 4.4 also show no evidence of oxidation. For lowly doped p-type Si(111) **S2** samples (Figure 4.9d), the current signal did not raise above noise level. However, the maximum zero-bias current density on modified lowly doped n-type Si(111) surface (Figure 4.9b) was 3.11×10^7 A/m², which is comparable to the output of for the longer chain samples (**S1**, 4.40×10^7 A/m², Figure 4.5b). It appears therefore that the band bending caused by alkoxide anions (R–O[−]) is independent of the length of the dielectric barrier separating molecular charge and semiconductor, or that another factor dominates the zero-bias output. As investigated in the next section, one of such factors could be flexoelectricity, which is not friction-related, but pressure-related.

4.3.3 Flexovoltage in static junctions

According to the tabulated work function difference between platinum and n-type silicon it is expected that for a “static” Schottky diode a current–voltage (I–V) curve should resemble, qualitatively, the one shown in Figure 4.10a, with a reverse bias region in the positive quadrant. For 4-pentyn-1-ol and 8-nonyl-1-ol coated surfaces (Figure 4.10b, c), the difference in current density magnitude, regardless of the bias polarity, is likely to reflect the difference in the carbonaceous tunneling barrier [85, 86]. More interestingly, for both surface chemistries (4-pentyn-1-ol and 8-nonyl-1-ol, **S2** and **S1**) a blocking regime typical of a diode under external reverse bias (positive semiconductor bias for n-type silicon) is happening under negative semiconductor bias, and vice-versa, a rapidly increasing current was found under positive semiconductor bias. To the best of our knowledge a similar “diode inversion” was only observed by Duan and co-workers for transferred and evaporated platinum based Schottky diodes [87], but our system is under a definitely greater junction

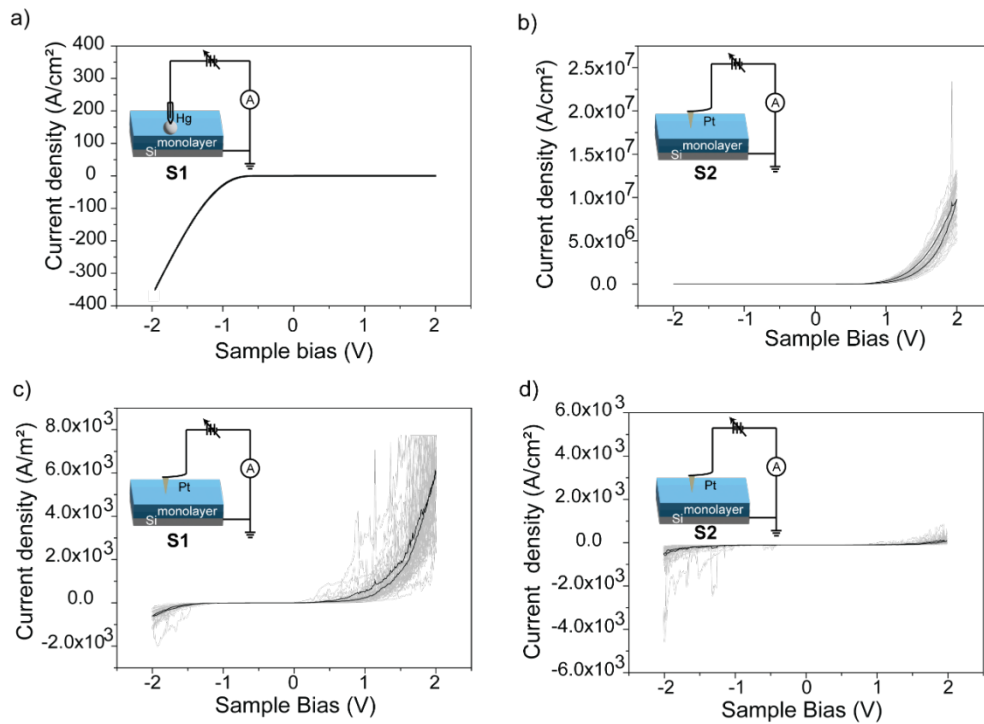


Figure 4.10. (a) Current-voltage (I–V) curve obtained with a macroscopic soft contact (mercury drop, estimated pressure of ~ 30 Pa) on 8-nonyl-1-ol modified Si(111) surface (S1). Experimental current–voltage (I–V) spectroscopy on (b) 4-pentyn-1-ol (S2) and on (c) 8-nonyl-1-ol (S1) functionalized lowly doped n-type Si(111) surfaces, and current-voltage (I–V) spectroscopy on (d) 4-pentyn-1-ol (S2) functionalized lowly doped p-type Si(111) surfaces recorded using platinum tips (C-AFM) under an estimated contact pressure of ~ 5 GPa. The black thick lines in panel b–d represent the mean value of the 25 individual I–V curves plotted in grey ink. The vertical axis range are chosen to more clearly show the rectification characteristics of each I–V curve.

pressure (~ 5 GPa), and, as such, an explanation suitable for a van der Waals diode is unlikely to be applicable here. As shown in Figure 4.10a, with a soft top contact (a mercury drop), the semiconductor is under a relatively low pressure of only ~ 30 Pa, while in the “inverted” junctions (platinum C-AFM tip, Figure 4.10b, c) the silicon is sensing around ~ 5 GPa. It is then important to verify whether or not such phenomenon (the inversion of the diode rectification direction) is also found on surfaces that yields no tribocurrent output. Static I–V measurements conducted on 4-pentyn-1-ol (S2) functionalized lowly doped p-type Si(111) surfaces (a poor TENG performer) are shown in Figure 4.10d. The normal behaviour of such junction would be that of allowing current to pass in the positive quadrant. This is indeed the case, but a current of similar, or even greater, magnitude is also seen in the negative quadrant. It is therefore probable that the flexovoltage has the direction of a reverse

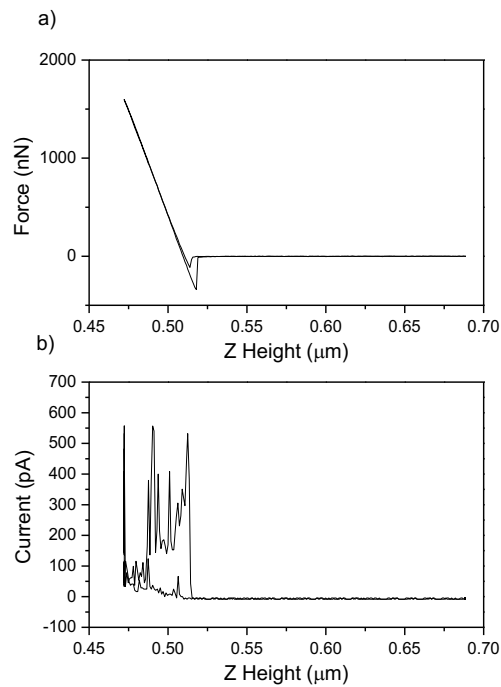


Figure 4.11. (a) A representative force–distance (F–D) curve and the corresponding (b) high-speed capture current profile. Data recorded under zero-bias on 8-nonyl-1-ol functionalized low-doped n-type Si(111) surfaces.

bias. Such pressure-induced voltage will therefore oppose the interfacial voltage due to static charges friction-induced, (Figure 4.7), ultimately causing p-type surfaces to be poorer TENG performers (Figure 4.9). In conclusion, contact pressure plays an important role that is just not causing larger friction, as the inverted I–Vs shown in Figure 4.10 were obtained when the tip is not sliding laterally. We believe that the explanation lies in the recently reported flexoelectricity under external load [88]. Under this hypothesis, external pressure would generate a flexovoltage that overwrites the instrument (external) bias, and the experimental inverted I–Vs suggest that the flexovoltage has the direction of a reverse bias. Reinforcing our interpretation of the data as the conclusions of Sun et al., who observed that current under bias could be increased by applying force on silicon based Schottky diodes [40]. Hence, we believe that the inverted diode behaviour is the result of flexoelectricity under high pressure. This is evident under static conditions (Figure 4.10), but it is most probably also present under dynamic (sliding) conditions. To further verify the

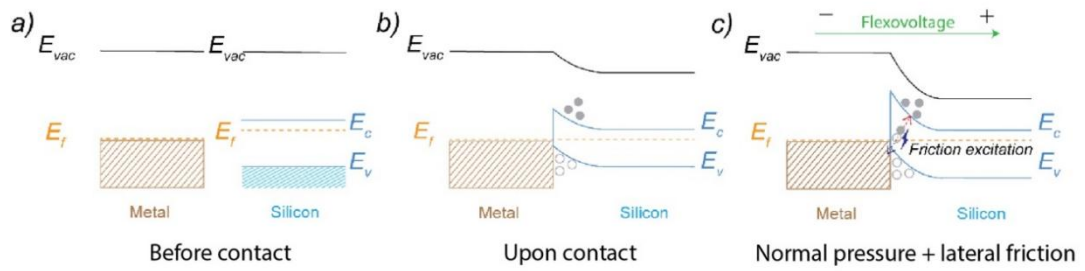


Figure 4.12. Band diagram for a Schottky junction made by a platinum AFM tip and n-type silicon substrate (monolayer-modified, details in Scheme 4.1) (a) before contact, (b) after contact, and (c) during sliding experiments under a large normal load. During the sliding process, the friction induced electron–hole pairs are separated by the junction in-built electric field, which leads to a DC current having the direction of leakage current (reverse bias current). Under high contact pressure there is also a flexovoltage which promotes the movement of electrons from metal to tip. E_{vac} , E_f , E_c , and E_v indicate the vacuum energy level, the Fermi level, the bottom of the conduction band, and the top of the valence band, respectively. The convention is such that the energy of an electron decreases as it moves towards the bottom of the diagram.

onset of flexoelectricity we recorded the current signal while conducting F–D measurements (i.e. with no deliberate lateral movement of the junction). The result of these controls are shown in Figure 4.11 and revealed a progressive increase in a positive sign current (from platinum to silicon) as the tip is forced against the silicon substrate under no external bias. Similarly to anomalous photovoltaic-to-micromechanics coupling effects in multiferroic materials [89], during the sliding process charge carriers are collected effectively by the tip and lead to a net leakage current. We believe that DC output is the result of both tribovoltage and flexovoltage effects (Figure 4.12). The Schottky diode formed by the platinum tip and silicon has a built-in voltage due to differences in work functions. During the sliding process, electron–hole pairs induced by friction are separated by the junction’s built-in electric field, in agreement with the output having the sign of a leakage current. In addition, there is the onset of a flexovoltage under high contact pressure. This pressure (or pressure-fluctuations) induced voltage manifests as an electric field that accelerates electrons in the same direction as in response to the tribovoltage (from tip to silicon).

4.4 Conclusion

We have explored the connections between zero-bias current and friction, and between current and pressure in metal–monolayer–silicon Schottky diodes (dynamic and static junctions). We bring clear evidence that beside probable friction-induced electron-hole pairs, static charging of the semiconductor is a major contributor to the DC output of a sliding Schottky TENG. Friction excess is readily measurable in junctions where the current flow is prevented, it is substrate doping and type-dependent and it strongly correlates with the DC output when the current is allowed to flow under zero external bias. This excess friction is however not measurable when current flows in the TENG, and exposure of the junction to conditions that remove surface statics (UV exposure) removes the excess friction. We also show that under pressures typical of an AFM experiment there is a significant flexovoltage even when the tip is not sliding. This flexovoltage is large in systems that are good TENG performers. It can be easily detected as “inverted” diode current–voltage (I – V) characteristics, suggesting that simple and readily accessible static AFM I – V is an ideal research tool in the search and screening for optimal Schottky TENG materials. Further development of DC-TENGs will benefit from an improved understanding of flexoelectricity, and materials with larger flexovoltages may represent a viable path to TENGs with a smaller reliance on friction, hence intrinsically less prone to degradation of performances under prolonged operation.

4.5 References

- [1] Kahn, F. J., The digital revolution in electronic projection display technology. SID International Symposium Digest of technical papers 31 (2000) 302–305. <http://doi.org/10.1889/1.1832943>
- [2] Reamer, F. G., The digital and electronic revolution in social work: rethinking the meaning of ethical practice. Ethics and social welfare 7 (2013) 2–19. <http://doi.org/10.1080/17496535.2012.738694>
- [3] Niu, S.; Wang, Z. L., Theoretical systems of triboelectric nanogenerators. Nano Energy 14 (2015) 161–192. <http://doi.org/10.1016/j.nanoen.2014.11.034>
- [4] Lai, Y. C.; Deng, J.; Zhang, S. L.; Niu, S.; Guo, H.; Wang, Z. L., Single-thread-based wearable and highly stretchable triboelectric nanogenerators and their applications in cloth-based self-powered human-interactive and biomedical sensing. Adv. Funct. Mater. 27 (2017) 1604462. <http://doi.org/10.1002/adfm.201604462>
- [5] Lin, Z.; Yang, J.; Li, X.; Wu, Y.; Wei, W.; Liu, J.; Chen, J.; Yang, J., Large-scale and washable smart textiles based on triboelectric nanogenerator arrays for self-powered sleeping monitoring. Adv. Funct. Mater. 28 (2018) 1704112. <http://doi.org/10.1002/adfm.201704112>
- [6] Wang, X.; Song, J.; Liu, J.; Zhong, L. W., Direct-current nanogenerator driven by ultrasonic waves. Science. 316 (2007) 102–105. <http://doi.org/10.1126/science.1139366>
- [7] Salauddin, M.; Toyabur, R. M.; Maharjan, P.; Rasel, M. S.; Kim, J. W.; Cho, H.; Park, J. Y., Miniaturized springless hybrid nanogenerator for powering portable and wearable electronic devices from human-body-induced vibration. Nano Energy 51 (2018) 61–72. <http://doi.org/10.1016/j.nanoen.2018.06.042>
- [8] Liang, Y.; Zhao, C. Z.; Yuan, H.; Chen, Y.; Zhang, W.; Huang, J. Q.; Yu, D.; Liu, Y.; Titirici, M. M.; Chueh, Y. L.; Yu, H.; Zhang, Q., A review of rechargeable batteries for portable electronic devices. InfoMat 1 (2019) 6–32. <http://doi.org/10.1002/inf2.12000>
- [9] Wu, C.; Wang, A. C.; Ding, W.; Guo, H.; Wang, Z. L., Triboelectric nanogenerator: A foundation of the energy for the new era. Adv. Energy Mater. 9 (2019) 1802906. <http://doi.org/10.1002/aenm.201802906>
- [10] Wang, Z. L. a., *Triboelectric nanogenerators*. 1st ed. 2016.. ed.; Cham : Springer International Publishing : Imprint: Springer: 2016.
- [11] Wang, Z. L., Triboelectric nanogenerators as new energy technology for self-powered systems and as active mechanical and chemical sensors. ACS Nano. 7 (2013) 9533–9557. <http://doi.org/10.1021/nn404614z>
- [12] Zi, Y.; Guo, H.; Wen, Z.; Yeh, M.-H.; Hu, C.; Wang, Z. L., Harvesting low-frequency (<5 Hz) irregular mechanical energy: a possible killer application of triboelectric nanogenerator. ACS Nano. 10 (2016) 4797–4805. <http://doi.org/10.1021/acsnano.6b01569>
- [13] Seol, M.-L.; Woo, J.-H.; Jeon, S.-B.; Kim, D.; Park, S.-J.; Hur, J.; Choi, Y.-K., Vertically stacked thin triboelectric nanogenerator for wind energy harvesting. Nano Energy 14 (2015) 201–208. <http://doi.org/10.1016/j.nanoen.2014.11.016>
- [14] Lee, J. H.; Kim, S.; Kim, T. Y.; Khan, U.; Kim, S.-W., Water droplet-driven triboelectric nanogenerator with superhydrophobic surfaces. Nano Energy 58 (2019) 579–584. <http://doi.org/10.1016/j.nanoen.2019.01.078>

- [15] Lin, S.; Chen, X.; Wang, Z. L., The tribovoltaic effect and electron transfer at a liquid-semiconductor interface. *Nano Energy* 76 (2020) 105070. <http://doi.org/10.1016/j.nanoen.2020.105070>
- [16] Liu, L.; Zhao, Z.; Li, Y.; Li, X.; Liu, D.; Li, S.; Gao, Y.; Zhou, L.; Wang, J.; Wang, Z. L., Achieving ultrahigh effective surface charge density of direct-current triboelectric nanogenerator in high humidity. *Small* (2022) e2201402. <http://doi.org/10.1002/sml.202201402>
- [17] Xu, R.; Zhang, Q.; Wang, J. Y.; Liu, D.; Wang, J.; Wang, Z. L., Direct current triboelectric cell by sliding an n-type semiconductor on a p-type semiconductor. *Nano Energy* 66 (2019) 104185. <http://doi.org/10.1016/j.nanoen.2019.104185>
- [18] Liu, J.; Goswami, A.; Jiang, K. R.; Khan, F.; Kim, S.; McGee, R.; Li, Z.; Hu, Z. Y.; Lee, J.; Thundat, T., Direct-current triboelectricity generation by a sliding Schottky nanocontact on MoS₂ multilayers. *Nat. Nanotechnol.* 13 (2018) 112–116. <http://doi.org/10.1038/s41565-017-0019-5>
- [19] Lin, S.; Lu, Y.; Feng, S.; Hao, Z.; Yan, Y., A high current density direct-current generator based on a moving van der Waals Schottky diode. *Adv. Mater.* 31 (2018) 1804398. <http://doi.org/10.1002/adma.201804398>
- [20] You, Z.; Wang, S.; Li, Z.; Zou, Y.; Lu, T.; Wang, F.; Hu, B.; Wang, X.; Li, L.; Fang, W.; Liu, Y., High current output direct-current triboelectric nanogenerator based on organic semiconductor heterojunction. *Nano Energy* 91 (2022) 106667. <http://doi.org/10.1016/j.nanoen.2021.106667>
- [21] Yang, R.; Benner, M.; Guo, Z.; Zhou, C.; Liu, J., High-performance flexible Schottky DC generator via metal/conducting polymer sliding contacts. *Adv. Funct. Mater.* 31 (2021) 2103132. <http://doi.org/10.1002/adfm.202103132>
- [22] Chen, S.; Liu, D.; Zhou, L.; Li, S.; Zhao, Z.; Cui, S.; Gao, Y.; Li, Y.; Wang, Z. L.; Wang, J., Improved output performance of direct-current triboelectric nanogenerator through field enhancing breakdown effect. *Adv. Mater. Technol.* 6 (2021) 2100195. <http://doi.org/10.1002/admt.202100195>
- [23] Lu, Y.; Gao, Q.; Yu, X.; Zheng, H.; Shen, R.; Hao, Z.; Yan, Y.; Zhang, P.; Wen, Y.; Yang, G.; Lin, S., Interfacial built-in electric field-driven direct current generator based on dynamic silicon homojunction. *Research* 2020 (2020) 5714754. <http://doi.org/10.34133/2020/5714754>
- [24] Huang, X.; Xiang, X.; Nie, J.; Peng, D.; Yang, F.; Wu, Z.; Jiang, H.; Xu, Z.; Zheng, Q., Microscale Schottky superlubric generator with high direct-current density and ultralong life. *Nat. Commun.* 12 (2021) 2268. <http://doi.org/10.1038/s41467-021-22371-1>
- [25] Ferrie, S.; Le Brun, A. P.; Krishnan, G.; Andersson, G. G.; Darwish, N.; Ciampi, S., Sliding silicon-based Schottky diodes: maximizing triboelectricity with surface chemistry. *Nano Energy* 93 (2022) 106861. <http://doi.org/10.1016/j.nanoen.2021.106861>
- [26] Ferrie, S.; Darwish, N.; Gooding, J. J.; Ciampi, S., Harnessing silicon facet-dependent conductivity to enhance the direct-current produced by a sliding Schottky diode triboelectric nanogenerator. *Nano Energy* 78 (2020) 105210. <http://doi.org/10.1016/j.nanoen.2020.105210>
- [27] Lyu, X.; Ferrie, S.; Pivrikas, A.; MacGregor, M.; Ciampi, S., Sliding Schottky diode triboelectric nanogenerators with current output of 10⁹A/m² by molecular

- engineering of Si(211) surfaces. *Nano Energy* (2022) 107658. <http://doi.org/10.1016/j.nanoen.2022.107658>
- [28] Xu, C.; Yu, J.; Huo, Z.; Wang, Y.; Sun, Q.; Wang, Z. L., Pursuing the tribovoltaic effect for direct-current triboelectric nanogenerators. *Energy Environ. Sci.* 16 (2023) 983–1006. <http://doi.org/10.1039/d2ee04019k>
- [29] Yang, R.; Xu, R.; Dou, W.; Benner, M.; Zhang, Q.; Liu, J., Semiconductor-based dynamic heterojunctions as an emerging strategy for high direct-current mechanical energy harvesting. *Nano Energy* 83 (2021) 105849. <http://doi.org/10.1016/j.nanoen.2021.105849>
- [30] Lyu, X.; Ciampi, S., Improving the performances of direct-current triboelectric nanogenerators with surface chemistry. *Curr. Opin. Colloid Interface Sci.* 61 (2022). <http://doi.org/10.1016/j.cocis.2022.101627>
- [31] Sharov, V. A.; Alekseev, P. A.; Borodin, B. R.; Dunaevskiy, M. S.; Reznik, R. R.; Cirlin, G. E., InP/Si heterostructure for high-current hybrid triboelectric/photovoltaic generation. *ACS Appl. Energy Mater.* 2 (2019) 4395–4401. <http://doi.org/10.1021/acsaem.9b00576>
- [32] Hurtado, C.; Lyu, X.; Ferrie, S.; Le Brun, A. P.; MacGregor, M.; Ciampi, S., Organic monolayers on Si(211) for triboelectricity generation: etching optimization and relationship between the electrochemistry and current output. *ACS Appl. Nano Mater.* 5 (2022) 14263–14274. <http://doi.org/10.1021/acsanm.2c02006>
- [33] Xu, J.; Zou, Y.; Nashalian, A.; Chen, J., Leverage surface chemistry for high-performance triboelectric nanogenerators. *Front. Chem.* 8 (2020) 577327. <http://doi.org/10.3389/fchem.2020.577327>
- [34] Wang, S.; Zi, Y.; Zhou, Y. S.; Li, S.; Fan, F.; Lin, L.; Wang, Z. L., Molecular surface functionalization to enhance the power output of triboelectric nanogenerators. *J. Mater. Chem. A* 4 (2016) 3728–3734. <http://doi.org/10.1039/c5ta10239a>
- [35] Pan, S.; Yin, N.; Zhang, Z., Time- & Load-dependence of triboelectric effect. *Sci Rep* 8 (2018) 2470. <http://doi.org/10.1038/s41598-018-20937-6>
- [36] Park, J. Y.; Salmeron, M., Fundamental Aspects of Energy Dissipation in Friction. *Chem. Rev.* 114 (2014) 677–711. <http://doi.org/10.1021/cr200431y>
- [37] Park, J. Y.; Ogletree, D. F.; Thiel, P. A.; Salmeron, M., Electronic control of friction in silicon pn junctions. *Science* 313 (2006) 186–186. <http://doi.org/10.1126/science.1125017>
- [38] Zhang, Z.; Jiang, D.; Zhao, J.; Liu, G.; Bu, T.; Zhang, C.; Wang, Z. L., Tribovoltaic effect on metal–semiconductor interface for direct-current low-impedance triboelectric nanogenerators. *Adv. Energy Mater.* 10 (2020) 1903713. <http://doi.org/10.1002/aenm.201903713>
- [39] Mizzi, C. A.; Marks, L. D., When flexoelectricity drives triboelectricity. *Nano Lett.* 22 (2022) 3939–3945. <http://doi.org/10.1021/acs.nanolett.2c00240>
- [40] Sun, L.; Zhu, L.; Zhang, C.; Chen, W.; Wang, Z., Mechanical manipulation of silicon-based Schottky diodes via flexoelectricity. *Nano Energy* 83 (2021) 105855. <http://doi.org/10.1016/j.nanoen.2021.105855>
- [41] Liu, J.; Jiang, K.; Nguyen, L.; Li, Z.; Thundat, T., Interfacial friction-induced electronic excitation mechanism for tribo-tunneling current generation. *Mater. Horiz.* 6 (2019) 1020–1026. <http://doi.org/10.1039/c8mh01259h>

- [42] Qi, Y. B.; Park, J. Y.; Hendriksen, B. L. M.; Ogletree, D. F.; Salmeron, M., Electronic contribution to friction on GaAs: An atomic force microscope study. *Phys. Rev. B* 77 (2008). <http://doi.org/10.1103/PhysRevB.77.184105>
- [43] Chen, P.; An, J.; Shu, S.; Cheng, R.; Nie, J.; Jiang, T.; Wang, Z. L., Super-durable, low-wear, and high-performance fur-brush triboelectric nanogenerator for wind and water energy harvesting for smart agriculture. *Adv. Energy Mater.* 11 (2021) 2003066. <http://doi.org/10.1002/aenm.202003066>
- [44] Spikes, H. A., Triboelectrochemistry: influence of applied electrical potentials on friction and wear of lubricated contacts. *Tribol. Lett.* 68 (2020). <http://doi.org/10.1007/s11249-020-01328-3>
- [45] Liu, J.; Miao, M.; Jiang, K.; Khan, F.; Goswami, A.; McGee, R.; Li, Z.; Nguyen, L.; Hu, Z.; Lee, J.; Cadien, K.; Thundat, T., Sustained electron tunneling at unbiased metal-insulator-semiconductor triboelectric contacts. *Nano Energy* 48 (2018) 320–326. <http://doi.org/10.1016/j.nanoen.2018.03.068>
- [46] Dong, Y., Effects of substrate roughness and electron–phonon coupling on thickness-dependent friction of graphene. *J. Phys. D: Appl. Phys.* 47 (2014) 055305. <http://doi.org/10.1088/0022-3727/47/5/055305>
- [47] Park, J. Y.; Qi, Y.; Ogletree, D. F.; Thiel, P. A.; Salmeron, M., Influence of carrier density on the friction properties of siliconpnjunctions. *Phys. Rev. B: Condens. Matter Mater. Phys.* 76 (2007). <http://doi.org/10.1103/PhysRevB.76.064108>
- [48] Linford, M. R.; Chidsey, C. E. D., Alkyl monolayers covalently bonded to silicon surfaces. *J. Am. Chem. Soc.* 115 (1993) 12631–12632. <http://doi.org/10.1021/ja00079a071>
- [49] Linford, M. R.; Fenter, P.; Eisenberger, P. M.; Chidsey, C. E. D., Alkyl monolayers on silicon prepared from 1-alkenes and hydrogen-terminated silicon. *J. Am. Chem. Soc.* 117 (1995) 3145–3155. <http://doi.org/10.1021/ja00116a019>
- [50] Zhang, S.; Ferrie, S.; Lyu, X.; Xia, Y.; Darwish, N.; Wang, Z.; Ciampi, S., Absence of a relationship between surface conductivity and electrochemical rates: redox-active monolayers on Si(211), Si(111), and Si(110). *J. Phys. Chem. C* 125 (2021) 18197–18203. <http://doi.org/10.1021/acs.jpcc.1c05023>
- [51] Zhang, S.; Ferrie, S.; Peiris, C. R.; Lyu, X.; Vogel, Y. B.; Darwish, N.; Ciampi, S., Common background signals in voltammograms of crystalline silicon electrodes are reversible silica–silicon redox chemistry at highly conductive surface sites. *J. Am. Chem. Soc.* 143 (2021) 1267–1272. <http://doi.org/10.1021/jacs.0c10713>
- [52] Vogel, Y. B.; Zhang, L.; Darwish, N.; Gonçalves, V. R.; Le Brun, A.; Gooding, J. J.; Molina, A.; Wallace, G. G.; Coote, M. L.; Gonzalez, J.; Ciampi, S., Reproducible flaws unveil electrostatic aspects of semiconductor electrochemistry. *Nat. Commun.* 8 (2017) 2066. <http://doi.org/10.1038/s41467-017-02091-1>
- [53] Zhang, L.; Laborda, E.; Darwish, N.; Noble, B. B.; Tyrell, J. H.; Pluczyk, S.; Le Brun, A. P.; Wallace, G. G.; Gonzalez, J.; Coote, M. L.; Ciampi, S., Electrochemical and electrostatic cleavage of alkoxyamines. *J. Am. Chem. Soc.* 140 (2018) 766–774. <http://doi.org/10.1021/jacs.7b11628>
- [54] Zhang, L.; Vogel, Y. B.; Noble, B. B.; Gonçalves, V. R.; Darwish, N.; Brun, A. L.; Gooding, J. J.; Wallace, G. G.; Coote, M. L.; Ciampi, S., TEMPO monolayers on Si(100) electrodes: electrostatic effects by the electrolyte and semiconductor space-charge on the electroactivity of a persistent radical. *J. Am. Chem. Soc.* 138 (2016) 9611–9619. <http://doi.org/10.1021/jacs.6b04788>

- [55] Li, S.; Nie, J.; Shi, Y.; Tao, X.; Wang, F.; Tian, J.; Lin, S.; Chen, X.; Wang, Z. L., Contributions of different functional groups to contact electrification of polymers. *Adv Mater* 32 (2020) e2001307. <http://doi.org/10.1002/adma.202001307>
- [56] Shin, S.-H.; Kwon, Y. H.; Kim, Y.-H.; Jung, J.-Y.; Lee, M. H.; Nah, J., Triboelectric charging sequence induced by surface functionalization as a method to fabricate high performance triboelectric generators. *ACS Nano*. 9 (2015) 4621–4627. <http://doi.org/10.1021/acsnano.5b01340>
- [57] Ahmed, A.; Hassan, I.; Pourrahimi, A. M.; Helal, A. S.; El-Kady, M. F.; Khassaf, H.; Kaner, R. B., Toward high-performance triboelectric nanogenerators by engineering interfaces at the nanoscale: looking into the future research roadmap. *Adv. Mater. Technol.* 5 (2020) 2000520. <http://doi.org/10.1002/admt.202000520>
- [58] Dufrêne, Y. F.; Martínez-Martín, D.; Medalsy, I.; Alsteens, D.; Müller, D. J., Multiparametric imaging of biological systems by force-distance curve-based AFM. *Nat. Methods* 10 (2013) 847–854. <http://doi.org/10.1038/nmeth.2602>
- [59] Park, J. Y.; Salmeron, M., Fundamental aspects of energy dissipation in friction. *Chem. Rev.* 114 (2014) 677–711. <http://doi.org/10.1021/cr200431y>
- [60] Hassel Ledbetter, S. K., Monocrystal elastic constants and derived properties of the cubic and the hexagonal elements. In *Handbook of elastic properties of solids, liquids and gases*, M. Levy, H. E. B., R.R. Stern, L. Furr, V. Keppens, Ed. Academic Press: San Diego, 2001; pp 97–106.
- [61] Schindelin, J.; Arganda-Carreras, I.; Frise, E.; Kaynig, V.; Longair, M.; Pietzsch, T.; Preibisch, S.; Rueden, C.; Saalfeld, S.; Schmid, B.; Tinevez, J.-Y.; White, D. J.; Hartenstein, V.; Eliceiri, K.; Tomancak, P.; Cardona, A., Fiji: An open-source platform for biological-image analysis. *Nat. Methods*. 9 (2012) 676–682. <http://doi.org/10.1038/nmeth.2019>
- [62] Cerofolini, G. F.; Galati, C.; Renna, L., Accounting for anomalous oxidation states of silicon at the Si/SiO₂ interface. *Surf. Interface Anal.* 33 (2002) 583–590. <http://doi.org/10.1002/sia.1424>
- [63] Baio, J. E.; Weidner, T.; Brison, J.; Graham, D. J.; Gamble, L. J.; Castner, D. G., Amine terminated SAMs: Investigating why oxygen is present in these films. *J. Electron Spectrosc. Relat. Phenom.* 172 (2009) 2–8. <http://doi.org/10.1016/j.elspec.2009.02.008>
- [64] Yaffe, O.; Scheres, L.; Segev, L.; Biller, A.; Ron, I.; Salomon, E.; Giesbers, M.; Kahn, A.; Kronik, L.; Zuilhof, H.; Vilan, A.; Cahen, D., Hg/Molecular monolayer–Si junctions: electrical interplay between monolayer properties and semiconductor doping density. *J. Phys. Chem. C*. 114 (2010) 10270–10279. <http://doi.org/10.1021/jp101656t>
- [65] Scheres, L.; Arafat, A.; Zuilhof, H., Self-assembly of high-quality covalently bound organic monolayers onto silicon. *Langmuir* 23 (2007) 8343–8346. <http://doi.org/10.1021/la701359k>
- [66] Wallart, X.; Henry de Villeneuve, C.; Allongue, P., Truly quantitative XPS characterization of organic monolayers on silicon: study of alkyl and alkoxy monolayers on H–Si(111). *J. Am. Chem. Soc.* 127 (2005) 7871–7878. <http://doi.org/10.1021/ja0430797>
- [67] Zheng, M.; Lin, S.; Tang, Z.; Feng, Y.; Wang, Z. L., Photovoltaic effect and tribovoltaic effect at liquid-semiconductor interface. *Nano Energy* 83 (2021) 105810. <http://doi.org/10.1016/j.nanoen.2021.105810>

- [68] Zheng, M.; Lin, S.; Xu, L.; Zhu, L.; Wang, Z. L., Scanning probing of the tribovoltaic effect at the sliding interface of two semiconductors. *Adv. Mater.* 32 (2020) e2000928. <http://doi.org/10.1002/adma.202000928>
- [69] Zhang, Z.; Wang, Z.; Chen, Y.; Feng, Y.; Dong, S.; Zhou, H.; Wang, Z. L.; Zhang, C., Semiconductor contact-electrification-dominated tribovoltaic effect for ultrahigh power generation. *Adv. Mater.* (Weinheim, Ger.) 34 (2022) e2200146. <http://doi.org/10.1002/adma.202200146>
- [70] Xu, X.; Li, J.; Tao, X.; Yan, Q.; Wu, H.; Guan, Z.; Liu, L.; Chen, X.; Ou-Yang, W., Study of interfacial design for direct-current tribovoltaic generators. *Nano Energy* 94 (2022) 106957. <http://doi.org/10.1016/j.nanoen.2022.106957>
- [71] Yang, D.; Zhang, L.; Luo, N.; Liu, Y.; Sun, W.; Peng, J.; Feng, M.; Feng, Y.; Wang, H.; Wang, D., Tribological-behaviour-controlled direct-current triboelectric nanogenerator based on the tribovoltaic effect under high contact pressure. *Nano Energy* 99 (2022) 107370. <http://doi.org/10.1016/j.nanoen.2022.107370>
- [72] Wang, W.; Yu, A.; Liu, X.; Liu, Y.; Zhang, Y.; Zhu, Y.; Lei, Y.; Jia, M.; Zhai, J.; Wang, Z. L., Large-scale fabrication of robust textile triboelectric nanogenerators. *Nano Energy* 71 (2020) 104605. <http://doi.org/10.1016/j.nanoen.2020.104605>
- [73] Lin, L.; Xie, Y.; Niu, S.; Wang, S.; Yang, P.-K.; Wang, Z. L., Robust triboelectric nanogenerator based on rolling electrification and electrostatic induction at an instantaneous energy conversion efficiency of ~55. *ACS Nano*. 9 (2015) 922–930. <http://doi.org/10.1021/nn506673x>
- [74] Zou, H.; Guo, L.; Xue, H.; Zhang, Y.; Shen, X.; Liu, X.; Wang, P.; He, X.; Dai, G.; Jiang, P.; Zheng, H.; Zhang, B.; Xu, C.; Wang, Z. L., Quantifying and understanding the triboelectric series of inorganic non-metallic materials. *Nat. Commun.* 11 (2020) 2093. <http://doi.org/10.1038/s41467-020-15926-1>
- [75] Inaba, H.; Ohmi, T.; Yoshida, T.; Okada, T., Neutralization of static electricity by soft X-rays and vacuum UV radiation. *J. Electrostat.* 33 (1994) 15–42. [http://doi.org/10.1016/0304-3886\(94\)90061-2](http://doi.org/10.1016/0304-3886(94)90061-2)
- [76] Gosho, Y.; Yamada, M.; Saeki, M., Static charge elimination of charged matter using UV lamp. *Jpn. J. Appl. Phys., Part 1* 29 (1990) 950–951. <http://doi.org/10.1143/JJAP.29.950>
- [77] Zhang, X. G., *Electrochemistry of silicon and its oxide*. Springer US: Boston, MA, 2001. <http://doi.org/10.1007/b100331>
- [78] Burgess, I.; Seivewright, B.; Lennox, R. B., Electric field driven protonation/deprotonation of self-assembled monolayers of acid-terminated thiols. *Langmuir* 22 (2006) 4420–4428. <http://doi.org/10.1021/la052767g>
- [79] Kolodner, P.; Lukashev, E. P.; Ching, Y.-C.; Rousseau, D. L., Electric-field-induced Schiff-base deprotonation in D85N mutant bacteriorhodopsin. *Proc. Natl. Acad. Sci. U. S. A.* 93 (1996) 11618–11621. <http://doi.org/10.1073/pnas.93.21.11618>
- [80] Delley, M. F.; Nichols, E. M.; Mayer, J. M., Interfacial acid–base equilibria and electric fields concurrently probed by in situ surface-enhanced infrared spectroscopy. *J. Am. Chem. Soc.* 143 (2021) 10778–10792. <http://doi.org/10.1021/jacs.1c05419>
- [81] Olson, K. P.; Mizzi, C. A.; Marks, L. D., Band bending and ratcheting explain triboelectricity in a flexoelectric contact diode. *Nano Lett.* 22 (2022) 3914–3921. <http://doi.org/10.1021/acs.nanolett.2c00107>
- [82] Halliday, D.; Resnick, R.; Walker, J., *Fundamentals of physics*. 7th, extended ed.; Wiley: Hoboken, NJ, 2005.

- [83] Li, T.; Dief, E. M.; Lyu, X.; Rahpeima, S.; Ciampi, S.; Darwish, N., Nanoscale silicon oxide reduces electron transfer kinetics of surface-bound ferrocene monolayers on dilicon. *J. Phys. Chem. C.* 125 (2021) 27763–27770. <http://doi.org/10.1021/acs.jpcc.1c07788>
- [84] Filipescu, M., Functional metal oxide thin films grown by pulsed laser deposition. IntechOpen: 2016. <http://doi.org/10.5772/62986>
- [85] Yaffe, O.; Scheres, L.; Segev, L.; Biller, A.; Ron, I.; Salomon, E.; Giesbers, M.; Kahn, A.; Kronik, L.; Zuilhof, H.; Vilan, A.; Cahen, D., Hg/Molecular Monolayer–Si Junctions: Electrical Interplay between Monolayer Properties and Semiconductor Doping Density. *J. Phys. Chem. C* 114 (2010) 10270–10279. <http://doi.org/10.1021/jp101656t>
- [86] Faber, E. J.; de Smet, L. C. P. M.; Olthuis, W.; Zuilhof, H.; Sudhölter, E. J. R.; Bergveld, P.; van den Berg, A., Si–C linked organic monolayers on crystalline silicon surfaces as alternative gate insulators. *Chemphyschem* 6 (2005) 2153–2166. <http://doi.org/10.1002/cphc.200500120>
- [87] Liu, Y.; Guo, J.; Zhu, E.; Liao, L.; Lee, S.-J.; Ding, M.; Shakir, I.; Gambin, V.; Huang, Y.; Duan, X., Approaching the Schottky-Mott limit in van der Waals metal-semiconductor junctions. *Nature* 557 (2018) 696–700. <http://doi.org/10.1038/s41586-018-0129-8>
- [88] Mizzi, C. A.; Lin, A. Y. W.; Marks, L. D., Does flexoelectricity drive triboelectricity? *Phys. Rev. Lett.* 123 (2019) 1. <http://doi.org/10.1103/PhysRevLett.123.116103>
- [89] Alexe, M.; Hesse, D., Tip-enhanced photovoltaic effects in bismuth ferrite. *Nat. Commun.* 2 (2011) 256. <http://doi.org/10.1038/ncomms1261>

Chapter 5 – Silicon-based triboelectric nanogenerators: surface chemistry isotope effects on the device performances and durability

Adapted from Lyu, X., MacGregor, Darwish, N. & Ciampi, S. Silicon-based triboelectric nanogenerators: surface chemistry isotope effects on the device performances and durability. *Friction* (Accepted). Some content from the Supporting Information file has been moved into the main text for clarity of this study. Rights are retained to reuse in the thesis by the authors. An attribution statement is included in Appendix III.

Abstract

Triboelectric nanogenerators (TENGs) are advanced devices designed to harness mechanical energy from various sources such as vibrations, friction, or shear and convert it into electrical energy. Schottky-based TENGs are a type of TENG that incorporates a semiconductor–metal barrier, known as a Schottky barrier, into their design. This barrier aids in rectifying the generated electrical output, eliminating the need for external current rectification circuits. Further, silicon-based Schottky TENGs can leverage existing surface functionalization procedures to improve device output and durability. Almost without exception, these procedures commence with an oxide-free and hydrogen-terminated silicon surface (Si–H). Replacing hydrogen with its heavier isotope deuterium (Si–D) does not hinder access to established surface chemistry procedures, and based on previous reports the isotope exchange is likely to improve resistance of the non-oxide semiconductor against its anodic decomposition. In this report we have developed the optimal surface chemistry procedures for preparing Si–D surfaces and explored to what extent this isotope effect translates into improved performances and durability of Schottky TENGs. Our findings reveal that the maximum current output of TENGs constructed on Si–D Si(111) crystals is comparable to that of mainstream Si–H devices. Additionally, we highlight a generally higher density of surface electrical defects in Si–D compared to Si–H, and verify the contribution of a flexoelectric term to the mechanical-to-electrical energy conversion mechanism. Ultimately, our experiments demonstrate that the primary advantage of replacing hydrogen with deuterium lies in enhancing device longevity.

5.1 Introduction

Triboelectric nanogenerators (TENGs) are a class of miniature power-generation devices that convert vibration into electrical energy, relying on the principles of triboelectricity, electrostatic induction and flexoelectricity [1-10]. TENGs can harvest mechanical energy from body motion [11-13], wind [14-17], fluid flow [18-20], falling rain droplets [21-23], and vibrations [24-26].

Unlike non-regenerative power sources such as batteries, TENGs are ideal for deployment in applications such as medical implants or remote sensors [27, 28], in other words, in situations where the action of replacing or recharging a battery is not straightforward. For most TENGs' designs and materials, the output is alternating current (AC-TENGs), which has to be rectified into direct current (DC) if used to power up an electronic device. Removing the rectification requirement adds therefore practical scope to TENGs, and explains the increase in research activities towards TENGs made of materials that can lead directly to DC (DC-TENGs) [3, 29-38]. Sliding diodes, such as metal–semiconductor and semiconductor–semiconductor rectifying junctions, are one of the most promising forms of DC-TENGs [4, 6, 39-45]. A comprehensive understanding of how friction, strain and/or shear result in the DC output of a sliding diode DC-TENG remain part of an open debate, but it is an established fact that the actual surface chemistry of the material making up the sliding junction can be engineered to maximise the DC-TENG output and extend its durability [4, 46].

Herein we focus on Schottky DC-TENGs made by sliding sharp metallic tips on oxide-free crystalline Si(111) surfaces. A key technical impediment to a broader adoption of this technology is the inevitable anodic decomposition, hence increase in electrical resistance, of silicon [47]. However, while oxidation of this non-oxide semiconductor is inevitable, it can be slowed down by chemical capping of the silicon surface atoms. In this context, one of the most successful chemical strategies to protect a silicon crystal from oxidation is the thermal or UV-assisted hydrosilylation reaction of 1-alkynes or 1-alkenes (monolayer-forming molecules, Si–C-bound monolayers) with hydrogen-terminated silicon (Si–H) [48-51]. As shown in Scheme 5.1, the Si–H surface can be prepared by dissolving the native silicon dioxide (SiO₂) top layer of a

commercial silicon wafer, through standard non-clean room chemistry procedures and using inexpensive fluoride-containing aqueous etching solutions, such as hydrofluoric acid (HF) or ammonium fluoride (NH_4F) [52-55]. However while hydride terminations remain the mainstream starting point for several silicon surface modification chemistries, there are alternatives to the Si-H “capping” strategy [56]. For example, Si-Cl and Si-Br can serve as the starting substrate for the formation of robust Si-C-bound monolayer [57, 58]. The choice of the etching and capping strategies are likely to be crucial to the performances of Si-based TENGs, and the reason is that the hydrosilylation step is never complete: around 50% of the Si-H atop sites remain unreacted upon the attachment of 1-alkynes [48, 59-62]. Since the hydrogen capping atom is therefore likely to be still present when the semiconductor is used as part of a Schottky TENG, it is important to gain experimental evidence on the impact, if any, of the capping agent on device output. This aspect has been to date entirely overlooked, and an obvious starting point is to explore whether or not replacing hydrogen with deuterium (Si-H vs Si-D) leads to an isotope effect on the zero-bias current output of a DC-TENG. Deuterium atoms chemisorbed on a silicon surface are harder to remove than hydrogen, and it has been suggested that deuterium-terminated silicon surfaces are less prone to oxidation than their hydrogen counterpart [63]. The surface energy of Si-D (2.67 eV) is lower than that of Si-H (3.90 eV), which suggests higher stability for the former [64, 65]. Recent research on nanoscale friction has also demonstrated lower friction on deuterium-terminated silicon surfaces compared to hydrogen-terminated ones [66]. Ganguly et al. have also observed that the light-induced drop in electrical conductivity is less marked in Si-D than in Si-H [67]. The Si-D appears therefore a very promising substrate on which to build DC-TENGs. To date a systematic comparison between Si-H and Si-D surfaces as TENG substrate is lacking, which is the purpose of this paper. We investigate isotope effects on the triboelectric performance (zero-bias electrical output) of sliding Schottky diodes made on monolayer-modified Si(111) crystals passivated by covalently grafting 8-nonyl-1-ol on either Si-D or Si-H substrates (Scheme 5.1). We explored relationships between zero-bias current and friction, nanoscale topography, flexoelectricity, static current-potential (I-V) characteristics, and transient photocurrent decays.

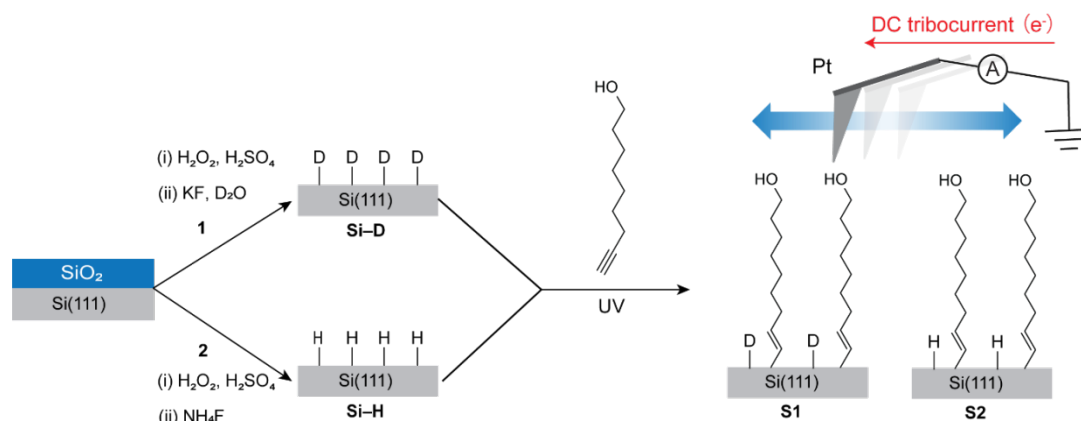
5.2 Experimental section

5.2.1. Chemicals

Hydrogen peroxide solution (MOS Puranal™, 30 wt % in water, Honeywell), sulfuric acid (VLSI Puranal™, 95–97%, Honeywell), aqueous ammonium fluoride solution (40 wt%, Sigma–Aldrich), potassium fluoride (99.0%, Sigma–Aldrich), deuterium oxide (D₂O, 99.9% atom %D, Cambridge Isotope Laboratories, Inc.), deuterated hydrochloric acid (DCI, 37%, Sigma–Aldrich), redistilled dichloromethane (DCM), deuterated DCM (CD₂Cl₂, 99.9% atom %D, Sigma–Aldrich) isopropanol and Milli-Q™ water (>18 MΩ cm) were used for silicon cleaning and etching procedures. Prime grade, single-side polished, (111)-oriented ($\pm 0.05^\circ$) silicon wafers (Siltronic, S.A.S, Archamps, France) were 475–525 μm thick, and lowly doped (7–13 Ω cm) n-type (phosphorous-doped). 8-Nonyl-1-ol (97%, Biosynth Carbosynth) used for monolayer assembly were used as received. Gallium–indium (Galn) eutectic (99.99%, Sigma–Aldrich) was used to ensure an ohmic electrical contact between the sample holder and the back of the silicon wafer.

5.2.2. Surface functionalization

Prior to surface functionalization, Si(111) wafers were cut into 1 × 1 cm squares and rinsed sequentially with DCM, isopropanol, and water. Samples were then blown dry under a nitrogen stream and cleaned by immersion for 30 min in a hot Piranha solution (a 3:1 mixture (v/v) of sulfuric acid (95–97%) and hydrogen peroxide (30%) heated at ~100 °C), followed by extensive rinsing with water. Si–D samples were prepared by immersing, under ambient light and at room temperature, the clean samples in an etching solution prepared by adding a small amount of ammonium sulfite (~10 mg) and 0.5 mL of 37% DCI to 30 mL of a KF solution (1 wt% or 10 wt%) in D₂O [68]. This procedure is based on minor modification of literature procedures [68]. The etching solution was argon-saturated (99.997%, Coregas) and during the etching the sample's polished side was facing upwards. A gentle flow of argon gas was maintained over the etching bath during the entire etching procedure. Si–H samples were prepared according to a previously published method [3, 55, 69], which is



Scheme 5.1. Surface passivation and functionalization of oxide-free n-type Si(111) substrates. Route 1. Silicon surfaces covered with a native oxide layer (SiO₂) were (i) cleaned with hot Piranha solution, and (ii) etched in potassium fluoride solutions (either 1 wt % or 10 wt % in D₂O) to form deuterium-terminated samples (Si-D). Route 2. Silicon surfaces were (i) cleaned with hot Piranha solution, and (ii) etched in ammonium fluoride solutions to prepare hydrogen-terminated samples (Si-H). Si-D and Si-H samples were then reacted with 8-nonyn-1-ol under UV light to yield **S1** and **S2** samples, respectively.

analogous to the Si-D procedure with the difference that the etching bath is deoxygenated 40% aqueous NH₄F. The freshly prepared Si-D samples were rinsed sequentially with D₂O and CD₂Cl₂, while the freshly prepared Si-H samples were rinsed sequentially with water and DCM. Both sample types were then blown dry under a nitrogen stream and placed inside a Petri dish prior to the monolayer forming step. Chemical passivation of the sample (tethering on oxide-free silicon of an organic monolayer) was performed as follows: the polished side of freshly prepared Si-D and Si-H samples was covered with 1–2 drops (~ 50 μL) of degassed 8-nonyn-1-ol. The liquid 8-nonyn-1-ol sample was then carefully contacted with a 1-mm thick, 75 × 75 mm, quartz plate (GE 124, SPI Supplies) to minimize its evaporation. The Petri dish containing the etched sample covered by the monolayer-forming liquid sample was then placed inside nitrogen-gas filled (>99.999%, Coregas) acrylate reaction chamber fitted with an UV light (312 nm, nominal power output of 30 W, VL-215.M, Vilber) located at a distance of ~200 mm from the sample. After a 2 h UV-assisted hydrosilylation reaction, samples were then rinsed with either DCM (Si-H samples) or CD₂Cl₂ (Si-D samples), transferred into a glass reaction tube, covered with either DCM (Si-H samples) or CD₂Cl₂ (Si-D samples), and rested at + 4°C until further analyzed.

5.2.3. Atomic force microscopy (AFM)

The simultaneous acquisition of topography, friction, and current maps was achieved through AFM experiments conducted in conductive mode (C-AFM) using a Park NX10 system (Park Systems Corporation, Suwon, Korea), equipped with a variable enhanced conductive (VECA) probe hand and a FEMTO current amplifier (DLPCA-200). Unless otherwise specified, all AFM data were processed and analyzed using the XEI software (Park System Corp.). The AFM tips were conductive solid platinum tips (25Pt300B, Rocky Mountain Nanotechnology, USA) with a radius <8 nm, a spring constant of 18 N/m and a nominal resonance frequency of 14 kHz. The default scan size was set to 5×5 μm and the scan rate was set to 1.0 Hz. Line scan lengths were 5 μm long. The bias routing is such that a current of positive sign indicates electrons flowing from the AFM tip to the silicon substrate.

Force–distance (F–D) spectroscopy measurements were conducted to measure the tip–silicon adhesion force, to estimate the tip–silicon contact area, and to acquire high-speed current transients across the junction. In the F–D measurements the maximum deflection was set to 2000 nN, the ramp speed to 300 nm/s, and the ramp size to 300 nm. F–D curves were analyzed using OriginPro 9.0.0 (OriginLab Corp.) in order to determine the pull-off force (the force at the lowest point of the retract trace). For each sample, 25 F–D curves at separate locations across the sample were recorded. A titanium roughness test sample (part RS-12M, Bruker, USA) was utilized to estimate the tip radius by analyzing the topography data in Gwyddion 2.59 (Czech Metrology Institute) using the blind estimation function. The silicon–platinum contact area of each junction was estimated based on the Derjaguin, Muller and Toporov (DMT) model of adhesion [70] (Section S1, Support Information). High-speed current profiles recorded during the F–D measurements were processed with OriginPro 9.0.0 (OriginLab Corp.). For the current–potential (I–V) AFM measurements the deflection set-point was set to 360 nN, and the applied bias (sample bias) was ramped from -2.0 V to 2.0 V (and then returned to -2.0 V) at a rate of 8 V/s. Prior to each measurement, the open-circuit current was manually adjusted to zero to offset the influence of instrument built-in voltage..

5.2.4. X-ray photoelectron spectroscopy

X-ray photoelectron spectroscopy (XPS) analysis of the chemically passivated silicon substrates was conducted using a Kratos Axis Ultra DLD instrument (Kratos Analytical Ltd, UK). The system was equipped with a monochromatic Al K α (1486.6 eV) radiation source operating at 225 W, and a hemispherical analyzer (165 mm radius) running in fixed analyzer transmission mode. The photoelectron take-off angle was set to normal to the silicon sample, and the chamber operated at 2×10^{-8} Torr. The analysis area was $300 \times 700 \mu\text{m}$, and an internal flood gun was used to minimize sample charging. Survey scans (accumulation of three scans) were acquired over the range of 0 to 1100 eV, with a dwell time of 55 ms, a pass energy of 160 eV, and a step size of 0.5 eV. High-resolution scans (accumulation of 10 scans) utilized a pass energy of 20 eV and a step size of either 0.05 eV (Si 2p, 90–110 eV) or 0.1 eV (C 1s, 277–300 eV). XPS data analysis was performed using CasaXPS (version 2.3.18), and any residual charging was corrected by applying a rigid shift to bring the main C 1s emission (C–C) to 285.0 eV..

5.2.5. Transient photocurrent mapping (PCM)

Time-resolved measurements of photocurrent decay (transient photocurrent mapping, PCM) were conducted using a NX10 AFM (Park Systems Corporation) equipped with a pulsed red laser (635 nm, nominal power output of 5 mW). The laser on/off timing was controlled by the PCM module attached to the SmartScanTM software, ensuring dark conditions by temporarily disabling the AFM tip feedback during the experiment. Photocurrent acquisition time was set to 20 ms, with a 4 ms period laser pulse initiated after a 3 ms delay from the start of acquisition. No external bias was applied throughout the process. The junction analyzed in the PCM experiments was formed by contacting AFM platinum tips (25Pt300B) with monolayer-coated silicon wafers, with no relative movement between them.

5.3 Results and discussion

Commercial Si(111) wafers were firstly etched to remove their native oxide (SiO₂) layer and to form deuterium- or hydrogen-terminated surfaces (Scheme 5.1, Si–D and Si–H). Si–D and Si–H samples were then reacted with a hydroxyl-terminated

monolayer-forming molecule (8-nonyl-1-ol) to protect the substrate from oxidation while retaining sufficient electrical conductivity. This monolayer surface chemistry (**S2** films) is known to yield high tribocurrent outputs when used as the frictional layer of a Si–H-based sliding Schottky diode DC-TENGs [3, 68]. XPS survey scans and narrow scans (Figures 5.1-5.3) for **S1** and **S2** samples indicate negligible substrate oxidation. However, such hydrosilylation reaction does not guarantee a full monolayer coverage, resulting in residual Si–D or Si–H sites, which cannot be detected by XPS [59-62, 69, 70]. As discussed in the introduction, deuterium-terminated Si electrodes have been suggested to be more resistant against oxidation than commonly used Si–H substrates [63, 71-73], however, their relative stability under TENG operational conditions and triboelectric/flexoelectric fields remain unknown. Herein, through atomic force microscopy (AFM) we compare the electrical performances of chemically passivated (**S1** and **S2**) Si–H and Si–D samples both under mechanically static and dynamic conditions.

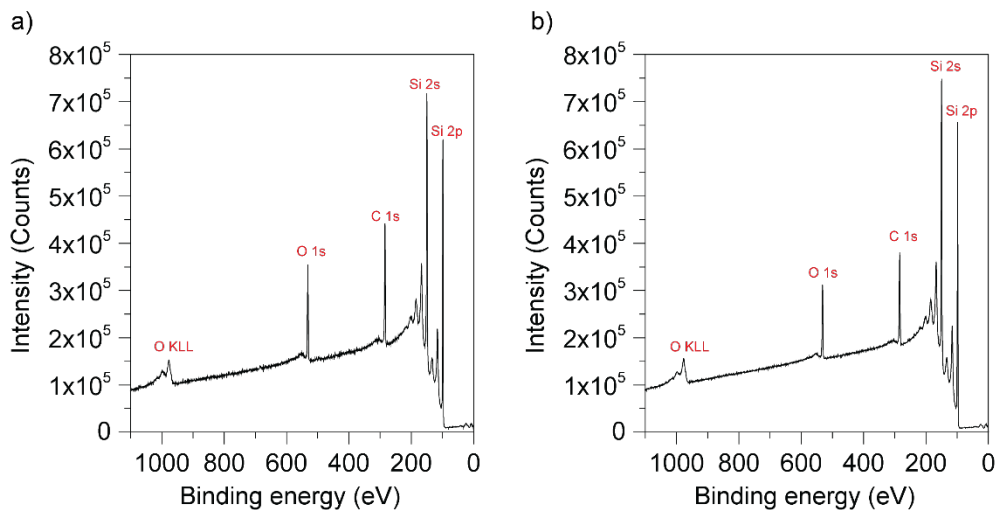


Figure 5.1. XPS survey scans of (a) deuterium-terminated (Si–D) samples and (b) hydrogen-terminated (Si–H) samples that were reacted with 8-nonyl-1-ol (**S1**). All survey scans showed elemental emissions in agreement with the chemical nature of the monolayer-forming molecule and substrate. Oxygen contaminations are ubiquitous in XPS, and most likely arising from the presence of oxygenated co-adsorbates, for instance, tightly bound water [74].

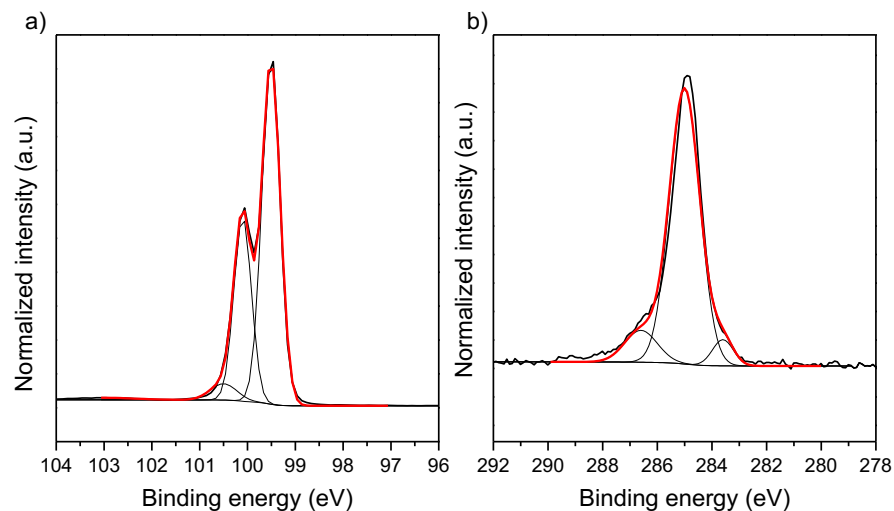


Figure 5.2. XPS narrow scans of a) Si 2p and b) C 1s regions for 8-nonyl-1-ol modified deuterium-terminated (Si-D) substrates (etched for 30 minutes in 10 wt% KF solution). The substrates were n-type of 7-13 ohm cm resistivity. The black thick lines are experimental XPS data (106-94 eV for Si 2p and 292-278 eV for C 1s), while the black thin traces are fitted contributions belonging to Si 2p_{3/2} at 99.5 eV (0.6 eV FWHM), Si 2p_{1/2} at 100.1 eV (0.6 eV FWHM)[75], Si-bound to hydrogen (Si-H) at 100.75 eV (0.9 eV FWHM)[76], methylene carbons (C-C) at 285.0 eV (1.4 eV FWHM), silicon bound olefinic carbons (Si-C=C) at 283.6 eV (0.9 eV FWHM), and oxygen bond carbon (C-O) at 286.3 eV (1.4 eV FWHM)[77].

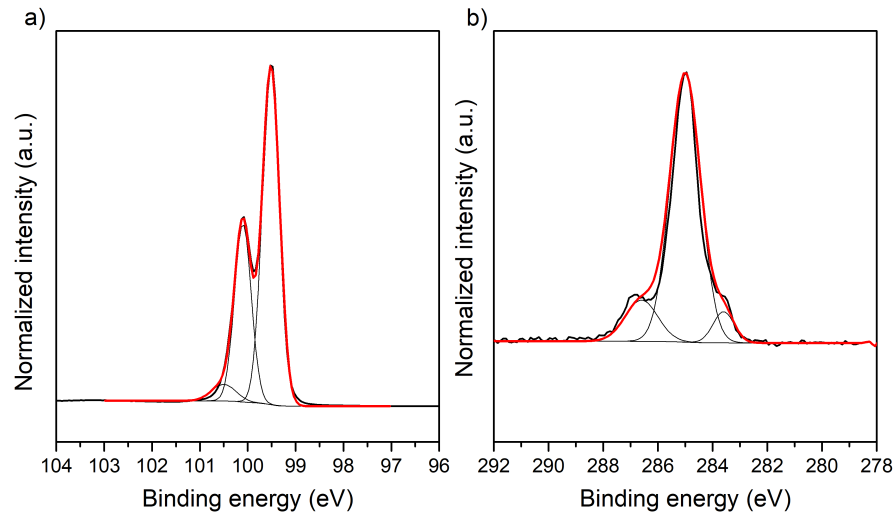


Figure 5.3. XPS narrow scans of a) Si 2p and b) C 1s regions for 8-nonyl-1-ol modified hydrogen-terminated (Si-H) substrates. The substrates were n-type of 7-13 ohm cm resistivity. The black thick lines are experimental XPS data (106-94 eV for Si 2p and 292-278 eV for C 1s), while the black thin traces are fitted contributions belonging to Si 2p_{3/2} at 99.5 eV (0.6 eV FWHM), Si 2p_{1/2} at 100.1 eV (0.6 eV FWHM)[75], Si-bound to hydrogen (Si-H) at 100.75 eV (0.9 eV FWHM)[76], methylene carbons (C-C) at 285.0 eV (1.4 eV FWHM), silicon bound olefinic carbons (Si-C=C) at 283.6 eV (0.9 eV FWHM), and oxygen bond carbon (C-O) at 286.3 eV (1.4 eV FWHM)[77].

5.3.1. Optimization of Si–D surface preparation

While the preparation of Si–H surfaces is well established, there are relatively fewer protocols for making Si–D surfaces. The previously reported wet chemistry approach towards Si–D substrates [71] did not yield surfaces of roughness as good as that of Si–H substrates prepared by the NH_4F -etching of native Si(111), whose root mean square roughness (R_q) is generally as good as 0.2 nm [68]. Therefore, since the surface preparation of Si–H is well established, this section focuses on the etching optimization towards Si–D, i.e. how to successfully passivate the Si(111) surface without sacrificing surface flatness. This is crucial for nanoscale DC-TENGs analysis, as differences in roughness are known to lead to different tribocurrent outputs and would have complicated the analysis of the tribocurrent data. We tested several concentrations of the etchant (1 and 10 wt % of KF in D_2O) and varied the etching time (1, 10, 30 min). Samples prepared under all these conditions were analysed by conductive AFM (C-AFM) to probe simultaneously their electrical performance (zero-bias current output) and their surface topography (Figure 5.4). Samples etched for 30 min with 10 wt % of KF led to an oxide-free surface (Figure 5.2), with relatively good topography and high zero-bias current output (Figure 5.4). We note that although all etching conditions led to satisfactorily flat samples of root mean square roughness (R_q) ranging from 0.21 to 0.35 nm, the zero-bias current varied significantly with etching time. The recorded zero-bias current density for surfaces immersed in 1 wt % KF solution (in D_2O) was $1.58 \times 10^4 \text{ A/m}^2$ (1 min, $R_q = 0.26 \text{ nm}$), $3.41 \times 10^5 \text{ A/m}^2$ (10 min, $R_q = 0.35 \text{ nm}$), $1.09 \times 10^4 \text{ A/m}^2$ (30 min, $R_q = 0.21 \text{ nm}$), and in 10 wt% KF solution (in D_2O) is $1.18 \times 10^5 \text{ A/m}^2$ (1 min, $R_q = 0.23 \text{ nm}$), $2.77 \times 10^5 \text{ A/m}^2$ (10 min, $R_q = 0.28 \text{ nm}$), $1.23 \times 10^7 \text{ A/m}^2$ (30 min, $R_q = 0.25 \text{ nm}$) respectively. All samples exhibit a zero-bias current of positive signs, indicates the electrons flow from tip to samples, which is the direction of leakage current. In conclusion, for 10 wt% KF solution (in D_2O), the zero-bias current density of surface functionalized Si(111) sample increases with etching time. As for 1 wt% KF solution, extending etching time cannot well passivate Si(111) surface due to incomplete elimination of the native oxide.

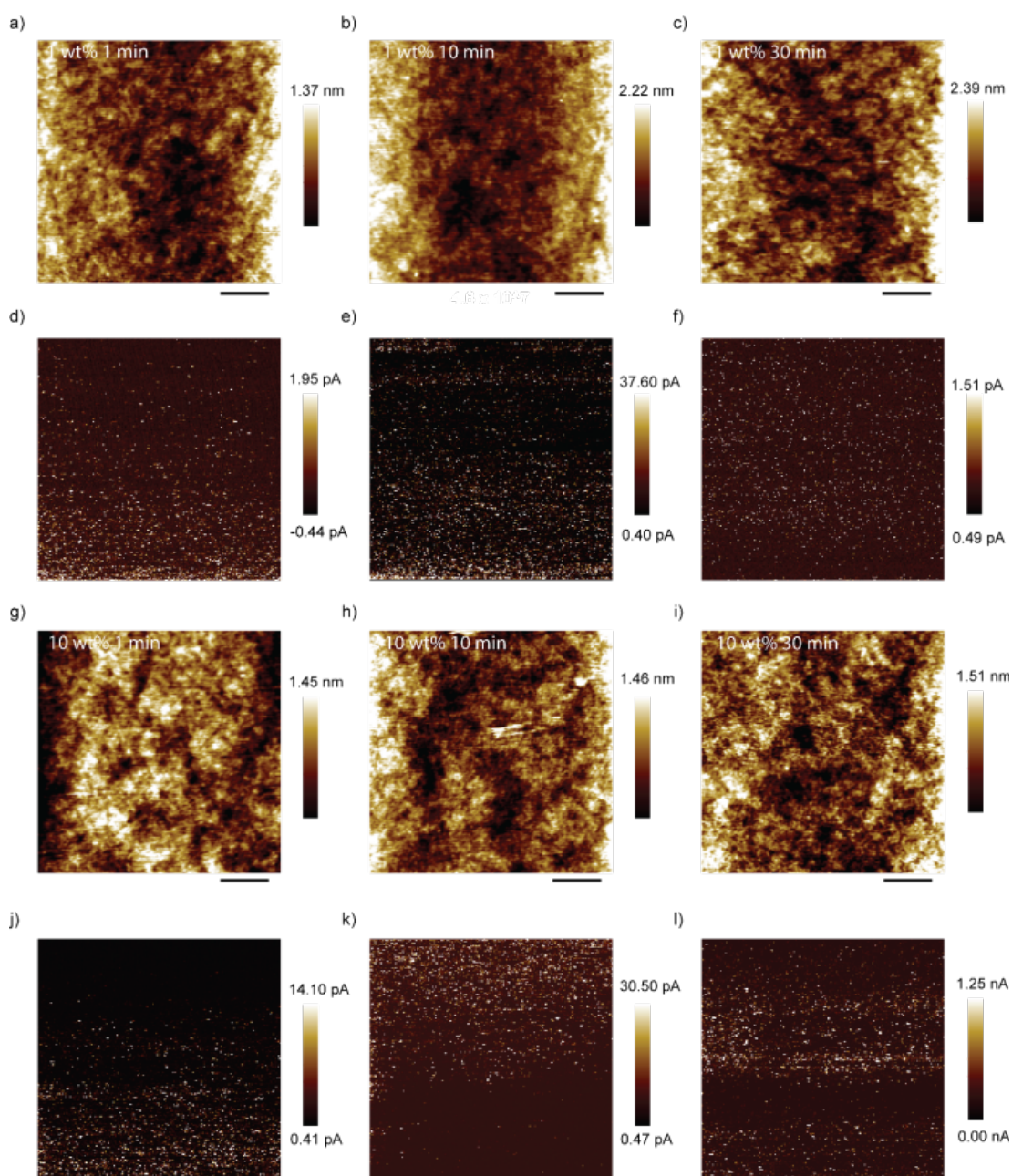


Figure 5.4. AFM height $5 \times 5 \mu\text{m}$ images and corresponding zero-bias current map of 8-nonyl-1-ol coated Si-D substrates etched in 1 wt % potassium fluoride solution (in D_2O) for (a, d) 1 min, (b, e) 10 min, and (c, f) 30 min, and in 10 wt % potassium fluoride solution (in D_2O) for (g, j) 1 min, (h, k) 10 min, and (i, l) 30 min. The applied force was set to 360 nN. The scale bar in panels (a–c) and (g–i) represents 1 μm . The positive signal of current indicates the electrons flowing from tip to sample.

Regardless of whether a Si-D surface is formed on Si(111) by etching in 1 wt % or 10 wt % KF in D_2O , samples etched for 10 min were consistently rougher than samples etched for shorter or longer times (1 and 30 min). With the 1 wt% KF etching solution, the zero-bias current density reached a maximum with 10 min of etching time. Surprisingly, extending the etching time to 30 min caused the zero-bias current to

return to the level observed with the 1 min etching. This could be due to incomplete coverage of Si–D sites [78], possibly causing surface re-oxidation over time, leading to a decrease in conductivity. For the 10 wt% KF etching solution, 30 min etching time enables the silicon surface to become atomically flat and allows for significant zero-bias current density to be observed in C-AFM measurements. No apparent oxidation is detected by XPS (Figure 5.2). Therefore, Si(111) samples that were etched for 30 min in 10 wt % KF in D₂O were selected as the model Si–D system on which to graft a monolayer (**S1** samples) and then perform a systematic comparison against Si–H surfaces as DC-TENG platform.

5.3.2. Zero-bias current on monolayer-modified Si–D and Si–H samples

We then moved to answer the question as to whether or not **S1** samples are less prone to oxidation than **S2** samples, and to what degree they maintain a stable zero-bias current output under friction and friction-induced electric fields (i.e. upon sliding of a metal tip against the sample's surface). In a C-AFM experiment, friction and current signals can be recorded simultaneously, and considering the previously reported suggestion of an electronic contribution to friction [79-81], we asked the question whether or not friction could influence the zero-bias current output observed during the sliding of the Schottky diode. We therefore conducted multiple lines scans along 5- μ m-long lines across both **S1** and **S2** samples in order to probe the distribution of zero-bias current peaks, their relationship with the friction profile, and the stability over time of the zero-bias current. Figure 5.5 shows topography, zero-bias current and friction profiles of 20 scans recorded along the lines marked in figure over the AFM images of **S1** (line A–B) and **S2** (line C–D) samples. Examination of the current and height data for **S1** samples (Figure 5.5a) indicates that there is no clear correlation between current distribution (peaks in current) and sample topography. Conversely, data in Figure 5.5d reveal that the current and height profiles of **S2** samples are somewhat more correlated, with the zero-bias (triboelectric) current spikes generally occurring at the edges of the Si(111) terraces, which are most likely (211) facets [68]: the electrical conductivity of Si(211) is higher than that of Si(111) [82-84]. The difference in the current–topography matching patterns, between

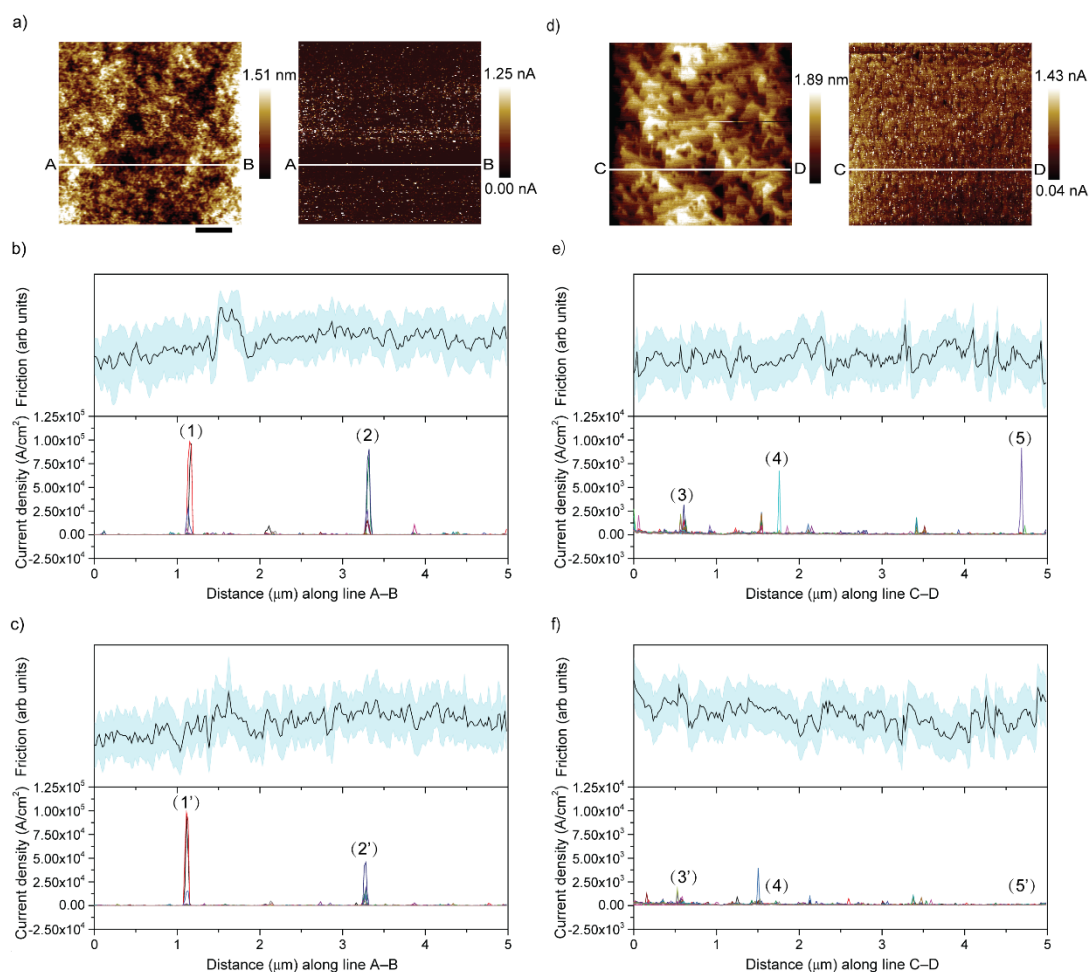


Figure 5.5. (a) AFM topography image (left), and zero-bias current map (right), (b) forward (from left to right) and (c) backward (from right to left) line (A–B line) scans of friction (upper) and zero-bias current (lower) data recorded on functionalized Si(111)–D substrates (Scheme 5.1, **S1**). The position of the A–B line is marked in panel (a). (d) AFM topography image (left), zero-bias current map (right), (e) forward (from left to right) and (f) backward (from right to left) line (C–D line) scans of friction (upper) and zero-bias current (lower) data acquired on functionalized Si(111)–H substrates (Scheme 5.1, **S2**). The position of the C–D line is marked in panel (d). The blue shaded regions marked in the friction profiles represent the standard deviation of 20 scans.

hydrogen- and deuterium-based samples may be attributed to the latter lacking a clear terraced structure, making it more difficult to identify such patterns. Nevertheless, we cannot rule out the possibility of Si(211) nanoscopic domains being exposed on the deuterium-based Si(111) surface (**S1** samples) which explains why in Si–D samples the zero-bias current distribution is not correlated with topography.

Interestingly, for **S1** samples the most prominent zero-bias current peaks persist in the same locations over 20 consecutive scans (multiple forward and backward scans over the same line). Additionally, out of the 20 scans conducted (shown in different colors in Figure 5.5b,c, lower plots), approximately 3 to 5 occurrences of current

spikes were consistently observed at the same location, namely, peaks 1 and 2 in the forward scan (Figure 5.5b, lower plot), and peaks 1' and 2' in the backward scan (Figure 5.5c, lower plot). However, the corresponding friction profiles (Figure 5.5b,c, upper plots) at the same location do not exhibit significant variation or identical features in that precise spot. On the contrary, the distribution of the current spikes over 20 scans on samples **S2** shows a more random pattern, with the majority of the current “spikes” occurring in the forward scan (peaks 3, 4, 5, Figure 5.5e) while there was a significant decrease, or even disappearance, at the same location in the backward scans (peaks 3', 4', 5', Figure 5.5f). As for the corresponding friction profiles (Figure 5.5e,f, upper plots), there is no significant change or identical feature within the areas of current spikes for sample **S2** either.

From a more general perspective, the root-mean-square roughness (R_q) of samples **S1** and **S2** is 0.25 ± 0.19 nm and 0.19 ± 0.145 nm respectively. In addition, according to the zero-bias current map (Figure 5.5d), the zero-bias current density for sample **S2** is obtained to be 1.19×10^7 A/m², which is comparable to the value reported above for sample **S1** (1.23×10^7 A/m²). Since the roughness are similar, so that any chemical difference between **S1** and **S2** (Si–D and Si–H) is not significant in terms of the electrical performance of DC-TENGs.

As mentioned above, the zero-bias current acquired during 20 scans along marked lines is more stable in sample **S1** than sample **S2** over time. This is consistent with the previously reported finding of deuterium-terminated silicon surface, suggesting that because sample **S1** is more resistant to oxidation under triboelectric field, thereby ensuring a stable output of tribocurrent. Conversely, zero-bias current map of sample **S2** (Figure 5.5d, right) is brighter than sample **S1** (Figure 5.5a, right). In addition, the mean current of sample **S2** is 0.656 nA, which is 10 magnitudes higher than sample **S1**, 0.061 nA, suggesting that the overall zero-bias current of sample **S2** tends to be higher, which may lead to a rapid oxidation under the triboelectric field coupled with thermal effect induced by friction [85], eventually resulting in a rapid decay of zero-bias current after prolonged operation.

5.3.3. Triboelectric and flexoelectric effect on Si–D and Si–H samples

Strain gradients can lead to surface polarization (i.e. a voltage) in many materials, including silicon [86-89]. A direct measurement of the (macroscopic) flexoelectric coefficient – magnitude and sign – of silicon is still lacking, mainly because of the technical challenge of introducing a macroscopic strain stimulus without breaking this hard and brittle material. There are however several reports indicating that a nanoscale strain gradient is likely to significantly polarize silicon [90, 91]. To explore the possible contribution of flexoelectricity on the observed zero-bias current, we conducted, high speed current capture tests (in F–D spectroscopy), transient photocurrent mapping and current–potential (I–V) measurements at 25 different locations either with or without current surges spotted on sample **S1** (Figure 5.6) and **S2** (Figure 5.8).

On the surface of a **S1** sample we randomly selected 25 different locations, including both regions with marked current spikes (marked with red crosses in Figure 5.6a) as well as regions of negligible tribocurrent output (marked with white crosses in Figure 5.6b) for testing. Figure 5.6c,d shows the zero- bias current signal recorded as the platinum AFM tip is pressed down and lifted up (along the sample normal direction) so that the normal force is increased and decreased cyclically during the F–D spectroscopy (Figure 5.7). Both locations that did output a tribocurrent (Figure 5.6c) as well as those that performed poorly as a TENG(Figure 5.6d), as normal force is increased there is a large current surge (with the direction of a reverse bias leakage current) observed when the applied force is beyond 1500 nN (contact pressure ~ 9.4 Gpa). Such high contact pressure could lead to plastic deformation (strain gradient) of silicon [92], potentially leading to flexoelectricity [93]. The key point is that a strain gradient is likely to cause surface polarization and that a similar situation is likely to occur when the tip is sliding laterally.

Interestingly, four F–D measurements out of the 25 conducted in areas that were good TENG performers (Figure 5.6c) exhibited a current density exceeding 1.0×10^3 A/cm² (when the load reaches 1500mN, contact pressure reaches ~ 9.4 Gpa) with 2

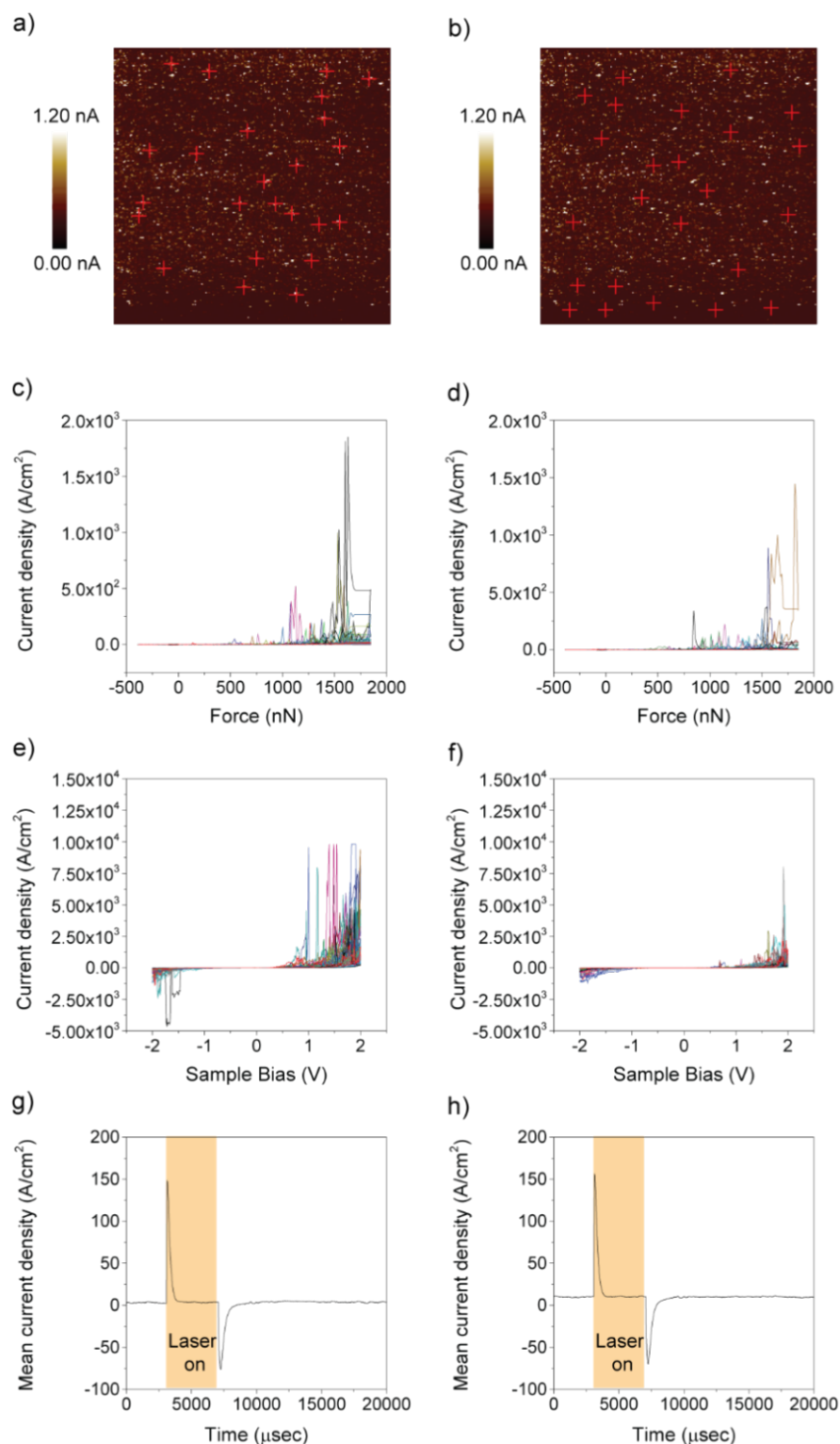


Figure 5.6. (a,b) Representative zero-bias AFM current map acquired on a S1 sample, with red cross symbols marking regions of interest that are further analysed through force–distance (F–D), current–potential (I–V) and transient photocurrent spectroscopies. (c,d) High-speed capture current profiles obtained during F–D measurements. (e,f) I–V measurements, and (g,h) transient photocurrent decay data. All data (except I–V curves) were recorded under zero external bias on 8-nonyl-1-ol functionalized low-doped n-type deuterium-terminated (Si–D) surfaces (S1 samples). A current of positive sign indicates a net flow of electrons from tip to sample.

instances reaching $\sim 1.75 \times 10^3 \text{ A/cm}^2$. Although the current feedback in other locations is not as pronounced, the current density can also generally reach $\sim 2.5 \times 10^2 \text{ A/cm}^2$. Conversely, in areas that were poor TENG performer (Figure 5.6d), only one F–D test showed a maximum current density of $\sim 1.5 \times 10^3 \text{ A/cm}^2$, and one a maximum current density of $\sim 1.0 \times 10^3 \text{ A/cm}^2$. The remaining locations exhibited relatively low current response under normal force, with the maximum current density being below $2.5 \times 10^2 \text{ A/cm}^2$. The putative flexoelectric effect is therefore more significant in areas with good TENG output, leading to a larger flexoelectric field (directed from sample to tip) in those regions.

This presence of a flexovoltage which bears the sign of an additional reverse bias term can be further revealed through the analysis of “static” current–potential (I–V) measurements (Figure 5.6e,f) where such “mechanical” term would add or subtract to the external (instrument-controlled) bias. When a positive external voltage bias is applied to the silicon (n-type) side of a Pt–Si Schottky diode, the junction is in reverse bias, and only a negligible leakage current flows [94, 95]. When a negative voltage bias is applied to the semiconductor, the diode is under forward bias and past an internal intrinsic barrier (knee voltage of $\sim 0.4 \text{ V}$) [96] the junction current increases exponentially with voltage [3, 94, 97]. However, a very surprising feature of the I–V curves obtained by pressing the platinum AFM tip onto n-type **S1** samples (Si–D based

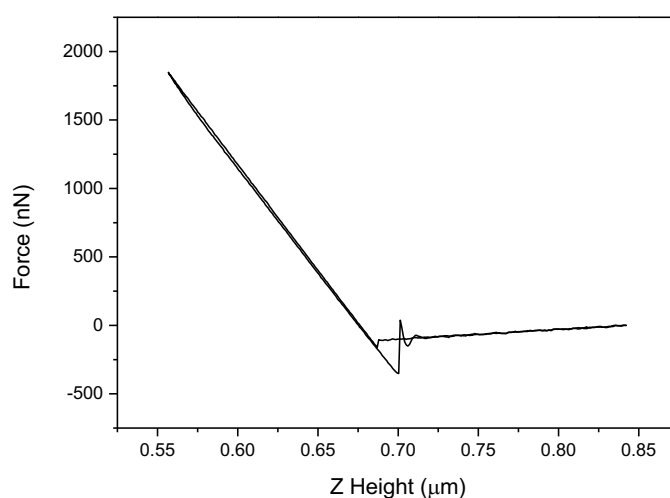


Figure 5.7. A representative force–distance (F–D) curve. Data recorded on 8-nonyl-1-ol functionalized low-doped n-type Si(111)–D surfaces.

monolayer-modified Si(111) samples) is an exceedingly large leakage. Under a moderately low external reverse bias (small positive sample bias) the extent of leakage flow is already significant. Conversely, the forward current is significantly hindered, as if the apparent knee voltage shifts positive. In other words, there appears to be an additional directional bias term (non-instrument-defined) which adds to the instrument reverse bias and detracts from the instrument forward bias. Notably we found that I–V data acquired at regions that were good TENG performers (Figure 5.6e) the leakage increases more than the forward current decreases, possibly indicating that beside the flexoelectric contribution, TENGs' performances also rely on electric conductivity.

We then turned to the role of surface states, such as electron–hole pairs recombination sites, in terms of affecting tribocurrent outputs [98, 99]. To this end we conducted measurements of transient photocurrent decays (Figure 5.6g,h) at the sample locations marked in Figure 5.6a,b. No difference was found between regions that performed well or poorly as TENG. With Si–D-based samples, all transient photocurrents appeared like the charging and discharging of a capacitor, indicating a large density of surface defects [100].

To reveal an isotope effect we conducted experiments analogous to those in Figure 5.6 also on **S2** samples, and the results are in Figure 5.8. The key tests on the presence or absence of a flexoelectric effect (Figure 5.8c,d) and tests on the presence or absence of an additional, strain-related, reverse bias term in I–V curves (Figure 5.8e,f) are essentially indistinguishable (qualitatively) between **S2** and **S1** samples. However, in quantitative term, both F–D and I–V curves yielded greater current values if the substrate was hydrogen- rather than deuterium-terminated. This observation can be explained by comparing the results of the transient photocurrent decay tests (Figure 5.8g,h versus Figure 5.6g,h). Unlike for **S1** samples, the photocurrent extracted from **S2** samples exhibits a typical on and off response, with a stable current density of $\sim 200 \text{ A/cm}^2$ during the laser-on period. Such a current response indicates fewer surface states on hydrogen- versus deuterium-based samples [100, 101]. Less surface states provide fewer recombination sites for electron-hole pairs, allowing more

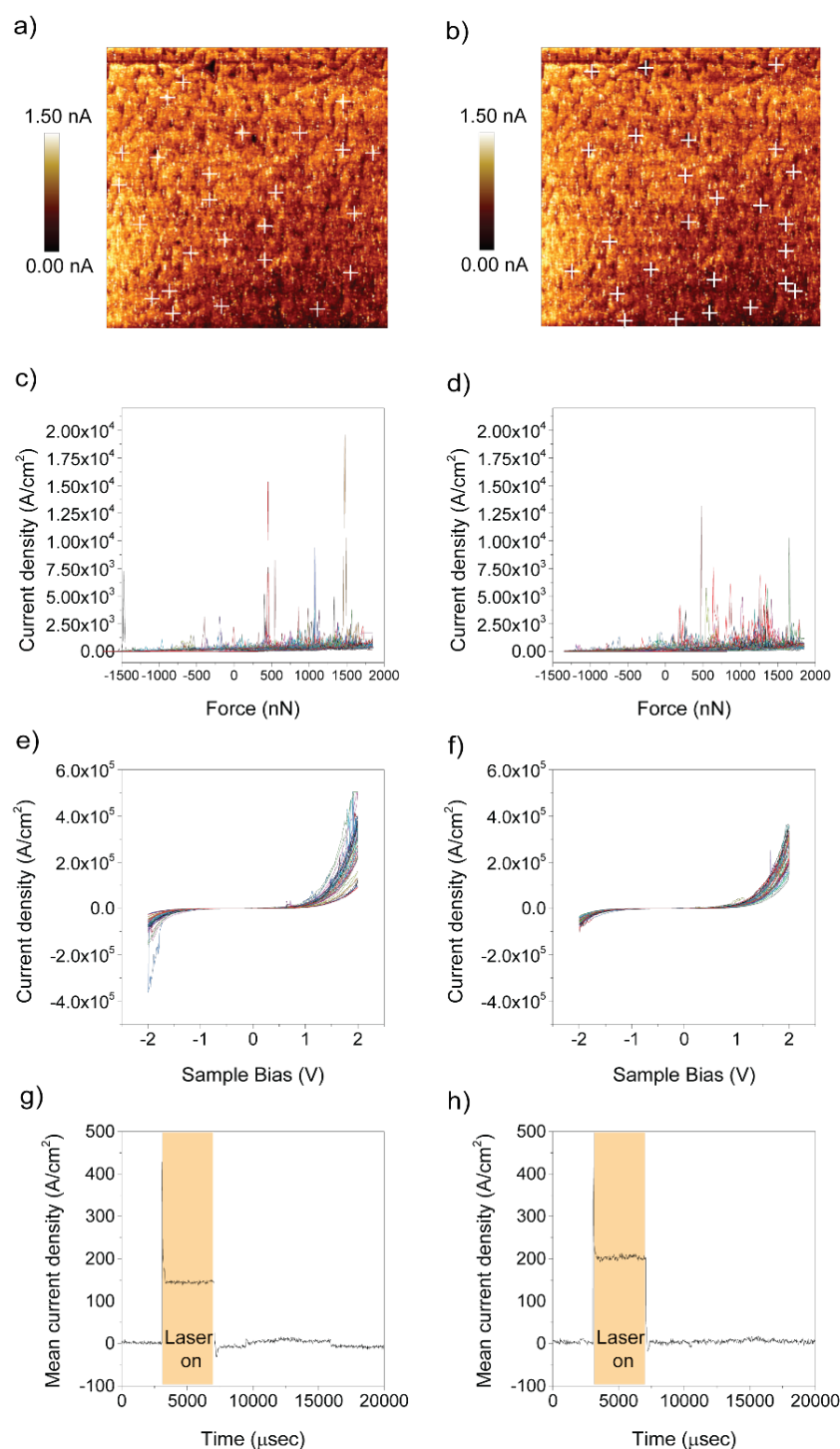


Figure 5.8. (a,b) Representative zero-bias AFM current map acquired on a **S2** sample, with white cross symbols marking regions of interest that are further analysed through force–distance (F–D), current–potential (I–V) and transient photocurrent spectroscopies. (c,d) High-speed capture current profiles obtained during F–D measurements. (e,f) I–V measurements, and (g,h) transient photocurrent decay data. All data (except I–V curves) were recorded under zero external bias on 8-nonyl-1-ol functionalized low-doped n-type deuterium-terminated (Si–H) surfaces (**S2** samples). A current of positive sign indicates a net flow of electrons from tip to sample.

charge carriers to move directionally under the electric field, resulting in a larger current.

5.4 Conclusions

We have refined the wet chemical etching protocols to achieve deuterium-terminated and oxide-free Si(111) crystals. Following surface chemical derivatization through monolayer chemistry, we conducted a systematic comparison between Si–D- and Si–H-based Schottky triboelectric nanogenerators (DC-TENGs). Despite detecting a higher occurrence of electrical defects on Si–D compared to Si–H, our investigations revealed no discernible isotope effect concerning the maximum attainable TENG current density. Both substrates exhibited comparable performance, with zero-bias current densities reaching as high as $\sim 10^7$ A/m².

The primary advantage of substituting hydrogen with its heavier isotope lies in enhancing device longevity. This observation aligns with prior studies demonstrating the superior ability of Si–D to mitigate anodic decomposition of the underlying substrate. Furthermore, our research unveils the presence of a flexoelectric component contributing to the TENG output, suggesting the potential significance of strain gradients in the mechanical-to-electrical energy conversion mechanism within a Schottky TENG. We also note that our findings underscore the necessity of minimizing or addressing strain, and potentially shear, when conducting routine nanoscopic electrical measurements on metal–semiconductor junctions. For instance, the accuracy of externally applied voltage, as defined by the instrumentation, during an AFM-based current–voltage measurement is likely to be compromised by the presence of a flexoelectric term.

5.5 References

- [1] Zhang, J.; Coote, M. L.; Ciampi, S., Electrostatics and electrochemistry: mechanism and scope of charge-transfer reactions on the surface of tribocharged insulators. *J. Am. Chem. Soc.* 143 (2021) 3019–3032. <http://doi.org/10.1021/jacs.0c11006>
- [2] Jamieson, W., The Electrification of Insulating Materials. *Nature* 83 (1910) 189. <http://doi.org/10.1038/083189a0>
- [3] Lyu, X.; MacGregor, M.; Liu, J.; Darwish, N.; Ciampi, S., Direct-current output of silicon–organic monolayer–platinum Schottky TENGs: Elusive friction-output relationship. *Nano Energy* 114 (2023) 108627. <http://doi.org/10.1016/j.nanoen.2023.108627>
- [4] Lyu, X.; Ciampi, S., Improving the performances of direct-current triboelectric nanogenerators with surface chemistry. *Curr. Opin. Colloid Interface Sci.* 61 (2022). <http://doi.org/10.1016/j.cocis.2022.101627>
- [5] Lin, S.; Chen, X.; Wang, Z. L., The tribovoltaic effect and electron transfer at a liquid-semiconductor interface. *Nano Energy* 76 (2020) 105070. <http://doi.org/10.1016/j.nanoen.2020.105070>
- [6] Zhang, Z.; Jiang, D.; Zhao, J.; Liu, G.; Bu, T.; Zhang, C.; Wang, Z. L., Tribovoltaic effect on metal–semiconductor interface for direct-current low-impedance triboelectric nanogenerators. *Adv. Energy Mater.* 10 (2020) 1903713. <http://doi.org/10.1002/aenm.201903713>
- [7] Wang, S.; Lin, L.; Wang, Z. L., Nanoscale Triboelectric-Effect-Enabled Energy Conversion for Sustainably Powering Portable Electronics. *Nano Lett.* 12 (2012) 6339–6346. <http://doi.org/10.1021/nl303573d>
- [8] Huang, W.; Yuan, F. G.; Jiang, X., 5 - Flexoelectric effect, materials, and structures. In *Structural Health Monitoring (SHM) in Aerospace Structures*, Elsevier Ltd: 2016; pp 119–148. <http://doi.org/10.1016/B978-0-08-100148-6.00005-6>
- [9] Deng, Q.; Kammoun, M.; Erturk, A.; Sharma, P., Nanoscale flexoelectric energy harvesting. *Int. J. Solids Struct.* 51 (2014) 3218–3225. <http://doi.org/10.1016/j.ijsolstr.2014.05.018>
- [10] Zubko, P.; Catalan, G.; Tagantsev, A. K., Flexoelectric effect in solids. *Annu. Rev. Mater. Res.* 43 (2013) 387–421. <http://doi.org/10.1146/annurev-matsci-071312-121634>
- [11] Kim, W.-G.; Kim, D.; Lee, H. M.; Choi, Y.-K., Wearable fabric-based hybrid energy harvester from body motion and body heat. *Nano Energy* 100 (2022) 107485. <http://doi.org/10.1016/j.nanoen.2022.107485>
- [12] Seung, W.; Gupta, M. K.; Lee, K. Y.; Shin, K.-S.; Lee, J.-H.; Kim, T. Y.; Kim, S.; Lin, J.; Kim, J. H.; Kim, S.-W., Nanopatterned Textile-Based Wearable Triboelectric Nanogenerator. *ACS Nano*. 9 (2015) 3501–3509. <http://doi.org/10.1021/nn507221f>
- [13] Zeng, Y.; Xiang, H.; Zheng, N.; Cao, X.; Wang, N.; Wang, Z. L., Flexible triboelectric nanogenerator for human motion tracking and gesture recognition. *Nano Energy* 91 (2022) 106601. <http://doi.org/10.1016/j.nanoen.2021.106601>
- [14] Xi, Y.; Guo, H.; Zi, Y.; Li, X.; Wang, J.; Deng, J.; Li, S.; Hu, C.; Cao, X.; Wang, Z. L., Multifunctional TENG for blue energy scavenging and self-powered wind-speed sensor. *Adv. Energy Mater.* 7 (2017) 1602397. <http://doi.org/10.1002/aenm.201602397>
- [15] Chen, P.; An, J.; Shu, S.; Cheng, R.; Nie, J.; Jiang, T.; Wang, Z. L., Super-durable, low-wear, and high-performance fur-brush triboelectric nanogenerator for wind and

- water energy harvesting for smart agriculture. *Adv. Energy Mater.* 11 (2021) 2003066. <http://doi.org/10.1002/aenm.202003066>
- [16] Yang, Y.; Zhu, G.; Zhang, H.; Chen, J.; Zhong, X.; Lin, Z.-H.; Su, Y.; Bai, P.; Wen, X.; Wang, Z. L., Triboelectric Nanogenerator for Harvesting Wind Energy and as Self-Powered Wind Vector Sensor System. *ACS Nano.* 7 (2013) 9461–9468. <http://doi.org/10.1021/nn4043157>
- [17] Seol, M.-L.; Woo, J.-H.; Jeon, S.-B.; Kim, D.; Park, S.-J.; Hur, J.; Choi, Y.-K., Vertically stacked thin triboelectric nanogenerator for wind energy harvesting. *Nano Energy* 14 (2015) 201–208. <http://doi.org/10.1016/j.nanoen.2014.11.016>
- [18] Xia, K.; Fu, J.; Xu, Z., Multiple-Frequency High-Output Triboelectric Nanogenerator Based on a Water Balloon for All-Weather Water Wave Energy Harvesting. *Adv. Energy Mater.* 10 (2020) 2000426. <http://doi.org/10.1002/aenm.202000426>
- [19] Rui, P.; Zhang, W.; Zhong, Y.; Wei, X.; Guo, Y.; Shi, S.; Liao, Y.; Cheng, J.; Wang, P., High-performance cylindrical pendulum shaped triboelectric nanogenerators driven by water wave energy for full-automatic and self-powered wireless hydrological monitoring system. *Nano Energy* 74 (2020) 104937. <http://doi.org/10.1016/j.nanoen.2020.104937>
- [20] Xu, Y.; Yang, W.; Lu, X.; Yang, Y.; Li, J.; Wen, J.; Cheng, T.; Wang, Z. L., Triboelectric Nanogenerator for Ocean Wave Graded Energy Harvesting and Condition Monitoring. *ACS Nano.* 15 (2021) 16368–16375. <http://doi.org/10.1021/acsnano.1c05685>
- [21] Lu, Y.; Yan, Y.; Yu, X.; Zhou, X.; Feng, S.; Xu, C.; Zheng, H.; Yang, Z.; Li, L.; Liu, K.; Lin, S., Polarized water driven dynamic PN junction-based direct-current generator. *Research* 2021 (2021) 7505638. <http://doi.org/10.34133/2021/7505638>
- [22] Lee, J. H.; Kim, S.; Kim, T. Y.; Khan, U.; Kim, S.-W., Water droplet-driven triboelectric nanogenerator with superhydrophobic surfaces. *Nano Energy* 58 (2019) 579–584. <http://doi.org/10.1016/j.nanoen.2019.01.078>
- [23] Xu, C.; Fu, X.; Li, C.; Liu, G.; Gao, Y.; Qi, Y.; Bu, T.; Chen, Y.; Wang, Z. L.; Zhang, C., Raindrop energy-powered autonomous wireless hyetometer based on liquid–solid contact electrification. *Microsyst. Nanoeng.* 8 (2022) 30–30. <http://doi.org/10.1038/s41378-022-00362-6>
- [24] Chen, J.; Wang, Z. L., Reviving Vibration Energy Harvesting and Self-Powered Sensing by a Triboelectric Nanogenerator. *Joule* 1 (2017) 480–521. <http://doi.org/10.1016/j.joule.2017.09.004>
- [25] Yang, W.; Chen, J.; Zhu, G.; Wen, X.; Bai, P.; Su, Y.; Lin, Y.; Wang, Z., Harvesting vibration energy by a triple-cantilever based triboelectric nanogenerator. *Nano Res.* 6 (2013) 880–886. <http://doi.org/10.1007/s12274-013-0364-0>
- [26] Li, S.; Liu, D.; Zhao, Z.; Zhou, L.; Yin, X.; Li, X.; Gao, Y.; Zhang, C.; Zhang, Q.; Wang, J.; Wang, Z. L., A Fully Self-Powered Vibration Monitoring System Driven by Dual-Mode Triboelectric Nanogenerators. *ACS Nano.* 14 (2020) 2475–2482. <http://doi.org/10.1021/acsnano.9b10142>
- [27] Khandelwal, G.; Maria Joseph Raj, N. P.; Kim, S.-J., Triboelectric nanogenerator for healthcare and biomedical applications. *Nano Today* 33 (2020) 100882. <http://doi.org/10.1016/j.nantod.2020.100882>

- [28] Wang, H.; Cheng, J.; Wang, Z.; Ji, L.; Wang, Z. L., Triboelectric nanogenerators for human-health care. *Sci. Bull.* 66 (2021) 490–511. <http://doi.org/10.1016/j.scib.2020.10.002>
- [29] Lu, Y.; Hao, Z.; Feng, S.; Shen, R.; Yan, Y.; Lin, S., Direct-current generator based on dynamic PN junctions with the designed voltage output. *iScience.* 22 (2019) 58–69. <http://doi.org/10.1016/j.isci.2019.11.004>
- [30] Wang, X.; Song, J.; Liu, J.; Zhong, L. W., Direct-current nanogenerator driven by ultrasonic waves. *Science.* 316 (2007) 102–105. <http://doi.org/10.1126/science.1139366>
- [31] Liu, J.; Goswami, A.; Jiang, K. R.; Khan, F.; Kim, S.; McGee, R.; Li, Z.; Hu, Z. Y.; Lee, J.; Thundat, T., Direct-current triboelectricity generation by a sliding Schottky nanocontact on MoS₂ multilayers. *Nat. Nanotechnol.* 13 (2018) 112–116. <http://doi.org/10.1038/s41565-017-0019-5>
- [32] Shan, C.; Li, K.; Cheng, Y.; Hu, C., Harvesting Environment Mechanical Energy by Direct Current Triboelectric Nanogenerators. *Nano-Micro Lett.* 15 (2023) 127. <http://doi.org/10.1007/s40820-023-01115-4>
- [33] Wei, K.-Q.; Sun, D.-J.; Liu, M.-N.; Song, W.-Z.; Zhu, K.-R.; Wu, L.-X.; Zhang, J.; Ramakrishna, S.; Long, Y.-Z., Direct Current Nanogenerator Based on Tribovoltaic Effect at WS₂ Semiconductor Interface. *ACS Appl. Nano Mater.* 7 (2024) 1748–1756. <http://doi.org/10.1021/acsnm.3c04869>
- [34] Lv, T.; Cheng, R.; Wei, C.; Su, E.; Jiang, T.; Sheng, F.; Peng, X.; Dong, K.; Wang, Z. L., All-Fabric Direct-Current Triboelectric Nanogenerators Based on the Tribovoltaic Effect as Power Textiles. *Adv. Energy Mater.* 13 (2023). <http://doi.org/10.1002/aenm.202301178>
- [35] Lin, S.; Lu, Y.; Feng, S.; Hao, Z.; Yan, Y., A high current density direct-current generator based on a moving van der Waals Schottky diode. *Adv. Mater.* 31 (2018) 1804398. <http://doi.org/10.1002/adma.201804398>
- [36] You, Z.; Wang, S.; Li, Z.; Zou, Y.; Lu, T.; Wang, F.; Hu, B.; Wang, X.; Li, L.; Fang, W.; Liu, Y., High current output direct-current triboelectric nanogenerator based on organic semiconductor heterojunction. *Nano Energy* 91 (2022) 106667. <http://doi.org/10.1016/j.nanoen.2021.106667>
- [37] Chen, S.; Liu, D.; Zhou, L.; Li, S.; Zhao, Z.; Cui, S.; Gao, Y.; Li, Y.; Wang, Z. L.; Wang, J., Improved output performance of direct-current triboelectric nanogenerator through field enhancing breakdown effect. *Adv. Mater. Technol.* 6 (2021) 2100195. <http://doi.org/10.1002/admt.202100195>
- [38] Huang, X.; Xiang, X.; Nie, J.; Peng, D.; Yang, F.; Wu, Z.; Jiang, H.; Xu, Z.; Zheng, Q., Microscale Schottky superlubric generator with high direct-current density and ultralong life. *Nat. Commun.* 12 (2021) 2268. <http://doi.org/10.1038/s41467-021-22371-1>
- [39] Yang, R.; Xu, R.; Dou, W.; Benner, M.; Zhang, Q.; Liu, J., Semiconductor-based dynamic heterojunctions as an emerging strategy for high direct-current mechanical energy harvesting. *Nano Energy* 83 (2021) 105849. <http://doi.org/10.1016/j.nanoen.2021.105849>
- [40] Ren, L.; Yu, A.; Wang, W.; Guo, D.; Jia, M.; Guo, P.; Zhang, Y.; Wang, Z. L.; Zhai, J., p-n Junction Based Direct-Current Triboelectric Nanogenerator by Conjunction of Tribovoltaic Effect and Photovoltaic Effect. *Nano Lett.* 21 (2021) 10099–10106. <http://doi.org/10.1021/acs.nanolett.1c03922>

- [41] You, Z. y.; Wang, X.; Lu, F.; Wang, S.; Hu, B.; Li, L.; Fang, W.; Liu, Y., An organic semiconductor/metal Schottky heterojunction based direct current triboelectric nanogenerator windmill for wind energy harvesting. *Nano Energy* 109 (2023) 108302. <http://doi.org/10.1016/j.nanoen.2023.108302>
- [42] Lee, Y.-S.; Jeon, S.; Kim, D.; Lee, D.-M.; Kim, D.; Kim, S.-W., High performance direct current-generating triboelectric nanogenerators based on tribovoltaic p-n junction with ChCl-passivated CsFAMA perovskite. *Nano Energy* 106 (2023) 108066. <http://doi.org/10.1016/j.nanoen.2022.108066>
- [43] Zhang, Z.; Wang, Z.; Chen, Y.; Feng, Y.; Dong, S.; Zhou, H.; Wang, Z. L.; Zhang, C., Semiconductor contact-electrification-dominated tribovoltaic effect for ultrahigh power generation. *Adv. Mater. (Weinheim, Ger.)* 34 (2022) e2200146. <http://doi.org/10.1002/adma.202200146>
- [44] Zhang, Z.; He, T.; Zhao, J.; Liu, G.; Wang, Z. L.; Zhang, C., Tribo-thermoelectric and tribovoltaic coupling effect at metal-semiconductor interface. *Mater. Today Phys.* 16 (2021). <http://doi.org/10.1016/j.mtphys.2020.100295>
- [45] Luo, Q.; Xiao, K.; Li, M.; Yan, X.; Yang, J.; Deng, J.; Sun, W., Metal-semiconductor direct-current triboelectric nanogenerator based on depletion mode u-GaN/AlGaN/AlN/GaN HEMT. *Appl. Phys. Lett.* 123 (2023). <http://doi.org/10.1063/5.0158240>
- [46] Xu, J.; Zou, Y.; Nashalian, A.; Chen, J., Leverage Surface Chemistry for High-Performance Triboelectric Nanogenerators. *Front. Chem.* 8 (2020) 577327. <http://doi.org/10.3389/fchem.2020.577327>
- [47] Zhao, X.; Scott, S. A.; Huang, M.; Peng, W.; Kiefer, A. M.; Flack, F. S.; Savage, D. E.; Lagally, M. G., Influence of surface properties on the electrical conductivity of silicon nanomembranes. *Nanoscale Res. Lett.* 6 (2011) 402. <http://doi.org/10.1186/1556-276X-6-402>
- [48] Linford, M. R.; Chidsey, C. E. D., Alkyl monolayers covalently bonded to silicon surfaces. *J. Am. Chem. Soc.* 115 (1993) 12631–12632. <http://doi.org/10.1021/ja00079a071>
- [49] Linford, M. R.; Fenter, P.; Eisenberger, P. M.; Chidsey, C. E. D., Alkyl monolayers on silicon prepared from 1-alkenes and hydrogen-terminated silicon. *J. Am. Chem. Soc.* 117 (1995) 3145–3155. <http://doi.org/10.1021/ja00116a019>
- [50] Fabre, B., Ferrocene-Terminated Monolayers Covalently Bound to Hydrogen-Terminated Silicon Surfaces. Toward the Development of Charge Storage and Communication Devices. *Acc. Chem. Res.* 43 (2010) 1509–1518. <http://doi.org/10.1021/ar100085q>
- [51] Fabre, B.; Hauquier, F., Single-Component and Mixed Ferrocene-Terminated Alkyl Monolayers Covalently Bound to Si(111) Surfaces. *J. Phys. Chem. B* 110 (2006) 6848–6855. <http://doi.org/10.1021/jp055698n>
- [52] Allongue, P.; Kieling, V.; Gerischer, H., Etching mechanism and atomic structure of H-Si(111) surfaces prepared in NH₄F. *Electrochim. Acta.* 40 (1995) 1353–1360. [http://doi.org/10.1016/0013-4686\(95\)00071-L](http://doi.org/10.1016/0013-4686(95)00071-L)
- [53] Allongue, P.; Henry de Villeneuve, C.; Morin, S.; Boukherroub, R.; Wayner, D. D. M., The preparation of flat H-Si(111) surfaces in 40% NH₄F revisited. *Electrochim. Acta.* 45 (2000) 4591–4598. [http://doi.org/10.1016/S0013-4686\(00\)00610-1](http://doi.org/10.1016/S0013-4686(00)00610-1)
- [54] Ouyang, J. H.; Zhao, X. S.; Li, T.; Zhang, D. C., Direct measurement of the etching rates on Si (111) and silicon dioxide surfaces in 40% ammonium fluoride aqueous

- solution via atomic force microscopy. *J. Appl. Phys.* 93 (2003) 4315–4320. <http://doi.org/10.1063/1.1559001>
- [55] Hurtado, C.; Lyu, X.; Ferrie, S.; Le Brun, A. P.; MacGregor, M.; Ciampi, S., Organic monolayers on Si(211) for triboelectricity generation: etching optimization and relationship between the electrochemistry and current output. *ACS Appl. Nano Mater.* 5 (2022) 14263–14274. <http://doi.org/10.1021/acsanm.2c02006>
- [56] Tian, F.; Taber, D. F.; Teplyakov, A. V., NH⁻ Termination of the Si(111) Surface by Wet Chemistry. *J. Am. Chem. Soc.* 133 (2011) 20769–20777. <http://doi.org/10.1021/ja205140h>
- [57] Silva-Quinones, D.; He, C.; Butera, R. E.; Wang, G. T.; Teplyakov, A. V., Reaction of BCl₃ with H- and Cl-terminated Si(100) as a pathway for selective, monolayer doping through wet chemistry. *Appl. Surf. Sci.* 533 (2020) 146907. <http://doi.org/10.1016/j.apsusc.2020.146907>
- [58] Xu, F. J.; Cai, Q. J.; Kang, E. T.; Neoh, K. G., Surface-Initiated Atom Transfer Radical Polymerization from Halogen-Terminated Si(111) (Si-X, X = Cl, Br) Surfaces for the Preparation of Well-Defined Polymer-Si Hybrids. *Langmuir* 21 (2005) 3221–3225. <http://doi.org/10.1021/la0473714>
- [59] Liu, Y.; Yamazaki, S.; Yamabe, S.; Nakato, Y., A mild and efficient Si (111) surface modification via hydrosilylation of activated alkynes. *J. Mater. Chem.* 15 (2005) 4906–4913. <http://doi.org/10.1039/b511535c>
- [60] Sieval, A. B.; van den Hout, B.; Zuilhof, H.; Sudhölter, E. J. R., Molecular Modeling of Covalently Attached Alkyl Monolayers on the Hydrogen-Terminated Si(111) Surface. *Langmuir* 17 (2001) 2172–2181. <http://doi.org/10.1021/la001494g>
- [61] Solares, S. D.; Yu, H.; Webb, L. J.; Lewis, N. S.; Heath, J. R.; Goddard, W. A., Chlorination-Methylation of the Hydrogen-Terminated Silicon(111) Surface Can Induce a Stacking Fault in the Presence of Etch Pits. *J. Am. Chem. Soc.* 128 (2006) 3850–3851. <http://doi.org/10.1021/ja055408g>
- [62] Nemanick, E. J.; Hurley, P. T.; Webb, L. J.; Knapp, D. W.; Michalak, D. J.; Brunschwig, B. S.; Lewis, N. S., Chemical and Electrical Passivation of Single-Crystal Silicon(100) Surfaces through a Two-Step Chlorination/Alkylation Process. *J. Phys. Chem. B* 110 (2006) 14770–14778. <http://doi.org/10.1021/jp056773x>
- [63] Mizsei, J.; Pap, A. E.; Gillemot, K.; Battistig, G., Effect of deuterium on passivation of Si surfaces. *Appl. Surf. Sci.* 256 (2010) 5765–5770. <http://doi.org/10.1016/j.apsusc.2010.03.095>
- [64] Koehler, B. G.; Mak, C. H.; Arthur, D. A.; Coon, P. A.; George, S. M., Desorption kinetics of hydrogen and deuterium from Si(111) 7 × 7 studied using laser-induced thermal desorption. *J. Chem. Phys.* 89 (1988) 1709–1718. <http://doi.org/10.1063/1.455117>
- [65] Wampler, W. R.; Myers, S. M.; Follstaedt, D. M., Surface silicon-deuterium bond energy from gas-phase equilibration. *Physical review. B, Condensed matter* 48 (1993) 4492–4497. <http://doi.org/10.1103/PhysRevB.48.4492>
- [66] Cannara, R. J.; Brukman, M. J.; Cimatu, K.; Sumant, A. V.; Baldelli, S.; Carpick, R. W., Nanoscale Friction Varied by Isotopic Shifting of Surface Vibrational Frequencies. *Science* 318 (2007) 780–783. <http://doi.org/10.1126/science.1147550>
- [67] Ganguly, G.; Yamasaki, S.; Matsuda, A., Control of photodegradation in amorphous silicon: The effect of deuterium. *Philosophical magazine. B, Physics of*

- condensed matter. Structural, electronic, optical, and magnetic properties. 63 (1991) 281–292. <http://doi.org/10.1080/01418639108224445>
- [68] Lyu, X.; Ferrie, S.; Pivrikas, A.; MacGregor, M.; Ciampi, S., Sliding Schottky diode triboelectric nanogenerators with current output of 10^9A/m^2 by molecular engineering of Si(211) surfaces. *Nano Energy* (2022) 107658. <http://doi.org/10.1016/j.nanoen.2022.107658>
- [69] O’Leary, L. E.; Rose, M. J.; Ding, T. X.; Johansson, E.; Brunshwig, B. S.; Lewis, N. S., Heck Coupling of Olefins to Mixed Methyl/Thienyl Monolayers on Si(111) Surfaces. *J. Am. Chem. Soc.* 135 (2013) 10081–10090. <http://doi.org/10.1021/ja402495e>
- [70] Webb, L. J.; Michalak, D. J.; Biteen, J. S.; Brunshwig, B. S.; Chan, A. S. Y.; Knapp, D. W.; Meyer, H. M.; Nemanick, E. J.; Traub, M. C.; Lewis, N. S., High-Resolution Soft X-ray Photoelectron Spectroscopic Studies and Scanning Auger Microscopy Studies of the Air Oxidation of Alkylated Silicon(111) Surfaces. *J. Phys. Chem. B* 110 (2006) 23450–23459. <http://doi.org/10.1021/jp063366s>
- [71] Li, T.; Peiris, C. R.; Aragonès, A. C.; Hurtado, C.; Kicic, A.; Ciampi, S.; MacGregor, M.; Darwish, T.; Darwish, N., Terminal Deuterium Atoms Protect Silicon from Oxidation. *ACS Appl. Mater. Interfaces.* (2023). <http://doi.org/10.1021/acsmi.3c11598>
- [72] Ciampi, S.; Böcking, T.; Kilian, K. A.; James, M.; Harper, J. B.; Gooding, J. J., Functionalization of acetylene-terminated monolayers on Si(100) surfaces: A click chemistry approach. *Langmuir* 23 (2007) 9320–9329. <http://doi.org/10.1021/la701035g>
- [73] Zhang, J.; Ciampi, S., Shape and charge: Faraday’s ice pail experiment revisited. *ACS Cent. Sci* 6 (2020) 611–612. <http://doi.org/10.1021/acscentsci.0c00298>
- [74] Baio, J. E.; Weidner, T.; Brison, J.; Graham, D. J.; Gamble, L. J.; Castner, D. G., Amine terminated SAMs: Investigating why oxygen is present in these films. *J. Electron Spectrosc. Relat. Phenom.* 172 (2009) 2–8. <http://doi.org/10.1016/j.elspec.2009.02.008>
- [75] Cerofolini, G. F.; Galati, C.; Renna, L., Accounting for anomalous oxidation states of silicon at the Si/SiO₂ interface. *Surf. Interface Anal.* 33 (2002) 583–590. <http://doi.org/10.1002/sia.1424>
- [76] Zhang, S.; Ferrie, S.; Peiris, C. R.; Lyu, X.; Vogel, Y. B.; Darwish, N.; Ciampi, S., Common background signals in voltammograms of crystalline silicon electrodes are reversible silica–silicon redox chemistry at highly conductive surface sites. *J. Am. Chem. Soc.* 143 (2021) 1267–1272. <http://doi.org/10.1021/jacs.0c10713>
- [77] Ciampi, S.; James, M.; Michaels, P.; Gooding, J., Tandem "Click" Reactions at Acetylene-Terminated Si(100) Monolayers. *Langmuir* 27 (2011) 6940–6949.
- [78] Nagpal, R.; Gusain, M., Chapter 25 - Synthesis methods of quantum dots. In *Graphene, Nanotubes and Quantum Dots-Based Nanotechnology*, Al-Douri, Y., Ed. Woodhead Publishing: 2022; pp 599–630. <http://doi.org/10.1016/B978-0-323-85457-3.00006-2>
- [79] Park, J. Y.; Ogletree, D. F.; Thiel, P. A.; Salmeron, M., Electronic control of friction in silicon pn junctions. *Science* 313 (2006) 186–186. <http://doi.org/10.1126/science.1125017>

- [80] Qi, Y. B.; Park, J. Y.; Hendriksen, B. L. M.; Ogletree, D. F.; Salmeron, M., Electronic contribution to friction on GaAs: An atomic force microscope study. *Phys. Rev. B* 77 (2008). <http://doi.org/10.1103/PhysRevB.77.184105>
- [81] Budakian, R.; Putterman, S. J., Correlation between charge transfer and stick-slip friction at a metal-insulator interface. *Phys. Rev. Lett.* 85 (2000) 1000–1003. <http://doi.org/10.1103/PhysRevLett.85.1000>
- [82] Zhang, S.; Ferrie, S.; Lyu, X.; Xia, Y.; Darwish, N.; Wang, Z.; Ciampi, S., Absence of a relationship between surface conductivity and electrochemical rates: redox-active monolayers on Si(211), Si(111), and Si(110). *J. Phys. Chem. C* 125 (2021) 18197–18203. <http://doi.org/10.1021/acs.jpcc.1c05023>
- [83] Hurtado, C.; Ciampi, S., Oxidative Damage during the Operation of Si(211)-Based Triboelectric Nanogenerators. *Surfaces* 6 (2023) 281–290. <http://doi.org/10.3390/surfaces6030020>
- [84] Tan, C. S.; Hsieh, P. L.; Chen, L. J.; Huang, M. H., Silicon wafers with facet-dependent electrical conductivity properties. *Angew. Chem.* 56 (2017) 15339–15343. <http://doi.org/10.1002/anie.201709020>
- [85] Wei, Z.; Kan, Y.; Zhang, Y.; Chen, Y., The frictional energy dissipation and interfacial heat conduction in the sliding interface. *AIP Adv.* 8 (2018) 115321. <http://doi.org/10.1063/1.5054876>
- [86] Wang, L.; Liu, S.; Feng, X.; Zhang, C.; Zhu, L.; Zhai, J.; Qin, Y.; Wang, Z. L., Flexoelectronics of centrosymmetric semiconductors. *Nat. Nanotechnol.* 15 (2020) 661–667. <http://doi.org/10.1038/s41565-020-0700-y>
- [87] Ma, W.; Cross, L. E., Flexoelectric effect in ceramic lead zirconate titanate. *Appl. Phys. Lett.* 86 (2005) 072905. <http://doi.org/10.1063/1.1868078>
- [88] Yang, Z.; Jie, L.; Xinping, H.; Baojin, C.; Shutao, C.; Salem, D., Flexoelectric effect in PVDF-based polymers. *IEEE Trans. Dielectr. Electr. Insul.* 24 (2017) 727–731. <http://doi.org/10.1109/TDEI.2017.006273>
- [89] Hou, Y.; Tian, D.; Chu, B., Flexoelectric response of (1-x)BaTiO₃-xSrTiO₃ ceramics. *Ceram. Int.* 46 (2020) 12928–12932. <http://doi.org/10.1016/j.ceramint.2020.02.060>
- [90] Dong-Bo, Z.; Chang, K., Giant Flexoelectricity in Bent Silicon Thinfilms. *arXiv.org* (2020). <http://doi.org/10.48550/arxiv.2008.11452>
- [91] Sun, L.; Zhu, L.; Zhang, C.; Chen, W.; Wang, Z., Mechanical Manipulation of Silicon-based Schottky Diodes via Flexoelectricity. *Nano Energy* 83 (2021) 105855. <http://doi.org/10.1016/j.nanoen.2021.105855>
- [92] Jung, J., High-pressure induced plastic deformation in silicon single crystals. *Acta Crystallogr., Sect. A: Found. Crystallogr.* 40 (1984) C334. <http://doi.org/10.1107/S0108767384090152>
- [93] Tripathy, A.; Saravanakumar, B.; Mohanty, S.; Nayak, S. K.; Ramadoss, A., Comprehensive Review on Flexoelectric Energy Harvesting Technology: Mechanisms, Device Configurations, and Potential Applications. *ACS Appl. Electron. Mater.* 3 (2021) 2898–2924. <http://doi.org/10.1021/acsaelm.1c00267>
- [94] Laughton, M. A.; Warne, D. F., *Electrical engineer's reference book*. 6th ed.; Newnes: Oxford ;, 2003.
- [95] Han, T., *Photoelectric materials and devices*. World Scientific Publishing: Hackensack, New Jersey ;, 2021.

- [96] Barnes, J. R., Diodes. In *Robust Electronic Design Reference Book*, Barnes, J. R., Ed. Springer US: New York, NY, 2004; pp 321–350. http://doi.org/10.1007/1-4020-7830-7_16
- [97] Kolasinski, K. W., The mechanism of galvanic/metal-assisted etching of silicon. *Nanoscale Res. Lett.* 9 (2014) 1–8. <http://doi.org/10.1186/1556-276X-9-432>
- [98] Zheng, M.; Lin, S.; Xu, L.; Zhu, L.; Wang, Z. L., Scanning probing of the tribovoltaic effect at the sliding interface of two semiconductors. *Adv. Mater.* 32 (2020) e2000928. <http://doi.org/10.1002/adma.202000928>
- [99] Lin, S.; Shen, R.; Yao, T.; Lu, Y.; Feng, S.; Hao, Z.; Zheng, H.; Yan, Y.; Li, E., Surface states enhanced dynamic Schottky diode generator with extremely high power density over 1000 W m⁻². *Adv. Sci.* 6 (2019) 1901925. <http://doi.org/10.1002/advs.201901925>
- [100] Peter, L. M.; Walker, A. B.; Bein, T.; Hufnagel, A. G.; Kondofersky, I., Interpretation of photocurrent transients at semiconductor electrodes: Effects of band-edge unpinning. *J. Electroanal. Chem.* 872 (2020) 114234. <http://doi.org/10.1016/j.jelechem.2020.114234>
- [101] Jiang, R.; Boschloo, G., The impact of non-uniform photogeneration on mass transport in dye-sensitised solar cells. *J. Mater. Chem. A.* 6 (2018) 10264–10276. <http://doi.org/10.1039/C8TA02083C>

Chapter 6 – Conclusion and future outlook

6.1. Conclusion

Chapter 1 and 2 introduced the physical and chemical properties of semiconductors, their roles, and functions in DC-TENGs. Through a survey and summary of the recent research on semiconductor-based DC-TENGs, Chapter 1 identified the key focus areas and research questions of this thesis: enhancing the output current density while controlling the material wear caused by frictional forces and exploring the main mechanisms and influencing factors of triboelectricity.

Results presented in Chapter 3, mainly through the surface functionalization of silicon surfaces, indicate that the zero-bias current output of an out-of-equilibrium Schottky diode does not directly correlate with the microscale dynamics of stick-slip friction. Furthermore, the chapter also reports on the observation that silicon surfaces containing abundant electrical defects tend to produce larger DC outputs when integrated into Schottky diode TENGs. Additionally, the results of this chapter contain implicit evidence that the incorporation of flexoelectricity significantly enhances DC outputs, resulting in zero-bias current densities of up to 10^9 A/m² recorded on hydroxyl-terminated monolayer-coated Si(211) substrates.

In Chapter 4, the relationship between zero-bias current and friction, as well as between current and pressure in metal-monolayer-silicon Schottky diodes, both dynamic and static junctions, is investigated in further details. The findings suggest that besides the possible generation of e–h pairs induced by friction, the static charging of the semiconductor significantly contributes to the DC output of a sliding Schottky TENG. Furthermore, we demonstrate that significant flexovoltage exists under typical AFM experiment pressures, even when the tip is not sliding, particularly in systems exhibiting good TENG performances. This flexovoltage, revealed visually as "inverted" diode current–voltage characteristics, underscores the potential of simple static AFM I–V measurements as an effective tool for researching and screening optimal Schottky TENG materials. The results presented and discussed in this chapter indicate that the advancement of DC-TENGs will greatly benefit from a deeper understanding of flexoelectricity, and materials with higher flexovoltages may offer a promising avenue towards TENGs with reduced reliance on friction, thus

exhibiting greater resilience to performance degradation during prolonged operation.

Having demonstrated in Chapters 3 and 4 the power of silicon surface chemistry, and in particular of hydrosilylation reactions, to augment the output of DC-TENGs, Chapter 5 addresses the question as to what scope and practical value there is in replacing the starting material from Si–H to Si–D. The rationale of this isotopic switch is in the putative lower friction and higher stability of deuterium-terminated silicon crystals versus hydrogen-terminated silicon. The results presented in Chapter 5 indicate that TENGs constructed on Si(111)–D crystals exhibit comparable maximum current output to mainstream Si(111)–H devices and that the DC output of a Schottky diode TENG does not correlate with friction-induced energy release.

We also observed a higher density of surface electrical defects in Si–D compared to Si–H and confirmed the contribution of a flexoelectric term to the mechanic-to-electrical energy conversion mechanism. Ultimately, the main, and not small, advantage revealed by our experiments is that replacing hydrogen with deuterium enhances device longevity.

Generally speaking, via this study, we ruled out the tenet of a connection between tribocurrent and friction. We also found that surface states, functional groups on material surfaces, flexoelectric effects under high contact pressures, and friction-induced e–h pairs collectively influence the output of DC tribocurrent. We believe that our findings will start a new debate among physicists, chemists and nanotechnologists whose interests span from green energy, autonomous power sources, control of friction and wear, electrostatic actuation and interfacial charge transport.

6.2. Future Outlook

While this study has explored several of the most obvious factors that may influence tribocurrent and has conducted a detailed investigation into each of them, there are still many unknowns regarding the working principles of TENGs. The existing framework cannot satisfactorily explain working mechanisms or explain several of

the issues encountered. Therefore, future research efforts are needed to clarify on the working principles and influencing factors of DC-TENGs.

One notable pending question, for example, is on the role and magnitude of the flexoelectric effect, and whether or not this can be maximised to achieve higher current outputs. Quantitative research on how zero-bias current respond to materials' deformation under applied strain can be further explored to determine the role of flexoelectricity on the zero-bias output of TENGs. To achieve this, soft materials, such as silicon thin films, fabric textiles, can be used for experiments, where the current signal and the deformation of materials (strain applied) can be recorded simultaneously.

Also, due to the presence of moisture in the air, water may gradually adsorb onto the sample surface, potentially affecting the tribocurrent output. Some open questions need to be addressed, such as, is surface water involved? Is the charge of the aerial surface of water playing a role? Or a wet interface is just leading to a larger contact?

Additionally, semiconductors with large band gap, for instance, perovskite, GaN, and SiC, can be attempted to probe their impacts on triboelectric field, hence the zero-bias current signal. One thing that needs more attention is to ensure their surface roughness is similar by adjusting the etching process. They can also form a p-n junction with themselves or other semiconductors to further explore the electrical performance of p-n junctions based DC-TENGs, which is similar to Schottky diode based TENGs.

For existing laboratory-scale TENG models, appropriate scale-up experiments can be conducted to investigate whether they still exhibit good electrical performance on a larger scale. Various fabrication methods and numerous functionalized materials (surface chemistry) can be attempted to enhance energy conversion efficiency and reliability, and eventually find the appropriate one for a durable, stable, flexible, and even bio-compatible DC-TENGs. Moreover, integration with other emerging technologies such as flexible electronics, Internet-of-Things (IoT) devices, and energy storage technologies, could open up new applications in flexible energy harvesting devices, self-powered sensors, and even medical monitoring systems.

As research continues to push boundaries and manufacturing processes mature, silicon-based DC-TENGs might be able to catalyse a sustainable energy revolution, driving innovation, and empowering a future where renewable energy are cornerstones of our technological landscape.

Appendix I

Determination of the binding configuration for the 8-nonyn-1-ol monolayer

While 1-alkynes are known to selectively yield Si–C-bound monolayers when reacted with Si–H surfaces [1-3], we nonetheless considered the possibility of alternative binding configurations for the bi-functional, and asymmetric, 8-nonyn-1-ol monolayer-forming molecule. This molecule bears both acetylene and hydroxyl groups, hence there is the possible formation of either Si=C–C or Si–O–C/Si–C(OH) surface bridges, as well as both configurations potentially coexisting. To this end we designed control experiments, shown in Figure 3.2, which rely on the orthogonality of the copper (I)-catalyzed alkyne–azide cycloaddition (CuAAC) reaction to detect the presence (or absence) of a free alkyne functionality at the monolayer distal end. An azide-tagged redox-active ferrocene molecule was thus reacted on (111)- and (211)-oriented silicon electrodes coated under UV-assisted conditions with either 1,8-nonadiyne or 8-nonyn-1-ol. By means of cyclic voltammetry-based measurements of the Faradaic charge for CuAAC-reacted electrodes we were able to directly measure the surface density of surface-confined ferrocene molecules. Using the 1,8-nonadiyne system as the reference system – a system that due to the adsorbate’s symmetry can only expose terminal acetylenes – quantitative electrochemical information allowed us to infer that almost all surface-confined molecules in a 8-nonyn-1-ol monolayer have hydroxyl units as their terminal groups (Figure 3.2). This finding indicates, as depicted in Scheme 3.1 (Chapter 3), a prevalent Si–C-bound configuration at the buried monolayer interface. This conclusion is reinforced by water contact angle measurements (Figure 3.7), which reveal that surface samples made from 8-nonyn-1-ol are significantly more hydrophilic than the 1,8-nonadiyne surface. A larger wettability (54° vs 74°, Figure 3.7) is consistent with a hydroxyl-terminated monolayer.

References

- [1] Ciampi, S.; Böcking, T.; Kilian, K. A.; James, M.; Harper, J. B.; Gooding, J. J., Functionalization of acetylene-terminated monolayers on Si(100) surfaces: A click chemistry approach. *Langmuir* 23 (2007) 9320–9329. <http://doi.org/10.1021/la701035g>
- [2] Sieval, A. B.; Opitz, R.; Maas, H. P. A.; Schoeman, M. G.; Meijer, G.; Vergeldt, F. J.; Zuilhof, H.; Sudhölter, E. J. R., Monolayers of 1-alkynes on the H-terminated Si(100) surface. *Langmuir* 16 (2000) 10359–10368. <http://doi.org/10.1021/la001109n>
- [3] Ng, A.; Ciampi, S.; James, M.; Harper, J. B.; Gooding, J. J., Comparing the reactivity of alkynes and alkenes on silicon 100 surfaces. *Langmuir* 25 (2009) 13934–13941. <http://doi.org/10.1021/la901526e>

Appendix II

Estimation of AFM platinum tip–silicon contact area

The DMT (Derjaguin–Muller–Toporov) model of solid adhesion is generally suitable for hard and weakly adhesive materials [1], such as silicon. The contact area estimated by this model is described as:

$$A = \pi \left\{ \frac{R}{K} (L + 2\pi R\gamma) \right\}^{\frac{2}{3}}$$

where

R is the tip radius, K is the reduced Young's modulus, L is the normal applied force, and $2\pi R\gamma$ is the adhesion force.

The adhesion force is obtained by averaging data from multiple F–D (force–distance) curves.

The reduced Young's modulus (K) is given by:

$$\frac{1}{K} = \frac{4}{3} \left(\frac{1 - \nu_1^2}{E_1} + \frac{1 - \nu_2^2}{E_2} \right)$$

where E is Young's modulus, and ν denotes the Poisson ratio. For silicon and platinum Poisson ratios are 0.222 and 0.395, respectively, and the Young's modulus are 162.9 GPa and 177.3 GPa, respectively [2]. The reduced Young's modulus is therefore 70.78 GPa. The experimental contact areas varied in the range 70–100 nm², the actual sample value was used to correct in each case absolute currents into current densities.

Appendix II

Table S1. Parameters for contact area and the current density estimation

	Molecule	I_{Max}	F_{Adhesion} (nN)	Load (nN)	R_{tip} (nm)	A_{Contact} (nm ²)	Current density (A/m ²)
Si(111)	1-nonanol	8.1 pA	262.1	365.0	19.8	98.4	8.2×10^4
	1-nonyne	3.1 pA	181.9			89.9	3.4×10^4
	8-nonyl-1-ol	3.0 nA	178.0			89.4	3.4×10^7
	1,8-nonadiyne	46.9 pA	238.5			96.0	4.9×10^5
Si(211)	1-nonanol	138.0 pA	37.5	365.0	18.9	71.0	1.9×10^6
	1-nonyne	30.2 pA	67.3			74.5	4.1×10^5
	8-nonyl-1-ol	349.0 nA	39.8			71.3	4.9×10^9
	1,8-nonadiyne	78.7 pA	72.0			75.0	1.0×10^6

References

- [1] Park, J. Y.; Salmeron, M., Fundamental aspects of energy dissipation in friction. *Chem. Rev.* 114 (2014) 677–711. <http://doi.org/10.1021/cr200431y>
- [2] Hassel Ledbetter, S. K., Monocrystal elastic constants and derived properties of the cubic and the hexagonal elements. In *Handbook of elastic properties of solids, liquids and gases*, M. Levy, H. E. B., R.R. Stern, L. Furr, V. Keppens, Ed. Academic Press: San Diego, 2001; pp 97–106.

Appendix III

Statement of Contribution

Statement of contributions for:

Xin Lyu.; Stuart Ferrie.; Almantas Pivrikas.; Melanie MacGregor.; Simone Ciampi., Sliding Schottky diode triboelectric nanogenerators with current output of 10^9 A/m² by molecular engineering of Si(211) surfaces. Nano Energy (2020), 78, 105210. Paper included in Chapter 3.

I, Xin Lyu, as the first author, performed surface functionalization experiments and AFM tests, collected and analyzed relevant data, drafted the first version, and prepared the necessary figures and schematics for the paper, except for the contributions of co-authors as specified below.

Stuart Ferrie designed the methodology and processed the data using related software.

Almantas Pivrikas analyzed the photocurrent mapping (PCM) data and validate it.

Melanie MacGregor performed XPS analysis.

Simone Ciampi designed the project, supervised the project, interpreted the data and co-wrote the manuscript.

Co-author's signatures:

Stuart Ferrie

Almantas Pivrikas

Melanie MacGregor

Simone Ciampi

Statement of contributions for:

Xin Lyu.; Melanie MacGregor.; Jun Liu.; Nadim Darwish.; Simone Ciampi., Direct-current output of silicon–organic monolayer–platinum Schottky TENGs: Elusive friction-output relationship. *Nano Energy* (2023), 224, 108627. Paper included in Chapter 4.

I, Xin Lyu, as the first author, performed surface functionalization experiments and AFM tests, collected and analyzed relevant data, drafted the first version, and prepared the necessary figures and schematics for the paper, except for the contributions of co-authors as specified below.

Melanie MacGregor performed XPS analysis.

Jun Liu, Nadim Darwish and Simone Ciampi designed the project, supervised the project, interpreted the data and co-wrote the manuscript.

Co-author's signatures:

Jun Liu

Melanie MacGregor

Nadim Darwish

Simone Ciampi

Statement of contributions for:

Xin Lyu.; Simone Ciampi., Improving the performances of direct-current triboelectric nanogenerators with surface chemistry. *Curr. Opin. Colloid Interface Sci.* 61 (2022). Paper included in Chapter 1.

I, Xin Lyu, as the first author, collected relevant materials, outlined the structure of the paper, drafted the first version, and prepared the necessary figures for the paper, except for the contributions of co-authors as specified below.

Simone Ciampi designed the project, supervised the project, interpreted the data and co-wrote the manuscript.

Co-author's signatures:

Simone Ciampi

Statement of contributions for:

Lyu, X., MacGregor, Darwish, N. & Ciampi, S. Silicon-based triboelectric nanogenerators: surface chemistry isotope effects on the device performances and durability. Friction (Under review). Paper included in Chapter 5.

I, Xin Lyu, as the first author, collected relevant materials, outlined the structure of the paper, drafted the first version, and prepared the necessary figures for the paper, except for the contributions of co-authors as specified below.

Melanie MacGregor performed XPS analysis.

Simone Ciampi and Nadim Darwish designed the project, supervised the project, interpreted the data and co-wrote the manuscript.

Co-author's signatures:

Melanie Macgregor

Nadim Darwish

Simone Ciampi

Appendix IV

Copyright Permission



Sequentially Deposited versus Conventional Nonfullerene Organic Solar Cells: Interfacial Trap States, Vertical Stratification, and Exciton Dissociation

Author: Artem A. Bakulin, Richard H. Friend, Yana Vaynzof, et al

Publication: Advanced Energy Materials

Publisher: John Wiley and Sons

Date: Oct 30, 2019

© 2019 The Authors. Published by WILEY-VCH Verlag GmbH & Co. KGaA, Weinheim.

Open Access Article

This is an open access article distributed under the terms of the [Creative Commons CC BY](#) license, which permits unrestricted use, distribution, and reproduction in any medium, provided the original work is properly cited.

You are not required to obtain permission to reuse this article.

For an understanding of what is meant by the terms of the Creative Commons License, please refer to [Wiley's Open Access Terms and Conditions](#).

Permission is not required for this type of reuse.

Wiley offers a professional reprint service for high quality reproduction of articles from over 1400 scientific and medical journals. Wiley's reprint service offers:

- Peer reviewed research or reviews
- Tailored collections of articles
- A professional high quality finish
- Glossy journal style color covers
- Company or brand customisation
- Language translations
- Prompt turnaround times and delivery directly to your office, warehouse or congress.

Please contact our Reprints department for a quotation. Email corporatesales@wiley.com or corporatesalesusa@wiley.com or corporatesalesDE@wiley.com.

© 2024 Copyright - All Rights Reserved | [Copyright Clearance Center, Inc.](#) | [Privacy statement](#) | [Data Security and Privacy](#) | [For California Residents](#) | [Terms and Conditions](#)
Comments? We would like to hear from you. E-mail us at customer-care@copyright.com

License Number 5726850684392

[Printable Details](#)

License date Feb 12, 2024

Licensed Content

Licensed Content Publisher Elsevier
Licensed Content Publication Journal of Electroanalytical Chemistry
Licensed Content Title Interpretation of photocurrent transients at semiconductor electrodes: Effects of band-edge unpinning
Licensed Content Author Laurence M. Peter, Alison B. Walker, Thomas Bein, Alexander G. Hufnagel, Ilina Kondofersky
Licensed Content Date Sep 1, 2020
Licensed Content Volume 872
Licensed Content Issue n/a
Licensed Content Pages 1

Order Details

Type of Use reuse in a thesis/dissertation
Portion figures/tables/illustrations
Number of figures/tables/illustrations 1
Format electronic
Are you the author of this Elsevier article? No
Will you be translating? No

About Your Work

Title of new work Direct-current Triboelectricity from Miniaturised Sliding Metal-monolayer-semiconductor Contacts
Institution name Curtin University
Expected presentation date Jun 2024

Additional Data

Portions Figure. 1

Requestor Location

Requestor Location Mr. Xin Lyu
 Bld 500, Kent St
 Curtin University
 Bentley, 6102
 Australia
 Attn: Xin Lyu

Tax Details

Publisher Tax ID GB 494 6272 12

Appendix IV

LICENSED CONTENT			
Publication Title	Science	Country	United States of America
Date	01/01/1880	Rightholder	American Association for the Advancement of Science
Language	English	Publication Type	Journal
REQUEST DETAILS			
Portion Type	Image/photo/illustration	Distribution	Worldwide
Number of Images / Photos / Illustrations	1	Translation	Original language of publication
Format (select all that apply)	Electronic	Copies for the Disabled?	No
Who Will Republish the Content?	Academic institution	Minor Editing Privileges?	No
Duration of Use	Life of current edition	Incidental Promotional Use?	No
Lifetime Unit Quantity	Up to 499	Currency	USD
Rights Requested	Main product		
NEW WORK DETAILS			
Title	Direct-current Triboelectricity from Miniaturised Sliding Metal-monolayer-semiconductor Contacts	Institution Name	Curtin University
Instructor Name	Simone Clampi	Expected Presentation Date	2024-06-30
ADDITIONAL DETAILS			
Order Reference Number	N/A	The Requesting Person / Organization to Appear on the License	Xin Lyu
REQUESTED CONTENT DETAILS			
Title, Description or Numeric Reference of the Portion(s)	Figure. 1	Title of the Article / Chapter the Portion Is From	Electronic Control of Friction in Silicon pn Junctions
Editor of Portion(s)	N/A	Author of Portion(s)	Jeong Young Park, D. F. Ogletree, P. A. Thiel, M. Salmeron
Volume / Edition	313	Issue, if Republishing an Article From a Serial	5784
Page or Page Range of Portion	186	Publication Date of Portion	2006-07-14

[Print License](#)

Fundamental Aspects of Energy Dissipation in Friction
 Author: Jeong Young Park, Miquel Salmeron
 Publication: Chemical Reviews
 Publisher: American Chemical Society
 Date: Jan 1, 2014
Copyright © 2014, American Chemical Society

PERMISSION/LICENSE IS GRANTED FOR YOUR ORDER AT NO CHARGE

This type of permission/license, instead of the standard Terms and Conditions, is sent to you because no fee is being charged for your order. Please note the following:

- Permission is granted for your request in both print and electronic formats, and translations.
- If figures and/or tables were requested, they may be adapted or used in part.
- Please print this page for your records and send a copy of it to your publisher/graduate school.
- Appropriate credit for the requested material should be given as follows: "Reprinted (adapted) with permission from (COMPLETE REFERENCE CITATION). Copyright (YEAR) American Chemical Society." Insert appropriate information in place of the capitalized words.
- One-time permission is granted only for the use specified in your RightsLink request. No additional uses are granted (such as derivative works or other editions). For any uses, please submit a new request.

If credit is given to another source for the material you requested from RightsLink, permission must be obtained from that source.

BACK
CLOSE WINDOW

Appendix IV

License Number	5726870840887	Printable Details	
License date	Feb 13, 2024		
Licensed Content		Order Details	
Licensed Content Publisher	Elsevier	Type of Use	reuse in a thesis/dissertation
Licensed Content Publication	Elsevier Books	Portion	figures/tables/illustrations
Licensed Content Title	Structural Health Monitoring (SHM) in Aerospace Structures	Number of figures/tables/illustrations	1
Licensed Content Author	W. Huang,F.-G. Yuan,X. Jiang	Format	electronic
Licensed Content Date	Jan 1, 2016	Are you the author of this Elsevier chapter?	No
Licensed Content Pages	30	Will you be translating?	No
About Your Work		Additional Data	
Title of new work	Direct-current Triboelectricity from Miniaturised Sliding Metal-monolayer-semiconductor Contacts	Portions	Figure. 5.1
Institution name	Curtin University		
Expected presentation date	Jun 2024		
Requestor Location		Tax Details	
Requestor Location	Mr. Xin Lyu Bld 500, Kent St Curtin University Bentley, 6102 Australia Attn: Xin Lyu	Publisher Tax ID	GB 494 6272 12

License Number	5734590881455	Printable Details	
License date	Feb 23, 2024		
Licensed Content		Order Details	
Licensed Content Publisher	Springer Nature	Type of Use	Thesis/Dissertation
Licensed Content Publication	Nature Nanotechnology	Requestor type	academic/university or research institute
Licensed Content Title	Flexoelectronics of centrosymmetric semiconductors	Format	electronic
Licensed Content Author	Longfei Wang et al	Portion	figures/tables/illustrations
Licensed Content Date	Jun 22, 2020	Number of figures/tables/illustrations	1
		Would you like a high resolution image with your order?	no
		Will you be translating?	no
		Circulation/distribution	100 - 199
		Author of this Springer Nature content	no
About Your Work		Additional Data	
Title of new work	Direct-current Triboelectricity from Miniaturised Sliding Metal-monolayer-semiconductor Contacts	Portions	Figure. 1
Institution name	Curtin University		
Expected presentation date	Jun 2024		
Requestor Location		Tax Details	
Requestor Location	Mr. Xin Lyu Bld 500, Kent St Curtin University Bentley, 6102 Australia Attn: Xin Lyu		

Appendix IV

Your confirmation email will contain your order number for future reference.

License Number 5736320148666

[Printable Details](#)

License date Feb 26, 2024

Licensed Content

Licensed Content Publisher Springer Nature
Licensed Content Publication Springer eBook
Licensed Content Title Basic Properties of the Silicon Lattice
Licensed Content Author Viktor Sverdlov
Licensed Content Date Jan 1, 2011

Order Details

Type of Use Thesis/Dissertation
Requestor type academic/university or research institute
Format electronic
Portion figures/tables/illustrations
Number of figures/tables/illustrations 1
Will you be translating? no
Circulation/distribution 100 - 199
Author of this Springer Nature content no

About Your Work

Title of new work Direct-current Triboelectricity from Miniaturised Sliding Metal-monolayer-semiconductor Contacts
Institution name Curtin University
Expected presentation date Jun 2024

Additional Data

Portions Figure. 4.1

Requestor Location

Requestor Location Mr. Xin Lyu
Bld 500, Kent St
Curtin University

Tax Details

Bentley, 6102
Australia
Attn: Xin Lyu

Your confirmation email will contain your order number for future reference.

License Number 5736320363019

[Printable Details](#)

License date Feb 26, 2024

Licensed Content

Licensed Content Publisher Elsevier
Licensed Content Publication Electrochimica Acta
Licensed Content Title Etching mechanism and atomic structure of H-Si(111) surfaces prepared in NH₄F
Licensed Content Author P. Allongue, V. Kieling, H. Gerischer
Licensed Content Date Jul 1, 1995
Licensed Content Volume 40
Licensed Content Issue 10
Licensed Content Pages 8

Order Details

Type of Use reuse in a thesis/dissertation
Portion figures/tables/illustrations
Number of figures/tables/illustrations 1
Format electronic
Are you the author of this Elsevier article? No
Will you be translating? No

About Your Work

Title of new work Direct-current Triboelectricity from Miniaturised Sliding Metal-monolayer-semiconductor Contacts
Institution name Curtin University
Expected presentation date Jun 2024

Additional Data

Portions Figure. 8

Requestor Location

Requestor Location Mr. Xin Lyu
Bld 500, Kent St
Curtin University

Tax Details

Publisher Tax ID GB 494 6272 12

Bentley, 6102
Australia
Attn: Xin Lyu

Illuminating Silicon Surface Hydrosilylation: An Unexpected Plurality of Mechanisms



Author: Jillian M. Buriak
Publication: Chemistry of Materials
Publisher: American Chemical Society
Date: Jan 1, 2014

Copyright © 2014, American Chemical Society

PERMISSION/LICENSE IS GRANTED FOR YOUR ORDER AT NO CHARGE

This type of permission/license, instead of the standard Terms and Conditions, is sent to you because no fee is being charged for your order. Please note the following:

- Permission is granted for your request in both print and electronic formats, and translations.
- If figures and/or tables were requested, they may be adapted or used in part.
- Please print this page for your records and send a copy of it to your publisher/graduate school.
- Appropriate credit for the requested material should be given as follows: "Reprinted (adapted) with permission from {COMPLETE REFERENCE CITATION}. Copyright {YEAR} American Chemical Society." Insert appropriate information in place of the capitalized words.
- One-time permission is granted only for the use specified in your RightsLink request. No additional uses are granted (such as derivative works or other editions). For any uses, please submit a new request.

If credit is given to another source for the material you requested from RightsLink, permission must be obtained from that source.

[BACK](#)

[CLOSE WINDOW](#)

Your confirmation email will contain your order number for future reference.

License Number 5736320918639

[Printable Details](#)

License date Feb 26, 2024

Licensed Content

Licensed Content Publisher Elsevier
 Licensed Content Publication Elsevier Books
 Licensed Content Title Encapsulation Technologies for Electronic Applications
 Licensed Content Author Haleh Ardebili, Jiawei Zhang, Michael G. Pecht
 Licensed Content Date Jan 1, 2019
 Licensed Content Pages 57

Order Details

Type of Use reuse in a thesis/dissertation
 Portion figures/tables/illustrations
 Number of figures/tables/illustrations 1
 Format electronic
 Are you the author of this Elsevier chapter? No
 Will you be translating? No

About Your Work

Title of new work Direct-current Triboelectricity from Miniaturised Sliding Metal-monolayer-semiconductor Contacts
 Institution name Curtin University
 Expected presentation date Jun 2024

Additional Data

Portions structure of atomic force microscopy

Requestor Location

Requestor Location Mr. Xin Lyu
 Bld 500, Kent St
 Curtin University
 Bentley, 6102
 Australia
 Attn: Xin Lyu

Tax Details

Publisher Tax ID GB 494 6272 12